Diplomarbeit

Multiskalenmodellierung von verdünnten polymeren Flüssigkeiten durch stochastische und Fokker-Planck-basierte Methoden

(Multiscale Modelling of Dilute Polymeric Fluids with Stochastic and Fokker-Planck-based Methods)

angefertigt am
Institut für Numerische Simulation

vorgelegt der
Mathematisch-Naturwissenschaftlichen Fakultät der
Rheinischen Friedrich-Wilhelms-Universität Bonn

September 2010

von

Alexander Rüttgers

aus

Düren

Danksagung

Contents

Einleitung

1.1 Motivation

Nicht-Newtonsche Fluide

Im Alltag begegnet man häufig Fließvorgängen in verschiedenster Form deren Entstehen und Verständnis die Menschheit schon immer fasziniert hat. Die bekannten Navier-Stokes Gleichungen erlauben es uns, Flüssigkeiten und Gase mathematisch zu beschreiben, die zur Klasse der *Newtonschen Fluide* gehören. Ein Newtonsches Fluid erfüllt Newtons Gesetz der Viskosität, wonach die im Fluid auftretende Spannung proportional zur ausgeübten Belastung ist. Die Viskosität bezeichnet in diesem Zusammenhang die Proportionalitätskonstante. Zu den Newtonschen Fluiden zählen Wasser sowie die meisten Gase.

Die Fortschritte im Bereich der chemischen Industrie im 20. Jahrhundert führten zur Entwicklung von komplexen Fluiden, die durch die klassischen Gleichungen nicht korrekt beschrieben werden. Beispiele dafür sind Farben, Maschinenöle mit additiven Zusätzen, Zahnpasta oder Shampoos. Sogar viele Flüssigkeiten in der Natur wie Eiweiß und Blut beziehungsweise alle Fluide mit einer Mikrostruktur größer als die atomare Struktur erfüllen Newtons Gesetz nicht. Alle Fluide, deren Viskosität einen komplexeren Zusammenhang aufweist, werden daher als *nicht-Newtonsch* bezeichnet. Der Chemieprofessor Eugene Bingham prägte 1920 den Begriff *Rheologie* für das Studium dieser nicht-Newtonschen Fluide.

Eine wichtige Klasse innerhalb der nicht-Newtonschen Fluide stellen die Polymerflüssigkeiten dar, mit denen sich diese Arbeit insbesondere befassen wird. Wir stellen uns eine Polymerflüssigkeit als ein Newtonsches Fluid vor, das zusätzlich langkettige Moleküle enthält. Durch den Strömungswiderstand im Fluid werden die Moleküle gedehnt oder gestaucht und richten sich gemäß der Strömung aus. Da die Moleküle wieder ihren Grundzustand anzunehmen versuchen, führt dies zu einer elastischen Kraft, die durch einen makroskopischen Spannungstensor beschrieben wird. Da Polymerflüssigkeiten demnach nicht nur viskose sondern auch elastische Eigenschaften aufweisen, bezeichnet man sie auch als *viskoelastische Fluide*.

Experimentelle Effekte

Wir veranschaulichen die Andersartigkeit zwischen Newtonschen und nicht-Newtonschen Flüssigkeiten durch mehrere Experimente.

Ein bemerkenswerter Unterschied wird durch den *Weißenberg-Effekt* beschrieben, bei dem man einen rotierenden Stab jeweils in einem Newtonschen und einem viskoelastischen Fluid betrachtet. Im Newtonschen Fluid entstehen Zentrifugalkräfte, die die Flüssigkeit vom Stab wegdrücken. Anders ist dies beim nicht-Newtonschen Fluid, in dem die Molekülketten in Richtung des rotierenden Stabes gezogen werden, wodurch sich die ganze Flüssigkeit entgegen der Schwerkraft am Stab hinaufzieht (siehe Abbildung 1.1 (a)). Wir können diesen Effekt in der

(a) Weißenberg-Effekt (siehe Psidot [76]).
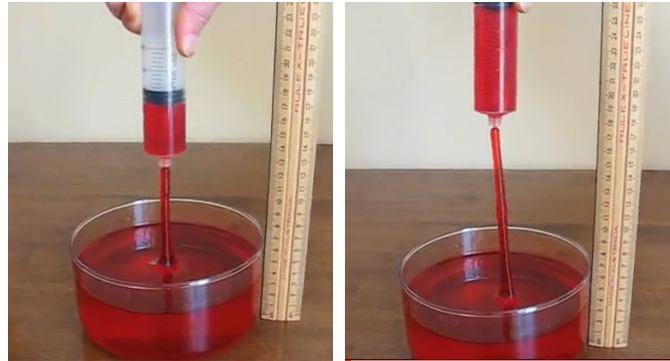
(b) Siphon-Effekt (siehe Psidot [74]).

Abbildung 1.1: Durch ihre elastischen Eigenschaften können sich viskoelastische Fluide entgegen der Schwerkraft bewegen.

(a) Barus-Effekt (siehe Psidot [75, 77]).

(b) Verdickungseffekt auf einem Lautsprecher (siehe Bend [7]).

Abbildung 1.2: Der Barus-Effekt tritt durch Normalspannungsdifferenzen auf. Für Maisstärke in Wasser beobachten wir eine Erhöhung der Viskosität unter Scherung.

Theorie durch unterschiedliche Normalspannugen in verschiedene Richtungen erklären, wodurch Zugspannung in Richtung des Rührstabs entsteht.

Der Effekt eines *röhrenlosen Siphons* veranschaulicht das Auftreten von starken elastischen Kräften, wenn man eine Polymerflüssigkeit in eine Richtung dehnt. Wird eine nadellose Spritze in ein nicht-Newtonsches Fluid getaucht und ein Teil der Flüssigkeit eingesaugt, kann der Einsaugvorgang selbst dann fortgesetzt werden, wenn die Spritze wieder aus dem Fluid entfernt wird (siehe Abbildung 1.1 (b)). Im Falle eines Newtonschen Fluids funktioniert dieser Vorgang nicht, da der Wasserstrahl sofort abreißt, wenn man die Spritze herausnimmt.

Ein weiterer Effekt in Verbindung mit Normalspannungen ist der sogenannte *Barus-Effekt*. Wenn ein viskoelastisches Fluid eine schmale Röhre verlässt, so führt dies zu einer Strangaufweitung über den Röhrendurchmesser hinaus. In Newtonschen Fluiden hängt dieser Effekt von der Reynoldszahl ab, tritt jedoch nur stark vermindert auf. Zum Vergleich veranschaulichen wir in Abbildung 1.2 (a) den Strangdurchmesser zwischen einem Newtonschen Fluid in rot und
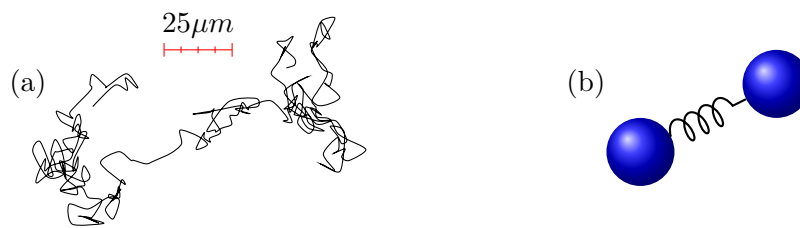
Abbildung 1.3: Gegenüberstellung eines Polymers und des vereinfachten Hantelmodells.

einem viskoelastischen Fluid in grün.

Wie zuvor erwähnt, existiert bei nicht-Newtonschen Fluiden ein komplexer Zusammenhang zwischen der auftretenden Spannung bei Scherung und der Rate der Scherung. Die meisten nicht-Newtonschen Fluide verändern dabei ihre Viskosität, die sich sowohl verringern als auch erhöhen kann. In Abbildung 1.2 (b) zeigen wir einen Verdickungseffekt für Maisstärke in Wasser, der durch einen mit 30 Hz vibrierenden Lautsprecher auftritt. Der Effekt zeigt sich durch das Auftreten von sonderbaren Strukturen auf der Fluidoberfläche.

Insgesamt veranschaulichen die Experimente verschiedene Phänomene, die ein mathematisches Modell wiedergeben muss. Darunter fallen Effekte der Viskositätsveränderung bei Scherung, Normalspannungsdifferenzen, das langsame Abklingen von Spannungen, kurzzeitige Geschwindigeitsüberschüsse im Fluid und Viskositätserhöhung unter Dehnung.

1.2 Modellierung viskoelastischer Fluide

Im Hinblick auf die Komplexität eines Polymers muss das mathematische Modell eingeschränkt werden, um überhaupt numerische Simulationen durchführen zu können. Trotzdem sollen dabei alle wichtigen Eigenschaften realer Polymere abgebildet werden. In dieser Arbeit machen wir zwei Vereinfachungen, indem wir

- das Polymer durch ein Hantelmodell darstellen, das aus zwei identischen Kugeln und einer elastischen Feder besteht (siehe Abbildung 1.3), und

- zwar die Interaktion zwischen dem Polymer und der umgebenden Newtonschen Flüssigkeit betrachten, jedoch keine Interaktion der Moleküle untereinander berücksichtigen.

Ein Hantelmodell mit einer geeigneten nichtlinearen Feder repräsentiert das einfachste Modell, das sowohl Molekülausrichtungen als auch Elastizitätseffekte durch Interaktion mit der Flüssigkeit wiedergibt. Der zweite Aspekt bedeutet, dass sich unsere Betrachtungen auf verdünnte Polymerflüssigkeiten konzentrieren. Das ist keine große Einschränkung, da die beschriebenen Effekte auch für Flüssigkeiten beobachtet werden, in denen nur geringe Polymerkonzentrationen auftreten. Trotzdem gibt es Ansätze, die die Interaktion von Molekülen berücksichtigen wie beispielsweise in Prakash und Öttinger [72] und Prakash [71] beschrieben. Diese Ansätze reduzieren den Aufenthaltsbereich der Moleküle auf ein beschränktes Volumen. Aufgrund ihrer Komplexität wurden diese Ansätze bisher nur auf analytisch bekannte Geschwindigkeitsfelder angewandt und nicht in praktischen Simulationen verwendet.

Makroskopische Modellierung

Ein viskoelastisches Fluid lässt sich durch das vorhandene Geschwindigkeitsfeld, den auftretenden Druck und einen zusätzlichen nicht-Newtonschen Spannungstensor beschreiben. Der Spannungstensor berücksichtigt den Polymeranteil an der Gesamtspannung. Allgemein basieren *makroskopische Modellierungsansätze* für nicht-Newtonsche Fluide darauf, den Navier-Stokes Gleichungen einen besonderen Spannungstensor hinzuzufügen, der durch eine differentielle Zustandsgleichung berechnet wird. Die meisten makroskopischen Gleichungen lassen sich durch Betrachtung der Kinetik eines Hantelmodells mit jeweiligem Federmodell herleiten. Die kinetischen Gleichungen werden dafür in eine geschlossene Zustandsgleichung für die makroskopische Spannung umgeformt, wodurch es nicht notwendig ist, weiterhin das mikroskopische Hantelmodell zu betrachten. Im Allgemeinen ist eine exakte Umformung in eine makroskopische Zustandsgleichung allerdings nicht möglich, es sei denn, man verwendet ein simples Federmodell wie bei der linearen Hooke-Feder und dem makroskopischen Oldroyd-B Modell. Aus diesem Grund muss das Hantelmodell noch weiter vereinfacht werden, was zu sogenannten *Schließungsansätzen* führt. Trotz des Fortschritts, der in den vergangenen dreißig Jahren in diesem Bereich erzielt worden ist, existieren immer noch keine zufriedenstellenden makroskopischen Gleichungen, die in der Lage sind, alle auftretenden Aspekte in verdünnten Polymerflüssigkeiten zu beschreiben.

Multiskalenansätze

Seit kurzem werden wesentlich fortgeschrittenere *Multiskalenansätze* verwendet, die die kinetischen Gleichungen des Hantelmodells direkt lösen, um damit die makroskopischen Spannungen zu bestimmen. Solche Ansätze vermeiden zusätzliche Fehler durch weitere Vereinfachungen und ermöglichen es, das Wissen über die konkrete Physik in die Bewegungsgleichung des Hantelmodells aufzunehmen. Da eine Brownsche Molekularbewegung auftritt, erhalten wir im Falle von dreidimensionalen Strömungen eine stochastische Differentialgleichung im sechsdimensionalen Raum. Die Gleichung weist sechs Dimensionen auf, da eine Hantel durch die räumliche Position $\vec{x}$ und durch ihre Ausrichtung $\vec{q}$ beschrieben wird. Die Verbindung zum makroskopischen Spannungstensor erfolgt als Erwartungswert über die aktuellen Hantelkonfigurationen mit Hilfe einer *Relation von Kramer*.

Weiterhin erlaubt die Theorie stochastischer Prozesse eine Umformulierung der stochastischen Differentialgleichung in eine sechsdimensionale, zeitabhängige Diffusionsgleichung für eine Wahrscheinlichkeitsdichtefunktion, die mit Hilfe deterministischer Verfahren gelöst werden kann. Allgemein bezeichnet man die Diffusionsgleichung als Fokker-Planck Gleichung.

Partikelbasierter Ansatz

Beide Multiskalenansätze sind vergleichsweise neu im Bereich der Rheologie, da sie im Hinblick auf den Speicherverbrauch und die Rechenzeit sehr teuer sind. 1993 wurde von Laso and Öttinger [53] die partikelbasierte *CONNFFESSIT*-Methode (**C**alculation **o**f **N**on-**N**ewtonian **F**low: **F**inite **E**lements and **S**tochastic **Si**mulation **T**echniques) entwickelt und auf zweidimensionale Strömungsprobleme angewendet. Der ursprüngliche CONNFFESSIT-Ansatz enthielt jedoch einige Nachteile, die zur Entwicklung von sogenannten „Mikro-Makro-Modellen der zweiten Generation" führten.

Gitterbasierter Ansatz

Eine gitterbasierte Methode der zweiten Generation stellt beispielsweise die Methode der *Brownschen Konfigurationsfelder* (BCF) dar, die 1997 von Hulsen et.al. [41] entwickelt worden ist. Bei der BCF-Methode ersetzt man die diskrete Menge von Polymeren durch feste Felder bezüglich ihrer Position im Fluid. Aus diesem Grund handelt es sich um einen Eulerschen Ansatz. Der wesentliche Vorteil im Vergleich zur ursprünglichen Methode besteht darin, dass der Spannungstensor einen glatten Verlauf im Strömungsgebiet besitzt, obwohl ein stochastisches Rauschen im zeitlichen Verlauf auftritt. Die BCF-Methode wurde beispielsweise von Bonvin [12] und von Vargas et.al. [90] für zweidimensionale Strömungsprobleme umgesetzt.

In den Jahren 2003 und 2004 stellten Lozinski und Chauvière [19, 20, 57, 58] einen Diskretisierungsansatz durch Spektralmethoden für die Fokker-Planck Gleichung vor. Aufgrund der Komplexität der Gleichung unterteilten sie das Lösen der Fokker-Planck Gleichung in zwei reduzierte Probleme, bei denen die Differentialoperatoren bezüglich $\vec{x}$ und $\vec{q}$ voneinander entkoppelt sind. Mit diesem Ansatz lösten sie zweidimensionale Strömungsprobleme (d.h. $\vec{x} \in \mathbb{R}^2$), bei denen die Molekülorientierung für die Fälle $\vec{q} \in \mathbb{R}^2$ und $\vec{q} \in \mathbb{R}^3$ untersucht worden ist. Im Jahr 2008 hat Knezevic [50] den Ansatz zur Entkoppelung der Differentialoperatoren auf dreidimensionale Stokes-Strömungen angewendet, wobei die Fokker-Planck Gleichung mit Hilfe von Spektralmethoden diskretisiert wird.

1.3 Überblick über die vorliegende Arbeit

Multiskalenbasierter Strömungslöser in 3D

In dieser Arbeit präsentieren wir erstmalig eine Koppelung eines existierenden, dreidimensionalen Strömungslösers für komplexe Geometrien mit einem stochastischen BCF-Ansatz zur Behandlung der vollen sechsdimensionalen, kinetischen Hantelgleichung. Der Strömungslöser NaSt3DGPF [2] verwendet Finite Differenzen zur Diskretisierung der Navier-Stokes Gleichungen, wobei für die Behandlung der konvektiven Terme Finite Volumen-Schemata höherer Ordnung wie VONOS, WENO oder ENO benutzt werden.

Um den Spannungstensor innerhalb des diskretisierten Strömungsgebietes zu berechnen, verwenden wir 8000 Konfigurationsfelder in jeder Gitterzelle, die die tatsächliche Hantelorientierung in dieser Zelle approximieren. Da dies die Komplexität des Problems im Vergleich zum alleinigen Lösen der Navier-Stokes Gleichungen stark erhöht, müssen wir unseren Ansatz parallelisieren. Beispielsweise werden wir ein Strömungsproblem mit 50^3 Gitterzellen untersuchen, wodurch sich $8000 \cdot 50^3 = 10^9$ stochastische Realisationen im Gesamtgebiet ergeben. Obwohl 8000 Realisationen pro Gitterzelle vergleichsweise gering erscheint, ist es im Hinblick auf das Lösen der Navier-Stokes Gleichungen wichtiger, dass der Spannungstensor innerhalb des Strömungsgebietes glatt ist, da nur die Divergenz des Spannungstensors für die Strömungsgleichungen von Relevanz ist. Die BCF-Methode stellt die Glattheit bezüglich des Ortes durch die Anwendung der gleichen Brownschen Kraft in jeder Gitterzelle sicher. Außerdem verweisen wir darauf, dass existierende 2D Ansätze mit der BCF-Methode zufriedenstellende Ergebnisse für das makroskopische Geschwindigkeitsfeld produzieren, obwohl nur 2000 Konfigurationsfelder pro Gitterzelle verwendet werden (vergleiche Vargas et.al. [90]).

Außerdem sei herausgestellt, dass der von uns verwendete BCF-Ansatz für den dreidimensio-

nalen Strömungslöser mehrere Vorteile gegenüber dem deterministischen Fokker-Planck-Ansatz bietet, da

- der stochastische Ansatz sehr robust im Hinblick auf die Komplexität der Strömung und die verwendete Weißenbergzahl[1] ist,

- der stochastische Ansatz sehr effizient parallelisiert werden kann und

- der Ansatz vergleichsweise günstig ist, sofern man nur an einer groben Approximation des Spannungstensorfelds interessiert ist.

Tatsächlich gibt es Untersuchungen von Chauvière und Lozinski [19] darüber, dass ein stochastischer Ansatz die Verwendung von Weißenbergzahlen erlaubt, die in dieser Höhe mit einem Fokker-Planck-Ansatz oder den schlechteren makroskopischen Ansätzen nicht mehr möglich sind. Im Gegensatz zum Spannungstensor weist die Fokker-Planck Gleichung bei hohen Weißenbergzahlen ein singuläres Verhalten auf, was eine feine Ortsdiskretisierung für ein numerisches Lösen erforderlich macht.

Nichtlineare FENE-Feder

Da sich unser Multiskalenansatz für das exakte Modellieren des physikalischen Systems eignet, verwenden wir zur Verbindung der Kugelmassen eine nichtlineare *FENE*-Feder (**F**initely **E**xtensible **N**onlinear **E**lastic), die 1972 von Warner [93] entwickelt worden ist. Diese beschränkt die Ausdehnung der Feder auf einen physikalisch korrekten, endlichen Wert. Dies hat jedoch eine Singularität der Feder am Rand des Definitionsbereiches zur Folge. Weiterhin besitzt die FENE-Feder aufgrund ihrer Komplexität kein makroskopisches Gegenstück, so dass wir in der Tat ein vollständiges Multiskalenproblem betrachten. Neben der FENE-Feder untersuchen wir noch einfachere Federmodelle wie das von Hooke und das FENE-P-Modell, um die Vorteile der verwendeten FENE-Feder herauszustellen. Für die beiden einfacheren Modelle existiert jeweils eine makroskopische Zustandsgleichung.

Homogene Strömungsprobleme

Obwohl das Hauptaugenmerk auf der Kopplung des instationären Strömungslösers mit dem BCF-Ansatz liegt, betrachten wir zusätzlich die Fokker-Planck-Gleichung für den Fall einer homogenen Strömung, um eine Validierung unserer Spannungstensorberechnungen und einen Vergleich mit dem stochastischen Ansatz zu ermöglichen. Wir verwenden dafür einen Spektralansatz in der Form von Lozinski [56]. Unsere Ergebnisse für homogene Strömungsfelder zeigen für das FP-Modell die gleichen Einschränkungen hinsichtlich Robustheit, einer möglichen Parallelisierung und dem Berechnungsaufwand, wie zuvor bereits erwähnt. Dies bestätigt unsere Wahl des stochastischen Ansatzes.

Weiter weisen wir darauf hin, dass im Falle eines homogenen Geschwindigkeitsfelds, bei dem die Geschwindigkeit analytisch bekannt ist, die Fokker-Planck Gleichung nicht von der Ortsvariablen $\vec{x}$ abhängt und sich das Problem abhängig von $\vec{q}$ auf zwei beziehungsweise drei Dimensionen reduziert.

---

[1] Eine dimensionslose Kennzahl, welche das Verhältnis zwischen der mikroskopischen und der makroskopischen Zeitskala angibt.

Eigene Beiträge

Wir fassen an dieser Stelle die wesentlichen Beiträge dieser Arbeit zusammen:

- Wir geben einen Überblick über die mikroskopische und makroskopische Modellierung von viskoelastischen Flüssigkeiten, über die modale und nodale Formulierung von Spektralmethoden und die Ansätze für stochastische Verfahren.

- Wir erweitern einen bestehenden Spektralmethodenansatz mit Legendre-Polynomen von Lozinski [56], um die Verwendung allgemeinerer Jacobi-Polynome zu ermöglichen.

- Wir präsentieren einen Algorithmus zur Erzeugung von Anfangskonfigurationen, die sich gemäß der FENE-Wahrscheinlichkeitsdichtefunktion verteilen.

- Wir implementieren den BCF-Ansatz in einen dreidimensionalen Navier-Stokes-Löser und diskutieren Möglichkeiten zur Randbehandlung der Konfigurationsfelder und Parallelisierung des Ansatzes.

- Wir zeigen erstmalig Simulationsergebnisse eines gekoppelten Navier-Stokes-BCF Systems. Die neuen Ergebnisse basieren auf einem nicht-homogenen, multiskalenbasierten, parallelen Strömungslöser, der komplexe Geometrien behandeln kann.

Aufbau der Arbeit

Die Arbeit ist wie folgt strukturiert:

Kapitel 2 liefert den theoretischen Hintergrund für die Simulation von rein Newtonschen, makroskopisch viskoelastischen und multiskalenbasierten viskoelastischen Fluiden. Wir analysieren die Nachteile verschiedener makroskopischer Ansätze und motivieren die Nutzung von Multiskalenansätzen.

Kapitel 3 führt in numerische Verfahren zur Behandlung von partiellen und stochastischen Differentialgleichungen ein. Wir diskutieren Finite Differenzen-Verfahren auf der Kugel und Spektralmethoden zur numerischen Behandlung deterministischer Gleichungen, sowie numerische Methoden zum Lösen von stochastischen Differentialgleichungen.

Kapitel 4 befasst sich mit homogenen Strömungsfeldern. Wir wenden die Spektralmethoden auf die 2D Fokker-Planck-Gleichungen an, diskutieren die Verwendung von Kugelflächenfunktionen für die 3D Fokker-Planck-Gleichung und implementieren Verfahren zur Zeitintegration von stochastischen Differentialgleichungen. Für die stochastischen Verfahren stellen wir eine Methode zur Erzeugung geeigneter Anfangskonfigurationen vor und diskutieren Möglichkeiten der Varianzreduktion.

Kapitel 5 beschäftigt sich mit dreidimensionalen, instationären, viskoelastischen Strömungsfeldern. Zunächst betrachten wir das gekoppelte Navier-Stokes-BCF Modell und analysieren die Vorteile gegenüber der CONNFFESSIT Methode. Anschließend konzentrieren wir uns auf die Orts- und Zeitdiskretisierung des Multiskalensystems und diskutieren die Randbehandlung der Konfigurationsfelder. Aufgrund der Komplexität des Problems parallelisieren wir unseren Ansatz und untersuchen das Scale-Up Verhalten.

Kapitel 6 beinhaltet unsere numerischen Ergebnisse. Wir präsentieren Ergebnisse für zwei-
und dreidimensionale homogene Scher- und Dehnungsströmungen und weiterhin für drei-
dimensionale, transiente Probleme wie die Strömung durch einen unendlichen Kanal,
eine Kontraktionsströmung im Verhältnis 4 zu 1 und die Umströmung einer Kugel. Im
Falle der homogenen Strömungsprobleme vergleichen wir den Spektralmethodenansatz
mit den stochastischen Berechnungen, analysieren verschiedene Feder-Modelle (FENE,
Hooke, FENE-P) und erzielen Ergebnisse für die stochastischen Rechnungen mit Wei-
ßenbergzahlen bis zu 10. Weiterhin validieren wir unser Navier-Stokes-BCF-Programm
durch Untersuchung einer Dehnungsströmung mit analytisch bekannter Lösung. Wir zei-
gen weiterhin, dass unser multiskalenbasierter Code für eine einfache Hooke-Feder das-
selbe Ergebnis wie eine Oldroyd-B Implementierung liefert. Zuletzt vergleichen wir die
weiteren instationären Rechnungen für die Kontraktionsströmung und die Umströmung
einer Kugel mit Ergebnissen in der Literatur, da es sich um klassische Benchmarkproble-
me handelt.

Kapitel 7 fasst die wesentlichen Ergebnisse dieser Arbeit zusammen und gibt einen Ausblick
auf zukünftige Fragestellungen und mögliche Erweiterungen.

1 Introduction

1.1 Motivation

Non-Newtonian Fluids

Fluid motion is a part of everyday experience and therefore has fascinated mankind for centuries. The well-known Navier-Stokes equations adequately describe a class of liquids and gases that is denoted as *Newtonian fluids*. For a Newtonian fluid we assume to fulfil Newton's law of viscosity, i.e. the exerted shear stress is proportional to the strain rate with the viscosity as proportionality constant. This fluid class contains water and most gases.

The development of the chemical industry in the 20th century resulted in various complex fluids that cannot be correctly described by classical fluid mechanics. For instance, this includes paint, engine oils with polymeric additives, toothpaste, and shampoo. Even worse, many fluids in nature like egg white and blood as well as all fluids with a microstructure larger in size than the atomic scale also violate Newton's law of viscosity. We denote all fluids that feature a more complex shear-stress relation as stated before as *non-Newtonian*. In the 1920's, chemistry professor Eugene Bingham coined the term *rheology* for the study of non-Newtonian fluids.

A very important subclass of non-Newtonian fluids are polymeric fluids which this thesis will concentrate on. Polymeric fluids consist of long-chain molecules immersed in a Newtonian fluid. Due to a drag force exerted by the liquid, polymeric molecules are stretched or compressed and change their orientation. As the molecules attempt to resume their initial configuration, this leads to an elastic force expressed by a macroscopic stress tensor. Consequently, since polymeric fluids do not only behave viscous as a Newtonian fluid but also feature elasticity effects as a solid, they are often called *viscoelastic fluids*.

Phenomena in Experiments

We illustrate the differences between Newtonian and non-Newtonian fluids by discussing several phenomena that are solely observed for viscoelastic fluids.

One of the most remarkable phenomena is the *Weissenberg effect*. In this experiment, a rotating rod is placed into a Newtonian as well as a viscoelastic fluid. In a Newtonian fluid the rotating motion induces a centrifugal force that pushes the fluid outward away from the rod. In contrast, the molecule chains of a viscoelastic fluid are pulled towards the rod so that the fluid climbs up the rod against gravity (cf. Figure 1.1 (a)). In theory, we explain this effect due to a non-zero normal stress difference that causes a tension in flow direction.

The *tubeless syphon experiment* exploits the occurrence of large elastic forces when extending a polymeric fluid. If we insert a syringe into a viscoelastic fluid, start to fill it with the fluid and simultaneously raise the syringe up, then the siphoning action still continues against gravity (cf. Figure 1.1 (b)). If we used a Newtonian liquid instead, the jet of fluid would immediately break.
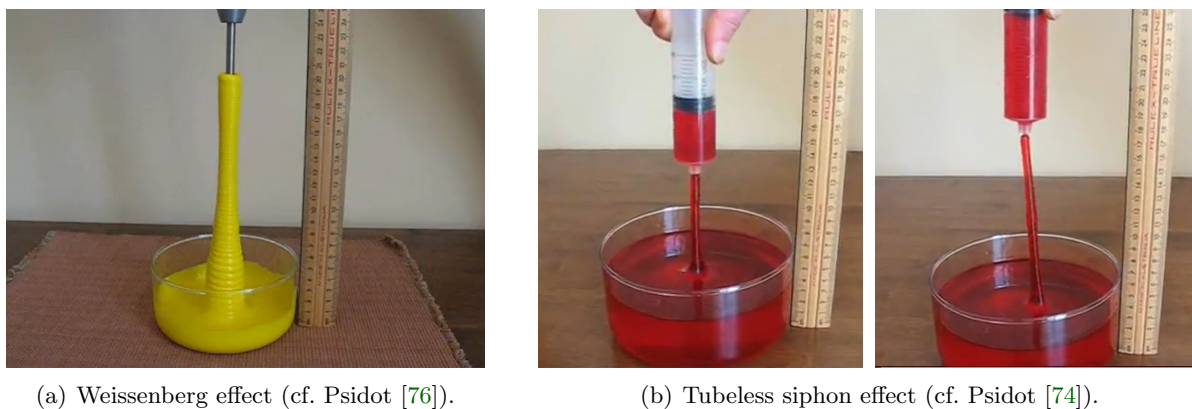
(a) Weissenberg effect (cf. Psidot [76]).   (b) Tubeless siphon effect (cf. Psidot [74]).

Figure 1.1: Viscoelastic fluids move against gravity due to their elastic behaviour.
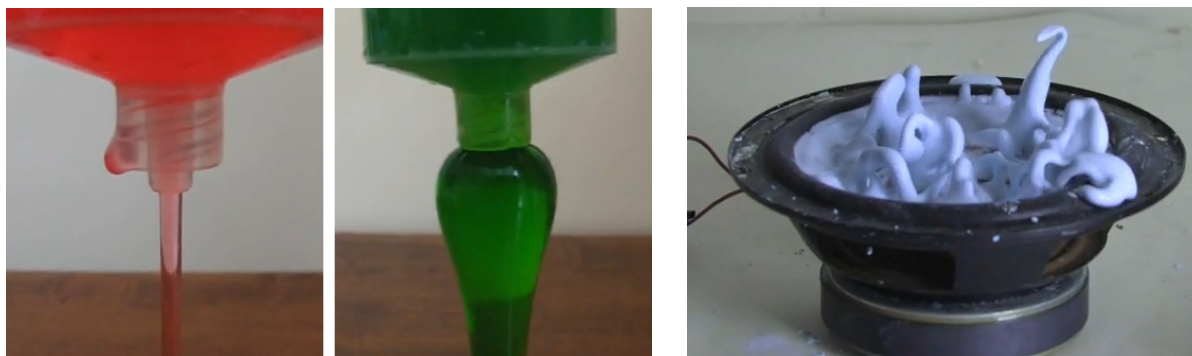
(a) Barus effect (cf. Psidot [75, 77]).   (b) Thickening effect on speaker (cf. Bend [7]).

Figure 1.2: Barus effect linked to non-zero normal stresses; shear thickening effect for corn starch.

A further effect that is linked to normal stresses is the *Barus effect*. When a viscoelastic fluid exits a small pipe, the jet that forms outside the pipe is much increased in diameter in contrast to the diameter of the opening. For Newtonian fluids, the effect depends on the Reynolds number but is strongly reduced. See Figure 1.2 (a) for a comparison of the Barus effect between water (dyed in red) and a viscoelastic fluid (dyed in green).

As mentioned before, a non-Newtonian fluid exhibits a complex relation between shear stress and strain rate. Most viscoelastic fluids are either *shear-thinning* or *shear-thickening* leading to a change of viscosity. In Figure 1.2 (b) we illustrate the effect of shear-thickening for corn starch in water that is put on a speaker cone vibrating at 30 Hz. The fluid is disturbed by the oscillations which lead to an increase in viscosity and formation of weird structures.

In conclusion, the experiments illustrate several phenomena that a mathematical model should necessarily describe. This includes shear-thinning or shear-thickening behaviour, non-zero normal stress differences, stress relaxation, velocity overshoots, and viscosity thickening effects under extensional flows.
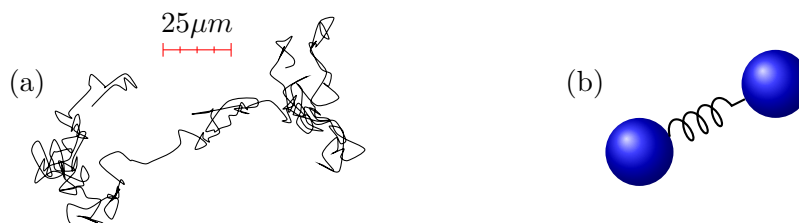
Figure 1.3: A real polymeric molecule in comparison with a simplified dumbbell model.

1.2 Modelling of Viscoelastic Fluids

In view of the complexity of polymeric molecules, a restriction to a simplified mathematical model is necessary that allows practicable numerical simulation but takes all essential characteristics of real molecules into account. Here, we apply two major restrictions:

- we represent the molecules with a dumbbell model that consists of two identical beads connected by an elastic spring (cf. Figure 1.3) and

- we model the interaction between the polymeric molecules and the Newtonian fluid but assume that the polymers have no interaction among each other.

A dumbbell model with an appropriate (nonlinear) spring force is the most simple polymeric model that adequately describes molecule orientation and elasticity effects caused by interaction with the Newtonian fluid.

Due to the second aspect, we concentrate on dilute polymeric fluids. This is no real restriction since the described phenomena can be clearly observed even for liquids with small polymeric concentrations. However, there have been attempts to incorporate molecule interactions which are denoted as excluded volume (EV) effects (cf. Prakash and Öttinger [72], Prakash [71]). Due to its complexity, the approach has only been applied to analytically known flow fields but not in practical simulations.

Macroscopic Modelling

A viscoelastic fluid is described by the velocity field, the pressure field, and an additional non-Newtonian stress tensor that represents the polymeric contribution to the stress. In general, *macroscopic modelling* of viscoelastic fluids consists of adding a special stress tensor to the Navier-Stokes equations and solving a further differential constitutive equation to compute the stress tensor components. Most macroscopic equations are derived by considering the kinetics of a dumbbell model connected with a more or less complex microscopic spring force and a reformulation in a constitutive equation in closed form for the macroscopic polymeric stress. Then it is unnecessary to further investigate the microscale of the problem. But in general, an equivalent macroscopic formulation is mostly lacking, except for the most simple spring forces (e.g. Hookean spring and the macroscopic Oldroyd-B model). For this reason, the kinetic models have to be simplified even further which leads to the so-called *closure approximations*. Despite the progress that has been made in the last thirty years, there still exists no satisfying macroscopic equation for correctly describing all aspects of dilute polymers.

Multiscale Approaches

More advanced *micro-macro approaches* have been recently introduced that directly solve the microscopic kinetic equations for a dumbbell molecule to obtain the macroscopic polymeric stress. Using this ansatz avoids further simplification errors and allows the inclusion of all knowledge of the physical system in the kinetic equations for the dumbbell model. The Brownian forces acting on the dumbbell are described by a stochastic process and give rise to a stochastic differential equation. Since we do not only require the spatial position $\vec{x}(t)$ of the dumbbells within the fluid domain but also their current orientation $\vec{q}(t)$ (i.e. $\vec{q}(t)$ represents the alignment of the dumbbells at time t) the problem is described in six dimensions. Then, *Kramer's expression* connects the macroscopic stress with the expectation value of the instantaneous dumbbell configurations.

Furthermore, the theory of stochastic processes allows for an alternative interpretation of the stochastic differential equation as a six-dimensional, time-dependent diffusion equation for a probability density function which can be solved deterministically. A common term for the diffusion equation in literature is *Fokker-Planck equation* (FP). Numerical methods that solve the kinematic equations of motion base either on a Lagrangian or on an Eulerian description of the system.

Lagrangian Description

The stochastic and the Fokker-Planck multiscale approach are comparatively new in rheology since they are very expensive in terms of computer memory and computation time. In 1993, Laso and Öttinger [53] introduced the particle-based, stochastic *CONNFFESSIT* method (**C**alculation **o**f **N**on-**N**ewtonian **F**low: **F**inite **E**lements and **S**tochastic **Si**mulation **T**echniques) and applied it to two-dimensional flow problems. The original CONNFFESSIT method exhibited several drawbacks which led to so-called "second generation micro-macro techniques" (cf. Lozinski et al. [59]).

Eulerian Description

Hulsen et al. [41] introduced in 1997 a grid based second generation technique called the *Brownian configuration field* (BCF) method. In the BCF method the discrete set of polymers is replaced by an ensemble of configuration fields with fixed spatial position $\vec{x}$ (i.e. an Eulerian approach). The BCF equation additionally includes a convective term to incorporate molecule movement. Its major advantage over the original method is that the additional stress tensor field is smooth in the physical flow space, although it exhibits stochastic noise in time. The BCF method has been successfully applied to flow problems in two dimensions (cf. Bonvin [12] or Vargas et al. [90]).

In 2003 and 2004, Lozinski and Chauvière [19, 20, 57, 58] introduced a spectral method approach for the numerical treatment of the Fokker-Planck equation. Considering the complexity of the problem, they proposed an operator splitting for the Fokker-Planck equation and decomposed the problem into two equations with respect to $\vec{x}$ and $\vec{q}$. Using this approach, they solved two-dimensional flow problems (i.e. $\vec{x} \in \mathbb{R}^2$) which contain dumbbell systems with orientation vectors $\vec{q} \in \mathbb{R}^2$ as well as $\vec{q} \in \mathbb{R}^3$. In 2008, Knezevic [50] recently applied the operator splitting

approach for the Fokker-Planck equation to three-dimensional Stokes flow problems and used spectral methods for the discretisation of the split FP equation.

1.3 About this Thesis

Multiscale Flow Solver in 3D

In this thesis, we present a first-time approach to couple an existing three-dimensional flow solver for complex geometries with a stochastic Brownian configuration field method for the full six-dimensional dumbbell equation. The flow solver NaSt3DGPF [2] employs finite differences to discretise the Navier-Stokes equations but uses high-order, finite volume-based schemes for the discretisation of the convective terms (e.g. VONOS, WENO, ENO).

For the computation of the polymeric stress in the discretised space, we place 8000 configuration fields or stochastic realisations in each grid cell to approximate the actual dumbbell configurations in that cell. As a consequence, we have to parallelise our algorithm since the complexity of the problem strongly increases in size in comparison to a purely Newtonian calculation in which we solely solve the Navier-Stokes equations. For instance, we will examine a flow problem with 50^3 grid cells in total which yields $8000 \cdot 50^3 = 10^9$ stochastic realisations in total. 8000 realisations per cell may seem coarse, however, it is more important to ensure that the stress tensor varies smoothly as it acts on the fluid velocities only via its divergence. This can be done by employing the same Brownian force on each grid cell as in the BCF method. Moreover, two-dimensional BCF approaches often apply only 2000 configuration fields per element (cf. Vargas et al. [90]) and obtain satisfying macroscopic flow field results.

Note that a stochastic approach for a multiscale flow solver in three dimensions features several advantages in contrast to a deterministic FP method as

- it is very robust with regard to the complexity of the problem and the chosen Weissenberg number[1] (cf. high Weissenberg number problem (HWNP) in Keunings [47]),

- the stochastic algorithms can be parallelised efficiently and

- the ansatz requires much less computation time if only a coarse approximation of the stress tensor field is required.

In fact, it has been discovered that a stochastic multiscale approach copes with high Weissenberg numbers that are impractical for multiscale Fokker-Planck simulations or the inferior macroscopic constitutive equations (cf. Chauvière and Lozinski [19]). In contrast to the stress tensor, the probability density function for the FP equation becomes singular for high Weissenberg numbers which requires fine spatial resolution for a numerical treatment.

Nonlinear FENE Spring Force

Since our multiscale approach allows for a precise modelling of the physical system, we employ a nonlinear *FENE* spring force (**F**initely **E**xtensible **N**onlinear **E**lastic) suggested by Warner [93] that restricts the dumbbells' length to a (physically correct) finite maximum extension.

---

[1]A dimensionless number representing the ratio between the microscopic and macroscopic time scale.

However, this results in a singularity at the boundary of the configuration domain. Due to its complexity, the FENE spring possesses no macroscopic equivalent and is thus a full multiscale problem. Beside the FENE spring force we also investigate the more simple Hookean and FENE-P spring forces for which macroscopic counterparts exist, primarily to emphasise their disadvantages in comparison to the FENE model.

Homogeneous Flow Problems

Although we couple a stochastic BCF method with a transient Navier-Stokes flow solver, we also solve the Fokker-Planck equation for homogeneous flow problems using a spectral method approach as in Lozinski [56] to validate the correctness of our stress tensor approximations. Furthermore, this allows for a comparison between both methods in simple flow fields. Our homogeneous flow results show the same restrictions for the FP model in view of robustness, parallel efficiency and computation time as mentioned before which confirms the choice of a stochastic method for transient flow fields.

   Note that for homogeneous flow fields, the Fokker-Planck equation does not depend on physical space $\vec{x}$ as the velocity field is analytically prescribed such that the Fokker-Planck equation simplifies to two or three dimensions in space according to whether $\vec{q} \in \mathbb{R}^2$ or $\vec{q} \in \mathbb{R}^3$ is used.

Main Contributions of this Thesis

The main contributions of this thesis are as follows:

- We give an overview of micro- and macroscopic viscoelastic fluid modelling as well as of spectral methods in modal and nodal formulation and stochastic simulation techniques.

- We extend an existing spectral discretisation of the Fokker-Planck equation with Legendre polynomials from Lozinski [56] to allow for the usage of more general Jacobi polynomials.

- We present an algorithm to generate initial configurations which are distributed according to a FENE probability density function.

- We apply the multiscale BCF method to a three-dimensional Navier-Stokes flow solver and discuss boundary treatment of the configuration fields as well as parallelisation aspects.

- We show first-time simulations for a coupled three-dimensional Navier-Stokes-BCF system. The new results are based on a full multiscale, non-homogeneous, parallel flow solver that can cope with complex geometries.

Outline

The remainder of this thesis is structured as follows:

Chapter 2 provides the basic theory for the simulation of purely Newtonian, macroscopic viscoelastic and multiscale viscoelastic fluids. We analyse the drawbacks of several macroscopic polymer models and motivate the usage of multiscale approaches.

Chapter 3 introduces numerical methods for the discretisation of partial and stochastic differential equations. We discuss finite differences on the sphere and spectral methods for a discretisation of deterministic differential equations on a spherical geometry as well as numerical techniques for stochastic equations.

Chapter 4 considers the case of a homogeneous flow field. We apply spectral methods to the two dimensional Fokker-Planck equation, discuss spherical harmonic basis functions for the three dimensional Fokker-Planck equation and use time-integration schemes for the discretisation of the stochastic differential equation. For the stochastic method, we further present a method to generate appropriate initial configurations and discuss variance reduction schemes.

Chapter 5 deals with three-dimensional, transient, viscoelastic flow fields. First, we present our coupled Navier-Stokes-BCF model and analyse its advantages over a CONNFFESSIT method. Then, we consider spatial and temporal discretisation of the multiscale system and discuss boundary treatment of the configuration fields. Due to the complexity of the problem, we parallelise the algorithm and investigate its scale-up behaviour.

Chapter 6 contains our numerical results. We present results for two- and three-dimensional homogeneous shear and extensional flows and furthermore for three-dimensional, transient flow problems like a flow through an infinite channel, a contraction flow with ratio 4:1 and a flow around a sphere. For homogeneous flows, we compare the spectral approach for the FP equation with stochastic results, analyse different spring force models (FENE, Hooke, FENE-P) and obtain results for stochastic simulations with Weissenberg numbers up to 10. Furthermore, we validate our Navier-Stokes-BCF code by investigating an extensional flow with an analytically known solution. Using a simple Hookean spring force, we also prove that our multiscale approach yields the same results as a macroscopic Oldroyd-B simulation. Lastly, we compare transient results of contraction flow and flow around a sphere with those from literature as they are classical benchmark experiments.

Chapter 7 summarises the main results of this thesis and gives an outlook on future perspectives and possible extensions.

2 The Mathematical Model

This chapter considers the mechanics of Newtonian and non-Newtonian fluids. In the beginning, we describe the basic laws of macroscopic Newtonian fluids and derive the Navier-Stokes equations. Considering the viscosity of fluids under shear and extensional flows, we develop macroscopic differential and integral models for non-Newtonian fluids. Further analysis of the internal structure leads to multiscale models that depend either on a Fokker-Planck equation (i.e. a diffusion equation for a density function) or on a stochastic differential equation. At last, we try to connect the microscopic and macroscopic description of non-Newtonian fluids with the introduction of the Kramers expression and closure approximations.

2.1 Newtonian Fluid Mechanics

In this section, we describe the major principles of continuum mechanics for compressible and incompressible fluid flows. The overview bases upon the books of Owens and Phillips [68], Huilgol and Phan-Thien [40], Tanner [84] and the thesis of Claus [22].

2.1.1 Conservation Laws

In the beginning, we consider Reynolds' transport theorem and use it for deriving the conservation of mass and linear momentum equations. Therefore, let $V \subset \mathbb{R}^3$ be a volume element filled with a fluid and let $\vec{u}(\vec{x}(t), t)$ be the velocity of a particle with position $\vec{x}(t) \in V$ at time t. We can calculate the acceleration of a particle that moves along the velocity field $\vec{u}$ by using the total derivative with respect to time

$$\vec{a}(\vec{x}(t), t) = \frac{d}{dt}\vec{u}(\vec{x}(t), t) = \frac{\partial \vec{u}}{\partial t} + \frac{\partial \vec{u}}{\partial x}\frac{dx}{dt} + \frac{\partial \vec{u}}{\partial y}\frac{dy}{dt} + \frac{\partial \vec{u}}{\partial z}\frac{dz}{dt} = \frac{\partial}{\partial t}\vec{u} + (\vec{u} \cdot \nabla)\vec{u}. \qquad (2.1)$$

In fluid mechanics, we are interested in the time-dependent behaviour of scalar and vector fields that move along the flow field $\vec{u}$ and therefore introduce the material derivative in an analogous manner as in (2.1).

Definition 2.1 [MATERIAL DERIVATIVE]
The material derivative operator describes the time-dependent change of a scalar- or vector-valued function that moves along a fluid field with velocity $\vec{u}$. We define the operator as

$$\frac{D}{Dt} \equiv \frac{\partial}{\partial t} + (\vec{u} \cdot \nabla)$$

with the convective term $\vec{u} \cdot \nabla$.

We can interpret the material derivative as a connection between the Eulerian description (i.e. frame of reference is fixed in space) and the Lagrangian description (i.e. frame of reference

changes to the same degree as a moving particle) of a flow field. A moving observer, as is the case in an Lagrangian description, would only notice the partial derivative with respect to t and not the convective term. As a result, we are able to compute derivatives of volume integrals.

Theorem 2.2 [REYNOLDS TRANSPORT THEOREM]
Let $f(\vec{x}, t)$ be a scalar- or vector-valued function defined over a volume $V(t) \subset \mathbb{R}^3$ at process time t. Then the theorem states that

$$\frac{d}{dt} \int_{V(t)} f \, dV = \int_{V(t)} \left(\frac{Df}{Dt} + f \nabla \cdot \vec{u} \right) dV$$
$$= \int_{V(t)} \frac{\partial f}{\partial t} \, dV + \int_{\partial V(t)} f \vec{u} \cdot \vec{n} \, dA$$

with $\vec{n}$ as the outward pointing normal vector on the surface of $V(t)$. For the second rearrangement, we use Gauss's divergence theorem and allude that the derivation with respect to t and integration do not commute as the volume $V(t)$ changes with time.

Proof: Huilgol and Phan-Thien [40] give a proof by converting the domain of integration to a stationary reference element.

In the following, we apply Reynolds theorem on the fundamental principle in physics that the mass of a closed system remains constant for all time.

Conservation of Mass

Let $\rho : \mathbb{R}^3 \times [0, t_{\max}] \to \mathbb{R}$ be the density function of a fluid element with volume $V(t)$, then $m = \int_{V(t)} \rho \, dV$ denotes the total mass of the system and the conservation of mass principle (i.e. $dm/dt = 0$) states

$$\frac{d}{dt} \int_{V(t)} \rho \, dV = 0. \tag{2.2}$$

We use Reynolds theorem to interchange differentiation and integration in (2.2) and receive

$$\int_{V(t)} \left(\frac{D\rho}{Dt} + \rho \nabla \cdot \vec{u} \right) dV = 0.$$

As size and shape of the volume are arbitrary, we deduce the continuity equation

$$\frac{D\rho}{Dt} + \rho \nabla \cdot \vec{u} = 0.$$

For incompressible fluids (e.g. water and most viscoelastic flows) the density ρ is assumed to be constant and thus the material derivative vanishes and the equation simplifies to

$$\nabla \cdot \vec{u} = 0. \tag{2.3}$$

Conservation of Linear Momentum

We subdivide forces acting on a fluid element into two categories. On the one hand, forces which operate on the whole volume such as gravity are called body forces. On the other hand,

we have surface forces which act by contact with the surface. Consequently, we write the total force as

$$\vec{F}_{\text{total}} = \int_{V(t)} \rho \vec{b} \, dV + \int_{\partial V(t)} \vec{t} \, dA$$

where $\vec{b}$ is the total body force per unit mass and $\vec{t}$ is the stress vector. The stress vector represents the exterior force on the surface element dA. Subsequently, we use the relation

$$\vec{t} = \boldsymbol{\sigma} \cdot \vec{n} \tag{2.4}$$

between the stress vector $\vec{t}$, the Cauchy stress tensor $\boldsymbol{\sigma}$ and the outward pointing unit normal $\vec{n}$ and refer to Section 2.1.2 for further analysis.

Newton's second law of motion in an inertial frame of references explains the change of linear momentum as a result of external forces $\vec{F}_{\text{total}}$ acting on the body which yields

$$\frac{d}{dt} \underbrace{\int_{V(t)} \rho \vec{u} \, dV}_{= \text{ momentum}} = \int_{V(t)} \rho \vec{b} \, dV + \int_{\partial V(t)} \vec{t} \, dA$$

Using Reynolds' transport theorem on the left-hand side and applying (2.4) on the right-hand side, we rewrite the equation as

$$\int_{V(t)} \left(\rho \frac{D\vec{u}}{Dt} + \underbrace{\vec{u} \frac{D\rho}{Dt} + \vec{u} \rho \nabla \cdot \vec{u}}_{=0 \ \text{(continuity equ.)}} \right) dV = \int_{V(t)} \rho \vec{b} \, dV + \int_{V(t)} \nabla \cdot \boldsymbol{\sigma} \, dV. \tag{2.5}$$

At last, since the equation holds for all closed bounded volumes $V(t)$ and we assume the integrands to be continuous, the conservation of momentum becomes

$$\rho \frac{D\vec{u}}{Dt} = \rho \vec{b} + \nabla \cdot \boldsymbol{\sigma}. \tag{2.6}$$

Additionally, for problems with relevance to thermal effects the conservation of energy becomes important but can be omitted in our applications.

2.1.2 The Stress Tensor

In the following section, we concentrate on surface forces (e.g. pressure, friction) and their modelling with a stress tensor $\boldsymbol{\sigma}$. In equation (2.4) we have used $\boldsymbol{\sigma}$ to describe the relation between the unit normal $\vec{n}$ on a surface element and the stress vector $\vec{t}$ on this element. Subsequently, we give an existence theorem for the stress tensor and illustrate the relation in Figure 2.1.

Theorem 2.3 [EXISTENCE OF A STRESS TENSOR]
Let $D \subset \mathbb{R}^3$ be a bounded region that includes $V(t)$ at any time and let $\vec{t}$ be the stress vector defined on $\partial V(t)$, then there exists a second-order tensor $\boldsymbol{\sigma}(\vec{x}, t)$, the Cauchy stress tensor, with the properties

-

$$\vec{t} = \boldsymbol{\sigma} \cdot \vec{n},$$
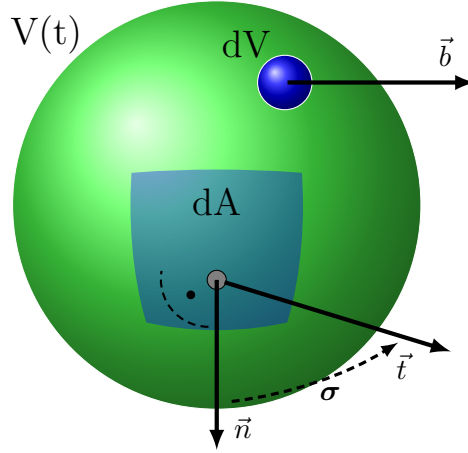
Figure 2.1: Two different forces act on a fluid element $V(t)$ which are the body force $\vec{b}$ (e.g. gravity, electromagnetic forces) and surface forces (e.g. pressure, friction). For the description of surface forces we consider the Cauchy stress tensor $\boldsymbol{\sigma}$ that we interpret as a linear mapping from $\vec{n}$ to the stress vector $\vec{t}$.

-

$$\boldsymbol{\sigma} \text{ is symmetric,}$$

i.e. $\boldsymbol{\sigma}$ *is a linear mapping from* $\vec{n}$ *to* $\vec{t}$ *with six independent components.*

<u>Proof:</u> Owens and Phillips [68] and Huilgol et al. [40] give detailed proofs of the theorem.

Additionally, the diagonal components σ_{xx}, σ_{yy} and σ_{zz} are called normal stresses whereas the other components $\sigma_{xy} = \sigma_{yx}$, $\sigma_{xz} = \sigma_{zx}$ and $\sigma_{yz} = \sigma_{zy}$ are denoted as shear stresses.

In a first attempt, we model the stress tensor for fluids without internal friction which are denoted as nonviscous or inviscid flows. No shear stresses occur in that case and the only contribution to the stress comes from the hydrostatic pressure p. In a flow problem, p must be found using the continuity equation (2.3) and the momentum equation (2.6) because the pressure is not connected to the motion by a constitutive equation. Owing to the fact that the pressure is uniform in all directions, the constitutive model for a fluid takes the form

$$\boldsymbol{\sigma} = -p\,\mathbf{Id} \quad (\sigma_{ij} = -p\delta_{ij}). \tag{2.7}$$

Accordingly, the stress vector $\vec{t}$ and the unit normal $\vec{n}$ are linearly dependent for an inviscid flow and $\vec{n}$ is an eigenvector of $\boldsymbol{\sigma}$ with eigenvalue p. Furthermore, for a fluid at rest the stress tensor $\boldsymbol{\sigma}$ takes the same form. Indeed, if other components than the normal stresses appeared, the fluid would be deformed.

For more complex flows, we expand $\boldsymbol{\sigma}$ with extra-stresses

$$\boldsymbol{\sigma} = -p\,\mathbf{Id} + \underbrace{\boldsymbol{\tau_s} + \boldsymbol{\tau_p}}_{\equiv\boldsymbol{\tau}} \tag{2.8}$$

whereas $\boldsymbol{\tau_s}$ represents the solvent contribution to the stress (i.e. Newtonian flow case) and $\boldsymbol{\tau_p}$ describes an additional term for non-Newtonian fluids (e.g. contribution of polymer molecules
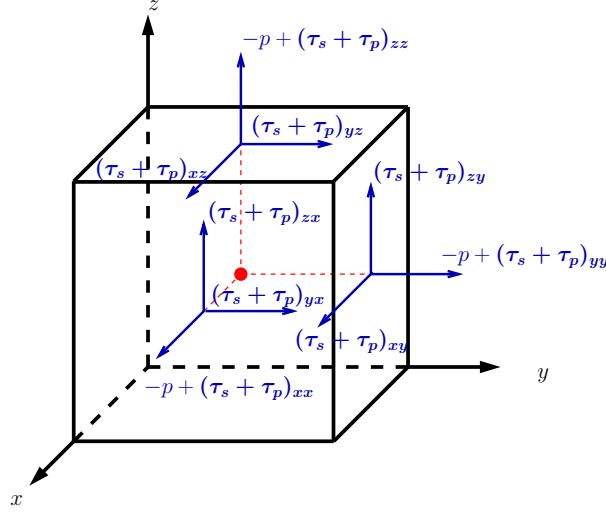
Figure 2.2: The components of $\boldsymbol{\sigma}$ are arranged on different faces.

immersed in the fluid). We illustrate the components of $\boldsymbol{\sigma}$ in Figure 2.2. Inserting (2.8) into the momentum equation yields

$$\rho \frac{D\vec{u}}{Dt} = -\nabla p + \nabla \cdot \boldsymbol{\tau_s} + \nabla \cdot \boldsymbol{\tau_s} + \rho \vec{b}. \tag{2.9}$$

In the following sections, we give a constitutive equation for $\boldsymbol{\tau_s}$ and examine different approaches (differential, integral and multiscale models) to connect the polymeric extra-stress tensor $\boldsymbol{\tau_p}$ with the motion of the fluid.

2.1.3 Viscosity in Simple Flows

For a given fluid, we want to investigate the relation between extra-stress ($\boldsymbol{\tau} = \boldsymbol{\tau_s} + \boldsymbol{\tau_p}$) and fluid motion and therefore need a measure for the internal resistance of the flow (i.e. viscosity). Therefore, we investigate two simple types of flow, shear flows and extensional flows, and define the shear viscosity and extensional viscosity correspondingly. The simplicity of these flows lies in the well known velocity field that is not influenced by additional polymeric characteristics. Actually, the velocity field is homogeneous in both cases which means that the velocity gradient

$$\nabla \vec{u}(\vec{x}, t) = \nabla \vec{u} = \begin{pmatrix} \frac{\partial u}{\partial x} & \frac{\partial u}{\partial y} & \frac{\partial u}{\partial z} \\ \frac{\partial v}{\partial x} & \frac{\partial v}{\partial y} & \frac{\partial v}{\partial z} \\ \frac{\partial w}{\partial x} & \frac{\partial w}{\partial y} & \frac{\partial w}{\partial z} \end{pmatrix} \tag{2.10}$$

does not depend on physical space $\vec{x}$ or process time t. Note that there are two different definitions for the velocity gradient in literature. In this thesis, we define the gradient as $(\nabla \vec{u})_{i,j} = \frac{\partial u_i}{\partial x_j}$ whereas most authors in rheology use the transpose definition $(\nabla \vec{u})_{i,j} = \frac{\partial u_j}{\partial x_i}$. In contrast to the stress tensor, $\nabla \vec{u}$ is not symmetric and therefore some equations have to be modified accordingly. Additionally, after we have introduced the concept of viscosity, we give
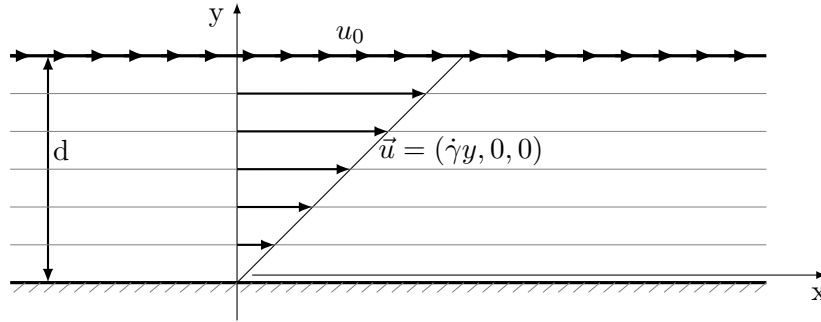
Figure 2.3: In a simple shear flow the fluid is contained between two infinite plates with distance d. The top plate moves with a constant velocity u_0 and creates an y-dependent velocity profile for the fluid because of internal friction.

precise definitions for Newtonian and non-Newtonian fluids.

Steady Shear Flow

In a steady xy-shear flow, the velocity field is given by

$$\vec{u} = (\dot{\gamma}y, 0, 0) \tag{2.11}$$

for a constant shear rate $\dot{\gamma}$. The velocity profile results from a fluid contained between two parallel and infinitely extended plates whereas the upper plate moves with a constant velocity u_0. For an illustration of this configuration, we refer to Figure 2.3.

Let d denote the distance between both plates, then we obtain the shear rate by the quotient $\dot{\gamma} = u_0/d$ and the velocity gradient is $\nabla \vec{u} = \dot{\gamma}\vec{e}_x \otimes \vec{e}_y$.

In view of further analysis of $\boldsymbol{\tau}$, we define the viscosity of a fluid.

Definition 2.4 [Shear Viscosity]
Let $\vec{u}$ be the velocity field of a steady shear flow in x-direction, then we define the (shear-rate dependent) viscosity

$$\eta(\dot{\gamma}) = \frac{\tau_{xy}}{\dot{\gamma}} \tag{2.12}$$

as the ratio between the shear stress component τ_{xy} and the shear rate. Furthermore, we term the limit

$$\eta_0 = \lim_{\dot{\gamma} \to 0} \eta(\dot{\gamma})$$

as zero-shear-rate viscosity and

$$\eta_\infty = \lim_{\dot{\gamma} \to \infty} \eta(\dot{\gamma})$$

as infinite-shear-rate viscosity.

In general, $\eta(\dot{\gamma})$ is a function depending on $\dot{\gamma}$ with finite boundary values for $\dot{\gamma} \to 0$ and $\dot{\gamma} \to \infty$. However, we denote a fluid

- as Newtonian if the viscosity is a constant that does not depend on $\dot{\gamma}$ and
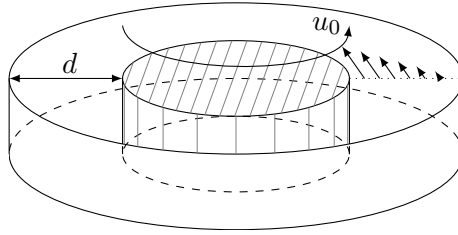
Figure 2.4: The picture presents a schematic overview of a rheometer. The inner disc rotates with a constant velocity u_0 and locally generates, after an initial phase, a simple shear flow.

- as non-Newtonian for the general case.

As $\eta(\dot{\gamma})$ is not constant in the non-Newtonian case, we classify fluids with

- monotonically decreasing viscosities as shear thinning or pseudo-plastic and with

- monotonically increasing viscosities as shear thickening or dilatant.

In practical applications, we are not able to use infinite plates but can create flows that are similar to simple shear flows and easy to produce experimentally (cf. a rheometer in Figure 2.4). We name these viscometric flows. Interestingly, for viscometric flows two of the three independent shear stresses of $\boldsymbol{\tau}$ are zero. In the coordinate system described above, we have $\tau_{xy} \neq 0$ and $\tau_{xz} = \tau_{yz} = 0$ and therefore get

$$\boldsymbol{\tau} = \begin{pmatrix} \tau_{xx} & \tau_{xy} & 0 \\ \tau_{xy} & \tau_{yy} & 0 \\ 0 & 0 & \tau_{zz} \end{pmatrix}. \tag{2.13}$$

For clarification, let z be the fixed reference point of two Cartesian coordinate systems whereas the second one is rotated by an angle of π around an axis through z in relation to the first one. We illustrate the relative orientation in Figure 2.5. Considering the fact that we have an isotropic material, both systems of reference exhibit the same flow field and therefore the same stresses. However, as the stress tensor components τ_{xz} and τ_{yz} point in different directions, they have to be zero.

At last, we define two other parameters which are important for the investigation of the flow field and which distinguish Newtonian and non-Newtonian fluids.

Theorem 2.5 [Viscometric Functions]
We denote the two independent stress differences

$$N_1(\dot{\gamma}) \equiv \tau_{xx} - \tau_{yy} \quad and \quad N_2(\dot{\gamma}) \equiv \tau_{yy} - \tau_{zz} \tag{2.14}$$

as the first and second normal stress differences. The three characteristic functions $\eta(\dot{\gamma})$, $N_1(\dot{\gamma})$ and $N_2(\dot{\gamma})$ are called viscometric functions.

Steady Extensional Flow

In an extensional flow a fluid element is stretched in one or several axes with constant elongation rate $\dot{\epsilon} > 0$. Depending on the form of $\vec{u}$, we distinguish uniaxial and planar extensional flows
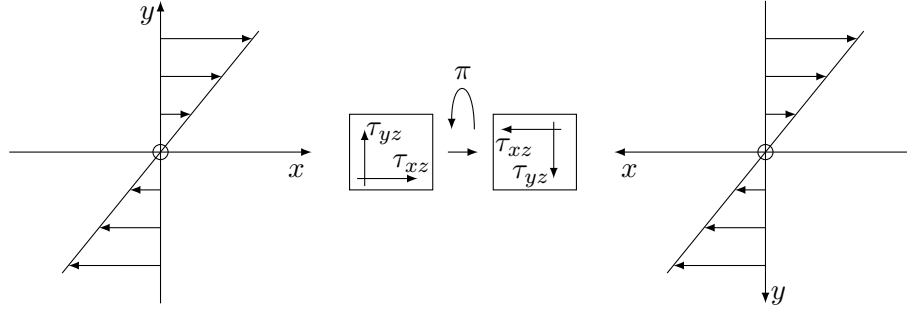
Figure 2.5: Two stress tensor components have to be zero in a shear flow because two systems of reference, rotated by π, show the same flow field and the same stresses. A similar illustration can be found in Böhme [11].

(cf. Figure 2.6). The corresponding velocity field takes the form

$$\vec{u} = (\dot{\epsilon}x, -\frac{\dot{\epsilon}}{2}y, -\frac{\dot{\epsilon}}{2}z) \quad \text{for an uniaxial extensional flow and} \tag{2.15a}$$

$$\vec{u} = (\dot{\epsilon}x, -\dot{\epsilon}y, 0) \quad \text{for a planar extensional flow.} \tag{2.15b}$$

As uniaxial extensional flows take place in three dimensions and therefore are difficult to visualise, we additionally describe the deformation of a cylindric volume element under such an extensional flow in Figure 2.7. We expect for this experiment

- an extension in the x-direction and a decrease in the $y - z$ cross section for an uniaxial extensional flow and

- an uniform increase and decrease in two axes and no change in the third direction for planar extensional flow.

Extensional flows behave differently than shear flows so that other fluid characteristics are emphasised. For instance, a shear flow given by (2.11) deforms a fluid element by a fixed angle and therefore produces one non-zero shear stress component (i.e. $\boldsymbol{\tau_{xy}} \neq 0$). In contrast, the stress tensor in extensional flows exhibits only normal stresses and takes the form

$$\boldsymbol{\tau} = \begin{pmatrix} \tau_{xx} & 0 & 0 \\ 0 & \tau_{yy} & 0 \\ 0 & 0 & \tau_{yy} \end{pmatrix} \tag{2.16}$$

with only two independent components. As we are interested in the evolution of $\tau_{xx} - \tau_{yy}$ with respect to $\dot{\epsilon}$, we consequently define an analogon to the shear viscosity for the extensional flow case.

Definition 2.6 [EXTENSIONAL VISCOSITY]
The extensional viscosity $\eta_E(\dot{\epsilon})$ is defined as the ratio of the normal stress difference $\tau_{xx} - \tau_{yy}$ to the extensional rate $\dot{\epsilon}$

$$\eta_E(\dot{\epsilon}) = \frac{\tau_{xx} - \tau_{yy}}{\dot{\epsilon}}. \tag{2.17}$$
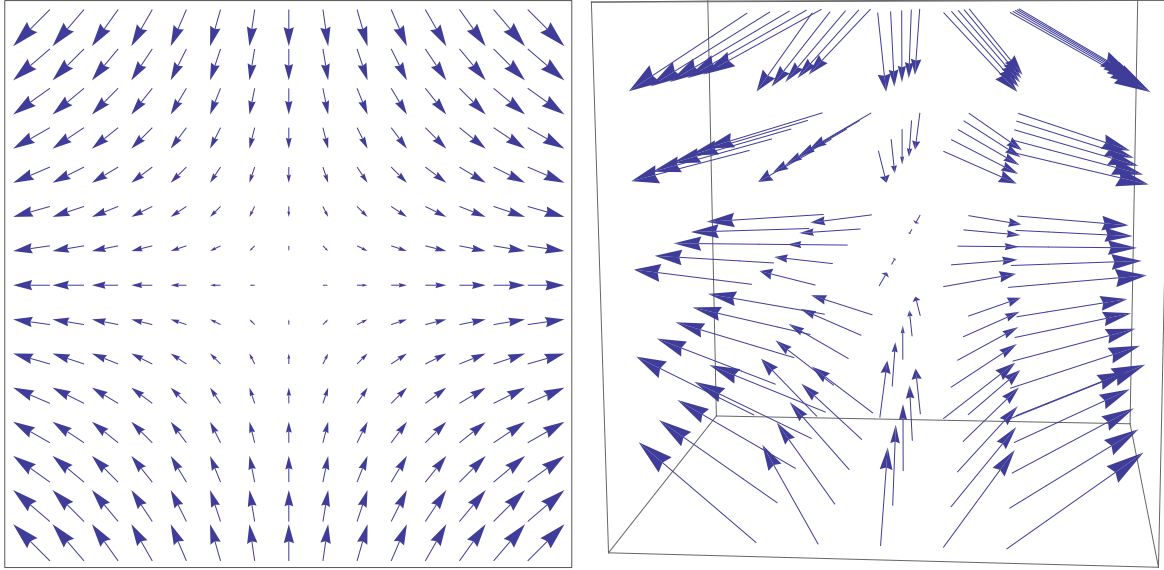
Planar extensional flow   Uniaxial Extensional Flow

Figure 2.6: A planar extensional flow as in the left picture exhibits only fluid motion in the xy-plane whereas an uniaxial extensional flow as in the right picture comes from two directions (e.g. y- and z-direction) and flows in the direction of the third axis (e.g. x-direction).

If the extensional viscosity of a fluid increases while the parameter $\dot{\epsilon}$ is increased, we denote this behaviour as extensional thickening. Obviously, the opposite case is called extensional thinning.

Another difference between shear and extensional flow lies in the curl of $\vec{u}$. In all non-trivial flow cases, we have

- $\nabla \times \vec{u} = 0$ for an extensional flow and

- $\nabla \times \vec{u} \neq 0$ for a shear flow.

We consider only flows in simply-connected regions and as the curl of $\vec{u}$ vanishes, we therefore conclude the existence of a scalar potential for extensional flows (i.e. extensional flow fields are conservative).

At last, we define a measure for the comparison of shear and extensional behaviour.

Definition 2.7 [TROUTON RATIO]
The Trouton ratio expresses the ratio between extensional viscosity and shear viscosity

$$Trouton\ ratio = \frac{\eta_E(\dot{\epsilon})}{\eta_0(\dot{\gamma})}. \tag{2.18}$$

2.1.4 Newtonian Fluids

In Section 2.1.2 we have decomposed the total stress tensor into

$$\boldsymbol{\sigma} = -p\,\mathbf{Id} + \boldsymbol{\tau_s} + \boldsymbol{\tau_p}.$$
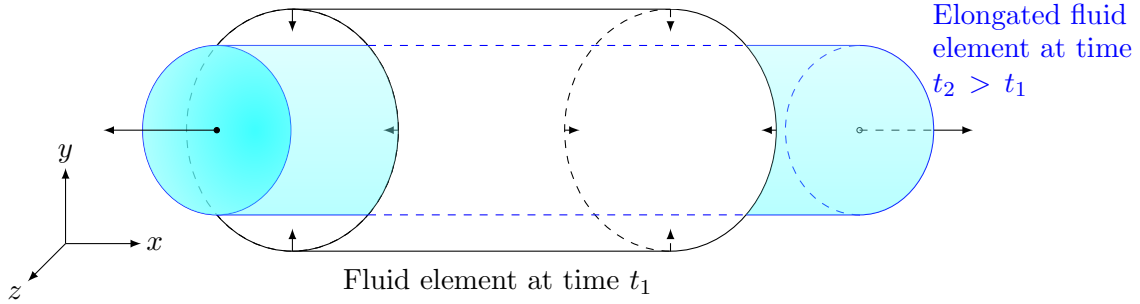
Figure 2.7: In a steady uniaxial extensional flow, a cylinder is stretched in the x-direction. Correspondingly, the $y - z$ cross section decreases but maintains its circular form.

Obviously, for Newtonian fluids we have $\boldsymbol{\tau_p} = 0$ and Newton's constitutive law states

$$\boxed{\boldsymbol{\tau_s} \;=\; 2\eta_0 \boldsymbol{D}.} \tag{2.19}$$

Concerning this matter, we have used the rate of deformation tensor

$$\boldsymbol{D} \;=\; \frac{1}{2}(\nabla \vec{u} + \nabla \vec{u}^T)$$

which is the symmetric part (i.e. $\boldsymbol{D}^T = \boldsymbol{D}$) of the velocity gradient. The diagonal elements of $\boldsymbol{D}$ are a measure for the stretching of filaments in the main coordinate direction. The parameter η_0 denotes the zero-shear-rate viscosity, but, as stated for the definition of viscosity, a Newtonian fluid has a constant viscosity that is independent of the shear rate.

Inserting Newton's law (2.19) into the momentum equation (2.9) and combining the result with the continuity equation (2.3), we obtain the incompressible Navier-Stokes equations

$$\boxed{\begin{aligned} \rho \frac{D\vec{u}}{Dt} &= -\nabla p \,+\, \eta_0 \Delta \vec{u}, + \rho \vec{b}, \\ \nabla \cdot \vec{u} &= 0. \end{aligned}} \tag{2.20}$$

Subsequently, we investigate the stress tensor of a Newtonian fluid for the simple flow cases as described in Section 2.1.3:

1. **Steady shear flow**
   We use Newton's law (2.19) to calculate the total stress tensor

$$\boldsymbol{\sigma} = -p\,\mathbf{Id} \,+\, \boldsymbol{\tau_s} \;=\; \begin{pmatrix} -p & \eta_0 \dot{\gamma} & 0 \\ \eta_0 \dot{\gamma} & -p & 0 \\ 0 & 0 & -p \end{pmatrix} \tag{2.21}$$

and we obtain

$$N_1(\dot{\gamma}) \;=\; \tau_{xx} - \tau_{yy} \;=\; 0,$$
$$N_2(\dot{\gamma}) \;=\; \tau_{yy} - \tau_{zz} \;=\; 0$$

for the first and second normal stress differences. Additionally, as the shear viscosity is constant, Newtonian flows are neither shear thinning nor shear thickening.

2. **Steady extensional flow**
   For an extensional flow, $\boldsymbol{\sigma}$ becomes

   $$\boldsymbol{\sigma} = -p\,\mathbf{Id} + \boldsymbol{\tau_s} = \begin{pmatrix} -p + 2\eta_0\dot{\epsilon} & 0 & 0 \\ 0 & -p + 2\eta_0\dot{\epsilon} & 0 \\ 0 & 0 & -p + 2\eta_0\dot{\epsilon} \end{pmatrix} \tag{2.22}$$

   which yields a constant extensional viscosity (cf. (2.17))

   $$\eta_{\mathrm{E}}(\dot{\epsilon}) \;=\; 3$$

   and therefore a Trouton ratio $\eta_{\mathrm{E}}(\dot{\epsilon})/\eta_0 = 3$.

We conclude from the analysis of both simple flows that Newton's law is only valid for a subclass of fluids that exhibit no shear-rate or extensional-rate dependent behaviour (e.g. water, air). One reason for this restriction is that the solvent stress tensor in (2.19) depends linearly on $\vec{u}$ and is isotropic (i.e. uniform in all directions). Accordingly, we introduce a generalised Newtonian fluid to lift some restrictions from the Newtonian case.

Generalised Newtonian Fluids

In industrial applications the most relevant characteristic of non-Newtonian fluids is the shear thinning effect (i.e. increasing shear rate $\dot{\gamma}$, decreases viscosity). Hence, we describe an extension for Newtonian fluids that

- includes the shear thinning or shear thickening effect for shear flows (cf. Section 2.1.3),

- also does not predict the first and second normal stress differences (i.e. differences are zero as for a Newtonian fluid), and

- is not suited for extensional flows.

Therefore, we postulate that η_0 may depend nonlinearly on the deformation tensor $\boldsymbol{D}$. As the viscosity is a scalar, it does not depend on a specific coordinate system. For this reason, η_0 can only depend on invariants of $\boldsymbol{D}$. As $\boldsymbol{D}$ is symmetric and can be diagonalised, we describe η_0 with three invariants $I_{\boldsymbol{D}}$, $II_{\boldsymbol{D}}$, and $III_{\boldsymbol{D}}$ which yields an expression

$$\boldsymbol{\tau_s} \;=\; 2\eta_0(I_{\boldsymbol{D}}, II_{\boldsymbol{D}}, III_{\boldsymbol{D}})\,\boldsymbol{D}.$$

The three invariants are given by (cf. Bird [9])

$$I_{\boldsymbol{D}} = \sum_{i=1}^{3} D_{ii} = \operatorname{tr}\boldsymbol{D} = \nabla \cdot \vec{u},$$

$$II_{\boldsymbol{D}} = \sum_{i=1}^{3}\sum_{j=1}^{3} D_{ij}D_{ji} = \|\boldsymbol{D}\|_{\text{Frobenius}}^{2},$$

$$III_{\boldsymbol{D}} = \sum_{i,j,k} D_{ij}D_{jk}D_{ki} = \operatorname{tr}\boldsymbol{D}^{3}.$$

We conclude that

- $I_{\boldsymbol{D}} = 0$ for incompressible fluids and

- $III_{\boldsymbol{D}} = 0$ for steady shear flows.

As a result, a constitutive equation for a generalised Newtonian fluid takes the form

$$\boxed{\boldsymbol{\tau_s} = 2\eta_0(\|\boldsymbol{D}\|_{\text{Frobenius}})\boldsymbol{D}.} \tag{2.23}$$

A generalised Newtonian fluid can also be considered as a non-Newtonian viscous fluid that is inelastic (i.e. the deformation of the fluid is not reversible). In the next chapter, we consider nonlinear models for non-Newtonian flows that include elasticity and explain more effects occurring for shear and extensional flows.

2.2 Macroscopic Models for Non-Newtonian Fluids

In this chapter, we concentrate on purely macroscopic models for non-Newtonian fluids. All considered models can be derived by the use of continuum mechanics. However, there is a relation between macroscopic and multiscale models that we consider in Section 2.3.6. Macroscopic theories are either based on differential or on integral models. Both approaches connect the non-Newtonian extra-stress $\boldsymbol{\tau_p}$ to the motion of a fluid described by $\nabla\vec{u}$ or the rate of deformation tensor D. However, differential models have been analysed in more detail because they can be implemented more easily in applications.

For the subsequent chapter, we use the books of Renardy [80], Macosko [60], Joseph [43], Owens and Phillips [68], and Böhme [11].

2.2.1 Overview of Viscoelastic Fluids

In Section 2.1.3, we defines a fluid as non-Newtonian if the shear viscosity varies with the shear rate $\dot{\gamma}$. A lot of different fluids fall into this category and therefore require a further categorisation. The subclass that we want to investigate are the viscoelastic fluids.

Definition 2.8 [Viscoelastic Fluids]
A non-Newtonian fluid that exhibits viscous and elastic properties is called a viscoelastic fluid. A body behaves

- *viscous if it resists deformation when a stress takes effect and*

- *elastic if a stress deforms it instantly, but it resumes to its original state directly after the stress has been removed.*

In general, a viscoelastic fluid shows different behaviour in shear and extensional flows than a Newtonian fluid. Most viscoelastic fluids exhibit (cf. Definition 2.5 on page 23)

- a shear viscosity $\eta(\dot{\gamma})$ as a decreasing function of $\dot{\gamma}$ (i.e. shear thinning),

- non-zero first and second normal stress differences $N_1(\dot{\gamma})$ and $N_2(\dot{\gamma})$ with $N_1(\dot{\gamma}) > N_2(\dot{\gamma})$,

- an extensional viscosity $\eta_{\mathrm{E}}(\dot{\epsilon})$ that increases with $\dot{\epsilon}$ (i.e. extensional thickening), and

- a Trouton ratio $\frac{\eta_{\mathrm{E}}(\dot{\epsilon})}{\eta_0(\dot{\gamma})} > 3$ (= Trouton ratio of Newtonian fluids).

Stress Relaxation after a Sudden Shearing

For illustration, we describe the different relations between stress and strain for viscous and elastic bodies. Strain denotes the deformation of a body when a force is applied on it. Subsequently, we perform an experiment in four steps, the stress relaxation experiment, that shows how stress depends on strain for ideal viscous fluids and Hookean elastic bodies:

1. For $0 < \epsilon \ll 1$, a viscous or elastic body is at rest for all times $t < -\epsilon$.

2. For $t \in [-\epsilon, \epsilon]$, we shear the body with a rate $\dot{\gamma}(t) \neq 0$ and obtain $\gamma_0 = \int_{-\epsilon}^{\epsilon} \dot{\gamma}(s)\, ds$ as the magnitude of shear.
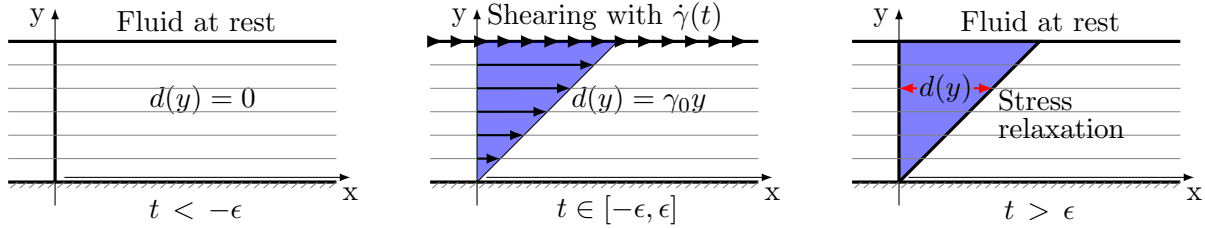
Figure 2.8: First, the body is at rest and the stress is zero. For a small period of time, we shear the body volume by a rate $\dot{\gamma}(t)$ such that a particle with height y has a displacement of $d(y)$. In the right picture, the particle still has a constant displacement of $d(y)$ in relation to the origin. The major value of interest is the decay of $\boldsymbol{\tau}$ for $t > \epsilon$.

3. For all $t > \epsilon$, we keep the shear magnitude γ_0 and the displacement $d(y)$ constant and therefore have a shear rate $\dot{\gamma}(t) = 0$.

4. We measure the stress $\boldsymbol{\tau}$ at each step.

In Figure 2.8 we give an illustration of the experiment.

For an ideal Newtonian fluid (cf. Definition 2.4 of viscosity), we have a constant relation for the stress component τ_{xy} of $\boldsymbol{\tau}$ and the (time-dependent) shear rate

$$\eta_0 \;=\; \frac{\tau_{xy}(t)}{\dot{\gamma}(t)}.$$

Using this relation and considering the limit $\epsilon \to 0$, we can calculate the shear variable $\gamma(t)$ as

$$\gamma(t) \;=\; \frac{1}{\eta_0} \int_{-\infty}^{t} \tau_{xy}(s)\, ds \;=\; \begin{cases} \gamma_0, & \text{for all } t \geqslant 0, \\ 0, & \text{for all } t < 0. \end{cases} \tag{2.24}$$

From (2.24) it follows that $\tau_{xy}(t)$ has the form of a delta function with a magnitude of $\eta_0 \gamma_0$. Consequently, an ideal viscous fluid behaves in the same way. In contrast, an elastic object shows a constant shear stress component $\tau_{xy}(t) > 0$ for all $t \geqslant 0$.

We visualise the development of τ_{xy} for an ideal viscous fluid, for a Newtonian fluid, for a typical viscoelastic fluid and for an ideal Hookean elastic body in Figure 2.9. If the considered object is a fluid, the limit value of the stress for $t \to \infty$ is zero. On the other hand, solid objects have a limit value unequal to zero.

Relaxation Time

In reality, no material is purely elastic or viscous, but the elasticity of water or the viscosity of ice are neglectable in most observations. Furthermore, even the distinction between "fluid" and "solid" relates on the frame of reference. Therefore, we have to introduce a measure for the time scale in which the fluid relaxes again and reaches an equilibrium state.

Definition 2.9 [RELAXATION TIME]
The time t that is required for the shear stress τ_{xy} in a simple shear flow, under constant-strain conditions, to return to zero (or to a specified percentage) is called relaxation time λ.

(a) Ideal viscous fluid

(b) Newtonian fluid

(c) Viscoelastic fluid
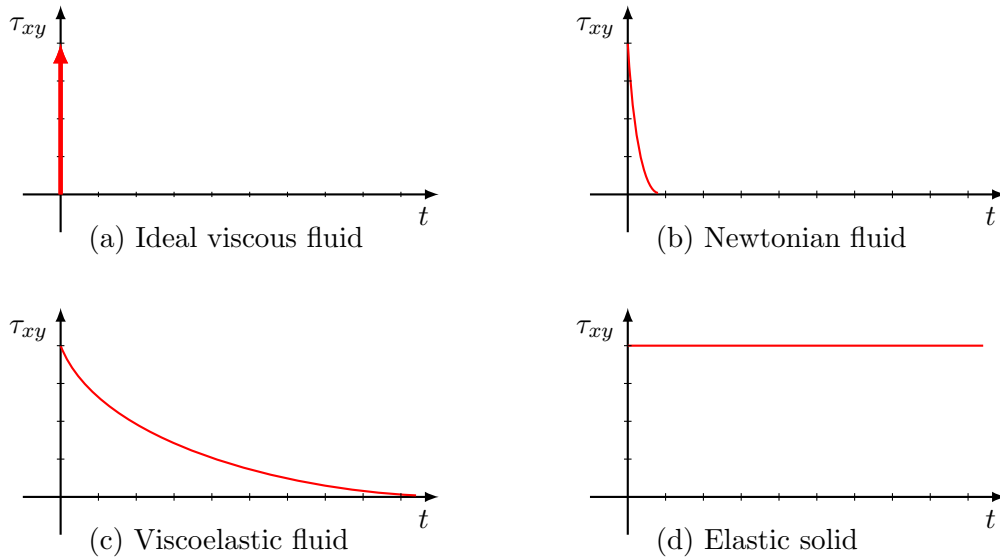
(d) Elastic solid

Figure 2.9: Stress relaxation after a sudden shearing of four different bodies. On the one hand, an ideal viscous fluid (a) shows a sudden response where the arrow represents a delta function. On the other hand, an elastic solid (d) exhibits a constant shear stress. Real fluids react in a combination of both effects, but for Newtonian fluids (b) the viscous behaviour is much more emphasised than for viscoelastic fluids (c).

Therefore, for every object we have a characteristic time scale which we express through λ. For positive values of λ, the current stress does not only depend on the current motion of a fluid but also on the history of the motion. A common term in this context is the "fading memory" of a fluid. The effect of "fading memory" is measured by the relaxation time.

Let T_0 be a characteristic time scale for an observer (e.g. the duration of an experiment), then for the observer the reaction of a fluid does not depend on λ itself but on the ratio

$$\text{De} = \frac{\lambda}{T_0} \tag{2.25}$$

which is called the Deborah[1] number. Accordingly, we interpret a body as a

- viscous fluid for $\text{De} \ll 1$,

- viscoelastic fluid for $\text{De} \approx 1$, and as a

- elastic solid for $\text{De} \gg 1$.

2.2.2 Differential Models

A basic model for a viscoelastic fluid in 1D is the linear Maxwell model. Moreover, if we want to describe one-dimensional fluids with a Newtonian component as well as a viscoelastic component, we could use the linear Jeffrey model (cf. Figure 2.10). A common approach to

---

[1]Interestingly, Deborah is the name of a prophet who stated in the bible that "the mountains flowed before the Lord." Therefore, on a large time scale T_0 we can consider a mountain as a flowing object.
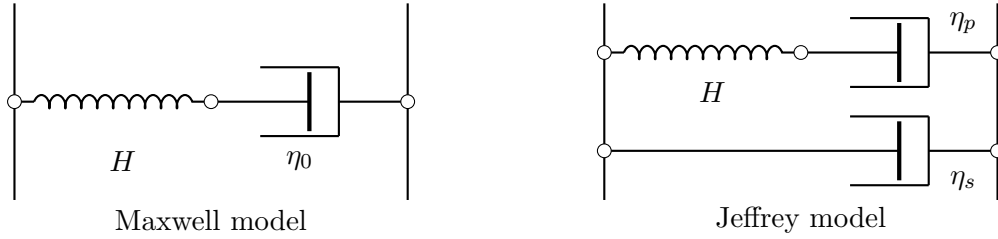
Figure 2.10: On the one hand, a common representation for the Maxwell model is a spring with spring constant H (elastic behaviour) and a purely viscous dashpot with viscosity η_0 in series. On the other hand, a Jeffrey model combines the viscoelastic behaviour of the Maxwell model with an additional dashpot that represents the Newtonian viscosity η_s of the solvent.

obtain a 3D constitutive equation is to generalise the 1D Maxwell or Jeffrey model into a tensor formulation. However, as our interest lies in the construction of multiscale models, we will shorten the introduction and only present the major results.

The 3D generalisation of the Maxwell model results in the Upper Convected Maxwell model; the 3D equivalent to the Jeffrey model is the Oldroyd-B model. Later on, we will derive the formal equivalence between a microscopic dumbbell with a Hookean spring and the Oldroyd-B model.

For our tensor formulation we need a time derivative that takes frame invariance into account (i.e. descriptions of material properties are invariant under changes of observers). Therefore, an invariant time derivative belongs to a coordinate system which experiences the same modification (e.g. deformation, rotation, stretching) as the fluid. We subsequently present an objective time derivative that necessarily leads to nonlinear models.

Definition 2.10 [Upper convected derivative]
*For an arbitrary tensor A, we define the **upper convected derivative** (Oldroyd derivative)*

$$\overset{\triangledown}{\boldsymbol{A}} \equiv \frac{D\boldsymbol{A}}{Dt} - \nabla\vec{u} \cdot \boldsymbol{A} - \boldsymbol{A} \cdot (\nabla\vec{u})^T \tag{2.26}$$

as a time derivative for a coordinate system that stretches and rotates with the material. As a consequence, stresses are only induced by deformations and not by elongations or rotations.

Applying the upper convected derivative (2.26) to the one-dimensional Maxwell model yields the Upper Convected Maxwell (UCM) model equation

$$\boxed{\boldsymbol{\tau_p} + \lambda\overset{\triangledown}{\boldsymbol{\tau_p}} = 2\eta_p\boldsymbol{D}} \tag{2.27}$$

with relaxation time λ, rate of deformation tensor $\boldsymbol{D}$ and shear viscosity η_0 as a constitutive equation for $\boldsymbol{\tau_p}$. If we also consider a Newtonian contribution to the UCM model, we obtain the Oldroyd-B model. Its constitutive equation takes the form

$$\boxed{\boldsymbol{\tau} + \lambda\overset{\triangledown}{\boldsymbol{\tau}} = 2\eta_0(\boldsymbol{D} + \lambda_s\overset{\triangledown}{\boldsymbol{D}}),} \tag{2.28}$$

where $\eta_0 = \eta_s + \eta_p$ is the total viscosity and $\lambda_s = \frac{\eta_s\lambda}{\eta_s+\eta_p} \equiv \beta\lambda$ is the characteristic retardation

time for the fluid. Here, β denotes the ratio of the solvent Newtonian viscosity to the total viscosity. The Oldroyd-B model combines solvent and polymeric contribution to the stress so that we can also write the equation in a split form

$$\boxed{\boldsymbol{\tau} \;=\; 2\eta_s \boldsymbol{D} \;+\; \boldsymbol{\tau_p}} \tag{2.29}$$

$$\boxed{\boldsymbol{\tau_p} + \lambda \overset{\triangledown}{\boldsymbol{\tau_p}} \;=\; 2\eta_p \boldsymbol{D}} \tag{2.30}$$

that emphasises the non-Newtonian extra-stress component $\boldsymbol{\tau_p}$ of $\boldsymbol{\tau}$.

Alternatively, we can define objective derivatives for a coordinate system that

- rotates and deforms with the material without considering elongations (lower convected derivative) or

- only rotates but does not follow deformations or elongations (corotational derivative).

By using the alternative time derivatives, we obtain other constitutive equations such as the Lower Convected Maxwell model or the Corotational Maxwell model. Other differential models differ from the UCM model by including further nonlinear terms.

Behaviour in Steady Shear Flows

In Section 2.1.4, we give reasons for a constant shear viscosity and zero normal stress differences $N_1(\dot{\gamma})$ and $N_2(\dot{\gamma})$ of Newtonian fluids. Therefore, we do not expect significant differences between the UCM and the Oldroyd-B model as the Newtonian contribution to the viscometric functions vanishes.

1. For a steady shear flow $\vec{u} = (\dot{\gamma}, 0, 0)$, the constitutive equation for the UCM model (2.27) becomes

$$
\begin{pmatrix} \tau_{xx} & \tau_{xy} & 0 \\ \tau_{xy} & \tau_{yy} & 0 \\ 0 & 0 & \tau_{zz} \end{pmatrix} - \lambda \left\{ \begin{pmatrix} 0 & \dot{\gamma} & 0 \\ 0 & 0 & 0 \\ 0 & 0 & 0 \end{pmatrix} \begin{pmatrix} \tau_{xx} & \tau_{xy} & 0 \\ \tau_{xy} & \tau_{yy} & 0 \\ 0 & 0 & \tau_{zz} \end{pmatrix} \right.
$$
$$
\left. + \begin{pmatrix} \tau_{xx} & \tau_{xy} & 0 \\ \tau_{xy} & \tau_{yy} & 0 \\ 0 & 0 & \tau_{zz} \end{pmatrix} \begin{pmatrix} 0 & 0 & 0 \\ \dot{\gamma} & 0 & 0 \\ 0 & 0 & 0 \end{pmatrix} \right\}
$$
$$
= \eta_p \begin{pmatrix} 0 & \dot{\gamma} & 0 \\ \dot{\gamma} & 0 & 0 \\ 0 & 0 & 0 \end{pmatrix}
$$

because the material derivative $\frac{D\boldsymbol{\tau}}{Dt}$ vanishes. The solution of the system is

$$\tau_{xx} = 2\eta_p \lambda \dot{\gamma}^2, \quad \tau_{xy} = \eta_p \dot{\gamma}, \quad \text{and} \quad \tau_{yy} = \tau_{zz} = 0 \tag{2.31}$$

and therefore the viscometric functions are

$$\eta(\dot{\gamma}) = \frac{\tau_{xy}}{\dot{\gamma}} = \eta_0, \quad N_1(\dot{\gamma}) = \tau_{xx} - \tau_{yy} = 2\eta_p \lambda \dot{\gamma}^2, \quad \text{and} \quad N_2(\dot{\gamma}) = \tau_{yy} - \tau_{zz} = 0. \tag{2.32}$$

As a result, the shear-rate viscosity of the UCM model is constant which does not coincide with the behaviour of viscoelastic fluids.

2. We obtain a similar result for a steady shear flow of an Oldroyd-B fluid whose constitutive equation (2.28) takes the form

$$
\begin{pmatrix} \tau_{xx} & \tau_{xy} & 0 \\ \tau_{xy} & \tau_{yy} & 0 \\ 0 & 0 & \tau_{zz} \end{pmatrix} - \lambda \left\{ \begin{pmatrix} 0 & \dot{\gamma} & 0 \\ 0 & 0 & 0 \\ 0 & 0 & 0 \end{pmatrix} \begin{pmatrix} \tau_{xx} & \tau_{xy} & 0 \\ \tau_{xy} & \tau_{yy} & 0 \\ 0 & 0 & \tau_{zz} \end{pmatrix} \right.
$$
$$
\left. + \begin{pmatrix} \tau_{xx} & \tau_{xy} & 0 \\ \tau_{xy} & \tau_{yy} & 0 \\ 0 & 0 & \tau_{zz} \end{pmatrix} \begin{pmatrix} 0 & 0 & 0 \\ \dot{\gamma} & 0 & 0 \\ 0 & 0 & 0 \end{pmatrix} \right\}
$$
$$
= \underbrace{(\eta_s + \eta_p)}_{= \eta_0} \begin{pmatrix} -2\lambda_s \dot{\gamma}^2 & \dot{\gamma} & 0 \\ \dot{\gamma} & 0 & 0 \\ 0 & 0 & 0 \end{pmatrix}.
$$

Analogously, solving the system yields

$$
\tau_{xx} = 2\eta_0(\lambda - \lambda_s)\dot{\gamma}^2, \quad \tau_{xy} = \eta_p\dot{\gamma}, \quad \text{and} \quad \tau_{yy} = \tau_{zz} = 0 \tag{2.33}
$$

and the viscometric functions for an Oldroyd-B fluid are

$$
\eta(\dot{\gamma}) = \frac{\tau_{xy}}{\dot{\gamma}} = \eta_0, \quad N_1(\dot{\gamma}) = \tau_{xx} - \tau_{yy} = 2\eta_0(\lambda - \lambda_s)\dot{\gamma}^2, \quad \text{and} \quad N_2(\dot{\gamma}) = \tau_{yy} - \tau_{zz} = 0. \tag{2.34}
$$

Unfortunately, both models are of limited use for shear description of a non-Newtonian fluid because the predicted shear viscosity is constant. The sole exception is the class of Boger fluids which are non-Newtonian, have a constant viscosity, possess a quadratic first normal stress difference and zero second normal stress difference, and therefore can be modeled accurately. Even worse, both models fail for the description of extensional flows.

Behaviour in Steady Extensional Flows

For this example, we only consider the constitutive equation for the Oldroyd-B model because this includes the UCM results for $\eta_0 = \eta_p$ and $\lambda_s = 0$. We examine an uniaxial extensional flow $\vec{u} = (\dot{\epsilon}x, -\frac{\dot{\epsilon}}{2}y, -\frac{\dot{\epsilon}}{2}z)$ as described in Section 2.1.3. In this case, we have to solve the linear system of equations

$$
\begin{pmatrix} \tau_{xx} & \tau_{xy} & 0 \\ \tau_{xy} & \tau_{yy} & 0 \\ 0 & 0 & \tau_{zz} \end{pmatrix} - \lambda \left\{ \begin{pmatrix} \dot{\epsilon} & 0 & 0 \\ 0 & -\frac{\dot{\epsilon}}{2} & 0 \\ 0 & 0 & -\frac{\dot{\epsilon}}{2} \end{pmatrix} \begin{pmatrix} \tau_{xx} & \tau_{xy} & 0 \\ \tau_{xy} & \tau_{yy} & 0 \\ 0 & 0 & \tau_{zz} \end{pmatrix} \right.
$$
$$
\left. + \begin{pmatrix} \tau_{xx} & \tau_{xy} & 0 \\ \tau_{xy} & \tau_{yy} & 0 \\ 0 & 0 & \tau_{zz} \end{pmatrix} \begin{pmatrix} \dot{\epsilon} & 0 & 0 \\ 0 & -\frac{\dot{\epsilon}}{2} & 0 \\ 0 & 0 & -\frac{\dot{\epsilon}}{2} \end{pmatrix} \right\}
$$
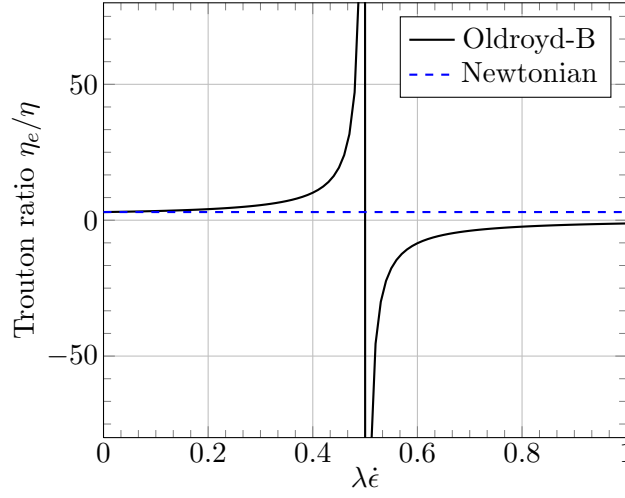
Figure 2.11: The figure illustrates the Trouton ratio $\eta_e/\eta(\dot\gamma)$ depending on the product $\lambda\dot\epsilon$ for an Oldroyd-B fluid with $\beta = 0.1$ and a Newtonian fluid. An Oldroyd-B fluid behaves strongly extensional thickening because η_e becomes infinite for $\dot\epsilon = \frac{1}{2\lambda}$. For a Newtonian fluid the Trouton ratio is equal to three for all time. Furthermore, for using the Trouton ratio as ordinate of the plot, we consider the fact that for Newtonian and Oldroyd-B fluids $\eta(\dot\gamma) = \eta_0 \; \forall\dot\gamma$ (i.e. the denominator of $\eta_e/\eta(\dot\gamma)$ is constant).

$$= \eta_0 \begin{pmatrix} 2\dot\epsilon - 4\lambda_s\dot\epsilon^2 & 0 & 0 \\ 0 & -\dot\epsilon - \lambda_s\dot\epsilon^2 & 0 \\ 0 & 0 & -\dot\epsilon - \lambda_s\dot\epsilon^2 \end{pmatrix}$$

for which we obtain the solution

$$\tau_{xx} = 2\eta_0\dot\epsilon\,\frac{1 - 2\lambda_s\dot\epsilon}{1 - 2\lambda\dot\epsilon}, \quad \tau_{yy} = \tau_{zz} = -\eta_0\dot\epsilon\,\frac{1 + \lambda_s\dot\epsilon}{1 + \lambda\dot\epsilon}, \quad \text{and} \quad \tau_{xy} = 0 \qquad (2.35)$$

and an extensional viscosity

$$\eta_e(\dot\epsilon) = \frac{\tau_{xx} - \tau_{yy}}{\dot\epsilon} = \frac{3\eta_0(1 - \lambda_s\dot\epsilon - 2\lambda\,\lambda_s\dot\epsilon^2)}{(1 - 2\lambda\dot\epsilon)(1 + \lambda\dot\epsilon)}. \qquad (2.36)$$

In Figure 2.11, we illustrate the reason for the Oldroyd-B/UCM model to fail for the simulation of extensional flows. For a given relaxation time λ, the extensional viscosity increases with stronger flows $\dot\epsilon$ and becomes infinite for $\dot\epsilon = \frac{1}{2\lambda}$. As a physical interpretation, this results in an unrestricted thickening of the fluid and accordingly does not describe characteristics of a real fluid. At the end of Section 2.3.5, we give a micromolecular interpretation of the problem.

Disadvantages of Differential Models

In comparison to integral or multiscale models, differential models have been investigated in more detail. They take the memory effect of a fluid into account with an objective time derivative of the current state variables. Therefore, in a differential model it is unnecessary to consider the previous state of the system.

If we want to obtain a realistic description of viscoelastic fluid behaviour, we have to carefully adapt the parameters of the differential model to a given problem or otherwise we obtain false results (cf. Oldroyd-B model for extensional flows). For this reason, we need a deep understanding of the physical properties so that we necessitate a microscopic description as explained in Chapter 2.3. With deeper insight, we present more differential models (FENE-P, FENE-L) that try to overcome the limitations of an Oldroyd-B fluid. However, there are microscopic properties that we cannot generalise to constitutive equations so that we have to accept restrictions for all macroscopic models.

2.2.3 Integral Models

For the description of integral models we need the concept of the relative deformation gradient which we illustrate in Figure 2.12. For this reason, consider a particle P in the fluid with position $\vec{x_1}$ at time t_1 and position $\vec{x_2}$ at time t_2 and $t_1, t_2 \in (-\infty, T]$. In this context, t_2 denotes the current time that we compare with previous states of the system (for this reason the lower bound is "$-\infty$"). Let $d\vec{x_1}$ and $d\vec{x_2}$ denote differentials that correspond to $\vec{x_1}$ and $\vec{x_2}$, then we define the deformation gradient tensor $\boldsymbol{F}(\vec{x_2}, t_2, t_1)$ as the linear mapping

$$d\vec{x_1} \;=\; \boldsymbol{F}(\vec{x_2}, t_2, t_1)d\vec{x_2}$$
$$\text{with} \quad F_{ij} \;=\; \frac{\partial x_{1,i}}{\partial x_{2,j}}, \; i,j = 1, \ldots, 3.$$

We introduce the deformation gradient tensor as a concept for strain that operates on the body. Unfortunately, $\boldsymbol{F}$ violates the principle of frame indifference that we have analysed in Section 2.2.2 for differential models. Indeed, the definition of $\boldsymbol{F}$ requires the identity

$$\boldsymbol{F}(\vec{x_2}, t_2, t_2) \;=\; \mathbf{Id} \quad \forall t_2 \in [-\infty, T]$$

for all systems of reference which is violated for rotated systems. However, the relative magnitude between both differentials is an invariant that we call the Cauchy-Green strain tensor.

Definition 2.11 [Cauchy-Green strain tensor]
For $\vec{x_2} \in \mathbb{R}^3$ and $t_2 \in [0, T]$, we define the symmetric Cauchy-Green strain tensor as

$$\boldsymbol{C}(\vec{x_2}, t_2, t_1) \;\equiv\; \boldsymbol{F}(\vec{x_2}, t_2, t_1)^T\, \boldsymbol{F}(\vec{x_2}, t_2, t_1) \;\text{where}\; t_1 \in (-\infty, T].$$

The strain tensor represents the strain or deformation history of the material and fulfils $\boldsymbol{C}(\vec{x_2}, t_2, t_2) = \mathbf{Id}$ for all systems of reference. The inverse mapping $\boldsymbol{C}^{-1}(\vec{x_2}, t_2, t_1)$ is called the Finger strain tensor.

The K-BKZ Model

We present one of the most widely used nonlinear models that was proposed by Kaye [46] and by Bernstein, Kearsley, and Zapas [8] and is therefore called K-BKZ model. The K-BKZ
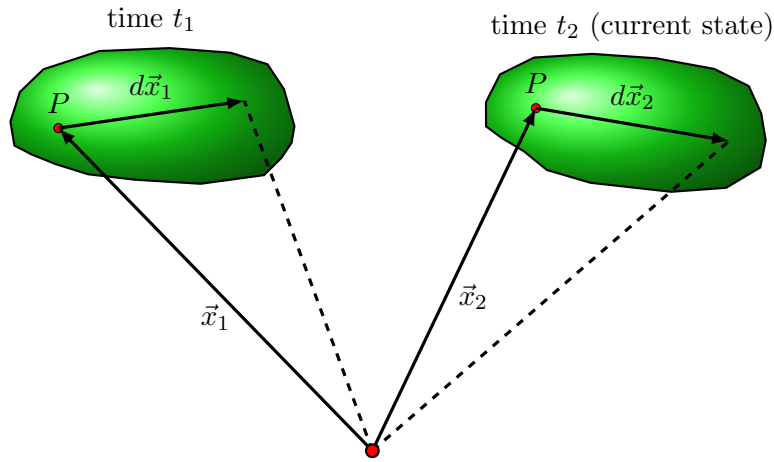
Figure 2.12: The deformation gradient tensor describes the difference in deformation between the current state of the system at t_2 and a previous state t_1 with $t_1 < t_2$.

equation for calculating the stress tensor takes in the notation of Le Bris [16] the form

$$\boldsymbol{\tau_p}(\vec{x_2}, t_2) = -\int_{-\infty}^{t_2} M(t_2 - s)\, f(\boldsymbol{C}^{-1}(\vec{x_2}, t_2, s))\, (\mathbf{Id} - \boldsymbol{C}^{-1}(\vec{x_2}, t_2, s))\, ds \tag{2.37}$$

for a given real-valued function f. The integrand is weighted by a memory function $M(t_2 - s)$ that considers all previous states of the system. In general, the mapping $s \mapsto M(t_2 - s)$ is zero for $s = \infty$ and an increasing function of s. Obviously, Newtonian fluids have a very short memory so that $M(t_2 - s) = 0$ for $s < t_2 - \epsilon$ and $\epsilon > 0$.

Apart from that, the factor $\mathbf{Id} - \boldsymbol{C}^{-1}(\vec{x_2}, t_2, s)$ in (2.37) sets the stress tensor to zero if the object is at rest (i.e. for $s = t_2$).

For the special choice

- $M(t_2 - s) = \frac{\eta_p}{\lambda^2} \exp(-\frac{t_2 - s}{\lambda})$,

- $f = 1$

we can show that (2.37) fulfils the UCM equation (2.27) in Section 2.2.2. Therefore, we can write an UCM fluid in an alternative integral form

$$\boldsymbol{\tau_p}(\vec{x_2}, t_2) = -\int_{-\infty}^{t_2} \frac{\eta_p}{\lambda^2} \exp(-\frac{t_2 - s}{\lambda})\, (\mathbf{Id} - \boldsymbol{C}^{-1}(\vec{x_2}, t_2, s))\, ds.$$

However, in general we cannot integrate nonlinear systems of differential equations in closed form so that only the simple differential models have a corresponding integral equivalent.

Disadvantages of Integral Models

The K-BKZ model in the presented form is a nonlinear model but bases upon an assumption of linearity. Indeed, the model assumes every previous configuration of $\boldsymbol{C}$ at time $t_1 < t_2$ to

be in a "temporary" equilibrium state. Different equilibrium states with $t_0 \neq t_1$ superimpose linearly. Real fluids violate this assumption and therefore limit the range of application for the K-BKZ model.

Moreover, the use of a memory kernel $M(t_2 - s)$ requires to trace the trajectories of the fluid particles back to their previous states. This increases the computational effort in comparison to differential models where only the present state and its derivatives are considered. Consequently, integral models are mostly used for simple laminar flows where the trajectories are already known.

As a result, the disadvantages of simple differential and integral models demand to consider the microscopic behaviour of fluids. The benefits are on the one hand more advanced macroscopic models and on the other hand full multiscale models that circumvent modelling restrictions.

	MACRO	MICRO-MACRO	
modelling capabilities	low	high	
current utilisation	industry	laboratories	
		Stochastic	Fokker-Planck
computational cost	low	high	moderate
computational bottleneck	HWNP	variance, HWNP	dimension, HWNP

Table 2.1: The table compares the macroscopic models from Chapter 2.2 with the multiscale models from Chapter 2.3 in respect of modelling capabilities, current utilisation, computational cost and their disadvantages. The computational cost is specified for models with low dimensional configuration spaces D (i.e. $\dim(D) = 2$) which we present later on. For more advanced models (i.e. high-dimensional configuration spaces), the Fokker-Planck approach becomes much more expensive than the stochastic model which we express by the term "dimension" in the last row. All models suffer from the high Weissenberg number problem (HWNP) that we describe in Section 6.2.5.

2.3 Multiscale Models for Non-Newtonian Fluids

In the following chapter, we introduce the multiscale micro-macro approach for computing the extra-stress tensor $\boldsymbol{\tau_p}$ in contrast to the macroscopic differential and integral models from the previous chapter. The advantage of multiscale simulations for non-Newtonian fluids is an adequate description of the underlying physics. On the contrary, micro-macro models require a higher computational effort than classical models.

In the first section, we derive the Fokker-Planck equation and its equivalent stochastic differential equation as the basic equation for polymeric fluids. In the next section, we describe the Kramers expression that connects a microscopic description with the macroscopic stress tensor $\boldsymbol{\tau_p}$. Then, we present analytical solutions and approximations for the Fokker-Planck equation in simple flows. At last, we introduce closure approximations that allow to disregard the Fokker-Planck equation in favour of a macroscopic tensor equation for $\boldsymbol{\tau_p}$.

As an overview to the subsequent chapter, we present Table 2.1 according to Le Bris et al. [16] which compares microscopic models from the previous chapter with multiscale models from the current chapter in terms of modelling capabilities, current utilisation, computational cost and its disadvantages.

2.3.1 Introduction

Polymeric fluids

Up to now, we have described Newtonian and non-Newtonian fluids using the macroscopic equations of continuum mechanics. However, we can interpret a viscoelastic fluid as a Newtonian fluid which contains an additional microstructure. Thus, we introduce the class of polymeric liquids.

Definition 2.12 [POLYMERIC FLUIDS]
A Newtonian solvent that contains polymer chains of large molecules is called a polymeric fluid. The polymer chains contribute elastic behaviour to the Newtonian solvent. If a fluid has
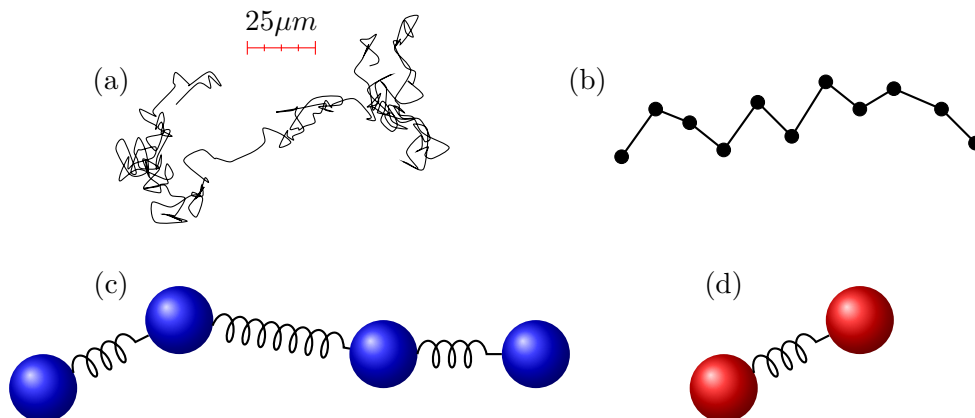
Figure 2.13: A real polymer (a) consists of 10^3 to 10^6 individual monomers that are chemically bonded and have a size in the order of 10^{-6} m. Subsequently, we present various models in descending order: the Kramers bead-rod chain model with eleven beads (b), the freely joined bead-spring chain model with four beads (c) and the dumbbell model (d).

a low concentration of polymers, we denote it as dilute. In contrast, we denote fluids with high concentrations of polymers as polymer melts or concentrated solutions.

The major differences between dilute and concentrated models are the following:

1. Dilute models treat polymers individually and only consider interactions between molecules and the surrounding Newtonian solvent. Therefore, individual polymers have no interaction with each other.

2. Concentrated polymeric models limit the orientation of polymers to less degrees of freedom because the polymers block each other. The most important models for concentrated solutions are network and reptation theories.

Owing to the presence of molecules within a Newtonian fluid, we split the viscosity of a fluid in two components

$$\eta = \eta_s + \eta_p \tag{2.38}$$

where η_s denotes the solvent viscosity and η_p the polymeric viscosity. Furthermore, we use the stress tensor splitting

$$\boldsymbol{\tau} = \boldsymbol{\tau_s} + \boldsymbol{\tau_p} \tag{2.39}$$

of equation (2.8).

Subsequently, we consider a dumbbell model for dilute polymeric fluids which is a multiscale model as we do not only model the macroscopic fluid but also the meso- or microscopic polymer molecule. Obviously, a dumbbell model is a very simplified approximation to a real molecule (cf. Figure 2.13). However, even such a model reproduces convection, orientation and extension of the polymers within the fluid which are the major parameters of influence.

The analysis of dumbbell models leads to a Fokker-Planck equation, a differential equation describing the time evolution of a probability density function (pdf), or to an equivalent stochastic differential equation (cf. stochastic processes in Section 3.3).
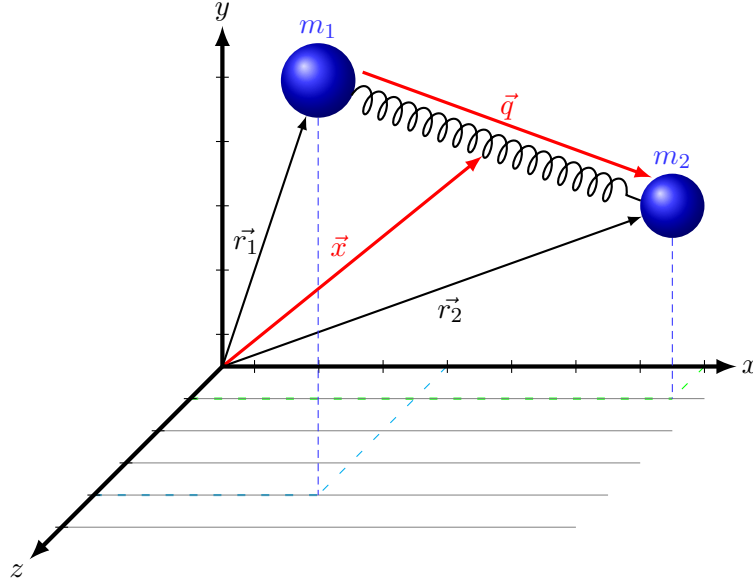
Figure 2.14: The dumbbell model consists of two beads with position $\vec{r_1}$ and $\vec{r_2}$ which interact through a spring. The spring represents intermolecular forces between both beads. Even if the model is comparatively simple, it can describe the major polymeric effects with a moderate computational effort. For description, we express the Fokker-Planck equation in adapted coordinates such as the centre of mass $\vec{x}$ and the orientation vector $\vec{q}$.

2.3.2 Derivation of the Fokker-Planck Equation

The derivation of the Fokker-Planck equation bases on Lozinski [56], Knezevic [50], Owens and Phillips [68], and Lozinski, Owens, and Phillips [59]. We consider a dumbbell within a Newtonian fluid which we illustrate in Figure 2.14. A dumbbell consists of two separate masses that are connected with a massless spring. The spring denotes intermolecular forces between both beads. For description, let $\vec{r_1}$ be the position vector of the first mass m_1 and in return let $\vec{r_2}$ be the position vector of m_2 with $\vec{r_1}, \vec{r_2} \in \Omega \subset \mathbb{R}^3$. We refer to Ω as the physical space in which the macroscopic fluid is located. We further assume, for simplicity, that both beads have the same mass $m_1 = m_2 = m$.

Newton's second law describes the equations of motion for the beads as

$$m_i \frac{d^2 \vec{r_i}}{dt^2} = \vec{F}_i^{drag} + \vec{F}_i + \vec{B}_i, \qquad i = 1, 2, \tag{2.40}$$

where we have the following components:

1. $\vec{F}_i^{drag}$ is the drag force on bead i. It opposes the relative motion of the beads through the fluid and can be seen as a kind of fluid resistance.

2. $\vec{F}_i$ denotes the spring force on bead i caused by bead j ($i \neq j$). In the derivation, we consider a general spring force so that we are able to use the results for different kind of intermolecular forces. Later on, we concentrate on Hookean and FENE spring forces.

3. $\vec{B}_i$ is the Brownian force due to random collisions between bead i and adjacent molecules.

The Drag Force

The drag force depends on the relative motion of the beads to the fluid $\vec{u}\left(\vec{r}_i, t\right) - \frac{d\vec{r}_i}{t}$ and on the friction tensor $\boldsymbol{\zeta}$ which is defined as

$$\vec{F}_i^{drag} = \boldsymbol{\zeta}\left(\vec{u}\left(\vec{r}_i, t\right) - \frac{d\vec{r}_i}{t}\right). \tag{2.41}$$

A general ansatz for the second order tensor $\boldsymbol{\zeta}$ is

$$\boldsymbol{\zeta} = \zeta\left(\vec{e_q} \otimes \vec{e_q} + \sigma^{-1}\left(\mathbf{Id} - \vec{e_q} \otimes \vec{e_q}\right)\right) \tag{2.42}$$

where $\vec{e_q}$ denotes a unit vector in the direction of $\vec{q}$ with ζ and σ as parameters. The parameter ζ is derived from Stokes' Law as demonstrated in Bird [9].

Theorem 2.13 [STOKES' LAW]
The drag force - also called frictional force - on a sphere with radius a that is moving unidirectionally with constant relative velocity $\vec{v}$ in a Newtonian solvent with viscosity η_s is

$$\vec{F}^{drag} = 6\pi\eta_s a\vec{v}$$
$$\equiv \zeta\,\vec{v}.$$

Here, we have introduced the constant friction coefficient $\zeta := 6\pi\eta_s a$ and $[\zeta] = \frac{kg}{s}$.

If $\sigma = 1$ in (2.42), then the friction tensor is isotropic (i.e. uniform in all directions) because it takes the form of the Kronecker Delta tensor $\boldsymbol{\zeta} = \text{diag}(\zeta, \zeta, \zeta)$. On the other hand, if $\sigma < 1$, then the friction force in directions normal to $\vec{q}$ is stronger than its tangential component. For simplicity, we concentrate on the case $\sigma = 1$.

Note that this ansatz neglects any influence from a molecule on the viscosity of the surrounding molecules. Therefore, this approach is restricted to dilute polymer solutions.

The Brownian Force

We write the Brownian force $\vec{B}_i$ in the form

$$\vec{B}_i = \sqrt{2k_BT\zeta}\left(\vec{e_q} \otimes \vec{e_q} + 1/\sqrt{\sigma}\left(\mathbf{Id} - \vec{e_q} \otimes \vec{e_q}\right)\right)d\vec{W}_i$$
$$\overset{\sigma=1}{=} \sqrt{2k_BT\zeta}\,d\vec{W}_i. \tag{2.43}$$

With $d\vec{W}_i = \left(W_{i,1}(t), ..., W_{i,n}(t)\right)^T$, $t \geq 0$ and $i \in \{1, 2\}$ we describe a multi-dimensional Wiener process, that means, a multidimensional Brownian motion. We can characterise the process by its expectation

$$\langle W_{i,j}\left(t\right)\rangle = 0 \qquad \text{for} \quad j = 1, ..., n$$

and the second moments

$$\langle W_{i,j}\left(t_1\right) W_{i,j}\left(t_2\right)\rangle = \int_0^{t_1} \int_0^{t_2} \delta\left(t' - t''\right) dt'' \, dt'$$

$$= min(t_1, t_2).$$

The factor $\sqrt{2k_B T \zeta}$ is a consequence of the equipartition of energy or equipartition theorem . It connects the temperature of a system with its average energy (here: kinetic energy). According to the theorem, the kinetic energy of the system is

$$E_{\text{kin}} = \frac{f}{2} k_B T$$

for a system with f degrees of freedom. Here, the coefficient k_B is the Boltzmann constant and T denotes the thermodynamic temperature in the SI base unit Kelvin.

Langevin Equation

In [82], Schieber and Öttinger give reasons why the acceleration forces $m_i \frac{d^2 \vec{r_i}}{dt^2}$ (for $i = 1, 2$) on the left-hand side (LHS) of (2.40) may be neglected. By substituting this assumption into (2.40), inserting the equations for the drag (2.41) and the Brownian force (2.43), and dividing the equation by ζ, we obtain a stochastic differential equation in the form of

$$d\vec{X}_t = \vec{\mu}\left(\vec{X}_t, t\right) dt + \boldsymbol{\sigma}\left(\vec{X}_t, t\right) d\vec{W}_t \tag{2.44}$$

which we also denote, in the context of statistical physics, as a Langevin equation. In doing so, we have set

$$\vec{X}_t = \begin{pmatrix} \vec{r_1}(t) \\ \vec{r_2}(t) \end{pmatrix}, \quad \vec{\mu}\left(\vec{X}_t, t\right) = \begin{pmatrix} \vec{u}(\vec{r_1}(t), t) + \zeta^{-1}\vec{F}(\vec{r_2}(t) - \vec{r_1}(t)) \\ \vec{u}(\vec{r_2}(t), t) + \zeta^{-1}\vec{F}(\vec{r_1}(t) - \vec{r_2}(t)) \end{pmatrix},$$

$$\boldsymbol{\sigma} = \sqrt{\frac{2k_B T}{\zeta}}\, \mathbf{Id}, \quad \text{and} \quad \vec{W}_t = \begin{pmatrix} \vec{W}_1(t) \\ \vec{W}_2(t) \end{pmatrix}.$$

Additionally, a stochastic differential equation is actually an integral equation that bases on the concept of Itô integration (cf. Chapter 3.3 about stochastic processes). At the moment, we do not try to solve the stochastic differential equation (2.44) but rather concentrate on the corresponding partial differential equation for the pdf. The following theorem connects both formulations and for this reason, it is of particular importance.

Theorem 2.14 [KOLMOGOROV FORWARD EQUATION]
*Let $\vec{X}(t) \in \mathbb{R}^d$ be the random variable of an Itô stochastic differential equation $d\vec{X}_t = \vec{\mu}\left(\vec{X}_t, t\right) dt +$
$\boldsymbol{\sigma}\left(\vec{X}_t, t\right) d\vec{W}_t$, where $\vec{W}_t \in \mathbb{R}^d$ is a d-dimensional Wiener process. If $\vec{X}(t)$ corresponds to a
probability density function $\psi \in C^{2,1}(\mathbb{R}^{2d} \times [0, T_{End}])$ and $X(t = 0) \sim \psi(\vec{x}, 0)$, then the evolution
of ψ is given by*

$$\frac{\partial \psi}{\partial t} + \sum_{i=1}^{2d} \frac{\partial}{\partial x_i}\left(\mu_i \psi\right) = \frac{1}{2} \sum_{i,j=1}^{2d} \frac{\partial^2}{\partial x_i \partial x_j}\left(\sigma_{i,j} \sigma_{j,i} \psi\right)$$

with a drift term $\vec{\mu}$ and a diffusion term $\boldsymbol{\sigma} \otimes \boldsymbol{\sigma}^T$.

Proof: Rigorous proofs are given in Arnold [4] and Kallianpur [44].

Using the Kolmogorov Forward Equation on (2.44), we obtain a Fokker-Planck equation

$$\frac{\partial \psi}{\partial t} + \nabla_{r_1} \cdot \left[\vec{u}\left(\vec{r_1}(t),t\right) + \zeta^{-1}\vec{F}\left(\vec{r_2}(t) - \vec{r_1}(t)\right) \right] \tag{2.45}$$
$$+ \nabla_{r_2} \cdot \left[\vec{u}\left(\vec{r_2}(t),t\right) + \zeta^{-1}\vec{F}\left(\vec{r_1}(t) - \vec{r_2}(t)\right) \right] = \frac{k_B T}{\zeta}\Delta_{r_1}\psi + \frac{k_B T}{\zeta}\Delta_{r_2}\psi.$$

A solution ψ of equation (2.45) gives the probability $\psi(\vec{x},\vec{q},t)\,d\vec{q}$ of finding a dumbbell with an orientation between $\vec{q}$ and $\vec{q}+d\vec{q}$ at $(\vec{x},t)$.

Barycentric Coordinates

The evolution of ψ is better described in a coordinate system that represents the mass centre and the orientation of the dumbbells. As illustrated in Figure 2.14, we define the centre of mass $\vec{x}(t)\in\Omega$ and the orientation vector $\vec{q}(t)\in D\subset\Omega$ as

$$\vec{x}(t) = \frac{\vec{r_1}(t) + \vec{r_2}(t)}{2} \quad \text{and} \quad \vec{q}(t) = \vec{r_2}(t) - \vec{r_1}(t). \tag{2.46}$$

Therefore, we switch from the $(\vec{r_1},\vec{r_2})$-coordinates to the $(\vec{x},\vec{q})$-system and denote D as the configuration space that includes all possible orientations. The configuration space normally exists on a mesoscopic length scale in comparison to the macroscopic space Ω. From (2.46) and the chain rule we obtain

$$\frac{\partial}{\partial\vec{r_1}} = \frac{1}{2}\frac{\partial}{\partial\vec{x}} - \frac{\partial}{\partial\vec{q}} \quad \text{and}$$
$$\frac{\partial}{\partial\vec{r_2}} = \frac{1}{2}\frac{\partial}{\partial\vec{x}} + \frac{\partial}{\partial\vec{q}}$$

for the divergence operator. Additionally, for the Laplacian we perform the substitutions

$$\frac{\partial^2}{\partial\vec{r_1}^2} = \frac{1}{4}\frac{\partial^2}{\partial\vec{x}^2} - \frac{1}{2}\frac{\partial^2}{\partial\vec{x}\partial\vec{q}} - \frac{1}{2}\frac{\partial^2}{\partial\vec{q}\partial\vec{x}} + \frac{\partial^2}{\partial\vec{q}^2} \quad \text{and}$$
$$\frac{\partial^2}{\partial\vec{r_2}^2} = \frac{1}{4}\frac{\partial^2}{\partial\vec{x}^2} + \frac{1}{2}\frac{\partial^2}{\partial\vec{x}\partial\vec{q}} + \frac{1}{2}\frac{\partial^2}{\partial\vec{q}\partial\vec{x}} + \frac{\partial^2}{\partial\vec{q}^2}.$$

By substituting these expressions into (2.45) and using the identity $\vec{F}(\vec{q}) = -\vec{F}(-\vec{q})$, we obtain

$$\frac{\partial\psi}{\partial t} + \nabla_q \cdot \left[\left(\vec{u}\left(\vec{x}+\vec{q}/2,t\right) - \vec{u}\left(\vec{x}-\vec{q}/2,t\right)\right)\psi - \frac{2}{\zeta}\vec{F}(\vec{q})\psi \right] \tag{2.47}$$
$$+ \nabla_x \cdot \left[\frac{1}{2}\left(\vec{u}\left(\vec{x}+\vec{q}/2,t\right) + \vec{u}\left(\vec{x}-\vec{q}/2,t\right)\right)\psi \right] = \frac{k_B T}{2\zeta}\Delta_x\psi + \frac{2k_B T}{\zeta}\Delta_q\psi,$$

where we have used the same notation $\psi = \psi(\vec{x},\vec{q},t)$ for the density function for simplicity.

The Spring Forces

The identity $\vec{F}(\vec{q}) = -\vec{F}(-\vec{q})$ is a consequence of Newton's third law of motion. We only consider conservative spring forces that can be derived as the negative gradient from a scalar potential $\phi(\vec{q})$, i.e.

$$\vec{F}(\vec{q}) = -\nabla_{\vec{q}}\,\phi(\vec{q}).$$

The scalar potentials that we are interested in, lead to the Hookean and FENE (Finitely Extensible Nonlinear Elastic) spring forces. Let H be the spring constant and let $\|\vec{q}_{\max}\|$ denote the maximum extensibility of a FENE dumbbell, then we define two model forces:

1. Hookean dumbbells:

$$\phi(\vec{q}) = -\frac{1}{2}H\|\vec{q}\|^2, \tag{2.48}$$

$$\vec{F}(\vec{q}) = H\vec{q}. \tag{2.49}$$

2. FENE dumbbells:

$$\phi(\vec{q}) = \frac{1}{2}H\,\|\vec{q}_{\max}\|^2 \log\left(1 - \frac{\|\vec{q}\|^2}{\|\vec{q}_{\max}\|^2}\right), \tag{2.50}$$

$$\vec{F}(\vec{q}) = \frac{H\vec{q}}{1 - \frac{\|\vec{q}\|^2}{\|\vec{q}_{\max}\|^2}} \quad \text{with } \|\vec{q}\| < \|\vec{q}_{\max}\|. \tag{2.51}$$

On the one hand, the nonlinear FENE spring force involves a more realistic description of physics as the linear Hookean dumbbell because the length of polymeric molecules is restricted. On the other hand, the FENE spring force is much more challenging as it exhibits a singularity at the boundary, i.e.

$$\lim_{\|\vec{q}\|\to\|\vec{q}_{\max}\|} \vec{F}_{\text{FENE}}(\vec{q}) = \infty.$$

Local Homogeneity Assumption

Subsequently, we consider two cases for the flow field in which the second one is a generalisation of the first one. These cases are

- homogeneous flows, i.e. flows with a velocity field $\vec{u}$ of the form

$$\vec{u}(\vec{p}) = \boldsymbol{\kappa}\,(\vec{p} - \vec{x}) + \vec{u}(\vec{x}), \quad p, x \in \Omega, \tag{2.52}$$

  and $\boldsymbol{\kappa}$ as an abbreviation for the velocity gradient $\nabla_{\vec{x}}\vec{u}$ that may depend on time t but not on the space variables $\vec{x}$ and $\vec{p}$ and

- non-homogeneous flows that satisfy a local homogeneity assumption.

For non-homogeneous flows, we cannot use a description as in equation (2.52) but drop this restriction at least locally on the length scale of a dumbbell. Therefore, using a Taylor

expansion up to the linear term, we can write $\vec{u}(p)$ in the vicinity of $\vec{x}$ as

$$\vec{u}(\vec{p}) = \nabla_{\vec{x}}\vec{u}\,(\vec{p} - \vec{x}) + \vec{u}(\vec{x}) \qquad \text{for all } p \in B_\epsilon\,(\vec{x}) \text{ and } x \in \Omega. \tag{2.53}$$

We make a similar assumption for the density function ψ (i.e. ψ is linear on the length scale of a dumbbell) as this simplifies the description of the configuration space D and we denote this as the local homogeneity assumption. The assumption is reasonable as the length scale of a dumbbell (cf. configuration vector $\vec{q}$) is normally orders of magnitude smaller than the macroscopic length scale (cf. dumbbell position vector $\vec{x}$) and will be used throughout the whole thesis.

Using the linearity assumption on $\vec{u}\,(\vec{x} + \vec{q}/2, t)$ and $\vec{u}\,(\vec{x} - \vec{q}/2, t)$, equation (2.47) becomes

$$\boxed{\frac{\partial \psi}{\partial t} + \nabla_q \cdot \left[\left(\nabla_{\vec{x}}\vec{u}\,\vec{q} - \frac{2}{\zeta}\vec{F}(\vec{q}) \right) \psi \right] + \nabla_x \cdot (\vec{u}\,\psi) = \frac{k_B T}{2\zeta}\Delta_x \psi + \frac{2 k_B T}{\zeta}\Delta_q \psi.} \tag{2.54}$$

For a homogeneous flow, $\psi\,(t, \vec{x}, \vec{q}) = \psi\,(t, \vec{q})$ does not depend on physical space $\vec{x}$ and the Fokker-Planck equation reduces to

$$\boxed{\frac{\partial \psi}{\partial t} + \nabla_q \cdot \left[\left(\boldsymbol{\kappa}\,\vec{q} - \frac{2}{\zeta}\vec{F}(\vec{q}) \right) \psi \right] = \frac{2 k_B T}{\zeta}\Delta_q \psi.} \tag{2.55}$$

Properties of the Probability Density Function

As $\psi(\vec{x}, \cdot, \cdot)\colon C^{2,1}(D, [0, T]) \to \mathbb{R}$ is a pdf for fixed $\vec{x} \in \Omega$, ψ has to fulfil two important properties:

1. The initial condition is non-negative, i.e.

$$\psi(\vec{x}, \vec{q}, 0) \geqslant 0 \qquad \forall\,(\vec{x}, \vec{q}) \in \Omega \times D. \tag{2.56}$$

2. The integral of ψ over the configuration space D is constant and can be normalised according to

$$\int_D \psi(\vec{x}, \vec{q}, t)\,d\vec{q} = 1 \qquad \forall\,(\vec{x}, t) \in \Omega \times [0, T]. \tag{2.57}$$

Indeed, any solution ψ of the Fokker-Planck equation (2.54) conserves the probability condition (2.57) which is proved in Knezevic [50]. Since any solution fulfils this condition, we use (2.57) as an error indicator for the numerical approximation ψ_N of ψ in Section 4.1.2 (cf. with equation (4.16)).

Strongly Non-homogeneous Flows

If we consider small tubes with diameters in the order of the molecules (e.g. blood in a vein), we would have to omit the linearity assumption of ψ as the molecules interact with the boundary region. This would lead to a configuration space D that depends on $\vec{x}$. For instance, for the FENE spring force (2.51) we assume D to be a ball with radius $\|\vec{q}_{\max}\|$ which would take,

without using the assumption, the form

$$D(\vec{x}) \;=\; \{\vec{q}\,|\,\|\vec{q}\| < \|\vec{q}_{\mathrm{max}}\|\} \cap \{\vec{q}\,|\,\vec{x} + \vec{q}/2 \in \Omega\}\,.$$

Due to boundary considerations, the configuration space D might become difficult to represent even for simple geometries Ω. In literature, these fluids are termed as strongly non-homogeneous flows. For the sake of simplicity, we will skip their consideration.

Dimensionless Formulation

Even if we could use the equations (2.54) or (2.55) for the computation of ψ, we prefer to solve the problem in a dimensionless formulation. Therefore, we introduce l_0, λ, L_0, and U_0 as intrinsic parameters of the system. In doing so, we have

- $l_0 = \sqrt{k_B T / H}$ as characteristic length-scale of a dumbbell ($[l_0]$=m),

- $\lambda = \frac{\zeta}{4H}$ as characteristic relaxation time of a dumbbell ($[\lambda]$=s),

- L_0 as characteristic length of a macroscopic flow ($[L_0]$=m),

- and U_0 as characteristic velocity of a macroscopic flow ($[U_0]$=m/s)

with H as spring constant. Using these characteristic units, we define new dimensionless quantities

$$\vec{x}^* := \vec{x}/L_0, \tag{2.58a}$$
$$\vec{q}^* := \vec{q}/l_0, \tag{2.58b}$$
$$\vec{u}^* := \vec{u}/U_0, \tag{2.58c}$$
$$t^* := U_0/L_0\, t, \tag{2.58d}$$

and transform the differential operators with the chain rule, e.g.

$$\frac{\partial}{\partial \vec{q}} = \frac{\partial}{\partial \vec{q}^*}\frac{d\vec{q}^*}{d\vec{q}} = \frac{1}{l_0}\frac{\partial}{\partial \vec{q}^*} \tag{2.59a}$$

$$\frac{\partial^2}{\partial \vec{q}^2} = \frac{\partial}{\partial \vec{q}^*}\left(\frac{\partial}{\partial \vec{q}}\right)\frac{d\vec{q}^*}{d\vec{q}} = \frac{1}{l_0^2}\frac{\partial^2}{\partial \vec{q}^{*2}}\,. \tag{2.59b}$$

If we substitute (2.58a) - (2.58d) and (2.59a) - (2.59b) into (2.54), we obtain

$$\frac{U_0}{L_0}\frac{\partial \psi}{\partial t^*} + \frac{\partial}{\partial \vec{q}^*}\cdot\left(\frac{U_0}{L_0}\nabla_{\vec{x}^*}\vec{u}^*\,\vec{q}^*\,\psi - \underbrace{2H/(\zeta)}_{=1/(2\,\lambda)}\,\vec{F}^*(\vec{q}^*)\psi\right)$$

$$+ \frac{U_0}{L_0}\frac{\partial}{\partial \vec{x}^*}\cdot(\vec{u}^*\psi) = \underbrace{\frac{k_B T}{2\zeta\, l_0^2}}_{=1/(8\,\lambda)}\left(\frac{l_0}{L_0}\right)^2 \Delta_{\vec{x}^*}\psi + \underbrace{\frac{2k_B T}{\zeta\, l_0^2}}_{=1/(2\,\lambda)}\Delta_{\vec{q}^*}\psi.$$

where we have used the relaxation time $\lambda = \frac{\zeta}{4H}$. Note that we describe the dimensionless form of the spring forces $\vec{F}^*(\vec{q}^*)$ in equation (2.64) and (2.66). Multiplying by L_0/U_0 and using the dimensionless Weissenberg number, we obtain

$$\frac{\partial \psi}{\partial t^*} + \frac{\partial}{\partial \vec{q}^*} \cdot \left((\nabla \vec{u}^*) \, \vec{q}^* \, \psi - \frac{1}{2\,Wi} \vec{F}^*(\vec{q}^*) \psi \right) + \frac{\partial}{\partial \vec{x}^*} \cdot (\vec{u}^* \psi) = \frac{1}{8\,Wi} \left(\frac{l_0}{L_0} \right)^2 \Delta_{\vec{x}^*} \psi + \frac{1}{2\,Wi} \Delta_{\vec{q}^*} \psi.$$
(2.60)

For further considerations, we drop the asterisk on the Fokker-Planck equation. Now, we give a definition for the Weissenberg number that we use in equation (2.60).

Definition 2.15 [Weissenberg number]
The Weissenberg number $Wi \equiv \lambda U_0/L_0$ is defined as the product of the microscopic time-scale λ with the macroscopic shear rate $\dot{\gamma} \approx U_0/L_0$ (cf. Definition 2.4 of shear viscosity).

It has a similar definition as the Deborah number in Section 2.2.1 but is used in other contexts. While the Weissenberg number is used to compare elastic forces (of solids) to viscous effects (of fluids), the Deborah number describes the ratio between the microscopic and macroscopic time-scale. Therefore, we can have situations with large Deborah number and small Weissenberg number and vice versa. However, some authors use both dimensionless numbers in an analogous manner.

Interestingly, equation (2.60) gives reasons for a further simplification of the Fokker-Planck equation. Given that $l_0 \ll L_0$, the diffusion in $\vec{x}$ is very small because $\left(\frac{l_0}{L_0} \right)^2 \ll 1$ and thus can be neglected. Even though this is a standard approach in literature, Barrett et al. [5] have shown that this ansatz leads to a degenerate parabolic equation with hyperbolic characteristics in physical space. Nevertheless, we also neglect the diffusion in physical space Ω and obtain equivalent dimensionless formulations of (2.54) and (2.55) which are

$$\boxed{\frac{\partial \psi}{\partial t} + \frac{\partial}{\partial \vec{q}} \cdot \left((\nabla \vec{u}) \vec{q} \psi - \frac{1}{2\,Wi} \vec{F}(\vec{q}) \psi \right) + \frac{\partial}{\partial \vec{x}} \cdot (\vec{u} \psi) = \frac{1}{2\,Wi} \Delta_{\vec{q}} \psi}$$
(2.61)

for non-homogeneous flows with a density function $\psi : \mathbb{R}^7 \to \mathbb{R}$ (i.e. ψ depends on $\vec{x}, \vec{q}$ and t) and

$$\boxed{\frac{\partial \psi}{\partial t} + \frac{\partial}{\partial \vec{q}} \cdot \left(\boldsymbol{\kappa} \, \vec{q} \psi - \frac{1}{2\,Wi} \vec{F}(\vec{q}) \psi \right) = \frac{1}{2\,Wi} \Delta_{\vec{q}} \psi}$$
(2.62)

for homogeneous problems and a simplified pdf $\psi : \mathbb{R}^4 \to \mathbb{R}$.

Dimensionless Spring Forces

Analogue to the nondimensional characteristic units of (2.58a) and (2.58d), we have to nondimensionalise the elastic spring forces $F(\vec{q})$ of equation (2.49) and (2.51) such that we get

1. Hookean dumbbells (nondimensionalised):

$$\phi(\vec{q}) = -\frac{1}{2}\|\vec{q}\|^2, \tag{2.63}$$

$$\vec{F}(\vec{q}) = \vec{q}, \tag{2.64}$$

2. FENE dumbbells (nondimensionalised):

$$\phi(\vec{q}) = \frac{1}{2}b\log\left(1 - \frac{\|\vec{q}\|^2}{b}\right), \tag{2.65}$$

$$\vec{F}(\vec{q}) = \frac{\vec{q}}{1 - \frac{\|\vec{q}\|^2}{b}} \quad \text{with } \|\vec{q}\| < \sqrt{b}. \tag{2.66}$$

Here, we have introduced b as a dimensionless unit for the maximum length of a FENE dumbbell which we define by

$$b = \frac{\|\vec{q}_{\mathrm{max}}\|^2}{l_0^2} = \frac{H\,\|\vec{q}_{\mathrm{max}}\|^2}{k_B T}.$$

2.3.3 Equivalent Stochastic Description

In the beginning of Section 2.3.2, we have examined a force balance equation (2.40) and after further analysis obtained a stochastic differential equation. Theorem 2.14 (Kolmogorov Forward Equation) provides a theoretical background for the equivalence between stochastic description and the description of a deterministic diffusion equation for ψ. For this reason, we write the stochastic counterparts of the deterministic equations (2.61) and (2.62) as

$$d\vec{Q}_t(\vec{x}) = \left(-\vec{u}(\vec{x},t)\,\nabla\vec{Q}_t(\vec{x}) + (\nabla\vec{u}(\vec{x},t))\vec{Q}_t(\vec{x}) - \frac{1}{2\,Wi}\vec{F}(\vec{Q}_t(\vec{x}))\right)dt + \sqrt{\frac{1}{Wi}}\,d\vec{W}_t \tag{2.67}$$

for non-homogeneous flows and

$$d\vec{Q}_t = \left(\boldsymbol{\kappa}\,\vec{Q}_t - \frac{1}{2\,Wi}\vec{F}(\vec{Q}_t)\right)dt + \sqrt{\frac{1}{Wi}}\,d\vec{W}_t \tag{2.68}$$

for homogeneous flow fields. Obviously, the stochastic process $\vec{Q}_t$ represents the vector $\vec{q}(t)$ of the dumbbell orientation.

We note that some authors prefer to leave the time parameter t dimensionful while nondimensionalise the other values as in (2.58a) - (2.58c). Nevertheless, the equations for ψ or the stochastic process only differ in the Weissenberg number Wi which has to be replaced by the relaxation time λ. Furthermore, the Itô integral depends on a dimensionful time parameter.

2.3.4 The Kramers Expression

In this section, we derive the connection between the solution ψ of the Fokker-Planck equation (on a microscopic length scale) and the polymeric extra-stress (on a macroscopic length scale) represented by the stress tensor $\boldsymbol{\tau_p}$ (cf. equation (2.8)). This concept was first proposed by Kramers [52] and is therefore called Kramers expression. We follow Bird [10] and Li et al. [54] in the derivation of the Kramers expression. Note that the ansatz bases on a dimensionful description of the stress and will be nondimensionalised later on.

The micromolecular dumbbells of the previous section cause extra stress to the Newtonian solvent because of three major effects. These are contributions from

- the spring force $\boldsymbol{\tau_p^{(c)}}$,

- the bead motion $\boldsymbol{\tau_p^{(b)}}$,

- external forces $\boldsymbol{\tau_p^{(e)}}$.

However, if the same force acts on each bead, which we suppose for Hookean and FENE spring forces, there is no external force contribution to the stress tensor (i.e. $\boldsymbol{\tau_p^{(e)}} = 0$) and the tensor itself is symmetric. Therefore, we only consider the first two effects.

Contribution from the Spring Force

We consider an arbitrary plane with an area S that moves along the fluid and is described by an unit normal vector $\vec{n}$. Dumbbells whose connecting vectors $\vec{q}$ interfere with the plane cause stress denoted by $\boldsymbol{\tau_p^{(c)}}$. For further analysis, we consider the average spring force if bead "1" is on the negative side (i.e. $\vec{n} \cdot \vec{q} > 0$) and bead "2" is on the positive side of the plane and vice versa (i.e. $\vec{n} \cdot \vec{q} < 0$). For the sign convention of the plane and an illustration of the problem, we refer to Figure 2.15.

First, we are interested in the number of intersecting dumbbells. This quantity depends on

- the number of dumbbells per unit volume or polymer number density $n_\mathrm{d} = N_p/V$,

- the volume $(\vec{n} \cdot \vec{q}) \, S$ in which a dumbbell remains, and

- the probability $\psi(\vec{q}, t) \, d\vec{q}$ to find a dumbbell with an orientation between $\vec{q}$ and $\vec{q} + d\vec{q}$.

As each dumbbell contributes a spring force of $F(\vec{q})$ and the identity $F(-\vec{q}) = -F(\vec{q})$ holds, we obtain the total amount of force $\vec{F}_\Sigma$ acting on the plane as

$$\vec{F}_\Sigma = \underbrace{n_\mathrm{d} \, S \int_{\text{all } \vec{q}} \vec{q} \otimes \vec{F}(\vec{q}) \psi(\vec{q}, t) \, d\vec{q}}_{\text{2nd order tensor}} \cdot \vec{n}. \tag{2.69}$$

If we divide (2.69) by S, we can identify the result with $\boldsymbol{\tau_p^{(c)}} \cdot \vec{n}$. Therefore, the stress $\boldsymbol{\tau_p^{(c)}}$ depending on the connecting spring is

$$\boldsymbol{\tau_p^{(c)}} = n_\mathrm{d} \int \vec{q} \otimes \vec{F}(\vec{q}) \psi(\vec{q}, t) \, d\vec{q} \equiv n_\mathrm{d} \left\langle \vec{q} \otimes \vec{F}(\vec{q}) \right\rangle. \tag{2.70}$$
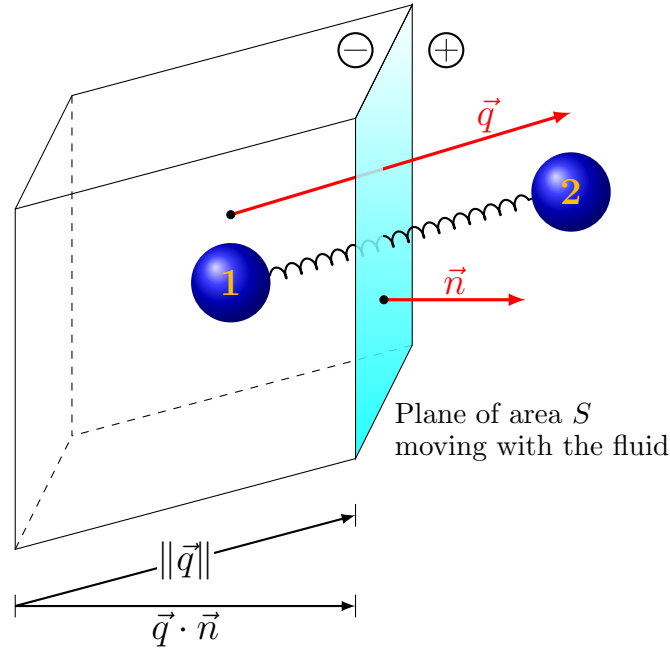
Figure 2.15: One contribution to the non-Newtonian stress tensor is given by springs that represent intermolecular forces between the beads. For the derivation, we consider those springs whose chaining intersects a surface element of area S.

Note that if g is a function that depends on the orientation vector $\vec{q}$, we can define the expectation of g as

$$\langle g(\vec{q}) \rangle \equiv \int g(\vec{q}) \psi(\vec{q}, t) \, d\vec{q}. \tag{2.71}$$

Moreover, for the cases of non-homogeneous flow fields, we note that $\boldsymbol{\tau}_{\boldsymbol{p}}^{(\boldsymbol{c})}$ and ψ also depend on the physical space Ω.

Contribution from the Bead Motion

An additional component $\boldsymbol{\tau}_{\boldsymbol{p}}^{(\boldsymbol{e})}$ of the extra-stress tensor $\boldsymbol{\tau}_{\boldsymbol{p}}$ appears from the movement of the dumbbells itself through the plane. First, we consider the number of beads "1" with mass m which cross a plane that moves along the fluid with velocity $\vec{u}$. Let $\dot{\vec{r_1}}$ denote the velocity of bead "1" at an interval Δt, then the volume of beads that intersect the plane depends on the relative motion $\dot{\vec{r_1}} - \vec{u}$ between the beads and the plane.

Using the notation of Figure 2.16, we deduce that

- the volume $\left(\frac{d\vec{r_1}}{dt} - \vec{u} \right) \cdot \vec{n} \, S \Delta t$ will cross the plane during an interval Δt,

- the total number of dumbbells within this volume element is

$$n_{\mathrm{d}} \left(\frac{d\vec{r_1}}{dt} - \vec{u} \right) \cdot \vec{n} \, S \Delta t$$

where n_{d} is the number of dumbbells per unit volume, and
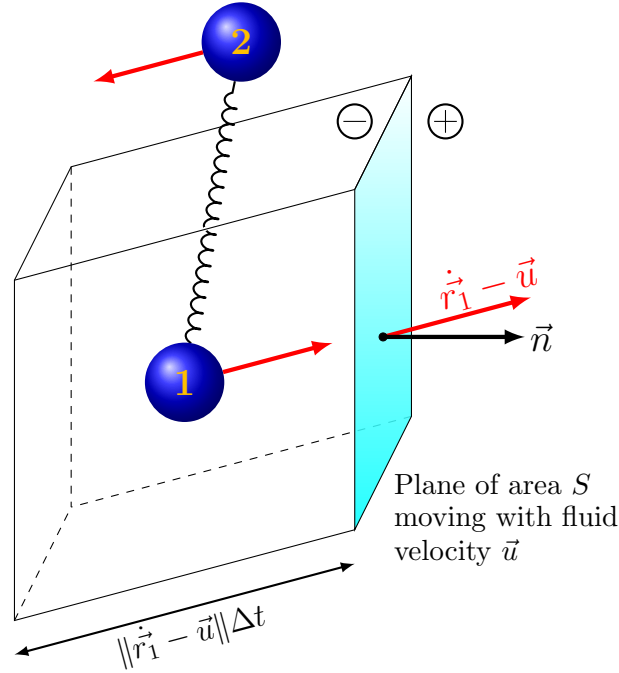
Figure 2.16: Dumbbells whose beads cross the marked plane contribute additional stress to it. The number of dumbbells depends on the relative velocity between the microscopic beads on the one hand and the plane on the other hand.

- the total momentum $\vec{p}_\Sigma$ transported across the plane is

$$\vec{p}_\Sigma = \underbrace{n_\mathrm{d}\left(\left(\frac{d\vec{r_1}}{dt} - \vec{u}\right) \cdot \vec{n}\,S\right)\Delta t}_{\text{total number of dumbbells}}\ \underbrace{m\left(\frac{d\vec{r_1}}{dt} - \vec{u}\right)}_{\text{momentum/dumbbell}}$$

Furthermore, for the polymers within the Newtonian solvent we assume that they are close to the thermodynamic equilibrium, i.e. the system is close to a steady state. Due to the previous assumption, we can describe the velocity distribution of the beads with the Maxwell-Boltzmann distribution from the kinetic gas theory. The Maxwell-Boltzmann distribution is a Gaussian distribution that is completely characterised by its first two moments, mean and variance, which take the form

$$\left\langle \vec{X} \right\rangle = 0 \tag{2.72}$$

$$\left\langle \vec{X}^2 \right\rangle = \frac{k_B T}{m}\mathbf{Id} \tag{2.73}$$

for the random variable $\vec{X}$. Accordingly, the expectation of $\vec{p}_\Sigma$ (more precisely the expectation

of its components) is described in the expression

$$
\begin{aligned}
\langle \vec{p}_\Sigma \rangle \; &= \; \left\langle n_{\mathrm{d}} \left(\frac{d\vec{r_1}}{dt} - \vec{u} \right)^2 \cdot \vec{n}\, S\, \Delta t m \right\rangle \\
&= \; n_{\mathrm{d}}\, S\, \Delta t\, m \left\langle \left(\frac{d\vec{r_1}}{dt} - \vec{u} \right)^2 \right\rangle \cdot \vec{n} \\
&\stackrel{(2.73)}{=} \; n_{\mathrm{d}} S\, \Delta t\, k_B T\, \mathbf{Id} \cdot \vec{n}.
\end{aligned}
$$

We identify now the average momentum flux (i.e. momentum per unit time per unit area), caused by all beads "1" that cross the plane, with half of the stress vector $\vec{t}$ (cf. theorem 2.3 on page 19) such that

$$
-\frac{1}{2}\vec{t} \; = \; -\frac{1}{2}\boldsymbol{\tau_p^{(b)}} \cdot \vec{n} \; = \; n_{\mathrm{d}} k_B T\, \mathbf{Id} \cdot \vec{n}.
$$

Obviously, the prefactor $1/2$ results from the fact that we have only considered bead "1" but expect the same results from bead "2". Consequently, the contribution from the bead motion to the polymeric stress $\boldsymbol{\tau_p}$ is

$$
\boldsymbol{\tau_p^{(b)}} \; = \; -2n_{\mathrm{d}} k_B T\, \mathbf{Id}. \tag{2.74}
$$

Kramers Expression (Dimensionful)

Combining equations (2.70) and (2.74), we deduce an expression to calculate the polymeric stress for a known number density n_{d} and pdf ψ. However, we cannot set "$\boldsymbol{\tau_p} \equiv \boldsymbol{\tau_p^{(c)}} + \boldsymbol{\tau_p^{(b)}}$" as there already is a polymeric contribution from the RHS of this sum to the pressure term in our basic equation (2.8) for the total stress $\boldsymbol{\sigma}$, i.e. in $\boldsymbol{\sigma} = -p\,\mathbf{Id} + \boldsymbol{\tau_s} + \boldsymbol{\tau_p}$.

In (2.83) of Section 2.3.5 we have considered equilibrium flows, one of the most simple flow fields, in which the fluid velocity is constant everywhere. Therefore, the velocity gradient $\boldsymbol{\kappa}$ is zero and $\psi_{eq}(\vec{q})$ only depends on configuration space D. For such a flow field we expect the dumbbells to be relaxed such that there is no polymeric stress contribution $\boldsymbol{\tau_p}$ and we hence demand

$$
\boldsymbol{\tau_p} \stackrel{!}{=} 0 \qquad \text{for } \psi = \psi_{eq}.
$$

On the contrary, we notice $\boldsymbol{\tau_p^{(c)}} + \boldsymbol{\tau_p^{(b)}} = -n_{\mathrm{d}} k_B T \mathbf{Id} \neq 0$ for $\psi = \psi_{eq}(\vec{q})$. As a solution, we separate the isotropic equilibrium stress (i.e. $-n_{\mathrm{d}} k_B T \mathbf{Id}$) from the above sum and add it to the pressure term for which only $\frac{\partial}{\partial \vec{x}} p(\vec{x})$ is relevant. Finally, we get the Kramers expression as

$$
\boxed{\boldsymbol{\tau_p}(\vec{x}, \vec{q}, t) \equiv \underbrace{\boldsymbol{\tau_p^{(c)}} + \boldsymbol{\tau_p^{(b)}} + n_{\mathrm{d}} k_B T\, \mathbf{Id}}_{\text{absorb equ. solution into } \nabla p} = n_{\mathrm{d}} k_B T \int \vec{q} \otimes \vec{F}(\vec{q}) \psi(\vec{x}, \vec{q}, t)\, d\vec{q} - n_{\mathrm{d}} k_B T\, \mathbf{Id}.}
$$

$$\tag{2.75}$$

Since equation (2.75) takes effect for the surface forces of the Navier-Stokes equations (cf. (2.9)) by its divergence, we could additionally omit the constant factor on the right hand side (RHS) if we simulate real fluids. However, we also investigate model problems (e.g. steady

shear and extensional flow) which require the complete equation (2.75) for comparison with the analytical solutions.

Kramers Expression (Non-dimensional)

In an analogous manner as for the Fokker-Planck equation (2.58a) - (2.58d), we nondimensionalise the Kramers expression by introducing a characteristic unit l_0 for the dumbbell length scale and get

$$\vec{q}^* = \vec{q}/l_0, \quad \vec{F}^*(\vec{q}^*) = \frac{1}{Hl_0^2}\vec{F}(\vec{q}) = \frac{1}{k_BT}\vec{F}(\vec{q}).$$

Hence, (2.75) can be rewritten as

$$\boldsymbol{\tau_p}(\vec{x}^*, \vec{q}^*, t^*) = n_{\mathrm{d}}k_BT\left(\int \vec{q}^* \otimes \vec{F}^*(\vec{q}^*)\psi(\vec{x}^*, \vec{q}^*, t^*)\,d\vec{q}^* - \mathbf{Id}\right). \tag{2.76}$$

Further considerations regarding the coefficient $n_{\mathrm{d}}k_BT$ allow a reformulation of the above equation in terms of the polymeric zero shear-viscosity η_p and the relaxation time λ (cf. (2.12)). For dilute dumbbell solutions in a shear flow we can show that η_p can be approximated by

$$\eta_p \equiv \frac{\tau_{xy}}{\dot{\gamma}} \approx \alpha_{b,d}\lambda n_{\mathrm{d}}k_BT \tag{2.77}$$

where $\alpha_{b,d}$ is a coefficient depending on the dimension d of the configuration space D with

$$\alpha_{b,d} \equiv \begin{cases} 1, & \text{for Hookean dumbbells } (b \to \infty), \\ \frac{b+d+2}{b}, & \text{for } d\text{-dimensional FENE dumbbells}, \\ \frac{b+d}{b}, & \text{for } d\text{-dimensional FENE-P dumbbells}. \end{cases} \tag{2.78}$$

We have $\dim(D) = 2$ or $\dim(D) = 3$ in our applications. Furthermore, the introduced FENE-P springs are an approximation to the FENE model where only the expected extension $\langle\vec{q}\rangle$ in the denominator is considered (we use $\langle\cdot\rangle$ in the sense of (2.71)), i.e.

$$\vec{F}^*(\vec{q}^*) = \frac{\vec{q}^*}{1 - \frac{\langle\|\vec{q}^*\|^2\rangle}{b}}. \tag{2.79}$$

We further describe the FENE-P spring force in Chapter 2.3.6.

Inserting (2.77) into (2.76) and multiplying the equation with $\frac{L_0}{U_0(\eta_s+\eta_p)}$, we obtain dimensionless equations that relate

- Hookean dumbbells to the macroscopic stress

$$\boxed{\boldsymbol{\tau_p}(\vec{x}, \vec{q}, t) = \frac{(1-\beta)}{Wi}\left(\int \vec{q} \otimes \vec{q}\,\psi(\vec{x}, \vec{q}, t)\,d\vec{q} - \mathbf{Id}\right),} \tag{2.80}$$

- FENE dumbbells to the stress tensor,

$$\boldsymbol{\tau_p}(\vec{x}, \vec{q}, t) \,=\, \frac{(1-\beta)}{Wi}\left(\frac{b+d+2}{b}\right)\left(\int \vec{q} \otimes \frac{\vec{q}}{1-\frac{\|\vec{q}\|^2}{b}}\,\psi(\vec{x}, \vec{q}, t)\,d\vec{q} \,-\, \mathbf{Id}\right),$$ (2.81)

- and FENE-P dumbbells to the stress tensor

$$\boldsymbol{\tau_p}(\vec{x}, \vec{q}, t) \,=\, \frac{(1-\beta)}{Wi}\left(\frac{b+d}{b}\right)\left(\frac{\langle \vec{q} \otimes \vec{q}\rangle}{1-\frac{\langle\|\vec{q}\|^2\rangle}{b}} \,-\, \mathbf{Id}\right).$$ (2.82)

Again, we omit the asterisk to denote non-dimensional units and use the expectation "$\langle\rangle$" in the sense of equation (2.71). Apart from that, we have reused the non-dimensional parameters

$$Wi \,=\, \lambda U_0/L_0,$$
$$\beta \,=\, \frac{\eta_s}{\eta_s + \eta_p}$$

with β as the ratio between the Newtonian viscosity to the total viscosity.

2.3.5 Fokker-Planck Equation for Simple Flows

Throughout the whole chapter, we have investigated the viscosity for two simple flow fields which are

- the steady state shear flow (cf. (2.12)),

- the steady state extensional flow (cf. (2.15a)-(2.15b)).

Now, we further consider the more simple case of a constant velocity field within the whole domain (i.e. $\boldsymbol{\kappa} = 0$ in the FP equation (2.62)) which we denote as

- the equilibrium solution.

The equilibrium solution represents the case of totally relaxed dumbbells so that the polymeric stress $\boldsymbol{\tau_p}$ vanishes and the solution does not depend on physical space Ω or process time t. Subsequently, we present solutions/ approximations for all three steady state flows in a similar manner as in Lozinski [56].

Equilibrium Solution

If we set $\vec{u} = 0$ for the velocity gradient, the Fokker-Planck equation (2.62) takes the form

$$\frac{\partial \psi_{eq}(\vec{q})}{\partial \vec{q}} \,+\, \vec{F}(\vec{q})\psi_{eq}(\vec{q}) \,=\, 0$$ (2.83)

which we can solve analytically. In short, the steady-state equilibrium solution ψ_{eq} is

$$\psi_{eq} = C_1 \exp\left(-\frac{\|\vec{q}\|^2}{2}\right) \tag{2.84}$$

for Hookean spring forces,

$$\psi_{eq} = C_2 \left(1 - \frac{\|\vec{q}\|^2}{b}\right)^{b/2} \tag{2.85}$$

for FENE dumbbells and

$$\psi_{eq} = C_3 \left(\frac{b+d}{b}\right)^{d/2} \exp\left(-\frac{b+d}{2b}\|\vec{q}\|^2\right) \tag{2.86}$$

for the FENE-P model.

The constants C_1, C_2, and C_3 are required to achieve the normalisation property of ψ in (2.57). Their explicit values can be found in an article from Herrchen et al. [38]. The importance of the equilibrium solution lies in two areas of applications which are

- the gauging of the Kramers expression (2.75) for the polymeric stress $\boldsymbol{\tau_p}$,

- the usage of the equilibrium solution as an initial condition for ψ as we expect the polymers to be relaxed in the beginning.

Steady Shear Flows

In equation (2.11) we describe a steady xy-shear flow with a velocity gradient of the form

$$\boldsymbol{\kappa} = \dot{\gamma} \begin{pmatrix} 0 & 1 & 0 \\ 0 & 0 & 0 \\ 0 & 0 & 0 \end{pmatrix}.$$

However, in this context the parameter $\dot{\gamma}$ is a dimensionless shear factor as we consider nondimensionalised units.

Although the steady shear flow is comparatively simple, there exists no analytical solution for the steady shear flow. Instead, we give a first-order approximation to the solution in terms of $\dot{\gamma}$. Therefore, we approximate ψ_{shear} as a sum of the equilibrium solution ψ_{eq} and an additional first-order shear contribution ψ_1 that we combine as

$$\psi_{\text{shear}} = \psi_{eq} \left(1 + Wi\,\dot{\gamma}\psi_1 + \mathcal{O}((Wi\,\dot{\gamma})^2)\right). \tag{2.87}$$

Inserting (2.87) into the homogeneous FP equation (2.62) and using the property (2.83), we obtain the equation

$$\frac{\partial}{\partial \vec{q}} \cdot \left(\psi_{eq}\frac{\partial \psi_1}{\partial \vec{q}}\right) = 2\frac{\partial}{\partial \vec{q}} \cdot \left(\frac{1}{\dot{\gamma}}\boldsymbol{\kappa}\vec{q}\psi_{eq}\right) \tag{2.88}$$

for the additional density component ψ_1 that exhibits the solution

$$\psi_1 \;=\; \frac{1}{\dot{\gamma}}\,\boldsymbol{\kappa} : \vec{q}\otimes\vec{q}.$$

Here, the operator " : " denotes the (scalar) double dot product of two second order tensors.

As a result, a first-order shear flow approximation in $\dot{\gamma}$ to ψ is

$$\psi_{\text{shear}} \;=\; C_4 \exp\left(-\frac{\|\vec{q}\|^2}{2}\right)\left(1 + Wi\,\boldsymbol{\kappa} : \vec{q}\otimes\vec{q}\right) \tag{2.89}$$

for a Hookean spring force and

$$\psi_{\text{shear}} \;=\; C_5 \left(1 - \frac{\|\vec{q}\|^2}{b}\right)^{b/2}\left(1 + Wi\,\boldsymbol{\kappa} : \vec{q}\otimes\vec{q}\right) \tag{2.90}$$

for FENE dumbbells. Note that some authors denote $\dot{\gamma}$ as dimensionful shear-rate (i.e. $[\dot{\gamma}] = 1/s$) and therefore use the relaxation time λ instead of the Weissenberg number Wi in the previous equations.

Steady Extensional Flows

We distinguish two different types of extensional flows (cf. (2.15a) - (2.15b)) which are the uni-axial extensional flow and the planar extensional flow. Fortunately, the FP equation possesses an analytical steady-state solution for all types of extensional flows if we use the FENE spring force. Actually, there exists an analytical solution for all homogeneous flow fields in which the velocity gradient $\boldsymbol{\kappa}$ is symmetric as it is the case for extensional flows. The solution is

$$\psi_{ext} \;=\; C \left(1 - \frac{\|\vec{q}\|^2}{b}\right)^{b/2}\exp\left(Wi\,\boldsymbol{\kappa} : \vec{q}\otimes\vec{q}\right) \tag{2.91}$$

with C as a normalisation constant. For further information, Bird et al. [10] present this formula in equation (13.2-14).

Otherwise, in equation (2.35) of Section 2.2.2 we have proved that the Oldroyd-B model and therefore also the multiscale Hookean dumbbell model fail for the description of steady extensional flows. For this reason there exists no finite density function in this case. A micromolecular description reveals the problem for an Oldroyd-B fluid, because as the Hookean spring is not restricted in length (cf. finite length $\sqrt{b}$ for FENE dumbbells), it becomes infinitely extended at a nondimensional extension rate of $\dot{\epsilon} = \frac{1}{2\,Wi}$ which leads to an infinite stress tensor.

2.3.6 Closure Approximations

The aim of this chapter is to get an insight into the mesoscopic behaviour of polymers to adequately describe their contribution to the polymeric stress. So far, we have considered three different spring forces which are the Hookean, the FENE, and the FENE-P spring. Normally,

we would have to solve a seven-dimensional (2.61) or four-dimensional (2.62) Fokker-Planck equation for ψ and then compute the polymeric stress with the Kramers expression which requires high computational effort.

However, there are spring forces for which it is unnecessary to solve the Fokker-Planck equation. More precisely, we subsequently present that

- the Hookean dumbbell model possesses a closed form constitutive equation which turns out to be the UCM/ Oldroyd-B differential model of Chapter 2.2.2 and

- the FENE-P model is a simplification of the classical FENE spring force so that we are able to find a corresponding macroscopic formulation.

Closed Formulation for Hookean Dumbbells

First, we derive the mathematical equivalence between the Hookean dumbbell model on the one hand and the UCM/ Oldroyd-B model on the other hand. For a more detailed analysis, we refer to the book of Owens and Phillips [68].

Therefore, we multiply the seven-dimensional Fokker-Planck equation (2.61), i.e.

$$\underbrace{\frac{\partial \psi}{\partial t} + \frac{\partial}{\partial \vec{x}} \cdot (\vec{u}\psi)}_{= \frac{D\psi}{Dt}} = \frac{\partial}{\partial \vec{q}} \cdot \left(-(\nabla \vec{u})\vec{q}\psi + \frac{1}{2\,Wi}\vec{F}(\vec{q})\psi \right) + \frac{1}{2\,Wi}\Delta_q \psi$$

with the (i,j)-component $q_i q_j$ of $\vec{q} \otimes \vec{q}$ and integrate it over the configuration space D such that the FP equation becomes

$$\frac{D}{Dt} \int_D q_i q_j \psi \, d\vec{q} = \int_D q_i q_j \sum_{k=1}^{3} \frac{\partial}{\partial q_k} \left(-\sum_{l=1}^{3} \frac{\partial u_k}{\partial q_l} q_l \psi + \frac{1}{2\,Wi}\frac{\partial \psi}{\partial q_k} + \frac{1}{2\,Wi}q_k \psi \right) d\vec{q}.$$

We then use integration by parts on the RHS (two times on the diffusive part of the equation), insert $\vec{F}(\vec{q}) = \vec{q}$ for Hookean dumbbells, and keep in mind that ψ vanishes at ∂D to obtain

$$\frac{1}{Wi} \int_D q_i q_j \psi \, d\vec{q} + \frac{D}{Dt} \int_D q_i q_j \psi \, d\vec{q} - \sum_{l=1}^{3} \left(\frac{\partial u_i}{\partial q_l} \int_D q_l q_j \psi \, d\vec{q} - \frac{\partial u_j}{\partial q_l} \int_D q_i q_l \psi \, d\vec{q} \right) = \frac{1}{Wi}\delta_{ij}.$$

Replacing the componentwise analysis with a full tensor $\vec{q} \otimes \vec{q}$ description and using (2.71), we introduce the conformation tensor

$$\langle \vec{q} \otimes \vec{q} \rangle \equiv \int_D \vec{q} \otimes \vec{q} \, \psi \, d\vec{q}$$

and rewrite the equation in a more compact tensor notation as

$$\frac{1}{Wi} \langle \vec{q} \otimes \vec{q} \rangle + \langle \vec{q} \overset{\triangledown}{\otimes} \vec{q} \rangle = \frac{1}{Wi}\mathbf{Id}. \tag{2.92}$$

Here, we have reused the upper convected derivative "$\triangledown$" from Definition 2.10 on page 32.

A comparison between the confirmation tensor and the dimensionless Kramers expression for Hookean dumbbells as in (2.80) reveals

$$\langle \vec{q} \otimes \vec{q} \rangle = \frac{Wi}{(1-\beta)} \boldsymbol{\tau_p} + \mathbf{Id}. \tag{2.93}$$

Inserting (2.93) into (2.92) and using $\overset{\triangledown}{\mathbf{Id}} = -(\nabla \vec{u} + \nabla \vec{u}^T)$, we obtain

$$\boldsymbol{\tau_p} + Wi \overset{\triangledown}{\boldsymbol{\tau_p}} = 2(1-\beta)\boldsymbol{D}$$

with $\boldsymbol{D}$ as the rate of deformation tensor from Chapter 2.1.4. For $\beta = 0$ (i.e. the fluid behaves totally non-Newtonian) this is the non-dimensional formulation of the UCM model as in (2.27); for $\beta \neq 0$ we have to add the solvent contribution to the stress and obtain the non-dimensional Oldroyd-B equation from equation (2.28) which proofs the stated equivalence.

Closure Approximations for FENE Dumbbells

For nonlinear spring forces (e.g. FENE spring force) it is not possible to find a closed system of equations. Alternatively, there exists a variety of approximations to the FENE potential which have such a closure. These are the so called closure approximations. We present some closure approximations and refer for a detailed description to a series of articles from Yu et al. [96], Du et al. [27] and Hyon et al. [42].

- A comparatively simple approximation to the FENE spring force is the FENE-P model by Peterlin [69]. The FENE-P closure approximates (2.81) by a pre-averaging assumption

$$\left\langle \frac{\vec{q} \otimes \vec{q}}{1 - \frac{\|\vec{q}\|^2}{b}} \right\rangle \approx \frac{\langle \vec{q} \otimes \vec{q} \rangle}{1 - \frac{\langle \|\vec{q}\|^2 \rangle}{b}} \equiv \frac{\boldsymbol{A}}{1 - \operatorname{tr}(\boldsymbol{A})/b}$$

  with the conformation tensor $\boldsymbol{A} = \langle \vec{q} \otimes \vec{q} \rangle$. In the same way as for the Oldroyd-B model, we obtain a constitutive equation for $\boldsymbol{A}$ which we write as

$$\frac{\boldsymbol{A}}{1 - \operatorname{tr}(\boldsymbol{A})/b} + Wi \overset{\triangledown}{\boldsymbol{A}} = \mathbf{Id}.$$

  Even if we only consider steady state situations, the FENE-P closure disagrees with the FENE spring force. This is caused by only restricting the average $\langle \vec{q}^2 \rangle^{1/2}$ by $\sqrt{b}$ which does not prevent that there are still configurations whose length exceeds $\sqrt{b}$.

- Lielens et al. [55] proposed another approximation, the FENE-L closure, in which the pdf ψ takes a product form
$$\psi(\vec{q}) = \psi^l(\vec{q})\, \psi^o(\vec{q}/\|\vec{q}\|)$$

  with $\psi^l(\vec{q})$ as the distribution of the dumbbells length and $\psi^o(\vec{q}/\|\vec{q}\|)$ as the distribution of the unit orientation vector. Both distributions are determined by using the conformation tensor $\boldsymbol{A}$ and a fourth-order moment $\langle \vec{q}^4 \rangle$. Instead of the FENE-P closure, the FENE-L

closure adequately models distributions that differ from the equilibrium ψ_{eq} but still fails for transient flows with high shear or extension rates.

Obviously, there exists a variety of closure approximations (e.g. FENE-CR, FENE-D_α,...) which dramatically reduce the computational effort but for some situations significantly differ from the original FENE spring force. As a result, aiming at a broad range of applications, we directly solve the Fokker-Planck equations for the FENE spring as this is the only possibility to circumvent modelling problems.

3 Numerical Methods

In this chapter, we describe different numerical techniques that we use later on. On the one hand, we consider methods for the solution of a density function like finite differences (FD) or spectral methods. On the other hand, we introduce stochastic processes because in Chapter 2.3 we also consider an alternative description of the FP equation as a stochastic differential equation (SDE). In general, spectral methods require much more effort in discretisation than FD schemes. In exchange, if spectral methods are carefully adapted to the problem, they outperform other methods with respect to convergence order. At last, we consider stochastic methods which are particularly suitable for high-dimensional problems.

3.1 Finite Differences on the Sphere

Finite differences are a comparatively simple approach for the discretisation of a partial differential equation. Indeed, the main idea of this method is to replace the infinitesimal limit value of a derivative with a finite differential quotient. We consider an interval $[a, b]$ and subdivide it equidistantly $a = x_0 < x_1 < ... < x_n = b$ according to

$$x_i = x_0 + ih \qquad \text{with} \quad i = 0, ..., n$$

and $h = (b - a)/n$. Suppose we want to approximate the first derivative of $u \in C^4((a, b))$, common schemes are the forward difference

$$u'(x_i) = \frac{u(x_{i+1}) - u(x_i)}{h} - \frac{h}{2}u''(\xi_i) \qquad \text{with} \quad \xi_i \in (x_i, x_{i+1}), \tag{3.1}$$

the backward difference

$$u'(x_i) = \frac{u(x_i) - u(x_{i-1})}{h} + \frac{h}{2}u''(\xi_i) \qquad \text{with} \quad \xi_i \in (x_{i-1}, x_i), \tag{3.2}$$

and the central difference

$$u'(x_i) = \frac{u(x_{i+1}) - u(x_{i-1})}{2h} - \frac{h^2}{6}u^{(3)}(\xi_i) \qquad \text{with} \quad \xi_i \in (x_{i-1}, x_{i+1}). \tag{3.3}$$

The intermediate value ζ_i results from the Taylor expansion of $u(x_i)$. A combination of first order schemes yields an approximation to the second derivative of $u''(x_i)$:

$$u''(x_i) = \frac{u(x_{i+1}) - 2u(x_i) + u(x_{i-1})}{h^2} - \frac{h^2}{12}u^{(4)}(\xi_i) \qquad \text{with} \quad \xi_i \in (x_{i-1}, x_{i+1}). \tag{3.4}$$

We note that finite differences are a local method. Actually, we consider only nearby nodal values for the approximation of a derivative and therefore obtain a sparse linear system of equations after discretisation. The approach possesses two options to improve the accuracy of the approximation:

1. Usage of high-order schemes to include more global information of the domain.

2. Decrease of the mesh size h which defines the distance between grid points.

Both strategies exhibit the drawback of an increase in computation time. Furthermore, a high-order scheme requires smoother functions and a special boundary treatment near the border of the domain. On the other hand, a decrease in the mesh size worsens the condition of the linear system of equations that follows from the discretisation of the underlying differential equations. A more detailed introduction to finite differences is given in Quarteroni [78] and in Smith [83].

Subsequently, we concentrate on finite differences in spherical, cylindrical and toroidal geometries as further described in Boyd [15] and Randall [79]. Despite the differences between distinct coordinate systems for these geometries, all systems have one problem in common: lines of constant polar or azimuthal angle converge in one singular point. For instance, the latitude and longitude lines on an earth globe converge in a singular point at the poles. Additionally, a sphere has a further singular point at the centre. Figure 3.1 illustrates the accumulation of grid values near singular points. As a result, this leads to two consequences for numerical computation. First, the time-step size for each time-discretisation scheme is restricted because of the fine grid resolution close to the singularities. In literature, a common term for this behaviour is the "pole problem". A second consequence is that the differential operator in spherical coordinates maintains a singularity itself, even if the solution is smooth at every point of the domain. Therefore, the numerical treatment has to deal with problems which are not only related to the physical system as a whole but also to the mathematical description of the system. The Courant-Friedrichs-Levy condition (CFL condition) provides the theoretical background for understanding the restriction in time-step size.

Definition 3.1 [COURANT-FRIEDRICHS-LEWY CONDITION]
A CFL condition denotes a necessary criterion for the stability of an explicit time-discretisation scheme for differential equations with hyperbolic behaviour. In general, the criterion restricts the convection of information between different grid cells in terms of numerical stability. The method was first published in 1928 by Richard Courant, Kurt Friedrich, and Hans Lewy [23]. In one-dimensional computation the restriction in time t takes the form

$$\Delta t \, < \, C_{pde} \, \frac{h_{min}}{u_{max}}$$

where u_{max} is the fastest wave speed permitted by the differential equation, h_{min} is the smallest mesh size of the computational grid, and C_{pde} is a problem-dependent constant.

Because of the CFL condition, the restriction is more severe for non-equidistant grids than for homogeneous grid distributions. On a sphere, a homogeneous subdivision of the spherical coordinates r, θ, and ϕ yields irregularly distributed grid points. In Figure 3.1 the distance between two grid points A and B on a circle in the $x - y$-plane with radius r_1 and inclination
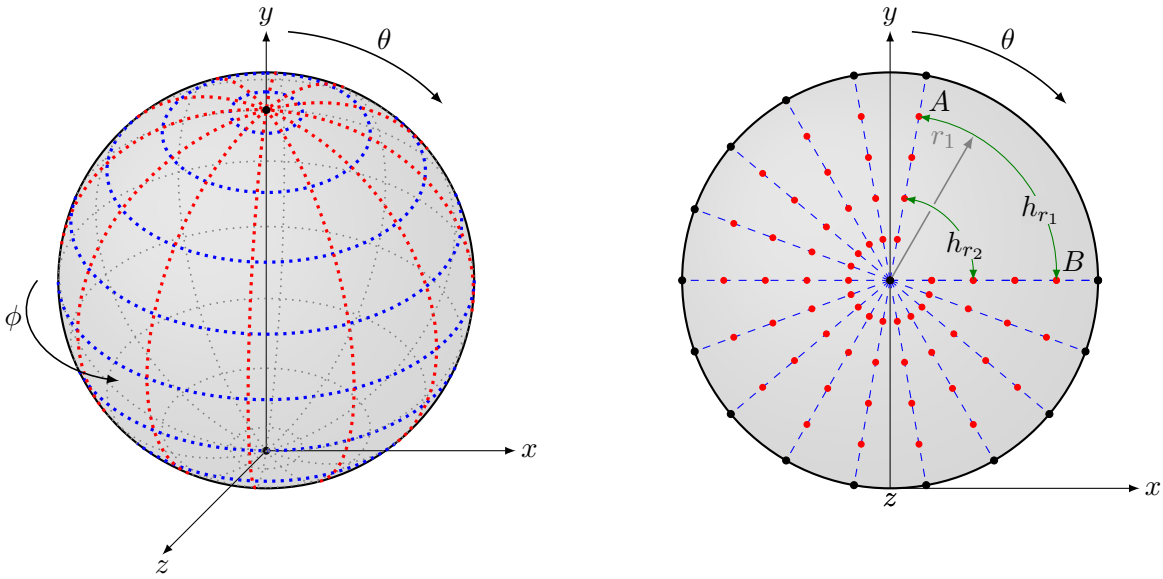
Figure 3.1: A sphere exhibits singularities at the poles and at the centre.

angle θ_A and θ_B is

$$h_{r_1} = r_1 \left(\theta_B - \theta_A\right), \tag{3.5}$$

which tends to zero at the centre of the sphere (i.e. $r_1 \to 0$). Therefore, an implementation necessitates additional considerations as implicit time-discretisation schemes, deletion of grid points, or heavy damping near singular points (i.e. low accuracy of the model).

The second consequence of the coordinate lines is the singular behaviour of the differential operators itself. For instance, the Laplacian for Cartesian coordinates in 3-dimensional Euclidean space takes the form

$$\Delta \equiv \frac{\partial^2}{\partial x^2} + \frac{\partial^2}{\partial y^2} + \frac{\partial^2}{\partial z^2} \tag{3.6}$$

and has constant coefficients. In contrast to this, the corresponding formulation in spherical coordinates

$$\Delta \equiv \frac{1}{r} \frac{\partial}{\partial r} \left(r^2 \frac{\partial}{\partial r}\right) + \frac{1}{r^2 \sin(\phi)} \frac{\partial}{\partial \phi} \left(\sin(\phi) \frac{\partial}{\partial \phi}\right) + \frac{1}{r^2 \sin^2(\phi)} \frac{\partial^2}{\partial \theta^2} \tag{3.7}$$

becomes singular for the cases $\phi \to 0$ and $r \to 0$. Although the singularity is only an effect of the mathematical description, finite differences require explicit boundary conditions for the grid point closest to $r = 0$.

Obviously, finite differences are not the method of choice for the Fokker-Planck equation in the homogeneous flow case (2.62). Nevertheless, we use them as a method for the solution of the 3D homogeneous extensional flow problem (cf. Section 6.2.2). The main idea is to be able to compare the advantages and disadvantages of various techniques and find the most appropriate method for the given differential equation. A simple solution that circumvents the pole problem is the usage of Cartesian coordinates. The Cartesian coordinate system in $\mathbb{R}^3$ is
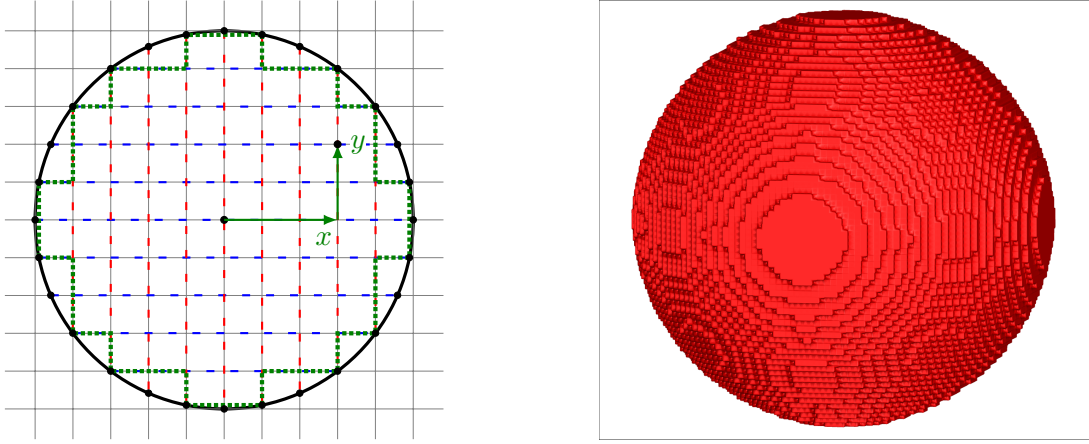
Figure 3.2: Finite difference approximation using Cartesian coordinates eliminates the pole problem on spheres and circles. On the other hand, the approximation of the surface is only first order accurate and requires fine grid discretisation.

Algorithm 1: Explicit low-storage third order Runge-Kutta scheme by Williamson for the solution of the Fokker-Planck equation in Cartesian coordinates. The algorithm requires fine grid resolutions ($\approx 300^3$ grid points) to reach a reasonable accuracy and therefore memory limitations become important. Low-storage schemes require only two levels of storage (for ψ and G) and are therefore an appropriate choice.

Data: Three-dimensional array ψ of size $i_{\max} \times j_{\max} \times k_{\max}$
Result: Discrete solution of Fokker-Planck ODE in the form of $\frac{\partial \psi}{\partial t} = \mathrm{f}(\psi, t)$
Set $n = 0$;
Subdivide interval $[x_{\min}, x_{\max}] = [-\sqrt{b}, \sqrt{b}]$ into $i_{\max}$ subintervals;
Analogue distribution for $[y_{\min}, y_{\max}]$ and $[z_{\min}, z_{\max}]$;
Assign initial values to ψ ;
while $n \leq n_{end}$ **do**
  if $x^2 + y^2 + z^2 \leq b$ **then**
    $G \leftarrow \mathrm{f}(\psi, t^{(n)})$;
    $\psi \leftarrow \psi + \frac{1}{3}\Delta t G$;
    $G \leftarrow -\frac{5}{9}G + \mathrm{f}(\psi, t^{(n)} + \frac{1}{3}\Delta t)$;
    $\psi \leftarrow \psi + \frac{15}{16}\Delta t G$;
    $G \leftarrow -\frac{153}{128}G + \mathrm{f}(\psi, t^{(n)} + \frac{3}{4}\Delta t)$;
    $\psi^{(n+1)} \leftarrow \psi + \frac{8}{15}\Delta t G$;
  else
    $\psi^{(n+1)} \leftarrow 0.0$ `// i.e. homogeneous Dirichlet boundary conditions`
  end
  Compute $\boldsymbol{\tau}$ by evaluation of $\psi[i][j][k]$ with Newton-Cotes rule for triple integrals;
  $t^{(n+1)} = t^{(n)} + \Delta t$, $n = n + 1$;
end

not adapted to spherical geometry and causes the problem to adequately describe the boundary of the sphere. This necessitates a fine grid size to obtain a sufficient resolution of the sphere (i.e. about 300^3 grid points), because the approximation of the spherical surface is only first order accurate. We demonstrate the coarse surface discretisation in Figure 3.2. In Cartesian coordinates the Fokker-Planck equation for the FENE spring force for homogeneous flow cases takes the form

$$
\begin{aligned}
\frac{\partial \psi}{\partial t} = &- \frac{\partial}{\partial q_1} \left[\psi(\frac{\partial u}{\partial x} q_1 + \frac{\partial u}{\partial y} q_2 + \frac{\partial u}{\partial z} q_3) \ - \ \frac{q_1 \psi}{2\,Wi \left(1 - \left(q_1{}^2 + q_2{}^2 + q_3{}^2\right)/b\right)} \right] \\
&- \frac{\partial}{\partial q_2} \left[\psi(\frac{\partial v}{\partial x} q_1 + \frac{\partial v}{\partial y} q_2 + \frac{\partial v}{\partial z} q_3) \ - \ \frac{q_2 \psi}{2\,Wi \left(1 - \left(q_1{}^2 + q_2{}^2 + q_3{}^2\right)/b\right)} \right] \\
&- \frac{\partial}{\partial q_3} \left[\psi(\frac{\partial w}{\partial x} q_1 + \frac{\partial w}{\partial y} q_2 + \frac{\partial w}{\partial z} q_3) - \ \frac{q_3 \psi}{2\,Wi \left(1 - \left(q_1{}^2 + q_2{}^2 + q_3{}^2\right)/b\right)} \right] \\
&+ \frac{1}{2\,Wi} \Delta_{\vec{q}} \psi.
\end{aligned}
\tag{3.8}
$$

With respect to $\vec{q}$ we use the schemes (3.1) - (3.4) for the discretisation of the derivatives, for time discretisation we use an explicit low-storage third order Runge-Kutta scheme. As a result, we obtain Algorithm 1 on page 64 to solve a problem in the form $\frac{\partial \psi}{\partial t} = f(\psi, t)$. The stress tensor as in (2.81) is computed with the discrete nodal values of ψ on the grid by using a triple integral Newton-Cotes formula described in Sadiku [81].

3.2 Spectral Methods

3.2.1 Basic Principles of Spectral Methods

The basic principle of spectral methods is to approximate the solution of a PDE by a finite sum of globally defined and orthogonal basis functions. For further information on spectral methods we refer to the textbooks of Canuto [18], Kopriva [51] and Karniadakis [45]. According to a given problem, different choices for basis functions are possible. First, we give answer to three questions that will be used to develop the theory of spectral methods in the one-dimensional case.

1. For an orthogonality property we necessitate an inner product space. With regard to the product space which requirements do we have to make?

2. Which choices for the basis functions do we have?

3. How do we calculate the time-dependent coefficients for a given orthogonal basis?

As for the answer to the first question, let $\omega : [a, b] \to \mathbb{R}^+$ be a positive valued weight function and $L_\omega^2([a, b])$ the Lebesgue space of square-integrable functions u on $[a, b]$ with respect to ω such that

$$\|u\|_{L_\omega^2} \equiv \|u\|_\omega \equiv \left(\int_a^b |u(x)|^2 \omega(x)\, dx \right)^{1/2} < \infty. \tag{3.9}$$

Actually, $L_\omega^2([a, b])$ possesses the same Hilbert space property as $L^2([a, b])$ which we obtain in the special case $\omega(x) = 1$ for all $x \in [a, b]$. We define the inner product $(\,.\,,.\,)_\omega : L_\omega^2 \times L_\omega^2 \to \mathbb{R}$ as

$$(u, v)_\omega \equiv \int_a^b u(x)\overline{v(x)}\omega(x)\, dx \tag{3.10}$$

and denote $u, v \in L_\omega^2$ as L_ω^2-orthogonal if

$$(u, v)_\omega = \|u\|_\omega \, \|v\|_\omega \, \delta_{u,v} \tag{3.11}$$

where $\delta_{u,v}$ is the Kronecker delta function. Consequently, in Table 3.1 we introduce several L_ω^2-orthogonal basis functions and their corresponding weight functions.

The Jacobi, Chebyshev and Legendre polynomials are eigenfunctions of the Sturm-Liouville problem. A detailed discussion of the problem is given in Zettl [98]. We use a similar formulation as in Chapter 5 of Teschl [86].

Theorem 3.2 [Sturm-Liouville theorem]
A Sturm-Liouville problem for $u \in C^2((a, b))$ is a second-order boundary value problem that takes the form

$$-\frac{d}{dx}\left(p(x)\frac{du(x)}{dx} \right) + q(x)\, u(x) = \lambda\, \omega(x)\, u(x) \qquad with \ \ a < x < b, \tag{3.12}$$
and boundary conditions for u.

Furthermore, we have q and ω in $C^0([a, b])$, p in $C^1([a, b])$ and $p(x), \omega(x) > 0$ for all $x \in (a, b)$. The problem is to find non-trivial eigenvalues λ and the corresponding eigenfunctions $u(x)$ of

Basis function	Notation	Domain	Weight function
Fourier basis	$\exp(ikx)$	$[0, 2\pi]$	1
Jacobi polynomials	$J_k^{(\alpha_J, \beta_J)}(x)$	$[-1, 1]$	$(1-x)^{\alpha_J}(1+x)^{\beta_J}$
Legendre polynomials	$L_k(x)$	$[-1, 1]$	1
Chebyshev polynomials	$T_k(x)$	$[-1, 1]$	$(1-x)^{-\frac{1}{2}}(1+x)^{-\frac{1}{2}}$
Spherical Harmonics	$\Omega_{nm}(\phi, \theta)$	$[0, 2\pi] \times [0, \pi]$	1

Table 3.1: The table lists orthogonal basis functions that are most common for spectral methods. Legendre ($\alpha_J = \beta_J = 0$) and Chebyshev polynomials ($\alpha_J = \beta_J = -1/2$) are special cases for the more general Jacobi polynomials. They are often used in numerical computation due to recurrence formulae that exist for them.

(3.12). *The problem is called singular if the coefficient $p(x)$ vanishes at the boundary (i.e. $p(a) = p(b) = 0$) and is called regular otherwise. For singular problems, the theorem states the existence of solutions, i.e. the Sturm-Liouville has a countable number of discrete eigenvalues $\lambda_1, \lambda_2, \ldots$ which accumulate only at ∞ and the corresponding eigenfunctions $u_1(x), u_2(x), \ldots$ are orthogonal in L_ω^2.*

Nevertheless, for spectral methods we require algebraic polynomial eigenbases because we can compute them and their derivatives efficiently. It turns out that on $[-1, 1]$ only one singular Sturm-Liouville problem has polynomial eigenfunctions, the Jacobi polynomials, which solve the problem

$$-\frac{d}{dx}\left((1-x)^{1+\alpha_J}(1+x)^{1+\beta_J}\frac{du(x)}{dx}\right) = \lambda (1-x)^{\alpha_J}(1+x)^{\beta_J} u(x)$$

with $-1 < x < 1$, $\alpha_J, \beta_J > -1$ and a weight function $\omega(x) = (1-x)^{\alpha_J}(1+x)^{\beta_J}$.

$$(3.13)$$

The Chebyshev polynomials result as a special case from the Jacobi polynomials with the choice $\alpha_J = \beta_J = -1/2$ in (3.13) and the Legendre polynomials from $\alpha_J = \beta_J = 0$. A Jacobi polynomial $J_N^{(\alpha_J, \beta_J)}(x)$ with degree N has exactly N distinct roots in the interval $[-1, 1]$ which is important for the Gauss quadrature formula in Section 3.2.3. An advantage of Legendre polynomials is the simplicity of the weight function (i.e. $\omega(x) = 1$) which eases to evaluate them analytically. Apart from that, for periodic problems we prefer to use exponential Fourier series of the form $\{\exp(ikx)\}_{k=0,1,2,\ldots}$ or the equivalent real interpretation with sine and cosine functions. Note that trigonometric functions are eigenfunctions of the Sturm-Liouville problem (3.12) for $p(x) = \omega(x) = 1$ and $q(x) = 0 \; \forall x \in [a, b]$. Problems on spherical geometry correlate with spherical harmonic basis functions which we discuss in Section 4.1.3.

Polynomial Approximation

Let $\Omega = [a, b] \times [0, T] \subset \mathbb{R}^2$ and let $\{p_k(x)\}_{k=0,1,2,\ldots}$ be a set of orthogonal polynomials with $x \in [a, b]$, are we able to approximate every $u \in L_\omega^2(\Omega)$ with polynomials uniformly? This is the result of the Weierstrass approximation theorem which states in our context that for a given $u \in L_\omega^2(\Omega)$ and fixed $t \in [0, T]$, there exists a system $s(r) \equiv \text{span}\{p_k(x)\}_{k=0,1,2,\ldots,r}$ and a

$\tilde{p} \in \mathrm{s}(r)$ such that

$$\|u(\cdot, t) - \tilde{p}\|_\omega \to 0 \qquad \text{as} \quad r \to \infty.$$

As a result, we are able to rewrite u in a series of the form

$$u = \sum_{k=0}^{\infty} \hat{u}_k \, p_k, \tag{3.14}$$

whereas in general the coefficients $\hat{u}_k$ depend on time but not on space and the opposite way round for the basis functions. In applications we approximate u on the space $\mathbb{P}_\mathrm{N}$ that contains all polynomials of degree $\leq$ N. Therefore, we define a truncated expansion of u as

$$P_\mathrm{N} u = \sum_{k=0}^{N} \hat{u}_k \, p_k \tag{3.15}$$

and try to obtain a rapid decay of the expansion coefficients to minimise the approximation error. We denote the relation between $u \leftrightarrow \hat{u}_k$ as the transform of u between physical space and frequency domain. Additionally, the truncated expansion $u \to P_\mathrm{N} u$ yields an orthogonal projection of $L^2_\omega \equiv L^2_\omega([a, b])$ upon $\mathbb{P}_\mathrm{N}$, which we write in the form

$$(P_\mathrm{N} u, q_k)_\omega = (u, q_k)_\omega \qquad \forall q_k \in \mathbb{P}_\mathrm{N}. \tag{3.16}$$

This is a further consequence of the orthogonality property of p_k.

As stated in the third initial question, the orthogonality of p_k in L^2_ω permits the computation of the coefficients by using the inner product on $L^2_\omega \times L^2_\omega$. By substituting (3.14) into $(u, p_k)_\omega$ we obtain

$$
\begin{aligned}
\frac{1}{\|p_k\|_\omega^2} (u, p_k)_\omega &= \frac{1}{\|p_k\|_\omega^2} \int_{-1}^{1} u(x) \, p_k(x) \, \omega(x) \, dx \\
&= \sum_{i=0}^{\infty} \frac{\hat{u}_i}{\|p_k\|_\omega^2} \underbrace{\int_{-1}^{1} p_i(x) \, p_k(x) \, \omega(x) \, dx}_{= \, \delta_{ik} \|p_k\|_\omega^2} \\
&= \hat{u}_k.
\end{aligned}
\tag{3.17}
$$

In the case of exponential basis functions $\exp(ikx)$ we denote the computation of the discrete Fourier components as the *forward transformation* and the synthesis of the Fourier modes back to physical space as the *backward transformation* of the Fourier transformation (FT).

Convergence Order

At last, we investigate the decay of the expansion coefficients and the approximation speed. For certain basis functions (e.g. Fourier series for periodic functions and Jacobi-type polynomials for non-periodic functions) that are sufficient smooth the expansion coefficients decay faster than any algebraic polynomial. Indeed, we expect a less oscillating behaviour for smooth functions. As high wavenumbers $\hat{u}_k$ correspond to high oscillation of u, the rapid decay of the coefficients

$\hat{u}_k$ is comprehensible. Subsequently, we use a more precise and more general definition from Boyd [15] and define the algebraic index of convergence for the expansion coefficients u_k as the largest number r which fulfils

$$\lim_{k \to \infty} |u_k| \, k^r \ < \ \infty.$$

If the expansion coefficients decay faster than any finite index r, we denominate this as exponential or spectral convergence. For this purpose, f has to be smooth in the sense of being infinite times differentiable or (even stronger) a complex analytic function. Spectral accuracy is an asymptotic property which appears after all essential structures of the function have been resolved. Nevertheless, in situations where spectral methods can be used they normally outperform other discretisation methods for given costs with regard to accuracy.

3.2.2 Gaussian Quadrature

In Section 3.2.3 we compare the concepts of modal and nodal approximation. For the explanation of the different methods, we first have to consider quadrature rules as they are strongly correlated with nodal approximations.

Theorem 3.3 [GAUSS INTEGRATION]
Let $x_0 < \ldots < x_{N-1}$ be the N distinct roots in $[-1,1]$ of an $\omega(x)$-orthogonal polynomial p_N in $\mathbb{P}_N$ (e.g. the Jacobi polynomial $J_N^{(\alpha_J, \beta_J)}(x)$) and let the quadrature weights $\omega_0 < \ldots < \omega_{N-1}$ be the solution of the linear system

$$\sum_{j=0}^{N-1} (x_j)^k \, \omega_j \ = \ \int_{-1}^{1} x^k \omega(x) \, dx, \qquad 0 \le k \le N-1. \tag{3.18}$$

Then, all quadrature weights ω_j are positive and numerical integration

$$Int_\omega(q) \ \equiv \ \sum_{j=0}^{N-1} q(x_j) \, \omega_j \tag{3.19}$$

is exact for all polynomials $q \in \mathbb{P}_{2N\text{-}1}$, i.e.

$$Int_\omega(q) \ = \ \int_{-1}^{1} q(x)\omega(x) \, dx \quad \forall q \in \mathbb{P}_{2N\text{-}1}. \tag{3.20}$$

Proof: see Canuto et al. [18] or Mercier [64].

Gauss integration (GI) is optimal with respect to the highest polynomial degree that can be integrated exactly for a given number of quadrature points. Therefore, by using just N quadrature points it is not possible to construct an integration scheme with exact integration of polynomials up to a degree of 2N. For the case that $p_N(x)$ in Theorem 3.3 is a Jacobi polynomial $J_N^{(\alpha_J, \beta_J)}(x)$, we denote the N roots $x_0 < \ldots < x_{N-1}$ as the Gauss-Jacobi quadrature points. In the same manner, we obtain the Gauss-Legendre and Gauss-Chebyshev points.

The quadrature points do not include the boundary of $[-1,1]$ so that they have to be included
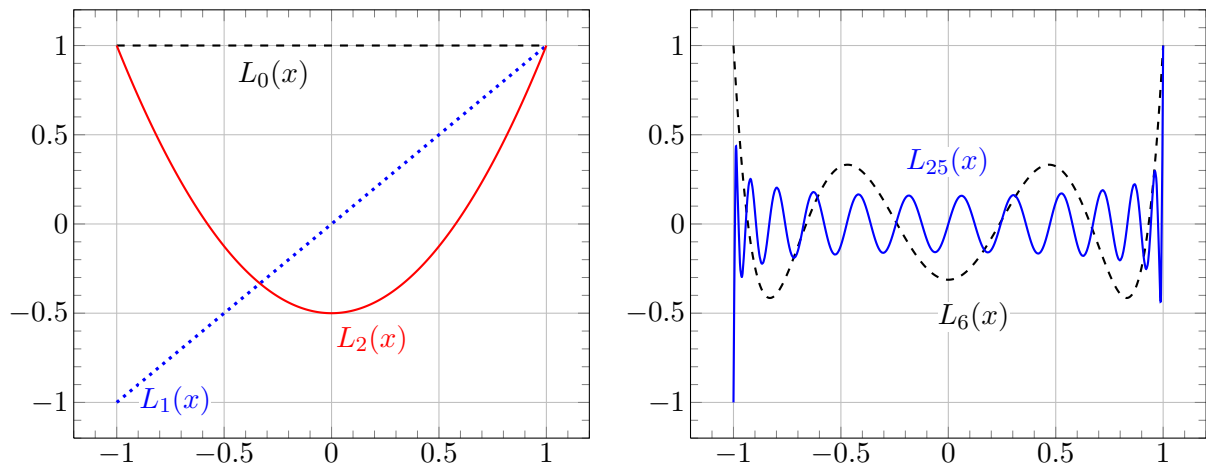
Figure 3.3: Low-order Legendre polynomials $L_0(x)$, $L_1(x)$ and $L_2(x)$ contribute low-frequency information to the approximation of the solution. An increase in the polynomial order, as can be seen from the polynomials $L_6(x)$ and $L_{25}(x)$, adds further high-frequency information to the approximation.

additionally. For the case $x_0 = -1 < \ldots < x_{N-1} = 1$ the method is accurate for polynomials up to a degree $2N - 3$ as the degrees of freedom are reduced by the two boundary points. If the boundary values are included in the quadrature formula, we use the term Gauss-Lobatto-Jacobi for the quadrature points and analogue terms for the other variants.

3.2.3 Modal and Nodal Approximation

In (3.15) we describe an approximation to the unknown solution in terms of orthogonal polynomials and corresponding coefficients, where each basis function contributes information from a special wave number. Low-order polynomials contribute low-frequency information to the approximation of the unknown function u and on the other hand high-order polynomials resolve the high-frequency oscillation. We illustrate the aspect of low- and high-frequency information with Legendre polynomials in Figure 3.3. A common term in literature for an approximation in the presented form is a modal (or hierarchical) basis representation. The term "modal" clarifies that each basis function is associated with one particular wave frequency of u.

On the other hand, an alternative ansatz requires the use of a grid. We then try to interpolate the unknown function on these grid point values in the domain. A spectral approximation based on grid points is called a nodal method. The approach is connected to the finite difference scheme, because both methods use a grid and approximate derivatives with derivatives of an interpolation polynomial. The major difference is that FD methods use a local low-order polynomial for approximation, whereas nodal approaches use global high-order representations. The global approach results in an immediate transport of information from a single disturbance up to the whole domain. Therefore, for spectral methods we cannot expect to obtain a sparse matrix after discretisation as it would be the case for FD methods. Nonetheless, in the case of a strong form PDE formulation Fornberg [31] considers nodal methods as a high-accuracy limit of finite difference methods.

Another difference is the choice of grid point values. In simple geometries a homogeneous
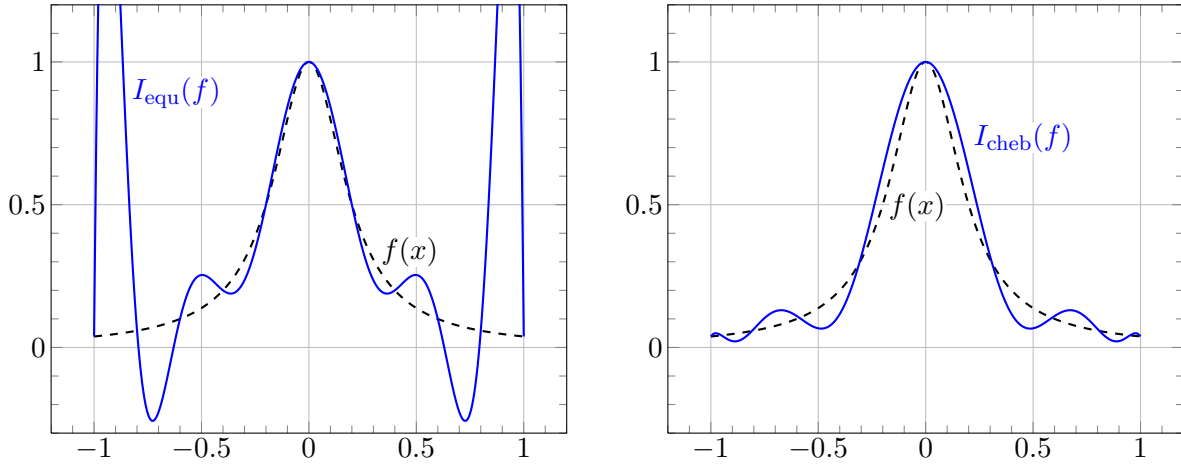
Figure 3.4: Both pictures present a Lagrange interpolation of the Runge function. Though, while the left interpolant $I_\text{equ}(f)$ uses eleven uniform interpolation points $\left\{-1, -\frac{4}{5}, \ldots, 1\right\}$, the right one bases on eleven Gauss-Lobatto-Chebyshev points (i.e. boundary points are included). Interestingly, the left interpolant yields an accurate interpolation at the centre but fails at the boundary. On the other hand, the right interpolant approximates the unknown uniformly and is the method of choice for spectral techniques.

distribution of nodal values makes sense for a FD discretisation, but a nodal spectral method always uses roots of orthogonal polynomials as listed in Table 3.1. For clarification, we interpolate the Runge function

$$u(x) = \frac{1}{1 + 25x^2}$$

by using the Lagrange polynomials $\{h_k(x)\}_{k=0,\ldots,N-1}$ of degree N-1 and write

$$I_{N-1}(u) = \sum_{k=0}^{N-1} u_{x_k} h_k(x) \tag{3.21}$$

with u_{x_k} as a discrete approximation of $u(x_k)$. Figure 3.4 illustrates two Lagrange interpolants of the form (3.21) but with different choices for the nodes $x_0 < \ldots < x_{N-1}$. The left interpolant uses a uniform distribution of $[-1, 1]$ whereas the right one uses the Gauss-Lobatto-Chebyshev points $x_k = \cos(\frac{k\pi}{N-1})$, $k = 0, \ldots, N - 1$. Runge proved that the interpolation error tends towards infinity if an equidistant distribution is used and the polynomial order is increased. This is caused by oscillation that occurs close to the boundary (Runge phenomenon). On the other hand, the more Gauss-Lobatto-Chebyshev points we use, the faster the error decays. This explains the effectiveness of Gaussian quadrature nodes.

Now, we further describe characteristics of Lagrange polynomials $h_k(x)$. Our interpolation of the unknown shall be exact at the $x_0 < \ldots < x_{N-1}$ and therefore has to feature the important property $h_k(x_j) = \delta_{kj}$ which we illustrate in Figure 3.5. Furthermore, the polynomials at the nodes are, roughly speaking, a discrete approximation to shifted delta-distributions $\delta(x - x_k)$. For instance, let $\{x_k\}_{k=0,\ldots,N-1}$ be the sequence of Gauss-Legendre nodes (i.e. we can neglect a

weight function in the integrand) and $j \in \{0, \dots, N-1\}$, then we have a relation of the form

$$\int_{-\infty}^{\infty} u(x)\delta(x-x_j)\,dx = u(x_j) \longleftrightarrow \int_{-1}^{1} u(x)\,h_j(x)\,dx \overset{GI}{\approx} \sum_{k=0}^{N-1} u(x_k)\omega_k \underbrace{h_j(x_k)}_{=\delta_{kj}} = u(x_j)\omega_j.$$

For efficient computation we write the Lagrange polynomials in the barycentric formulation

$$h_k(x) = \prod_{\substack{i=0 \\ i\neq k}}^{N-1} \frac{x-x_i}{x_k-x_i} = \frac{b_k}{(x-x_k)\sum_{i=0}^{N-1}\frac{b_i}{x-x_i}} \quad \text{with} \quad b_k = \frac{1}{\prod_{\substack{j=0 \\ j\neq k}}^{N-1}(x_k-x_j)} \tag{3.22}$$

as the barycentric weights. The second equal sign in (3.22) is written in the sense that the RHS possesses a removable singularity at $x = x_i$, $i = 0, \dots, N-1$, $i \neq k$ and allows a continuous extension (i.e. $h_k(x_i) \equiv 0$) in the form of the classical Lagrange interpolation. The advantage of the formulation with barycentric weights b_k in (3.22) lies in the efficient computation of the Lagrange interpolant. In this formulation it is possible to evaluate (3.21) in $\mathcal{O}(N)$ instead of $\mathcal{O}(N^2)$ operations because the factor $\sum_{i=0}^{N-1}\frac{b_i}{x-x_i}$ in the denominator is independent of k and the weights b_k can be precomputed and stored for further usage.

The different approaches of the modal approximation $P_N u$ and the nodal interpolation $I_N(u)$ lead to different numerical results. The error between both formulations $\|P_N u - I_N(u)\|_\omega$ is called aliasing error. An analysis of the error reveals the relation

$$\|u - I_N(u)\|_\omega^2 = \|u - P_N u\|_\omega^2 + \|P_N u - I_N(u)\|_\omega^2$$

such that the aliasing error is orthogonal to the truncation error. Therefore the interpolation error on the left hand side (LHS) is always larger than the modal approximation error. Nonetheless, both methods exhibit a similar asymptotic behaviour and are comparable in their errors for practical usage.

3.2.4 Weak and Strong Formulation of Differential Equations

In general, a given problem like the Poisson problem on the square $\Omega = [-1,1] \times [-1,1]$ can be formulated differently according to the numerical method of choice. For finite differences we use the strong formulation of a PDE and search for an $u \in C^2(\Omega)$ that fulfils

$$\begin{aligned} -\Delta u &= s \quad \text{on } \Omega, \\ u &= u_0 \quad \text{at } \partial\Omega \end{aligned} \tag{3.23}$$

for a given source term $s \in L^2(\Omega)$. On the other hand, finite elements require the weak formulation of the problem. We search now for a $u \in H^1(\Omega)$ (Hilbert space of square-integrable functions with finite L^2-norm for weak derivatives up to order one) that solves, for a given right hand side $s \in L^2(\Omega)$, the weak problem

$$\int_\Omega \nabla u \cdot \nabla v\,dx = \int_\Omega s\,v\,dx \quad \forall v \in C_c^\infty(\Omega). \tag{3.24}$$
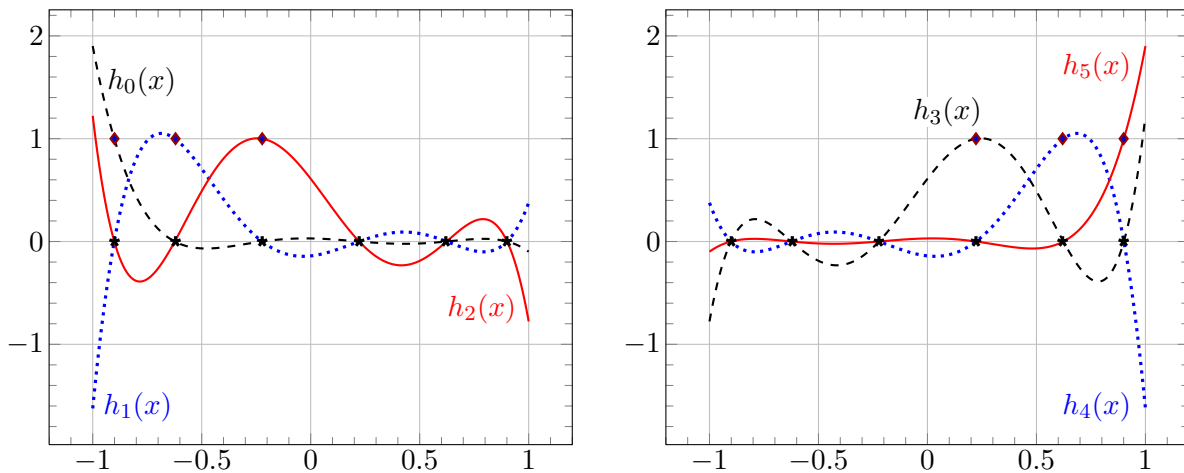
Figure 3.5: The Jacobi polynomial $J_6^{(0.5,0.5)}$ has six roots $x_0 \approx -0.9$, $x_1 \approx -0.62$, $x_2 \approx -0.22$, $x_3 \approx 0.22$, $x_4 \approx 0.62$, and $x_5 \approx 0.9$ that we use as nodes for the Lagrange polynomials $h_0(x), \ldots, h_5(x)$. An important property of Lagrange interpolation is the behaviour at the nodal values in the form $h_k(x_j) = \delta_{kj}$.

One of the advantages of the weak formulation is that the requirements on the solution are less strict (one time weak differentiable instead of twice differentiable).

Multidimensional Approximation

For a given Poisson problem in $\mathbb{R}^2$ we need a method to extend spectral approximations to multiple space dimensions. In two-dimensional rectangular domains we use tensor product expansions of two one-dimensional basis functions and extend the method for multidimensional rectangular domains accordingly. As a consequence, we decide for different basis representations if the problem differs in every direction. For instance, we approximate a problem that is periodic in the x direction and non-periodic in the y direction with an ansatz

$$P_{NM}u(x,y,t) = \sum_{k=-N/2}^{N/2} \sum_{l=0}^{M} \hat{u}_{kl}(t) \underbrace{\exp(ikx)}_{\text{periodic}} \underbrace{h_l(y)}_{\text{non-periodic}}. \tag{3.25}$$

In the case of an irregular domain we have two possibilities to apply spectral methods. First, we find a coordinate transformation that allows the mapping of an irregular domain onto a rectangular or spherical domain which is not always possible. Otherwise, we decompose the domain in small subdomains (e.g. triangulation) and apply the tensor product approach on a reference element. This leads to the so called spectral element method which combines characteristics of finite elements (domain decomposition) with spectral methods (high-order orthogonal polynomials).

	Spectral methods	
	periodic	non-periodic
basic functions	Fourier basis	Legendre polynomials
	Spherical harmonics	Chebyshev polynomials
	(periodic in ϕ)	Jacobi polynomials
differential equation	strong form	weak form
basis representation	modal	nodal

Table 3.2: Spectral methods do not only differ in the choice of an appropriate basis function but also in the basis representation and the weak or strong formulation of the underlying problem.

Example of a Weak and Strong Poisson Problem

For spectral methods we have the freedom of choice which formulation for a PDE we prefer as a wide class of spectral methods exists and makes a classification more difficult. Our aim is not to explain every method in detail but rather give a categorisation for the different methods. Therefore, we skip the treatment of the boundary conditions and concentrate on the major discretisation ansatz. The categorisation we use bases on the summary in Chapter 4.8 of Kopriva [51]. Later on, we use it to classify our method of choice for the solution of the Fokker-Planck equation.

Subsequently, we present a list with several possibilities to cope with the Poisson problem in (3.23) or (3.24). Additionally, Table 3.2 provides an overview of different approaches for spectral methods.

1. **Strong form of the equation - nodal representation**
   In literature the most common name for this approach is *collocation* method. We apply the Laplace operator on the interpolation polynomial $I_N(u)$ for u in a two-dimensional analogue of (3.21), interpolate the forcing term $s(x,y)$ on the right hand side, and obtain

   $$-\Delta(I_N(u)) = -\sum_{k,l}^{N} u_{x_k,y_l}\, h_k''(x)\, h_l(y) - \sum_{k,l}^{N} u_{x_k,y_l}\, h_k(x)\, h_l''(y) = \sum_{k,l}^{N} s_{x_k,y_l}\, h_k(x)\, h_l(y).$$

   Using a grid on the square we demand the equation to be solved exactly on the nodal values (x_i, y_j). We then get

   $$-\sum_{k,l}^{N} u_{x_k,y_l}\, h_k''(x_i)\, \delta_{lj} - \sum_{k,l}^{N} u_{x_k,y_l}\, \delta_{ki}\, h_l''(y_j) = \sum_{k,l}^{N} s_{x_k,y_l}\, \delta_{ki}\, \delta_{jl} \quad \text{for } i,j = 0,\ldots,N$$

   which can be further simplified and written in the form of a matrix-vector product. For further explanation of collocation methods we refer to the books of Fornberg [31] and Trefethen [88].

2. **Weak form of the equation - modal representation**
   Depending on the chosen orthogonal polynomial, this approach is called a *Legendre-Galerkin, Jacobi-Galerkin, Fourier-Galerkin, ...* method. For the Legendre polynomials

we approximate the unknown u and the the force term s in the form

$$P_{NN}(u(x,y)) = \sum_{k,l=0}^{N} \hat{u}_{kl} \, L_k(x) \, L_l(y),$$

$$P_{NN}(s(x,y)) = \sum_{k,l=0}^{N} \hat{s}_{kl} \, L_k(x) \, L_l(y) \qquad (3.26)$$

with the unknown coefficients $\hat{u}_{kl}$ and $\hat{s}_{kl}$. The weak formulation (3.24) is valid for every test function and, for the case of identical test and trial functions, therefore is also valid for all Legendre polynomials of order $\leq N$ which gives

$$(\nabla P_{NN}(u), \nabla \{L_m(x) \, L_n(y)\})_{\omega=1} = (P_{NN}(s), L_m(x) \, L_n(y))_{\omega=1} \quad \forall \, m, n = 0, \ldots, N.$$

for the inner product in L_ω^2. By substituting (3.26) into the last equation we have to solve the weak problem

$$\sum_{k,l=0}^{N} \hat{u}_{kl} \int_{-1}^{1} \int_{-1}^{1} \left\{ \frac{\partial L_k(x)}{\partial x} L_l(y) \frac{\partial L_m(x)}{\partial x} L_n(y) + L_k(x) \frac{\partial L_l(y)}{\partial y} L_m(x) \frac{\partial L_n(y)}{\partial y} \right\} \, dx \, dy$$

$$= \sum_{k,l=0}^{N} \hat{s}_{kl} \int_{-1}^{1} \int_{-1}^{1} L_k(x) L_l(y) \, L_m(x) L_n(y) \, dx \, dy \quad \forall \, m, n = 0, \ldots, N.$$

For the derivatives of the basis functions we use recurrence formulae that connect the polynomials and its derivatives, for instance $(2k+1)L_k(x) = L'_{k+1}(x) - L'_{k-1}(x)$. After that, we utilise the L^2-orthogonality of the basis functions and receive a linear system of equations.

3. **Weak form of the equation - nodal representation**
   At last, we describe an approach that combines certain elements from the previous methods. The method has different terms in literature. Whereas Kopriva [51] calls it a *nodal Galerkin* method, Canuto [18] uses the term *Galerkin with numerical integration* (G-NI). Again, we interpolate the unknown $I_N(u)$ with Lagrange polynomials in the form (3.21) but in contrast to the collocation method we insert the interpolation in the weak formulation (3.24) of the Poisson problem. We further use that Lagrange basis functions of the interpolated test function $I_N(v) = \sum v_{mn} h_m(x) h_n(y)$ are linearly independent to get the product

$$\sum_{k,l=0}^{N} u_{x_k,y_l} \int_{-1}^{1} \int_{-1}^{1} \left\{ \frac{\partial h_k(x)}{\partial x} h_l(y) \, \frac{\partial h_m(x)}{\partial x} h_n(y) + h_k(x) \frac{\partial h_l(y)}{\partial y} \, h_m(x) \frac{\partial h_n(y)}{\partial y} \right\} \, dx \, dy$$

$$= \sum_{k,l=0}^{N} s_{x_k,y_l} \int_{-1}^{1} \int_{-1}^{1} h_k(x) h_l(y) \, h_m(x) h_n(y) \, dx \, dy \quad \forall \, m, n = 0, \ldots, N.$$

$$(3.27)$$

The difference now is that we do not solve the integrals exactly but approximate them with a separate Gaussian quadrature relating to the x and y component by using Fubini's theorem, e.g.

$$\int_{-1}^{1} h_k(x)\, h_m(x)\, dx \approx \sum_{i=0}^{N} h_k(x_i)\, h_m(x_i)\, \omega_i \,=\, \delta_{km}\, \omega_k$$

for a given set of quadrature nodes $\{x_i\}$ and the corresponding Lagrange polynomials $\{h_i\}$. Finally, we get a problem in a similar form as in the collocation approach but with additional quadrature weights $\omega^{(x)}$ and $\omega^{(y)}$ for the integration with respect to x and y.

3.3 Stochastic Processes

3.3.1 Basic Concepts of Stochastic Calculus

We use the theory of stochastic processes and stochastic differential equations (SDEs)

- for the derivation of Brownian force in a FP equation like (2.67) or (2.68) and

- for the development of efficient numerical techniques to solve problems with high-dimensional configuration spaces.

Therefore, we have to introduce some basic concepts of stochastic analysis to formulate the underlying problems properly. For a more detailed introduction to the theory of SDEs we refer to the book of Øksendal [65]; an introduction with applications to polymeric fluids is given in Öttinger [66]. We only describe major characteristics of stochastic calculus in a similar way as Le Bris et al. [16] or Higham [39].

In the following section, we describe a probability space with the triple (Ω, Σ, P), where Ω denotes a sample space, Σ is a σ-algebra over Ω and P is a probability measure. In our context, the canonical probability space that characterises polymer configurations is $(\mathbb{R}^n, B^n, P : B^n \to \mathbb{R}^+)$ with B^n as the Borel σ-algebra generated by open intervals on $\mathbb{R}^n$. We furthermore necessitate real-valued random variables X which are functions $X : \Omega \to \mathbb{R}$ that fulfil

$$\{\omega \in \Omega | X(\omega) \leq s\} \in \Sigma \qquad \forall\, s \in \mathbb{R},$$

i.e. every set of the form $\{\omega \in \Omega | X(\omega) \leq s\}$ is an event for any real s. Based on random variables, we introduce stochastic processes which represent the idea of time-dependent random variables.

Definition 3.4 [Stochastic Process]
Let (Ω, Σ, P) be a probability space, then we denote a family of real-valued random variables $\boldsymbol{X} = (X_t)_{t \in T}$

$$\boldsymbol{X} : \Omega \times T \to \mathbb{R}, \;\; (\omega, t) \mapsto X_t(\omega)$$

as a (real-valued) stochastic process. In the multidimensional case $\vec{\boldsymbol{X}} : \Omega \times T \to \mathbb{R}^n$, we name a collection of n real-valued random variables $\vec{X}_t(\omega) = (X_{t,1}(\omega), \dots, X_{t,n}(\omega))$ a vector-valued stochastic process. For a fixed $\omega \in \Omega$, the function $t \mapsto X_t(\omega)$ is called a trajectory and we think of t as a variable for the current time in either a closed interval $T = [0, t_{max}]$ or the nonnegative axis $T = [0, \infty)$.

In the derivation of the Fokker-Planck equation, we use a stochastic process for modelling random collisions between beads of the dumbbells and surrounding molecules. The associated process is called Brownian motion or Wiener process.

Definition 3.5 [Wiener process]
A Wiener process $W_t(\omega)$ is a Gaussian stochastic process that is characterised by the properties

- *$P(W_{t=0} = 0) = 1$ (i.e. the event occurs P almost surely),*

- *its trajectories are (almost surely) continuous, and*

- *the increments are independent and are normally distributed with zero mean and variance $t - s$ for $0 \leq s < t$ (i.e. $W_t(\omega) - W_s(\omega) \sim N(0, t - s)$).*

Furthermore, we can interpret the trajectory of a Wiener process as limit of a random walk (i.e. successive sequence of random, nondirectional steps). Consequently, the trajectory of a Wiener Process is not differentiable at all because a random walk is not differentiable at any change of direction.

3.3.2 Stochastic Differential Equations

Subsequently, before dealing with stochastic differential equations, we have to declare the meaning of a stochastic integral with respect to a Wiener process. First, similar to Riemann integration, we consider stochastic integration for piecewise constant functions and afterwards extend it to locally bounded (i.e. $\int_T X_t(\omega)^2 \, dt < \infty$) and non-anticipating processes X_t (note that from now on we do not mention the reference to ω). An informal definition for X_t to be non-anticipating is that the future development of $X_{t>t_0}$ is independent from the previous development $X_{t<t_0}$ for all $t_0 \in T$. We require the integrand to be non-anticipating to be able to define the Itô integral properly.

Definition 3.6 [Itô stochastic integral]
Let X_t be a real-valued, locally bounded and non-anticipating stochastic process and W_t a Wiener process based on the same probability space (Ω, Σ, P), then we define the Itô integral of X_t with respect to W_t as limit

$$\int_0^{t_{max}} X_t \, dW_t \equiv \lim_{n \to \infty} \sum_{t_{j-1}, t_j \in \Xi_n} X_{t_{j-1}}(W_{t_j} - W_{t_{j-1}}) \tag{3.28}$$

for a partition Ξ_n of T with mesh size $1/n$ going to zero for $n \to \infty$. Again, we obtain the stochastic integral of a vector-valued stochastic process $\vec{X}_t$ by integrating every component separately.

The integral itself is also a random variable and the sequence on the RHS of (3.28) converges in probability which is a consequence of the weak law of large numbers. When we use the Itô integral, we always evaluate an integrand X_t at the left side of each interval $[t_{j-1}, t_j]$ in Ξ_n; an alternative evaluation at the midpoint $(X_{t_{j-1}} + X_{t_j})/2$ yields the Stratonovich integral. Instead of the deterministic case, the stochastic integrals actually depends on the point of evaluation if W_t and X_t are not independent from each other. Indeed, for the integral of W_t on $T = [0, t_{max}]$ we obtain

$$\underbrace{\int_0^{t_{max}} W_t \, dW_t}_{\text{Itô integral}} = \frac{1}{2}W_{t_{max}}^2 - \frac{1}{2}t_{max} \overset{t_{max}>0}{\neq} \frac{1}{2}W_{t_{max}}^2 = \underbrace{\int_0^{t_{max}} W_t \, dW_t}_{\text{Stratonovich integral}}.$$

Both integral definitions have their theoretical advantages, but, due to the explicit Euler scheme we use further on, we henceforth concentrate on the Itô integral. With the existence of an integration concept for stochastic processes, we can develop a stochastic analogon to a deterministic differential equation. However, we cannot define a concept for SDEs based on derivatives of

stochastic processes as they do not exist in general (e.g. a Wiener process is not differentiable). Therefore, we formulate a SDE as an equivalent integral equation.

Definition 3.7 [STOCHASTIC DIFFERENTIAL EQUATION]
Let $\vec{W}_t$ be an m-dimensional Wiener process and $\vec{X}_t$ an n-dimensional stochastic process which fulfils the requirements for the definition of an Itô integral. We denote $\vec{X}_t$ as a solution of the multicomponent stochastic differential equation

$$d\vec{X}_t \;=\; \vec{A}(t, \vec{X}_t)dt \;+\; \boldsymbol{B}(t, \vec{X}_t) \cdot d\vec{W}_t \tag{3.29}$$

for an n-dimensional column vector $\vec{A}$ and an $n \times m$-matrix $\boldsymbol{B}$, if $\vec{X}_t = (X_{t,1}, \ldots, X_{t,n})$ solves the integral equation

$$\underbrace{X_{t,i} \;=\; X_{0,i}}_{\text{componentwise view}} \;+\; \underbrace{\int_0^t A_i(s, \vec{X}_s)\, ds}_{\text{Lebesgue integral}} \;+\; \underbrace{\sum_{j=1}^m \int_0^t B_{ij}(s, \vec{X}_s)\, dW_{s,j}}_{\text{Itô integrals}} \qquad \text{for } i = 1, \ldots, n$$

and $t \in [0, t_{max}]$. We call $\vec{A}$ the drift term, $\boldsymbol{B}$ the diffusion tensor, and $d\vec{W}_t$ the white noise.

Subsequently, we present a fundamental result for the existence and uniqueness of solutions to SDEs.

Theorem 3.8 [EXISTENCE AND UNIQUENESS RESULT]
If the integrands $\vec{A}(t, \vec{X}_t)$ and $\boldsymbol{B}(t, \vec{X}_t)$ in (3.29) satisfy a Lipschitz condition

$$\|\vec{A}(t, \vec{u}) - \vec{A}(t, \vec{v})\| \;\leq\; C_1 \|\vec{u} - \vec{v}\|,$$
$$\|\boldsymbol{B}(t, \vec{u}) - \boldsymbol{B}(t, \vec{v})\| \;\leq\; C_2 \|\vec{u} - \vec{v}\|$$

for all $t \in T$, $u, v \in \mathbb{R}^n$, fulfil a linear growth condition

$$\|\vec{A}(t, \vec{u})\| \;\leq\; C_3(1 + \|\vec{u}\|),$$
$$\|\boldsymbol{B}(t, \vec{u})\| \;\leq\; C_4(1 + \|\vec{u}\|)$$

for some positive constants $C_1, \ldots, C_4$, and the initial condition $d\vec{X}_0$ is independent of $\vec{W}_t$, then there exists a unique solution to the underlying stochastic differential equation for all $t \in T$.

<u>Proof:</u> Rigorous proofs for the theorem above can be found in the books of Øksendal [65] and Gard [33].

3.3.3 Numerical Integration Schemes

Stochastic differential equations are only analytically solvable in some special cases and mainly for linear equations, similar to their deterministic counterparts. Therefore, we have to concentrate on numerical approximation schemes for a SDE based on a nonlinear FENE spring force. We investigate the quality of approximation schemes with the concept of strong and

weak convergence order. For every $\omega \in \Omega$, we could in principle compare the error

$$\|\vec{X}_{t,\text{appr.}} - \vec{X}_{t,\text{exact}}\|$$

between the approximation $\vec{X}_{t,\text{appr.}}$ and the exact trajectory $\vec{X}_{t,\text{exact}}$. However, most events $\omega \in \Omega$ have a low probability $P(\omega)$ and the quantity of major interest is the expectation

$$\left\langle \|\vec{X}_{t,\text{appr.}} - \vec{X}_{t,\text{exact}}\| \right\rangle \equiv \sum_{j=1}^{\infty} \|\vec{X}_{t,\text{appr.}}(\omega_j) - \vec{X}_{t,\text{exact}}(\omega_j)\| \, P(\omega_j) \quad \text{for discrete } \Omega = \{\omega_1, \omega_2, \dots\}.$$

In order to apply a numerical method, we divide $T = [0, t_{max}]$ equidistantly into $t_0 = 0 < t_1 < \cdots < t_{max}$ with time step size Δt and give the following definition.

Definition 3.9 [Strong Order of Convergence]
A numerical scheme with discrete time step size Δt converges strongly with order $v > 0$ against the exact solution $\vec{X}_{t,exact}$ with $t \in \{t_0, \dots, t_n\}$, if there exists a constant $c > 0$, such that

$$\left\langle \|\vec{X}_{t,appr.} - \vec{X}_{t,exact}\| \right\rangle \leq c \, (\Delta t)^v$$

for all time steps Δt.

The strong order of convergence is essential when single trajectories need to be fully resolved. However, in the case of polymeric fluids we are not interested in individual trajectories but rather in certain averages of the form $\left\langle \varphi(\vec{X}_{t,\text{appr.}}) \right\rangle$ for a sufficiently smooth function φ. The expression that we actually think about is the extra-stress tensor as in (2.81) that takes a similar form as $\left\langle \vec{F}(\vec{X}_{t,\text{appr.}}) \otimes \vec{X}_{t,\text{appr.}} \right\rangle$ in this context. This relates to the weak solution of the differential equation.

Definition 3.10 [Weak Order of Convergence]
An approximation scheme $\vec{X}_{t,appr.}$ converges weakly with order v against $\vec{X}_{t,exact}$, if, for all $\varphi \in C^{2v+1}(\mathbb{R}^n)$ and all time step sizes Δt, there exists a constant $c > 0$, such that

$$\left| \left\langle \varphi(\vec{X}_{t,appr.}) \right\rangle - \left\langle \varphi(\vec{X}_{t,exact}) \right\rangle \right| \leq c(\Delta t)^v.$$

Analogously to the deterministic case, strong convergence for a SDE implies weak convergence but not vice versa.

We now introduce the most simple numerical scheme, the Euler-Maruyama method, which we write componentwise (i.e. for $i = 1, \dots, n$) as

$$X_{t_r,i} = X_{t_{r-1},i} + \int_{t_{r-1}}^{t_r} A_i(s, \vec{X}_s) \, ds + \sum_{j=1}^{m} \int_{t_{r-1}}^{t_r} B_{ij}(s, \vec{X}_s) \, dW_{s,j} \tag{3.30}$$

$$\approx X_{t_{r-1},i} + A_i(t_{r-1}, \vec{X}_{t_{r-1}}) \, \Delta t + \sum_{j=1}^{m} B_{ij}(t_{r-1}, \vec{X}_{t_{r-1}}) \, (W_{t_r,j} - W_{t_{r-1},j})$$

$$= X_{t_{r-1},i} + A_i(t_{r-1}, \vec{X}_{t_{r-1}}) \Delta t + \sum_{j=1}^{m} B_{ij}(t_{r-1}, \vec{X}_{t_{r-1}}) \underbrace{\sqrt{\Delta t}\, \mathrm{N}(0,1)}_{=\mathrm{N}(0,\Delta t)}$$

where $t_r, t_{r-1} \in \{t_0, t_1, \ldots, t_{\max}\}$ and $\mathrm{N}(0,1)$ is a (j-dependent) Gaussian random variable with zero mean and variance one. With the use of the Itô integral, the stochastic integrals on the RHS have to be evaluated at the left side t_{r-1} of $[t_{r-1}, t_r]$ and therefore all numerical schemes have to be explicit in the stochastic term. For this reason we cannot define a full implicit Euler-Maruyama scheme as it would produce wrong results. Otherwise, at least the deterministic drift vector $\vec{A}(t, \vec{X}_t)$ can be evaluated implicitly. With respect to convergence order, the explicit scheme yields

- a strong convergence order 1/2 in general (i.e. multiplicative noise),

- a strong convergence order 1 if $\boldsymbol{B}(t, \vec{X}_t) = \boldsymbol{B}(t)$ does not depend on $\vec{X}_t$ (i.e. additive noise), and

- a weak convergence order 1 in general.

Subsequently, we try to give reasons for the lower strong convergence order of the Euler-Maruyama method in comparison to the explicit Euler method for ODEs and refer to the book of Gard [33] for a detailed proof. The Itô stochastic integral and therefore the Euler-Maruyama scheme evaluates $\boldsymbol{B}(t)$ at t_{r-1}, but the diffusion tensor changes its values during an interval of size Δt in the order of its standard deviation $(\Delta t)^{1/2}$ which reduces the accuracy of the method.

In the view of the low convergence order for the Euler-Maruyama scheme, we further present a higher-order scheme. On the one hand, we could try to perform a Taylor-like expansion of the diffusion $\boldsymbol{B}(t, \vec{X}_t)$ which is called an Itô-Taylor expansion in this context. On the other hand, the evaluation of the integral is more expensive for an Itô-Taylor expansion and therefore we concentrate on a predictor-corrector approach and use the Euler-Trapezoidal method to get

$$\vec{Y}_{t_r,i} = \vec{X}_{t_{r-1},i} + A_i(t_{r-1}, \vec{X}_{t_{r-1}}) \Delta t + \sum_{j=1}^{m} B_{ij}(t_{r-1}, \vec{X}_{t_{r-1}}) \sqrt{\Delta t}\, \mathrm{N}(0,1) \qquad (3.31)$$

$$\vec{X}_{t_r,i} = \vec{X}_{t_{r-1},i} + \frac{1}{2} \left[A_i(t_r, \vec{Y}_{t_r}) + A_i(t_{r-1}, \vec{X}_{t_{r-1}}) \right] \Delta t$$
$$+ \sum_{j=1}^{m} \frac{1}{2} \left[B_{ij}(t_r, \vec{Y}_{t_r}) + B_{ij}(t_{r-1}, \vec{X}_{t_{r-1}}) \right] \sqrt{\Delta t}\, \mathrm{N}(0,1)$$

which is also written by components $i = 1, \ldots, n$. The predictor step computes $\vec{Y}_{t_m,i}$ as an approximation to $\vec{X}_{t_r,i}$ and then uses the idea of a Crank-Nicolson discretisation in the corrector step to compute $\vec{X}_{t_r,i}$. Additionally, the predictor-corrector pair has

- a weak convergence order 1 in general (i.e. multiplicative noise) and

- a weak convergence order 2 if $\boldsymbol{B}(t, \vec{X}_t) = \boldsymbol{B}(t)$ does not depend on $\vec{X}_t$ (i.e. additive noise)

as mentioned in Lozinski et al. [59]. In Chapter 4.2, we investigate the stochastic equation for a dumbbell model which has a constant diffusion coefficient and therefore, we expect to obtain a weak convergence order 2 for the predictor-corrector scheme.

4 Stress Tensor Approximation for Homogeneous Flows

This chapter concentrates on stationary flow systems in which the velocity gradient tensor is constant in the fluid domain Ω. In this case, the Fokker-Planck equation reduces from a six-dimensional to a three-dimensional diffusion equation which we can either solve by using deterministic discretisation schemes as in Chapter 4.1 or applying Monte Carlo techniques to the equivalent stochastic differential equation as in Chapter 4.2. Later on, we present numerical results for both approaches in Chapter 6.

4.1 Fokker-Planck Equation for Homogeneous Flows

The aim of this chapter is to solve the Fokker-Planck equation which we obtain in the case of a homogeneous flow field. This is a flow field in which the velocity gradient tensor $\vec{\nabla}_x \vec{u}$ is constant throughout Ω,

$$
\vec{\nabla}_x \vec{u} = \begin{pmatrix} \frac{\partial u}{\partial x} & \frac{\partial u}{\partial y} & \frac{\partial u}{\partial z} \\ \frac{\partial v}{\partial x} & \frac{\partial v}{\partial y} & \frac{\partial v}{\partial z} \\ \frac{\partial w}{\partial x} & \frac{\partial w}{\partial y} & \frac{\partial w}{\partial z} \end{pmatrix} = \begin{pmatrix} \kappa_{11} & \kappa_{12} & \kappa_{13} \\ \kappa_{21} & \kappa_{22} & \kappa_{23} \\ \kappa_{31} & \kappa_{32} & \kappa_{33} \end{pmatrix} = \text{constant.}
$$

In literature, a constant velocity gradient is often denoted with the symbol $\boldsymbol{\kappa}$. A homogeneous flow field greatly simplifies the description of the underlying flow problem. Indeed, in that case

- we do not need to solve the Navier-Stokes equations,

- the probability density function $\psi(t, \vec{x}, \vec{q}) = \psi(t, \vec{q})$ does not depend on physical space $\vec{x}$ and therefore

- the non-dimensional FP equation takes the form

$$
\frac{\partial \psi}{\partial t} + \vec{\nabla}_{\vec{q}} \cdot \left[\left(\boldsymbol{\kappa} \cdot \vec{q} - \frac{1}{2\,Wi} \vec{F}(\vec{q}) \right) \psi(\vec{q}) \right] = \frac{1}{2\,Wi} \Delta_{\vec{q}} \psi(\vec{q}). \tag{4.1}
$$

4.1.1 2D Fokker-Planck Equation in the Plane

In the following section, we use an approach for the solution that was first proposed by Lozinski and Chauviere [57] and is further explained in Lozinski [56] and in Lozinski et al. [59]. We restrict the orientation of the configuration vector, i.e. the dumbbell orientation, to the plane which leads to a two-dimensional Fokker-Planck equation in configuration space. Due to the

fact that in the case of a FENE spring force the probability density function (pdf) ψ is restricted to a disc with radius $\sqrt{b}$, we describe the problem in polar coordinates

$$q_1 = r\cos(\phi), \quad q_2 = r\sin(\phi) \qquad \text{with } r \in [0, \sqrt{b}] \text{ and } \phi \in [0, 2\pi]. \tag{4.2}$$

Moreover, at the end of the section we also discuss the more simple Hooke spring force where the density ψ is unbounded in its domain of definition as a boundary case of the FENE dumbbell case. (i.e. $b \to \infty$). With (4.2) and the differential operators

$$\text{div}_{\vec{q}}\,\vec{v} = \frac{1}{r}v_r + \frac{\partial v_r}{\partial r} + \frac{1}{r}\frac{\partial v_\phi}{\partial \phi} \qquad \text{(for a vector-valued } \vec{v}(r, \phi)) \quad \text{and}$$

$$\Delta_{\vec{q}}\,f = \frac{1}{r}\frac{\partial f}{\partial r} + \frac{\partial^2 f}{\partial r^2} + \frac{1}{r^2}\frac{\partial^2 f}{\partial \phi^2} \qquad \text{(for a scalar-valued } f(r, \phi))$$

in polar coordinates we are able to express (4.1) in the form

$$\begin{aligned}
\frac{\partial \psi}{\partial t} &= -\,r\,b_1(\boldsymbol{\kappa}, \phi)\frac{\partial \psi}{\partial r} \;-\; b_2(\boldsymbol{\kappa}, \phi)\frac{\partial \psi}{\partial \phi} \;+\; \frac{1}{2\,Wi}\left(\frac{br}{b - r^2} + \frac{1}{r}\right)\frac{\partial \psi}{\partial r} \\
&\quad +\; \frac{b^2}{Wi\,(b - r^2)^2}\psi \;+\; \frac{1}{2\,Wi}\frac{\partial^2 \psi}{\partial r^2} \;+\; \frac{1}{2\,Wi\,r^2}\frac{\partial^2 \psi}{\partial \phi^2}.
\end{aligned} \tag{4.3}$$

Thereby, we have used the abbreviations

$$b_1(\boldsymbol{\kappa}, \phi) = \kappa_{11}\cos(2\phi) + \frac{\kappa_{12} + \kappa_{21}}{2}\sin(2\phi),$$

$$b_2(\boldsymbol{\kappa}, \phi) = -\kappa_{11}\sin(2\phi) + \frac{\kappa_{12} + \kappa_{21}}{2}\cos(2\phi) + \frac{\kappa_{21} - \kappa_{12}}{2},$$

and the identity $\kappa_{11} + \kappa_{22} = 0$ because of the source-free velocity field $\vec{u}$. Before we are able to discretise (4.3), we have to deal with the singularities of the FENE coefficients $\frac{br}{b - r^2} + \frac{1}{r}$, $\frac{b^2}{(b - r^2)^2}$ and $\frac{1}{r^2}$ at the boundaries $r = 0$ and $r = \sqrt{b}$. We introduce a coordinate transformation $[0, \sqrt{b}] \to [-1, 1]$, a standard operation for spectral methods, and a new unknown α that arises out of the behaviour of ψ at the boundary. For ψ we know that

- $\psi(t, r, \phi) = 0$ for $r = \sqrt{b}$ (dumbbells cannot leave the sphere) and

- $\frac{\partial \psi(t, r, \phi)}{\partial r} = 0$ for $r = 0$ (a consequence of the symmetry of ψ with respect to $\vec{q}$).

We fulfil these requirements with the transformation

$$\psi(t, r, \phi) = \left(\frac{1 - \eta}{2}\right)^s \alpha(t, \eta, \phi) \quad \text{with } r^2 = b\frac{1 + \eta}{2}, \tag{4.4}$$

$$\eta \in [-1, 1] \text{ and } s \in \mathbb{R}^+ \setminus \{0\}$$

and obtain an additional parameter s for optimisation. Indeed, in literature the optimal choice for s is a subject of ongoing discussion because

- $s = \frac{b}{2}$ (i.e. a transformation of the form $\psi = (1 - |\vec{q}|^2/b)^{b/2}\alpha = \psi_{eq}\alpha$) lets disappear the spring force in the weak formulation of (4.3) (see Knezevic [28]),
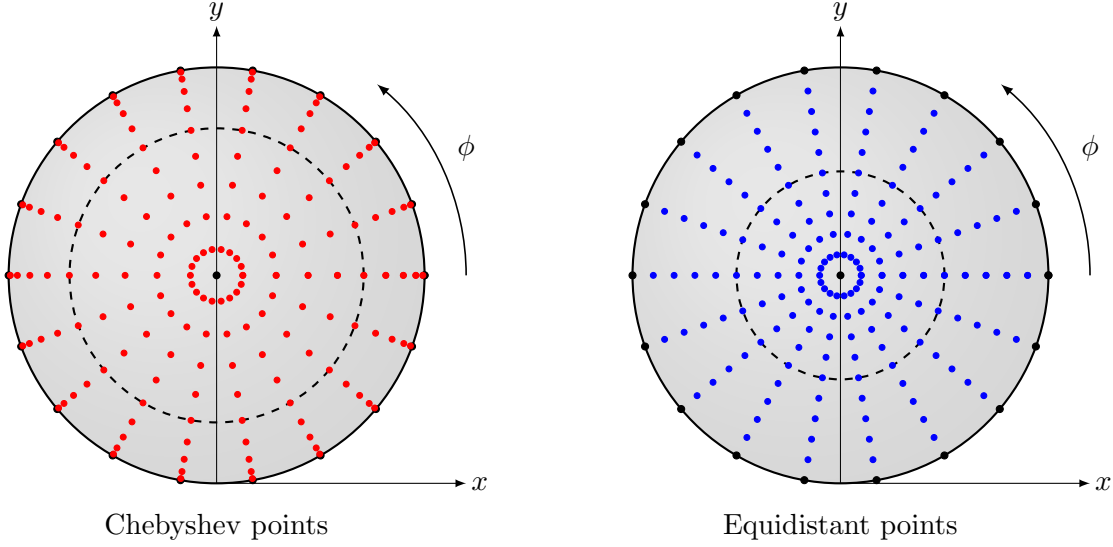
Figure 4.1: The left picture shows a nine-point Chebyshev discretisation of $[-1, 1]$ transformed on $[0, \sqrt{b}]$, whereas the boundary points are not included. Half of the points lie in a circle that fills $\approx 50\%$ of the total area. Therefore, we are able to achieve a reasonable point distribution for the disc in the case of Chebyshev points. In contrast, 25% of the total area contains half of the grid points for an equidistant distribution. For further information we refer to the book of Trefethen [88].

- $s = \frac{b}{4}$ (i.e. a transformation of the form $\psi = (1 - |\vec{q}|^2/b)^{b/4} \alpha = \sqrt{\psi_{eq}} \, \alpha$) yields a symmetric bilinear form in the weak formulation of (4.3) (see Knezevic [50]),

- a large value for s yields a more accurate solution for ψ, but

- a small value for s increases the stability of the algorithm because steep gradients of ψ at the boundary are less pronounced then.

As a result of transformation (4.4) we do not further concentrate on the boundary conditions for the new unknown α since the boundary conditions for ψ are fulfilled automatically. Moreover, a distribution of the interval $[-1, 1]$ with Gauss-Legendre or Gauss-Chebyshev points yields a better filling of the disc after retransformation on $[0, \sqrt{b}]$ than an equidistant interval distribution that we describe in Chapter 3.1. We illustrate the theoretical advantages of our spectral method approach in Figure 4.1.

By substituting (4.4) into (4.3), we get an equation of the form

$$\frac{\partial \alpha}{\partial t} = L_0 \alpha + \kappa_{11} L_1 \alpha + \kappa_{12} L_2 \alpha + \kappa_{21} L_3 \alpha. \tag{4.5}$$

Here, L_0, L_1, L_2 and L_3 denote linear operators independent of $\boldsymbol{\kappa}$ that we write in the notation of Lozinski [56] as

$$L_0 = \frac{2(b - 2s)(2 - s - s\eta)}{b\lambda(1 - \eta)^2} + \frac{2}{b\lambda} \left(\frac{(b - 4s)(1 + \eta)}{1 - \eta} + 2 \right) \frac{\partial}{\partial \eta}$$

$$+ \frac{4(1+\eta)}{\lambda b} \frac{\partial^2}{\partial \eta^2} + \frac{1}{\lambda b(1+\eta)} \frac{\partial^2}{\partial \phi^2},$$

$$L_1 = \frac{2s(1+\eta)}{1-\eta} \cos(2\phi) - 2(1+\eta)\cos(2\phi)\frac{\partial}{\partial \eta} + \sin(2\phi)\frac{\partial}{\partial \phi},$$

$$L_2 = \frac{s(1+\eta)}{1-\eta} \sin(2\phi) - (1+\eta)\sin(2\phi)\frac{\partial}{\partial \eta} - \frac{1}{2}\cos(2\phi)\frac{\partial}{\partial \phi} + \frac{1}{2}\frac{\partial}{\partial \phi}, \text{ and}$$

$$L_3 = \frac{s(1+\eta)}{1-\eta} \sin(2\phi) - (1+\eta)\sin(2\phi)\frac{\partial}{\partial \eta} - \frac{1}{2}\cos(2\phi)\frac{\partial}{\partial \phi} - \frac{1}{2}\frac{\partial}{\partial \phi}. \tag{4.6}$$

4.1.2 Discretisation using Spectral Methods

Although we have various possibilities to discretise the Fokker-Planck equation in configuration space, most authors prefer the usage of spectral methods. A reason for that is the simplicity of the underlying domain in polar coordinates which allows us to use a spectral approach without the necessity of a domain decomposition (cf. spectral elements). Furthermore, for most flow situations we expect a smooth development of ψ in time since the domain of definition does not contain any obstacles that would affect the probability of a certain configuration. Nevertheless, other schemes as finite difference methods (see Yu et al. [97] or Du et al. [28]) or finite element methods as in Knezevic [50] have also been applied to the problem.

For $N = (N_F, N_R) \in \mathbb{N}^2$, our approximation space for the spectral methods is

$$V_N = \text{span}\{h_k(\eta)\Phi_{il}(\phi), i = 0, 1; \ i \leq l \leq N_F, \ 0 \leq k \leq N_R\} \tag{4.7}$$

with basis functions

- $\{h_k(\eta)\}_{0 \leq k \leq N_R}$ as Lagrange interpolation polynomials that base on the Gauss-Chebyshev or Gauss-Legendre points η_r and

- $\{\Phi_{il}(\phi) = (1-i)\cos(2l\phi) + i\sin(2l\phi)\}_{i=0,1; \ i \leq l \leq N_F}$ as the even ordered trigonometric functions.

Therefore, we use a tensor product expansion that is modal in the angular coordinate ϕ and nodal in the radial coordinate r. Furthermore, we restate the differential equation in the weak form so that we have a classical Galerkin approach in ϕ and a nodal Galerkin or Galerkin with numerical integration (G-NI) scheme in η as described in Section 3.2.4. The different approaches for the angular and radial coordinates implicate a different computation of the involved integrals. Actually, we solve the integrals with respect to ϕ analytically, whereas we use Gaussian quadrature for integrals with respect to η. We illustrate the approximation space for $N_R = 3$ with the Gauss-Legendre points and four basis functions $h_0(\eta)\Phi_{0,1}(\phi)$, $h_1(\eta)\Phi_{0,1}(\phi)$, $h_2(\eta)\Phi_{0,1}(\phi)$, and $h_3(\eta)\Phi_{0,1}(\phi)$ in Figure 4.2.

The decision between the Gauss-Legendre and Gauss-Chebyshev points depends on personal preferences because both methods offer a similar convergence behaviour. However, we skip the boundary values $\eta = -1$ and $\eta = 1$ in every possible sequence $\{\eta_r\}$ since ψ satisfies the boundary conditions regardless the boundary values of α (cf. (4.4)). In addition, we only notice
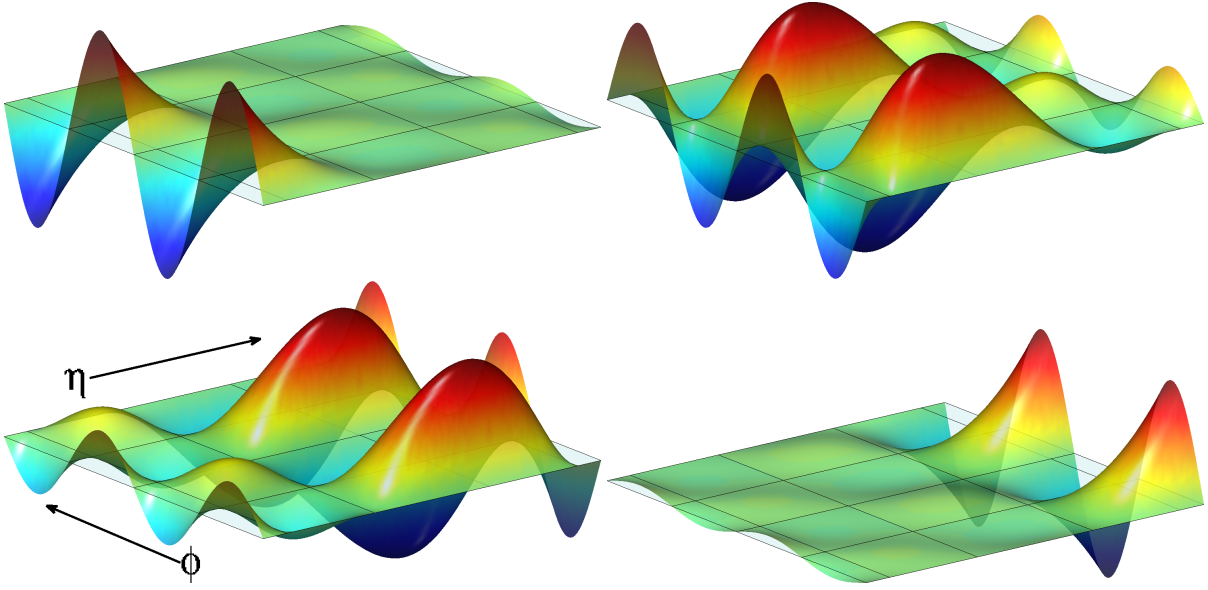
Figure 4.2: The figure visualises four tensor product basis functions $h_0(\eta)\cos(2\phi)$, $h_1(\eta)\cos(2\phi)$, $h_2(\eta)\cos(2\phi)$, and $h_3(\eta)\cos(2\phi)$ for the discretisation of the Fokker-Planck equation on the sphere. The Lagrange polynomials are of order four and are based on the four roots of the Legendre polynomial $L_4(x)$ which are $x_0 \approx -0.86$, $x_1 \approx -0.34$, $x_2 \approx 0.34$, and $x_3 \approx 0.86$. Four auxiliary lines perpendicular to the η-axis signalise the quadrature nodes; on the other hand, five auxiliary lines perpendicular to the ϕ-axis signalise the roots of $\cos(2\phi)$ at 0, $\pi/2$, π, $3\pi/2$, and 2π.

even ordered trigonometric functions in the approximation space which is a direct consequence of the symmetry of ψ with respect to $\vec{q}$ (or $\alpha(\eta, \phi) = \alpha(\eta, \phi + \pi)$ for all η and ϕ).

We now write (4.5) in the weak form and therefore multiply the equation by a test function $v(t, \eta, \phi)$ and a weight function $\omega(\eta)$, which is equal to one in the case of the Legendre points and otherwise $\omega(\eta) = (1 - \eta)^{-0.5}(1 + \eta)^{-0.5}$ (cf. table 3.1 on page 67), and perform integration over the configuration space. By doing so, we obtain

$$
\int_0^{2\pi} \int_{-1}^1 \frac{\partial \alpha}{\partial t}\, v(t, \eta, \phi)\, \omega(\eta)\, d\eta\, d\phi
$$
$$
= \int_0^{2\pi} \int_{-1}^1 (L_0\alpha + \kappa_{11}L_1\alpha + \kappa_{12}L_2\alpha + \kappa_{21}L_3\alpha)\, v(t, \eta, \phi)\, \omega(\eta)\, d\eta\, d\phi
\tag{4.8}
$$

for all test functions v. Next, we replace α by its approximation

$$
\alpha_N(t, \eta, \phi) = \sum_{i=0}^{1} \sum_{l=i}^{N_F} \sum_{k=0}^{N_R} \alpha_{ilk}(t)\Phi_{il}(\phi)h_k(\eta)
\tag{4.9}
$$

to get the Galerkin approximation and take the test function v to be any polynomial of the

same degree as α_N so that we can write v as

$$v(t, \eta, \phi) = \sum_{j=0}^{1} \sum_{m=j}^{N_F} \sum_{n=0}^{N_R} v_{jmn}(t) \Phi_{jm}(\phi) h_n(\eta). \tag{4.10}$$

As it is sufficient to consider only the basis functions $h_n(\eta)\Phi_{jm}(\phi)$ as test functions, we obtain $(2N_F + 1)(N_R + 1)$ equations

$$\int_0^{2\pi} \int_{-1}^{1} \frac{\partial \alpha}{\partial t} h_n(\eta)\Phi_{jm}(\phi) \, \omega(\eta) \, d\eta \, d\phi$$

$$= \int_0^{2\pi} \int_{-1}^{1} (L_0\alpha + \kappa_{11}L_1\alpha + \kappa_{12}L_2\alpha + \kappa_{21}L_3\alpha) \, h_n(\eta)\Phi_{jm}(\phi) \, \omega(\eta) \, d\eta \, d\phi, \tag{4.11}$$

$$\text{for } j = 0, 1; \ m = j, \ldots, N_F; \ n = 0, \ldots, N_R.$$

Now, we insert our approximation α_N from (4.9) into (4.11), evaluate the integrals with respect to η (numerical) and ϕ (analytical), and receive discretised operators $(\frac{\partial \alpha_N}{\partial t})_{jmn}$, $(L_0\alpha_N)_{jmn}$, $(L_1\alpha_N)_{jmn}$, $(L_2\alpha_N)_{jmn}$ and $(L_3\alpha_N)_{jmn}$. In this context, $(\frac{\partial \alpha_N}{\partial t})_{jmn}$ is a short term for

$$\left(\frac{\partial \alpha_N}{\partial t}\right)_{jmn} = \left(\frac{\partial \alpha}{\partial t}, \underbrace{\Phi_{jm}h_n}_{=v_{jmn}}\right)_{L^2_\omega[-1,1]\otimes L^2[0,2\pi]} = \int_0^{2\pi} \int_{-1}^{1} \frac{\partial \alpha}{\partial t} v_{jmn}(\eta, \phi) \, \omega(\eta) \, d\eta \, d\phi$$

and analogue for the other operators. We describe the conversions for the first two operators in detail and just give the final results for the other operators as they can be transformed analogously.

For the first operator $(\frac{\partial \alpha_N}{\partial t})_{jmn}$ on the left of (4.11), we have the approximation

$$\left(\frac{\partial \alpha_N}{\partial t}\right)_{jmn} = \sum_{i=0}^{1} \sum_{l=i}^{N_F} \sum_{k=0}^{N_R} \frac{\partial \alpha_{ilk}(t)}{\partial t} \int_0^{2\pi} \int_{-1}^{1} h_k(\eta)\Phi_{il}(\phi) \, h_n(\eta)\Phi_{jm}(\phi) \, \omega(\eta) \, d\eta \, d\phi$$

$$\overset{GI}{\approx} \sum_{i=0}^{1} \sum_{l=i}^{N_F} \sum_{k=0}^{N_R} \frac{\partial \alpha_{ilk}(t)}{\partial t} \int_0^{2\pi} \Phi_{il}(\phi)\Phi_{jm}(\phi) \sum_{r=0}^{N_R} \underbrace{h_k(\eta_r)}_{=\delta_{rk}} \underbrace{h_n(\eta_r)}_{=\delta_{rn}} \omega_r \, d\phi$$

$$= \sum_{i=0}^{1} \sum_{l=i}^{N_F} \frac{\partial \alpha_{iln}(t)}{\partial t} \omega_n \underbrace{\int_0^{2\pi} \Phi_{il}(\phi)\Phi_{jm}(\phi) \, d\phi}_{=\delta_{ij}\delta_{lm}(1+\delta_{i0}\delta_{l0})\,\pi}$$

$$= \frac{\partial \alpha_{jmn}(t)}{\partial t} \omega_n \, (1 + \delta_{j0}\delta_{m0})\,\pi.$$

In general, Gaussian integration, as performed from the first to the second row, is not exact and therefore introduces an additional error. Furthermore, the sequence $\{\omega_r\}$ denotes the quadrature weights that we describe in more detail in Section 3.2.3.

Second, we derive $(L_0\alpha_N)_{jmn}$ and therefore use the definition of L_0 in (4.6) to obtain

$$
(L_0\alpha_N)_{jmn}
$$

$$
= \sum_{i,l,k} \alpha_{ilk}(t) \int_0^{2\pi} \int_{-1}^{1} \left\{ \frac{2(b-2s)(2-s-s\eta)}{b\lambda(1-\eta)^2} h_k(\eta)\Phi_{il} + \frac{2}{b\lambda}\left(\frac{(b-4s)(1+\eta)}{1-\eta} + 2 \right) h_k'(\eta)\Phi_{il} \right.
$$

$$
\left. + \frac{4(1+\eta)}{\lambda b} \frac{\partial^2 h_k(\eta)}{\partial\eta^2}\Phi_{il}(\phi) + \frac{1}{\lambda b(1+\eta)} \underbrace{\frac{\partial^2 \Phi_{il}(\phi)}{\partial\phi^2}}_{= -4l^2\,\Phi_{il}(\phi)} h_k(\eta) \right\} h_n(\eta)\Phi_{jm}(\phi)\,\omega(\eta)\,d\eta\,d\phi
$$

$$
\overset{GI}{\approx} \sum_{i=0}^{1}\sum_{l=i}^{N_F}\sum_{k=0}^{N_R} \alpha_{ilk}(t) \int_0^{2\pi} \Phi_{il}(\phi)\Phi_{jm}(\phi) \sum_{r=0}^{N_R} \left\{ \frac{2(b-2s)(2-s-s\eta_r)}{b\lambda(1-\eta_r)^2} \underbrace{h_k(\eta_r)}_{= \delta_{rk}} \right.
$$

$$
\left. + \frac{2}{b\lambda}\left(\frac{(b-4s)(1+\eta_r)}{1-\eta_r} + 2 \right) h_k'(\eta_r) + \frac{4(1+\eta_r)}{\lambda b} h_k''(\eta_r) - \frac{4l^2}{\lambda b(1+\eta_r)} \underbrace{h_k(\eta_r)}_{= \delta_{rk}} \right\} \underbrace{h_n(\eta_r)}_{= \delta_{rn}}\,\omega_r\,d\phi
$$

$$
= \sum_{i,l} \left\{ \left(\frac{2(b-2s)(2-s-s\eta_n)}{b\lambda(1-\eta_n)^2} - \frac{4l^2}{\lambda b(1+\eta_n)} \right)\alpha_{iln} + \sum_{k=0}^{N_R}\left(\frac{2}{b\lambda}\left(\frac{(b-4s)(1+\eta_n)}{(1-\eta_n)} + 2 \right) h_k'(\eta_n) \right. \right.
$$

$$
\left. \left. + \frac{4(1+\eta_n)}{\lambda b} h_k''(\eta_n) \right)\alpha_{ilk} \right\}\omega_n \underbrace{\int_0^{2\pi} \Phi_{il}(\phi)\Phi_{jm}(\phi)\,d\phi}_{= \delta_{ij}\delta_{lm}(1+\delta_{i0}\delta_{l0})\,\pi}
$$

$$
= \left\{ \left(\frac{2(b-2s)(2-s-s\eta_n)}{b\lambda(1-\eta_n)^2} - \frac{4m^2}{\lambda b(1+\eta_n)} \right)\alpha_{jmn} + \sum_{k=0}^{N_R}\left(\frac{2}{b\lambda}\left(\frac{(b-4s)(1+\eta_n)}{(1-\eta_n)} + 2 \right) h_k'(\eta_n) \right. \right.
$$

$$
\left. \left. + \frac{4(1+\eta_n)}{\lambda b} h_k''(\eta_n) \right)\alpha_{jmk} \right\}\omega_n\,(1+\delta_{j0}\delta_{m0})\,\pi.
$$

In the same way, we derive the other operators as

$$
(L_1\alpha_N)_{jmn} = \sum_{i=0}^{1}\sum_{l=i}^{N_F}\sum_{k=0}^{N_R}\left\{ \left(\frac{2s(1+\eta_n)}{1-\eta_n}\delta_{kn} - 2(1+\delta_n)h_k'(\eta_n) \right) J_{iljm}^0 + K_{iljm}^1\delta_{kn} \right\}\alpha_{ilk}\,\omega_n
$$

$$
(L_2\alpha_N)_{jmn} = \sum_{i=0}^{1}\sum_{l=i}^{N_F}\sum_{k=0}^{N_R}\left\{ \left(\frac{s(1+\eta_n)}{1-\eta_n}\delta_{km} - (1+\eta_n)h_k'(\eta_n) \right) J_{iljm}^1 - \frac{1}{2} K_{iljm}^1\delta_{kn} \right\}\alpha_{ilk}\,\omega_n
$$

$$
+ (-1)^j n\,\alpha_{(1-j)mn}\,\omega_n\,\pi
$$

$$
(L_3\alpha_N)_{jmn} = \sum_{i=0}^{1}\sum_{l=i}^{N_F}\sum_{k=0}^{N_R}\left\{ \left(\frac{s(1+\eta_n)}{1-\eta_n}\delta_{km} - (1+\eta_n)h_k'(\eta_n) \right) J_{iljm}^1 - \frac{1}{2} K_{iljm}^1\delta_{kn} \right\}\alpha_{ilk}\,\omega_n
$$

$$
- (-1)^j n\,\alpha_{(1-j)mn}\,\omega_n\,\pi
$$

in which we have introduced abbreviations J_{iljm}^0, J_{iljm}^1, K_{iljm}^0, and K_{iljm}^1 for the integrals with

respect to ϕ. We evaluate these integrals analytically which yields

$$
\begin{aligned}
J_{iljm}^{p} &= \int_{0}^{2\pi} \cos(2\phi - p\frac{\pi}{2})\, \Phi_{il}(\phi)\Phi_{jm}(\phi)\, d\phi \\
&= \frac{\pi}{2}\left[\delta_{l+m,1}\cos\left((p-i-j)\frac{\pi}{2}\right) + \delta_{m-l,1}\cos\left((p+i-j)\frac{\pi}{2}\right) + \delta_{l-m,1}\cos\left((p-i+j)\frac{\pi}{2}\right)\right]
\end{aligned}
$$

for $p = 0, 1$ and on the other hand, we use the relation $\Phi'_{il}(\phi) = 2l\,(-1)^{1-i}\sin(2l\phi + i\pi/2)$

$$
K_{iljm}^{p} = \int_{0}^{2\pi} \sin(2\phi + p\frac{\pi}{2})\, \Phi'_{il}(\phi)\Phi_{jm}(\phi)\, d\phi = 2l\,(-1)^{p}\,\mathrm{sgn}(m - l)\, J_{iljm}^{p}
$$

where

$$
\mathrm{sgn}(x) = \begin{cases} 1, & \text{for all } x > 0, \\ 0, & \text{for } x = 0 \ \ (\text{sufficient to be finite}), \\ -1, & \text{for all } x < 0. \end{cases}
$$

The result we have achieved so far can be simplified further by a division through the collective factor $\pi\omega_n$ in all operators of (4.11). On the contrary, Kopriva [51] supposes that for general nodal Galerkin approaches in both directions (our approach is only nodal in η) the symmetry of the coefficient matrix would be destroyed when one divides the equation through the quadrature weights. After the division has been performed, we have a similar formulation than in a collocation approach.

Basis Representation for Initial Condition

In (2.85), we have derived the equilibrium state for ψ in two dimensions

$$
\psi_{eq}(\vec{q}) = \frac{b+2}{2\pi b}\left(1 - \frac{|\vec{q}|^{2}}{b}\right)^{\frac{b}{2}}
$$

that we use as an initial condition. First, we convert ψ into the new unknown α, as described in (4.4), and receive

$$
\alpha_{eq}(\eta, \phi) = \frac{b+2}{2\pi b}\left(\frac{1-\eta}{2}\right)^{\frac{b}{2}-s}.
$$

For a discrete approximation of α_{eq}, we have to represent the equilibrium state in the form

$$
\alpha_{N,eq}(\eta, \phi) = \sum_{i=0}^{1}\sum_{l=i}^{N_F}\sum_{k=0}^{N_R} \alpha_{ilk}(0)\Phi_{il}(\phi)h_k(\eta)
$$

with up to now unknown coefficients $\alpha_{ilk}(0)$. We determine the coefficients as

$$
\alpha_{ilk}(0) = \frac{(\alpha_{eq}(\eta, \phi), \Phi_{il}(\phi)h_k(\eta))_\omega}{(\Phi_{il}(\phi)h_k(\eta), \Phi_{il}(\phi)h_k(\eta))_\omega}
$$

$$
= \frac{\int_0^{2\pi} \int_{-1}^{1} \frac{b+2}{2\pi b} (\frac{1}{2} - \frac{1}{2}\eta)^{b/2-s} \Phi_{il}(\phi) h_k(\eta) \omega(\eta) \, d\eta \, d\phi}{\int_0^{2\pi} \int_{-1}^{1} \Phi_{il}^2(\phi) h_k^2(\eta) \, d\eta \, d\phi}
$$

$$
\stackrel{GI}{\approx} \frac{b+2}{2\pi b} \frac{\sum_{r=0}^{N_R} \omega_r (\frac{1}{2} - \frac{1}{2}\eta_r)^{b/2-s} \delta_{rk} \int_0^{2\pi} \Phi_{il}(\phi) \, d\phi}{\sum_{t=0}^{N_R} \omega_t \delta_{tk} \int_0^{2\pi} \Phi_{il}^2(\phi) \, d\phi}
$$

$$
= \frac{b+2}{2\pi b} \left(\frac{1}{2} - \frac{1}{2}\eta_k \right)^{b/2-s} \delta_{i0}\delta_{l0} \tag{4.12}
$$

in which we have used $\int_0^{2\pi} \Phi_{il}(\phi) \, d\phi = 2\pi \delta_{i0}\delta_{l0}$ and $\int_0^{2\pi} \Phi_{il}^2(\phi) \, d\phi = (1 + \delta_{i0}\delta_{l0})\,\pi$. Therefore, the initial condition solely depends on the radial basis functions which was expected since $\alpha(\eta, \phi) = \alpha(\eta)$ is uniform with respect to the angle ϕ.

Computation of the Extra-stress Tensor

In Section 2.3.4, we derive equation (2.81) to compute the additional non-Newtonian stress tensor that takes the form

$$
\boldsymbol{\tau} = \frac{1-\beta}{Wi} \left(\frac{b+4}{b} \right) \left(-\mathbf{Id} + \int_{|\vec{q}|<\sqrt{b}} \vec{q} \otimes \vec{F}(\vec{q}) \psi \, d\vec{q} \right) \tag{4.13}
$$

in two dimensions. With the transformation to η in (4.4) and the radial unit vector $\vec{e_r} = (\cos(\phi), \sin(\phi))$ (with $\vec{q} = r\vec{e_r}$), we rewrite $\vec{q} \otimes \vec{F}(\vec{q})$ as

$$
\vec{q} \otimes \vec{F}(\vec{q}) = \frac{r^2}{1 - \frac{r^2}{b}} \vec{e_r} \otimes \vec{e_r} = b \frac{1+\eta}{1-\eta} \vec{e_r} \otimes \vec{e_r}.
$$

We formulate the integral in (4.13) for a general Jacobi-weight function $\omega(\eta) = (1-\eta)^{\alpha_J}(1+\eta)^{\beta_J}$ as this includes the special case of Legendre weight functions we use in Chapter 6.1 (see Theorem 3.2 for further information). Hence we write

$$
\int_{|\vec{q}|<\sqrt{b}} \vec{q} \otimes \vec{F}(\vec{q}) \psi \, d\vec{q} = \int_0^{2\pi} \int_{-1}^{1} \frac{b^2}{2^{s+2}} (1+\eta)^{1-\beta_J} (1-\eta)^{s-1-\alpha_J} \alpha(\eta, \phi) \vec{e_r} \otimes \vec{e_r} \, \omega(\eta) \, d\eta \, d\phi,
$$

insert (4.9), and evaluate the integrals in a similar manner as before (Gaussian quadrature for η and analytical evaluation with respect to ϕ). For τ_{xx}, the first component of $\boldsymbol{\tau}$, we use the identity $\int_0^{2\pi} \cos^2(\phi) \cos(2l\phi - i\frac{\pi}{2}) \, d\phi = \pi \delta_{i0}\delta_{l0} + \frac{\pi}{2}\delta_{i0}\delta_{l1}$ and may write τ_{xx} as

$$
\tau_{xx}(t) = \frac{1-\beta}{Wi} \left(\frac{b+4}{b} \right) \left(-1 + \frac{\pi b^2}{2^{s+3}} \sum_{k=0}^{N_R} \omega_k (1+\eta_k)^{1-\beta_J} (1-\eta_k)^{s-1-\alpha_J} \{2\alpha_{0,0,k}(t) + \alpha_{0,1,k}(t)\} \right)
$$

$$
\tag{4.14}
$$

with $\{\omega_k\}_{k=0,\dots,N_R}$ as the corresponding weights to $\omega(\eta)$. Analogously, we calculate the other stress tensor components as

$$\tau_{xy}(t) = \tau_{yx}(t) = \frac{1-\beta}{Wi}\left(\frac{b+4}{b}\right)\frac{\pi b^2}{2^{s+3}}\sum_{k=0}^{N_R}\omega_k(1+\eta_k)^{1-\beta_J}(1-\eta_k)^{s-1-\alpha_J}\alpha_{1,1,k}(t) \quad \text{and}$$

$$\tau_{yy}(t) = \frac{1-\beta}{Wi}\left(\frac{b+4}{b}\right)\left(-1+\frac{\pi b^2}{2^{s+3}}\sum_{k=0}^{N_R}\omega_k(1+\eta_k)^{1-\beta_J}(1-\eta_k)^{s-1-\alpha_J}\left\{2\alpha_{0,0,k}(t)-\alpha_{0,1,k}(t)\right\}\right).$$
$$(4.15)$$

At last, to integrate ψ over the whole configuration space, we obtain

$$\int_{|\vec{q}|<\sqrt{b}}\psi\,d\vec{q} \approx \frac{\pi b}{2^{s+1}}\sum_{k=0}^{N_R}\omega_k(1+\eta_k)^{-\beta_J}(1-\eta_k)^{s-\alpha_J}\alpha_{0,0,k}(t). \qquad (4.16)$$

We compute (4.16) because of its relevance as an error indicator. Due to the fact that we have a probability measure, the integral of ψ over the domain should be one at all times. Actually, Lozinski et al. prove in [59] the conservation property of the spectral method for ψ provided the parameter s is an integer from 0 to N_R.

Time Discretisation for Fokker-Planck Scheme

We now concentrate on the discretisation of the ODE system

$$\frac{\partial\vec{\alpha}_N}{\partial t} = \left(\boldsymbol{L_0} + \kappa_{11}\boldsymbol{L_1} + \kappa_{12}\boldsymbol{L_2} + \kappa_{21}\boldsymbol{L_3}\right)\vec{\alpha}_N \qquad (4.17)$$

with $\vec{\alpha}_N = \{\alpha_{ilk}(t)\}$ as the vector of unknowns which determine $\alpha_N(t,\eta,\phi)$ in (4.9) and $\boldsymbol{L_i}$ as the matrix representation of the differential operator L_i, $i=0,1,2,3$. In Algorithm 1 we present an explicit low-storage Runge-Kutta scheme and therefore now focus on an alternative implicit Crank-Nicolson method in Algorithm 2. The implicit method requires the solution of a linear system of equations in every time-step which we solve with an iterative CG solver in the notation of Meister [61]. Nevertheless, we have also used an explicit Runge-Kutta method in this case and refer to Algorithm 1 for any specific differences. Note that for postprocessing purposes we have to retransform $\vec{\alpha}_N \to \vec{\psi}_N$ with the inverse of (4.4) and evaluate (4.9).

4.1.3 3D Fokker-Planck Equation on the Sphere

In literature most multiscale, non-Newtonian flow problems base on two-dimensional planar flows. Nevertheless, even for the two-dimensional Navier-Stokes equations, there is no necessity for the configuration vector $\vec{q}$ to be also restricted to two dimensions although the difference between the two- and three-dimensional results is rather small in that situation. Additionally, for a three-dimensional flow field the usage of a 3d Fokker-Planck equation is required.

In the following, we describe a natural extension for the approximation space to three dimensions and the theoretical advantages of spherical harmonics for the underlying problem. However, we do not discuss a derivation of a discretised operator and refer to Lozinski [56]

Algorithm 2: Implicit Crank-Nicolson scheme for the solution of the Fokker-Planck equation. The implicit method requires the solution of a linear system of equations in every time-step which we solve with an iterative CG solver in the notation of Meister [61]. In every step we expect the iterative solver to require a low number of iterations, because we use the previous solution $\vec{\alpha}_N^{(n)}$ as an initial guess for the new unknown.

Data: Vector of quadrature points $\{\eta_r\}$, quadrature weights ω_r, derivative matrices $\boldsymbol{L_i}$, tolerance ϵ and three-dimensional coefficient matrix for α_N.

Result: Discrete approximation of pdf ψ and extra-stress tensor values.

Set $n = 0$;

Compute quadrature points $\{\eta_r\}$ and corresponding weights ω_r;

Calculate coefficients $\alpha_{ilk}(0)$ of initial condition with (4.12) $\rightarrow \vec{\alpha}_N^{(0)}$;

Compute barycentric weights for Lagrange interpolation as in (3.22);

Precompute and save derivative matrices $h_k'(\eta_n)$ and $h_k''(\eta_n)$ for later usage;

while $n \leq n_{end}$ **do**

    $\vec{\alpha}_{N,0}^{(n)} \leftarrow \vec{\alpha}_N^{(n)}$ // additional index counts CG iterations

    $\boldsymbol{A} \leftarrow (1 - \frac{1}{2}\Delta t\,(\boldsymbol{L_0} + \kappa_{11}\boldsymbol{L_1} + \kappa_{12}\boldsymbol{L_2} + \kappa_{21}\boldsymbol{L_3}))$;

    $\vec{b} \leftarrow (1 + \frac{1}{2}\Delta t\,(\boldsymbol{L_0} + \kappa_{11}\boldsymbol{L_1} + \kappa_{12}\boldsymbol{L_2} + \kappa_{21}\boldsymbol{L_3}))\,\vec{\alpha}_{N,0}^{(n)}$;

    $\vec{p}_0 \leftarrow \vec{b} - \boldsymbol{A}\vec{\alpha}_{N,0}^{(n)}, \quad \vec{r}_0 \leftarrow \vec{b} - \boldsymbol{A}\vec{\alpha}_{N,0}^{(n)}$;

    $\beta_0 \leftarrow \|\vec{r}_0\|_2^2$;

    for $m = 0, 1, \ldots, itermax$ and $\beta_m > \epsilon$ **do**

        $\vec{v}_m \leftarrow \boldsymbol{A}\vec{p}_m$;

        $\lambda_m \leftarrow \frac{\beta_m}{(\vec{v}_m, \vec{p}_m)_2}$;

        $\vec{\alpha}_{N,(m+1)}^{(n)} \leftarrow \vec{\alpha}_{N,(m)}^{(n)} + \lambda_m\vec{p}_m$;

        $\vec{r}_{m+1} \leftarrow \vec{r}_m - \lambda_m\vec{v}_m$;

        $\beta_{m+1} \leftarrow \|\vec{r}_{m+1}\|_2^2$;

        $\vec{p} \leftarrow \vec{r}_{m+1} + \frac{\beta_{m+1}}{\beta_m}\vec{p}_m$;

    end

    $\vec{\alpha}_N^{(n+1)} \leftarrow \vec{\alpha}_{N,(m+1)}^{(n)}$;

    Compute $\boldsymbol{\tau}^{(n+1)}$ with (4.14) and (4.15);

    $t^{(n+1)} = t^{(n)} + \Delta t, n = n + 1$;

end

---

for that. The coordinates of choice for a configuration vector $\vec{q}$ restricted to the interior of a sphere, are spherical coordinates

$$q_1 = r\sin(\theta)\cos(\phi), \quad q_2 = r\sin(\theta)\sin(\phi), \quad q_3 = r\cos(\theta) \tag{4.18}$$

where $r \in [0, \sqrt{b}]$, $\phi \in [0, 2\pi]$ and $\theta \in [0, \pi]$.

Again, as in (3.7) we consider the Laplace problem of a scalar-valued function $f : \mathbb{R}^3 \to \mathbb{R}$

$$\frac{1}{r}\frac{\partial}{\partial r}\left(r^2\frac{\partial}{\partial r}\right) + \frac{1}{r^2\sin(\phi)}\frac{\partial}{\partial \phi}\left(\sin(\phi)\frac{\partial}{\partial \phi}\right) + \frac{1}{r^2\sin^2(\phi)}\frac{\partial^2}{\partial \theta^2} = 0 \qquad (4.19)$$

but limit our interest to the surface of the sphere (i.e. $r = 1$) and to functions f without any dependence with respect to r. We are interested in solutions for the eigenvalue problem

$$\Delta_{r=1}\Omega(\phi,\theta) = -n(n+1)\Omega(\phi,\theta)$$

for $n \in \mathbb{N}$, $\Omega : S^2 \to \mathbb{R}$ and $\Delta_{r=1}$ as the surface Laplace operator. It turns out that for a given n the eigenvalue problem has $(2n+1)$ independent solutions $m = -n, \ldots, n$ which we write in a real-valued form

$$\Omega_{nm}(\phi,\theta) = \begin{cases} P_{nm}(\cos(\theta))\cos(m\phi), & m \geqslant 0, \\ P_{n|m|}(\cos(\theta))\sin(|m|\phi), & m < 0 \end{cases} \qquad (4.20)$$

as in Weisstein [94]. Thereby, we term the normalised associated Legendre functions with $P_{nm}(\cos(\theta))$ which are further explained in Fornberg [32]. The solutions in the presented form are called real spherical harmonics and our interest lies in emphasising their importance for the pole problem (cf. Chapter 3.1 for a discussion of the pole problem). Therefore, we rewrite the associated Legendre functions P_{nm} in the form

$$P_{nm}(\cos(\theta)) = (-1)^m \sin^m(\theta)\frac{d^m L_n(\cos(\theta))}{d(\cos(\theta))^m} \qquad (4.21)$$

and interpret them as derivative of order m of the Legendre polynomial L_n with an additional factor $\sin^m(\theta)$. Considering that $\theta \in [0,\pi]$, the prefactor implies an m-th order zero of the spherical harmonic Ω_{mn} at the poles. The harmonics circumvent the pole problem because of the high-order zero in $\theta = 0$ and $\theta = \pi$ as its degree m is coupled to the wavenumber $\cos(m\phi)$ or $\sin(m\phi)$ in longitude ϕ (cf. equation (4.20)). The basis functions of high-order m would normally lead to a fine discretisation of the angle ϕ at latitudes close to the pole (cf. Figure 3.1). For this reason, we want to dampen the amplitude of the harmonics far away from the equator which is just the effect of the coefficient $\sin^m(\theta)$ in (4.21). In Figure 4.3, we illustrate the effect of damping for an increasing order of m so that these harmonics have low amplitudes outside an area around the equator.

For $(N_F, N_R) \in \mathbb{N}^2$, an appropriate choice for a three-dimensional approximation space is

$$V_N = \text{span}\,\{h_k(\eta)\Omega_{nm}(\phi,\theta),\, 0 \leq n \leq N_F,\, m = -n\ldots,n,\, 0 \leq k \leq N_R\} \qquad (4.22)$$

with $h_k(\eta)$ as the Lagrange polynomials based on Gauss-Jacobi points and $\Omega_{nm}(\phi,\theta)$ as real-valued spherical harmonics. According to the pole problem on the sphere this ansatz

- avoids the singularity at the centre of the sphere (i.e. $r = 0$), because quadrature points transformed on $[-1,1]$ thin out there and

- circumvents the singularities at the poles (i.e. $\theta = 0$ and $\theta = \pi$)

and therefore realises a uniform discretisation of the sphere. In conclusion, if we want to
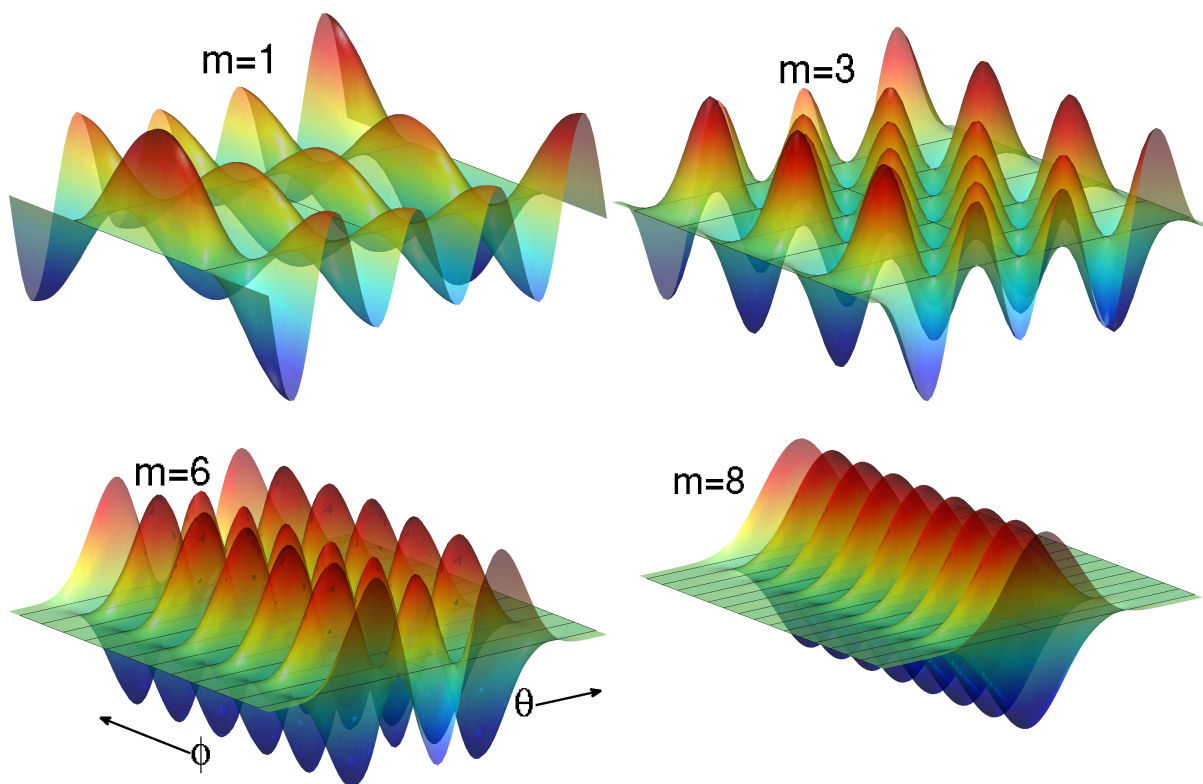
Figure 4.3: Spherical harmonic basis functions $P_{nm}(\cos(\theta))\cos(m\phi)$ for $n = 8$ and $m = 1, 3, 6, 8$. Except for $P_{8,0}(\cos(\theta))$, all harmonics satisfy the zero boundary property at $\theta = 0$ and $\theta = \pi$. Furthermore, for an increasing m, the peaks of the harmonics shift to the area around the equator and ensure an equidistant resolution of the sphere.

discretise an equation of Fokker-Planck type on a sphere, we obtain the best results by the use of spherical harmonic basis functions.

4.2 Stochastic Simulation Techniques for Homogeneous Flows

4.2.1 Time Integration Schemes

In this chapter, we consider the stochastic partial differential equation (SPDE)

$$d\vec{Q}_t = \left(\boldsymbol{\kappa}\,\vec{Q}_t - \frac{1}{2\,Wi}\vec{F}(\vec{Q}_t) \right) dt + \sqrt{\frac{1}{Wi}}\,d\vec{W}_t \qquad (4.23)$$

in its non-dimensional formulation which we obtain in (2.68) for the description of a homogeneous flow field. Obviously, the three-dimensional stochastic process $\vec{Q}_t = (Q_{t,x}, Q_{t,y}, Q_{t,z})$ represents the dumbbell orientations in the x-, y- and z-directions at time $t \in T = [0, t_{\max}]$. As mentioned above, the velocity gradient tensor $\vec{\nabla}_x \vec{u}$ in a homogeneous flow field is constant throughout Ω (physical space) which we denote by the symbol $\boldsymbol{\kappa} \equiv \vec{\nabla}_x \vec{u}$.

For an introduction to the fundamental concepts of stochastic differential equations and adequate numerical integration schemes we refer to Chapter 3.3.

Euler-Maruyama Method

Subdividing the observation time $T = [0, t_{\max}]$ into n subintervals $[t_{r-1}, t_r)$ with $t_{r-1}, t_r \in \{t_0 = 0, t_1, \ldots, t_n = t_{\max}\}$ and applying the Euler-Maruyama scheme (3.30) to the SPDE (4.23) yields a discrete approximation of the stochastic process

$$\vec{Q}_{t_r} = \vec{Q}_{t_{r-1}} + \left(\boldsymbol{\kappa}\,\vec{Q}_{t_{r-1}} - \frac{1}{2\,Wi}\vec{F}(\vec{Q}_{t_{r-1}}) \right) \Delta t_{r-1} + \sqrt{\frac{1}{Wi}}\,\Delta\vec{W}_{t_{r-1}}, \quad \text{for } r = 1, \ldots, n \quad (4.24)$$

with $\Delta\vec{W}_{t_{r-1}} = \vec{W}_{t_r} - \vec{W}_{t_{r-1}} = \sqrt{\Delta t_{r-1}}\,\vec{N}(0,1)$. Here, we denote $\vec{N}(0,1)$ as a sequence of three independent Gaussian random variables with zero mean and variance one. Accordingly, the product $\sqrt{\Delta t_{r-1}}\,\vec{N}(0,1)$ characterises Gaussian random variables with zero mean and variance Δt_{r-1}.

Additionally, we give a componentwise description of (4.24) in a Cartesian system of reference and use, for example, a dimensionless FENE spring force $\vec{F}(\vec{Q}) = \frac{\vec{Q}}{1 - \frac{\|\vec{Q}\|^2}{b}}$ as in (2.66). Then we obtain

$$\begin{pmatrix} Q_{t_r,x} \\ Q_{t_r,y} \\ Q_{t_r,z} \end{pmatrix} = \begin{pmatrix} Q_{t_{r-1},x} \\ Q_{t_{r-1},y} \\ Q_{t_{r-1},z} \end{pmatrix} + \Delta t_{r-1} \begin{pmatrix} \kappa_{11}Q_{t_{r-1},x} & \kappa_{12}Q_{t_{r-1},y} & \kappa_{13}Q_{t_{r-1},z} \\ \kappa_{21}Q_{t_{r-1},x} & \kappa_{22}Q_{t_{r-1},y} & \kappa_{23}Q_{t_{r-1},z} \\ \kappa_{31}Q_{t_{r-1},x} & \kappa_{32}Q_{t_{r-1},y} & \kappa_{33}Q_{t_{r-1},z} \end{pmatrix}$$

$$- \Delta t_{r-1} \frac{1}{1 - \frac{\|\vec{Q}_{t_r}\|^2}{b}} \begin{pmatrix} Q_{t_r,x} \\ Q_{t_r,y} \\ Q_{t_r,z} \end{pmatrix} + \sqrt{\frac{\Delta t_{r-1}}{Wi}} \begin{pmatrix} r_x \\ r_y \\ r_z \end{pmatrix}$$

for $r = 1, \ldots, n$ and random numbers r_x, r_y, and $r_z \sim N(0,1)$.

Predictor-corrector Method

A predictor-corrector method for a given process time t_{r-1} is a two-step scheme which

- first calculates an intermediate stochastic process $\vec{P}_{t_r}$ by extrapolating $\vec{Q}_{t_{r-1}}$ to the next discrete time-step t_r and then

- uses the additional information from $\vec{P}_{t_r}$ to obtain a numerical approximation to $\vec{Q}_t$ at $t = t_r$.

Using the same notation as before in combination with the predictor-corrector scheme as described in (3.31), we get the algorithm

$$\vec{P}_{t_r} = \vec{Q}_{t_{r-1}} + \left(\boldsymbol{\kappa}\, \vec{Q}_{t_{r-1}} - \frac{1}{2\,Wi} \vec{F}(\vec{Q}_{t_{r-1}}) \right) \Delta t_{r-1} + \sqrt{\frac{1}{Wi}}\, \Delta \vec{W}_{t_{r-1}}, \quad \text{for } r = 1, \dots, n$$

$$\text{(4.25)}$$

$$\vec{Q}_{t_r} = \vec{Q}_{t_{r-1}} + \frac{1}{2} \left(\boldsymbol{\kappa}\, \left(\vec{Q}_{t_{r-1}} + \vec{P}_{t_r} \right) - \frac{1}{2\,Wi} \underbrace{\left(\vec{F}(\vec{Q}_{t_{r-1}}) + \vec{F}(\vec{P}_{t_r}) \right)}_{\text{in general nonlinear}} \right) \Delta t_{r-1} + \sqrt{\frac{1}{Wi}}\, \Delta \vec{W}_{t_{r-1}}.$$

We note that both steps of (4.25) share the same vector increment $\Delta \vec{W}_{t_{r-1}}$, i.e. they use the same realisation of the Wiener process $\vec{W}_t$ at $t = t_{r-1}$. During the analysis of the predictor-corrector ansatz in Chapter 3.3 we have stated that we expect a weak convergence order 2 if the diffusion term does not depend on the stochastic process $\vec{Q}_t$ itself. Indeed, the prefactor $\sqrt{\frac{1}{Wi}}$ fulfils this requirement so that we expect a higher (weak) order of convergence as for the Euler-Maruyama method.

Polymeric Stress Tensor

However, the numerical integration schemes model only one trajectory or path of the stochastic process $\vec{Q}$ for one realisation of the Wiener process, i.e. for the corresponding probability space (D, Σ, ψ) we describe the evolution $t \to \vec{Q}_t(\omega)$ for a fixed outcome $\omega \in D$ (configuration space) with respect to one realisation of $\vec{W}_t$. In other words, we investigate the time-dependent development of one possible dumbbell orientation. Actually, we are interested in describing the evolution of $\vec{Q}$ which determines the complete system.

Accordingly, we have to generate a set of N_f independent outcomes $\vec{Q}_t^{(s)}$, $s = 1, \dots, N_f$ and use scheme (4.24) or (4.25) to develop their individual trajectories. Therefore, each $\vec{Q}_t^{(s)}$ experiences its own independent Brownian motion $\vec{W}_t^{(s)}$. We characterise the trajectories in time by the sequence $(\vec{Q}_{t_0}^{(s)}, \vec{Q}_{t_1}^{(s)}, \dots, \vec{Q}_{t_r}^{(s)})$. At process time $t = t_r$, we compute the current stress tensor $\boldsymbol{\tau_p}$ by taking an ensemble average (i.e. performing a Monte Carlo integration) over the N_f realisations of the stochastic process $\vec{Q}_{t_r}$. For instance, the stress tensor for dumbbells with a FENE spring force (cf. equation (2.81)) can be approximated by

$$\boldsymbol{\tau_p}(\vec{Q}, t_r) = \frac{(1 - \beta)}{Wi} \left(\frac{b + d + 2}{b} \right) \left(\left\langle \vec{Q}_{t_r} \otimes \frac{\vec{Q}_{t_r}}{1 - \frac{\|\vec{Q}_{t_r}\|^2}{b}} \right\rangle - \mathbf{Id} \right) \tag{4.26}$$

$$\approx \frac{(1-\beta)}{Wi} \left(\frac{b+d+2}{b} \right) \left(\frac{1}{N_f} \sum_{s=1}^{N_f} \frac{\vec{Q}_{t_r}^{(s)} \otimes \vec{Q}_{t_r}^{(s)}}{1 - \frac{\|\vec{Q}_{t_r}^{(s)}\|^2}{b}} - \mathbf{Id} \right) \tag{4.27}$$

The arithmetic mean in (4.27) converges in probability to the average in (4.26) for $N_f \to \infty$ if the stochastic processes $\vec{Q}^{(s)}, s = 1, \dots, N_f$ are independent among each other. This is a consequence from the strong law of large numbers which guarantees an almost surely convergence. On the contrary, the disadvantage of the stochastic method lies in the variance of the computed result and the low order of convergence. Therefore, variance reduction methods become important which we will discuss at the end of this chapter.

4.2.2 Equilibrium Configurations

Since problem (4.23) is time-dependent, we require initial conditions $\vec{Q}_0^{(s)} \equiv \vec{Q}_{t_0}^{(s)}$ for realisations of the stochastic process. In Chapter 2.3.5, we have analysed the equilibrium solution ψ_{eq} for the Fokker-Planck equation ψ. The equilibrium solution represents a fully relaxed dumbbell system (i.e. $\boldsymbol{\tau_p} = 0$) and takes the form

$$\psi_{eq} = C_1 \exp\left(-\frac{\|\vec{q}\|^2}{2} \right) \tag{4.28}$$

for Hookean spring forces,

$$\psi_{eq} = C_2 \left(1 - \frac{\|\vec{q}\|^2}{b} \right)^{b/2} \tag{4.29}$$

for FENE dumbbells and

$$\psi_{eq} = C_3 \left(\frac{b+d}{b} \right)^{d/2} \exp\left(-\frac{b+d}{2b} \|\vec{q}\|^2 \right) \tag{4.30}$$

for the FENE-P model with normalisation constants C_1, C_2 and C_3.

Due to the correspondence between the Fokker-Planck equation on the one hand and its stochastic interpretation on the other hand, we have to generate equilibrium approximations $\vec{Q}_0^{(s)}$ whose distributions belong to the probability density ψ_{eq} as in (4.28), (4.29) or (4.30).

For Gaussian equilibrium distributions as in (4.28) and (4.30), there exist various random number generators. For illustration, in Figure 4.4 we present a two-dimensional Gaussian distribution that corresponds to a Hookean equilibrium distribution ψ_{eq}^{Hooke} from (4.28). Here we have used a kernel density estimator (i.e. an estimator for the probability density function of a random variable) from Botev [14] that assumes the density function to be Gaussian.

Von Neumann Rejection Sampling

The problem in generating random numbers for (4.29) is that the equilibrium distribution is not Gaussian. As a result, a pre-implemented random number generator from a library normally cannot create numbers that distribute according to this density function. In this case, the method of choice is the rejection sampling or acceptance-rejection method proposed by von
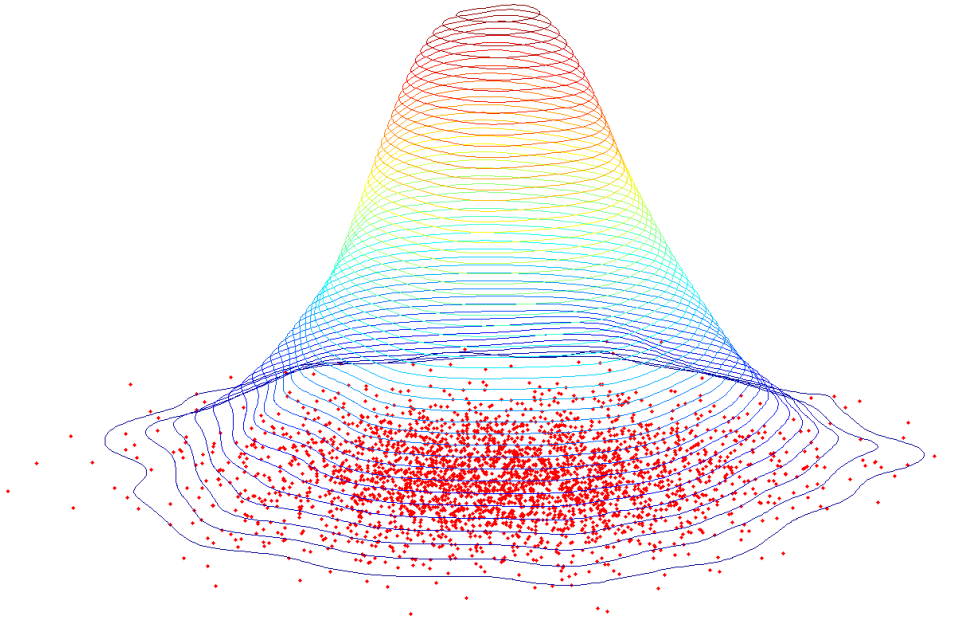
Figure 4.4: The figure illustrates a sequence of 3000 two-dimensional normal random numbers whose corresponding density function has been reconstructed by a kernel density estimator. Note that the reconstructed function has been smoothed so that it takes a regular shape.

Neumann [91]. Subsequently, we give an introduction of the method and refer to Section 7.3.6 of Numerical Recipes [73] for more information.

The main idea of the method bases on a geometrical argument that we present in one dimension. Let $\psi(x)$ be a given probability density with $x \in [a, b]$ or $x \in (-\infty, \infty)$ so that there exists no direct method to create corresponding random numbers (e.g. the inverse transform method necessitates the cumulative distribution function and its inverse to be implemented which we do not know in general). We draw the graph of $\psi(x)$ in a coordinate system so that by definition the integral $\int_c^d \psi(x)\,dx$ (i.e. the area below the graph) represents the probability of generating a random number in the interval $[c, d] \subset [a, b]$ (cf. Figure 4.5). If we consider the whole graph in two dimensions $(x, \psi(x))$ and find a method to fill the area under the graph with points $(x_s, y_s), s \in \mathbb{N}$ uniformly, then the x-value of these point x_s would belong to the desired distribution ψ, i.e. we have found a correct sequence of random numbers.

Now, we add a further graph $(x, f(x))$ to the figure with an almost arbitrary probability density function $f(x)$ and denote $f(x)$ as comparison function. The only restriction to $f(x)$ is that

- it fulfils $\psi(x) \leq f(x)$ for all $x \in [a, b]$ and

- we have the possibility to generate random numbers for $f(x)$.

If we generate random numbers x_s that belong to $f(x)$ and choose an arbitrary $y_s \in [0, f(x_s)]$ as y-coordinate in Figure 4.5, we fill the area under $(x, f(x))$ randomly. The rejection sampling method then

- accepts those points (x_s, y_s) which also lie in the area below the graph $(x, \psi(x))$ and
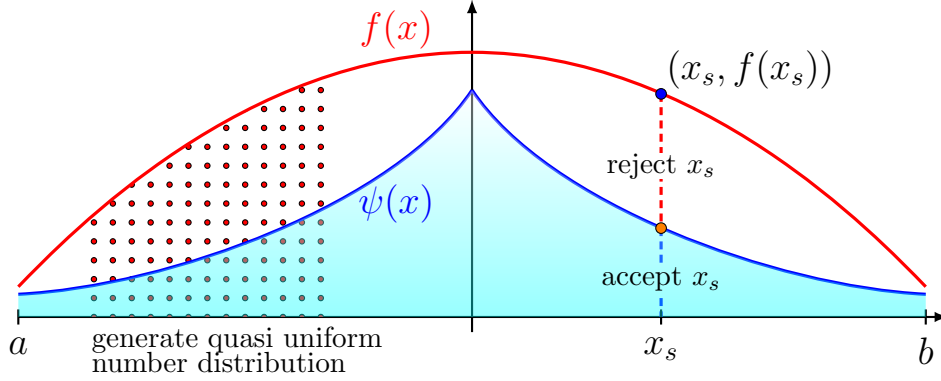
Figure 4.5: The von Neumann rejection sampling generates random numbers x_s according to a comparison function f. If we choose an arbitrary but uniform y-coordinate $y_s \in [0, f(x_s)]$, we receive a random but quasi uniform sampling of the area below the graph $(x, f(x))$. We illustrate this on the left hand side of the figure. Now, we accept only those numbers that also lie below the graph $(x, \psi(x))$.

- rejects the other ones.

As a result, we implement the von Neumann rejection method in the form of Algorithm 3. However, the first requirement $\psi(x) \leq f(x)$ for all $x \in [a, b]$ cannot be fulfilled by any probability density function f. Indeed, as probability density functions have to satisfy $\int \psi \, dx = \int f \, dx = 1$ there exists an $x_s \in [a, b]$ with $\psi(x_s) > f(x_s)$. For this reason, Algorithm 3 includes a real constant $M > 1$ so that $\psi(x) \leq M f(x)$ for all x.

The parameter choice for M correlates with the efficiency of the algorithm, because we can show that the percentage of accepted random numbers x_s from $f(x)$ for $\psi(x)$ is exactly $1/M$. Therefore, the optimal choice M_{opt} for M is

$$M_{\text{opt}} = \max_{x \in [a,b]} \frac{\psi(x)}{f(x)} > 1.$$

The parameter is optimal in the sense that the number of rejected sampling points is minimised for a given function f. We note that $M_{\text{opt}} = 1$ implies $\psi = f$ and we do not receive additional information in that case. Nevertheless, the comparison function f has to be similar to ψ as this reduces the value of M_{opt} and therefore our computational effort.

Unfortunately, the algorithm suffers from the curse of dimensionality, because high-dimensional functions f concentrate their sampling points at the "corner regions". If a high-dimensional f approximates ψ, the percentage of accepted sample points tends to zero for increasing dimensions of the underlying space. However, for homogeneous flow problems and an initial process time $t = 0$ we have $\psi_{eq}(\cdot, 0) : \mathbb{R}^3 \to \mathbb{R}^+$ and therefore notice no severe restriction from the mentioned problem.

Subsequently, we apply Algorithm 3 to the case of three-dimensional FENE distributions. In this case we use $\psi_{eq}(\cdot, 0) : B_{\sqrt{b}}(0) \to \mathbb{R}^+$ from (4.29) as initial density function, because the configuration space is restricted to a sphere with radius $\sqrt{b}$. Furthermore, we decide for $U : B_{\sqrt{b}}(0) \to \mathbb{R}^+$ as comparison function f. The character "U" signalises that this is a uniform

---

Algorithm 3: The von Neumann rejection sampling generates random numbers that belong to a given density function $\psi(x)$ if a suitable comparison function $f(x)$ can be found. It uses a Monte Carlo technique to filter random numbers of $f(x)$ that also belong to $\psi(x)$. However, the efficiency of the algorithm depends on the similarity between $\psi(x)$ and $f(x)$. The better $f(x)$ matches $\psi(x)$, the more realisations are accepted.

Data: Density function $\psi(x)$, comparison function $f(x)$, random number generator for
$\quad\quad f(x)$, and a generator $U(0,1)$ for uniform distributed numbers in $[0,1]$
Result: Sequence of random numbers for $\psi(x)$
Find real constant $M > 1$ with $\psi(x) \leq M f(x)$ for all x;
$s \leftarrow 1$;
while $s \leq N_f$ **do**
$\quad$ Sample random number x_s from $f(x)$;
$\quad$ Generate random number $u \in U(0,1)$;
$\quad$ **if** $(uMf(x_s)) \leq \psi(x_s)$ **then**
$\quad\quad$ Accept x_s as an realisation of $\psi(x)$;
$\quad\quad$ $s \leftarrow s + 1$;
$\quad$ **else**
$\quad\quad$ Reject the value x_s;
$\quad$ **end**
end

---

density function on the sphere with constant density $U(\vec{q}) = 3/(4\pi b^{\frac{3}{2}})$ for all orientations $\vec{q}$. As ψ_{eq} has its maximum at the origin and U is constant everywhere, we calculate the optimal constant M_{opt} for the estimation as

$$M_{\text{opt}}^{\text{FENE}} = \frac{\psi(0)}{U(0)} = \frac{2}{3\,B(\frac{3}{2}, \frac{b+2}{2})} \tag{4.31}$$

with $B(x, y)$ the Eulerian beta function. Here we have used that the constant C_2 for the equilibrium density (4.29) in three dimensions takes the form

$$C_2 = 2\pi b^{\frac{3}{2}}\, B\left(\frac{3}{2}, \frac{b+2}{2}\right).$$

Altogether, we present Algorithm 4 to generate a three-dimensional FENE equilibrium configuration $\vec{Q}_0^j$ distributed according to ψ_{eq}^{FENE}.

At last, we note that Algorithm 4 describes the problem in Cartesian coordinates. We have chosen this coordinate system to avoid the occurrence of inhomogeneities which might appear in spherical coordinate systems and might lead to a non-uniform distribution that we necessitate for the comparison function U (cf. pole problem on the sphere in Chapter 3.1). Nevertheless, another approach that uses the von Neumann rejection method and spherical coordinates is presented in the thesis of Bonvin [12].

Algorithm 4: The algorithm samples N_f initial configurations $\vec{Q}_0^{(s)}$ for the SPDEs (4.24) and (4.25). Note that we evaluate the probability density function ψ_{eq}^{FENE} in Cartesian coordinates, because this coordinate system guarantees a uniform point distribution which we require on $B_{\sqrt{b}}(0)$ (cf. pole problem in Chapter 3.1).

Data: Generator $U(0,1)$ for uniform distributed numbers in $[0,1]$
Result: Sequence of initial processes $\vec{Q}_0^{(1)}, \ldots, \vec{Q}_0^{(N_f)}$ according to ψ_{eq}^{FENE}
$s \leftarrow 1$;
$\text{updf} \leftarrow 3/(4\pi b^{\frac{3}{2}})$ // uniform density on $B_{\sqrt{b}}(0)$
$M_{\text{opt}} \leftarrow 2/(3\,B(\frac{3}{2},\frac{b+2}{2}))$ // compare with (4.31)
while $s \leq N_f$ **do**
    Generate random numbers q_1, q_2, and $q_3 \in U(0,1)$;
    $q_i \leftarrow \sqrt{b}(2q_i - 1)$ for $i = 1, 2, 3$ // Transform numbers $[0,1]^3 \to [-\sqrt{b}, \sqrt{b}]^3$
    // Restrict $[-\sqrt{b}, \sqrt{b}]^3$ to $B_{\sqrt{b}}(0)$
    if $q_1^2 + q_2^2 + q_3^2 \leq b$ **then**
        Generate random number $u \in U(0,1)$;
        if $(u \cdot M_{opt} \cdot updf) \leq \psi_{eq}(q_1, q_2, q_3)$ **then**
            $\vec{Q}_0^{(s)} \leftarrow (q_1, q_2, q_3)$;
            $s \leftarrow s + 1$;
        end
    end
end

4.2.3 Variance Reduction Schemes

The basic concept of a variance reduction scheme is to reduce the statistical error or variance of a stochastic simulation without increasing the computational effort, i.e. the number of simulated trajectories N_f. In every time step t, we compute the stress tensor $\boldsymbol{\tau}(t)$ by evaluating an expectation of the form

$$\left\langle \vec{X}_t \right\rangle \equiv \left\langle \vec{Q}_t \otimes \vec{F}\left(\vec{Q}_t\right) \right\rangle \approx \frac{1}{N_f} \sum_{s=1}^{N_f} \vec{Q}_t^{(s)} \otimes \vec{F}\left(\vec{Q}_t^{(s)}\right) \tag{4.32}$$

with Monte Carlo methods. On the contrary, let $\text{Var}(\vec{X}_t) = \langle \vec{X}_t^2 \rangle - \langle \vec{X}_t \rangle^2$ denote the variance of $\vec{X}$ then the statistical error for N_f samples is reduced by a factor of $\sqrt{N_f/N_{f_2}}$ in comparison to N_{f_2} (for $N_{f_2} < N_f$) realisations. Consequently, the computational effort increases enormously if high numerical accuracy is intended. Accordingly, this emphasises the importance of variance reduction. Subsequently, we present the basic principles of variance reduction in a similar manner as Bonvin [12] and Lozinski et al. [59].

As far as we know, two variance reduction methods are primarily used for the simulation of polymer dynamics which are importance sampling and the idea of control variates.

Importance Sampling

Importance sampling is a widely used method in the context of equilibrium statistical mechanics which can also be applied to non-equilibrium problems. The method investigates the importance of different trajectories for the accuracy of the expectation (4.32). As the equilibrium densities (4.28) to (4.30) have their maximum at the origin, most configurations are generated there (cf. with Figure 4.4). However, these configurations contribute only marginal information to the calculation of the average. On the other hand, realisations that are arranged far away from the origin have a significant influence on the result. If few realisations are considered (i.e. N_f is small), these realisations lead to a high statistical error. The method avoids this by giving those realisations a greater weight that have a more significant influence to the result of the expectation. For a more detailed description of the approach in the context of polymeric fluids, we refer to two articles from Melchior et al. [62, 63].

Control Variates

The control variate method reduces the variance of a stochastic process $\vec{X}_t$ by introducing a "control" process $\vec{Y}_t$. Instead of computing $\langle \vec{X}_t \rangle$ directly, we decompose the calculation according to

$$\underbrace{\left\langle \vec{X}_t \right\rangle}_{\text{stochastic}} = \underbrace{\left\langle \vec{X}_t - \vec{Y}_t \right\rangle}_{\text{stochastic}} + \underbrace{\left\langle \vec{Y}_t \right\rangle}_{\text{deterministic}}. \qquad (4.33)$$

The idea is to choose a process $\vec{Y}_t$ whose expectation can be computed deterministically so that the variance of $\vec{Y}_t$ is zero. Furthermore, we want the RHS of (4.33) to exhibit a reduced variance in comparison to $\langle \vec{X}_t \rangle$, i.e.

$$\text{Var}(\vec{X}_t) \geq \text{Var}(\vec{X}_t - \vec{Y}_t) = \text{Var}(\vec{X}_t) + \text{Var}(\vec{Y}_t) - 2\text{Cov}(\vec{X}_t, \vec{Y}_t) \qquad (4.34)$$

with $\text{Cov}(\vec{X}_t, \vec{Y}_t)$ the covariance of $\vec{X}_t$ and $\vec{Y}_t$. Therefore, the variance is only reduced if both processes are strongly correlated. We achieve this correlation by applying the same stochastic noise (i.e. the same random numbers) on $\vec{X}_t$ and $\vec{Y}_t$.

We consecutively describe how to create a control variate for the stochastic processes (4.23). The same ansatz can also be used for the SPDE (2.67) of a general non-homogeneous flow field which possesses an additional convective term and a dependency of $\vec{Q}_t$ from the position $\vec{x}$ in physical space (i.e. for a coupled Navier-Stokes-Stochastic system). We denote all variables that belong to the control variate with a subscript "c" to distinguish them from the original processes. Hence, the underlying equation (4.23) becomes

$$d\vec{Q}_{t,c} = \left(\boldsymbol{\kappa}_c \, \vec{Q}_{t,c} - \frac{1}{2\,Wi}\vec{F}_c(\vec{Q}_{t,c}) \right) dt + \sqrt{\frac{1}{Wi}}\, d\vec{W}_t \qquad (4.35)$$

with $\vec{Q}_{t,c}$ as control variate. Comparing (4.35) with the original equation, we conclude that we can on the one hand use a more simple spring force $\vec{F}_c(\vec{Q}_{t,c})$ or on the other hand describe a more simple flow field $\vec{u}_c$ to be able to determine $\left\langle \vec{Q}_{t,c} \otimes \vec{F}_c(\vec{Q}_{t,c}) \right\rangle$ deterministically. Applying scheme (4.33) on the equation for calculating the stress tensor and neglecting any coefficients

yields

$$\boldsymbol{\tau_p} \approx \left\langle \vec{Q}_t \otimes \vec{F}(\vec{Q}_t) - \vec{Q}_{t,c} \otimes \vec{F}_c(\vec{Q}_{t,c}) \right\rangle + \left\langle \vec{Q}_{t,c} \otimes \vec{F}_c(\vec{Q}_{t,c}) \right\rangle \tag{4.36}$$

for all $t \in T$. Obviously, the closer the velocity field $\vec{u}_c$ approximates $\vec{u}$ and the spring force $\vec{F}_c(\vec{Q}_{t,c})$ approximates $\vec{F}_c(\vec{Q}_{t,c})$, the better reduction rates can be achieved.

We describe two examples of control variates which are

1. the equilibrium control variate and

2. the Hookean control variate.

In Section 6.2.3, we investigate the variance reduction of an equilibrium variate for a homogeneous extensional flow. The method of Hookean control variates could be ideally used in combination with the three-dimensional NaSt3DGPF solver [2] that we use at the Institute for Numerical Simulation (cf. Chapter 5) as the solver features a method to compute the Hookean stress tensor deterministically (i.e. an implementation of the macroscopic Oldroyd-B model).

Equilibrium Control Variate

We obtain an **equilibrium control variate** for the choice

- $\vec{u}_c = 0$ (i.e. $\boldsymbol{\kappa}_c = \vec{\nabla}_x \vec{u}_c$ is also zero) and

- $\vec{F}_c(\vec{Q}_{t,c}) = \vec{F}(\vec{Q}_{t,c})$ (i.e. reuse the original spring force).

Then, the SPDE (4.35) simplifies to

$$d\vec{Q}_{t,c} = -\frac{1}{2\,Wi}\vec{F}_c(\vec{Q}_{t,c})dt + \sqrt{\frac{1}{Wi}}\,d\vec{W}_t. \tag{4.37}$$

This stochastic equation does not change the initial distribution of $\vec{Q}_{t=0,c}$ at all with the exception of a minor stochastic noise that results from the Wiener process. Consequently, we obtain $\langle \vec{Q}_{t,c} \otimes \vec{F}(\vec{Q}_{t,c}) \rangle \approx 1$ and $\boldsymbol{\tau_{p,c}} \approx 0$ for all t. Actually, we only subtract stochastic noise in the stress tensor equation (4.36) which we hope to reduce the overall noise term.

Interestingly, for the case of a non-homogeneous flow field as in (2.67) we note that the equilibrium control variate does not depend on physical space $\vec{x}$. Therefore, we only have to model one N_f-dimensional vector $\vec{Q}_{t,c}$ to apply the method to a transient flow solver which results in a very low computational effort.

On the contrary, Bonvin [12] points out that there are situations in which the equilibrium control variate may differ strongly from the original process $\vec{Q}_t$. Indeed, this effect appears in simulations with complex velocity fields and large Weissenberg numbers. Then, the equilibrium variate might actually increase the stochastic noise. Therefore, we only investigate this method for the case of homogeneous flow fields as in Section 6.2.3.

Hookean Control Variate

In view of a multiscale simulation, we are primarily interested in the simulation of the nonlinear FENE spring force as there exists no equivalent macroscopic constitutive equation. For this

spring force, we describe the implementation of a **Hookean control variate**. Therefore, we set

- $\vec{u}_c = \vec{u}$ (i.e. we take the original velocity field) and

- $\vec{F}_c(\vec{Q}_{t,c}) = \vec{F}_{\mathrm{Hooke}}(\vec{Q}_{t,c}) = \vec{Q}_{t,c}$ (cf. Hookean spring force (2.64))

and use $\vec{F}(\vec{Q}_t) = \vec{F}_{\mathrm{FENE}}(\vec{Q}_t)$ as original spring force. Now we consider two synchronous problems which are

- calculation of $s = 1, \ldots, N_f$ stochastic processes $\vec{Q}_t^{(s)}$ with the FENE spring force and

- calculation of an equal amount of control variates $\vec{Q}_{t,c}^{(s)}$ with the linear Hookean spring force.

Furthermore, the ansatz requires to determine the stress tensor contribution from $\vec{Q}_{t,c}^{(s)}$ deterministically for which we use the Oldroyd-B model. This is a consequence of the equivalence between the micromolecular Hookean dumbbell model and the macromolecular Oldroyd-B constitutive equation (cf. proof in Section 2.3.6). For illustration, we rewrite equation (4.36) but additionally apply it to the case of a Hookean control variate which yields

$$\boldsymbol{\tau_p} \approx \left\langle \underbrace{\vec{Q}_t \otimes \vec{F}(\vec{Q}_t)}_{\substack{\text{stochastic:} \\ \text{FENE}}} - \underbrace{\vec{Q}_{t,c} \otimes \vec{F}_c(\vec{Q}_{t,c})}_{\substack{\text{stochastic:} \\ \text{Hooke}}} \right\rangle + \left\langle \underbrace{\vec{Q}_{t,c} \otimes \vec{F}_c(\vec{Q}_{t,c})}_{\substack{\text{deterministic:} \\ \text{Oldroyd-B}}} \right\rangle . \tag{4.38}$$

On the one hand, a Hookean control variate disposes almost all stochastic noise for situations in which both spring forces predict similar stress tensor values. On the other hand, there are situations in which both models differ from each other (e.g. extensional flow case). In such situations, we expect better results if we simply increase the number of trajectories from N_f to $2N_f$ which requires the same computational effort as using a Hookean control variate.

At last, we mention that there exist various control variates for polymeric fluids. Indeed, any model that possesses a closure equation (e.g. the FENE-P spring force) can be used as a control variate. Then, one additionally has to solve the corresponding constitutive equation. However, this is not a part of this thesis and we refer to Bonvin et al. [13] for further information.

5 Multiscale Viscoelastic Flow Solver

The primary purpose of this chapter is to describe the implementation of the considered multiscale model for viscoelastic fluids into an existing three-dimensional, free-surface Navier-Stokes flow solver - NaSt3DGPF [2]. The two-phase modelling capabilities of NaSt3DGPF are described in more detail in the thesis of Croce [24] and in an article by Croce, Griebel and Schweitzer [25]. It employs finite differences to discretise spatial derivatives but uses high-order, finite volume-based schemes for the discretisation of the convective terms (e.g. VONOS, WENO, ENO). NaSt3DGPF is fully parallelised using a domain decomposition approach that is described in Griebel et al. [35]. We also consider the parallelisation of our viscoelastic model but restrict ourselves to the case of non-Newtonian one-phase flows.

5.1 Multiscale Navier-Stokes-BCF Model

In this section, we concentrate on the coupling between the dimensionless macroscopic Navier-Stokes equations (5.1) and (5.2) on the one hand and the microscopic stochastic differential equation (5.3) and the Kramers expression (5.4) for dilute polymeric fluids on the other hand. Combining these equations yields the system

$$\frac{\partial \vec{u}^*}{\partial t^*} = -\vec{u}^* \cdot \vec{\nabla} \vec{u}^* - \vec{\nabla} p^* + \frac{1}{Re} \beta \Delta \vec{u}^* + \frac{1}{Re} \vec{\nabla} \cdot \boldsymbol{\tau_p}^* + \frac{1}{Fr^2} \vec{g}^* \qquad (5.1)$$

$$\vec{\nabla} \cdot \vec{u}^* = 0 \qquad (5.2)$$

$$d\vec{Q}_t^* = \left(-\vec{u}^* \, \vec{\nabla} \vec{Q}_t^* + \vec{\nabla} \vec{u}^* \, \vec{Q}_t^* - \frac{1}{2\,Wi} \vec{F}^*(\vec{Q}_t^*) \right) dt^* + \sqrt{\frac{1}{Wi}} \, d\vec{W}_t^* \qquad (5.3)$$

$$\boldsymbol{\tau_p}^* = \frac{\alpha_{b,d}\,(1-\beta)}{Wi} \left(\left\langle \vec{Q}_t^* \otimes \vec{F}^*(\vec{Q}_t^*) \right\rangle - \mathbf{Id} \right) \qquad (5.4)$$

$$\text{with initial conditions:} \quad \vec{u}^*(\vec{x}^*, 0) = \vec{u}_0^*(\vec{x}^*), \quad \vec{x}^* \in \Omega \text{ (physical space)}$$

$$\vec{Q}_0^*(\vec{x}^*) \sim \psi(\vec{x}^*, \vec{q}^*, 0) = \psi_{eq}(\vec{q}^*), \quad \vec{q}^* \in D \text{ (configuration space)}.$$

Here, the physical space Ω represents the fluid domain. Furthermore, the configuration space $D \subset \mathbb{R}^3$ denotes the space of possible dumbbell orientations that is represented by realisations of the stochastic process $\vec{Q}_t^*(\vec{x}^*)$. Therefore, we use the capital letter "Q" to signalise that the orientation is a stochastic process and calculate the realisations of its initial state according to a density function ψ_{eq}.

Furthermore, we have accomplished the non-dimensionalisation of the basic equations by setting

$$\vec{x}^* = \frac{\vec{x}}{L_0}, \qquad \vec{u}^* = \frac{\vec{u}}{U_0}, \qquad t^* = \frac{U_0}{L_0} t, \qquad \rho^* = \frac{\rho}{\rho_0},$$

$$p^* = \frac{p - p_0}{\rho_0 \, U_0^2}, \qquad \vec{Q}_t^* = \frac{\vec{Q}_t}{l_0}, \qquad \boldsymbol{\tau_p}^* = \frac{L_0}{U_0(\eta_s + \eta_p)}\boldsymbol{\tau_p}, \qquad \vec{g}^* = \frac{\vec{g}}{\|\vec{g}\|}.$$

Note that we describe the non-dimensionalisation of $\vec{x}$, $\vec{q}$, $\vec{u}$, and t in connection with the Fokker-Planck equation in (2.58a) - (2.58d). In doing so, we have used the characteristic units

- L_0 as characteristic length of a macroscopic flow ($[L_0]$=m),

- U_0 as characteristic velocity of a macroscopic flow ($[U_0]$=m/s),

- ρ_0 as fluid density ($[\rho_0]$=kg/m^3),

- p_0 as characteristic pressure ($[p_0]$=kg/(m s^2)),

- $l_0 = \sqrt{k_B T / H}$ as characteristic length-scale of a dumbbell ($[l_0]$=m) and

- $\lambda = \frac{\zeta}{4H}$ as characteristic relaxation time of a dumbbell ($[\lambda]$=s).

Interestingly, the Navier-Stokes equations for the velocity and the pressure field and the dilute polymeric equations for the non-Newtonian extra-stress tensor $\boldsymbol{\tau_p}$ describe the flow system on the <u>same</u> time scale. Therefore, although the equations represent different length scales of the system, we use a successive time integration scheme for the complete system. The relation between both time scales is represented by the Weissenberg number which we define subsequently.

Definition 5.1 [DIMENSIONLESS NUMBERS IN FLUID DYNAMICS]
In fluid dynamics, we denote the ratio of inertial forces to viscous forces

$$Re \equiv \frac{\rho_0 \, U_0 \, L_0}{\eta_s + \eta_p}$$

*as **Reynolds number**. Additionally, we term the ratio of inertial forces to gravitational forces*

$$Fr \equiv \frac{U_0}{\sqrt{L_0 \|\vec{g}\|}}$$

*as **Froude number**. Furthermore, for the calculation of non-Newtonian fluids the **Weissenberg number** becomes important which gives the ratio*

$$Wi \equiv \lambda \frac{U_0}{L_0}$$

*between the microscopic relaxation time of a dumbbell λ and a characteristic fluid process time L_0/U_0. Note that the preceding definition is also termed Deborah number in literature. Another dimensionless number of interest is the **elasticity number** that we define as*

$$El \equiv \frac{Wi}{Re}$$

and which we interpret as the ratio between elasticity and inertial forces.

The coupled system (5.1) - (5.4) contains two additional dimensionless units. These are

$$\beta = \frac{\eta_s}{\eta_0} = \frac{\eta_s}{\eta_s + \eta_p} \leq 1$$

to describe the percentage of the Newtonian viscosity to the total viscosity η_0 of the fluid and

$$\alpha_{b,d} \equiv \begin{cases} 1, & \text{for Hookean dumbbells } (b \to \infty), \\ \frac{b+d+2}{b}, & \text{for } d\text{-dimensional FENE dumbbells}, \\ \frac{b+d}{b}, & \text{for } d\text{-dimensional FENE-P dumbbells}. \end{cases}$$

as a specific spring force constant (cf. (2.78)). For the sake of simplicity, we subsequently drop the asterisk indicating non-dimensional units as all considered equations are dimensionless.

5.2 Eulerian and Lagrangian Representations

Obviously, the SPDE (5.3) for the stochastic process $\vec{Q}_t(\vec{x})$ depends on the fluid domain Ω. As we discretise the Navier-Stokes equations on Ω using a staggered finite difference grid, we have to calculate $\boldsymbol{\tau_p}$ at these grid points. To keep it simple, there are two different implementations to achieve this. These are a particle-based Lagrangian description on the one hand and a grid-based Eulerian interpretation on the other hand. Relating to the area of non-Newtonian fluids we have

- the **CONNFFESSIT** method (Lagrangian point of view) and

- the **Brownian configuration field** method (Eulerian point of view)

as corresponding implementations. Actually, the equation we use in (5.3) bases on the concepts of Brownian configuration fields (BCFs).

However, historically the CONNFFESSIT approach has been developed first. Therefore, we start with the CONNFFESSIT ansatz and analyse its several drawbacks which we circumvent by using BCFs.

CONNFFESSIT

The techniques of micro-macro simulation for non-Newtonian fluids have been developed in the early nineties. All previous calculations based on solving closed form constitutive equations. In 1993, Laso and Öttinger [53] introduced the concept of CONNFFESSIT which bases on solving a stochastic differential equation. CONNFFESSIT is an abbreviation for "**C**alculation **o**f **N**on-**N**ewtonian **F**low: **F**inite **E**lements and **S**tochastic **Si**mulation **T**echniques".

Originally, the method solves the Navier-Stokes equations by using a finite element mesh but this can be replaced by other appropriate discretisation schemes. Then we obtain the following scheme which we illustrate in Figure 5.1:

- At initial time, we insert a large number of dumbbells described by the pair $(\vec{x}^{(s)}, \vec{Q}^{(s)})$, $s = 1, \ldots, M$ into the fluid and distribute them uniformly in Ω.
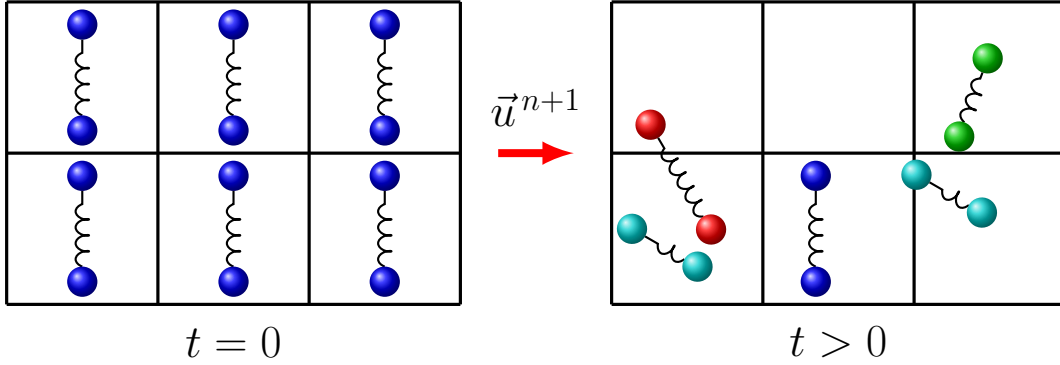
Figure 5.1: At initial time the CONNFFESSIT approach distributes the dumbbell molecules equidistantly and advects their spatial position in every time-step according to the new velocity field. Every dumbbell contributes information to the new stress tensor $\boldsymbol{\tau_p}$ of its current grid cell. As each dumbbell is influenced by its own Brownian motion, their orientations become uncorrelated with ongoing time ($t > 0$) even if the velocity field $\vec{u}$ is smooth. We illustrate the different orientations with separate colours on the right hand side of the figure.

At each time-step $n \to n+1$ we perform a three-step procedure:

- We use the current approximation of the polymeric stress $\boldsymbol{\tau_p}^n$ to compute $\vec{u}^{n+1}$ and p^{n+1} in the Navier-Stokes equations.

- Using the new velocity field $\vec{u}^{n+1}(\vec{x})$, we advect every dumbbell centre of mass and approximate its new orientation by employing

$$d\vec{Q}_{n+1}^{(s)} = \left(\vec{\nabla}\vec{u}^{n+1}\, \vec{Q}_n^{(s)} - \frac{1}{2\,Wi}\vec{F}(\vec{Q}_n^{(s)}) \right) \left(t^{n+1} - t^n \right) + \sqrt{\frac{1}{Wi}}\, \Delta\vec{W}_n^{(s)} \qquad (5.5)$$

  for $s = 1, \ldots, M$.

- We calculate the new polymeric stress $\boldsymbol{\tau_p}^{n+1}$ in each element or grid cell with the Kramers expression (cf. (5.4)) and integrate over all dumbbells that currently remain in that element.

As a result, the CONNFFESSIT scheme is similar to the presented system of equations (5.1) to (5.4) with the exception of the convective term $-\vec{u}^{n+1}\,\vec{\nabla}\vec{Q}_n^{(s)}$ from (5.3) that lacks in the SPDE (5.5). Of course, this is taken into account by transporting the dumbbells' centre of mass separately.

Disadvantages of CONNFFESSIT

Although the method allows the description of purely microscopic models (e.g. dumbbells with nonlinear FENE spring force), it exhibits several shortcomings that we note subsequently:

- Assuming that we inject M polymer fluids in a fluid domain that is discretised in N_g grid cells (normally, we have $M \gg N_g$), then an average cell contains approximately M/N_g

molecules at the beginning. As the dumbbells move within the fluid, we obtain grid cells with higher and lower polymeric density than M/N_g.
$\rightarrow$ Inject new particles in regions with low polymeric density.
$\rightarrow$ Delete particles where the concentration exceeds M/N_g by far.

- As each molecule experiences an individual Brownian force, the dumbbell orientations are uncorrelated.
$\rightarrow \boldsymbol{\tau_p}$ exhibits wild spatial fluctuations that can only be reduced by increasing the ratio M/N_g.

- In every time-step, we have to compute the Brownian force for M polymeric molecules which is expensive for high values of M.

- For the calculation of $\boldsymbol{\tau_p}$, we have to assign the dumbbells to their current grid cells which requires additional effort for the allocation.

- The CONNFFESSIT ansatz is difficult to parallelise, because different processors have to communicate with each other if molecules change between their subdomains which requires a dynamic communication pattern.

- It is difficult to use variance reduction schemes like the equilibrium control variate (cf. Section 4.2.3), because the control variate is only weakly coupled to the widespread polymeric system.

In 1998, Halin et al. [36] introduced the Lagrangian particle method (LPM). This ansatz also bases on a Lagrangian point of view but circumvents several of its shortcomings. In fact, the LPM does not transport individual polymers but collections of molecules. However, as we are interested in a grid-based description we refer to the book of Owens and Phillips [68] for further information.

Brownian Configuration Fields

In this thesis, we implement the BCF method that was first introduced in an article from Hulsen et al. [41] and further analysed in Öttinger et al. [67]. We first consider its basic concepts and therefore use the theses of Bonvin [12] and of Van Heel [89].

As our coupled system of equations (5.1) - (5.4) employs the BCF method, we denote it as a Navier-Stokes-BCF model. First, we present a schematic survey of the initial configuration and a typical time-step and then examine its advantages concerning the CONNFFESSIT ansatz. Note that we describe temporal discretisation of the coupled system in more detail in Section 5.3.
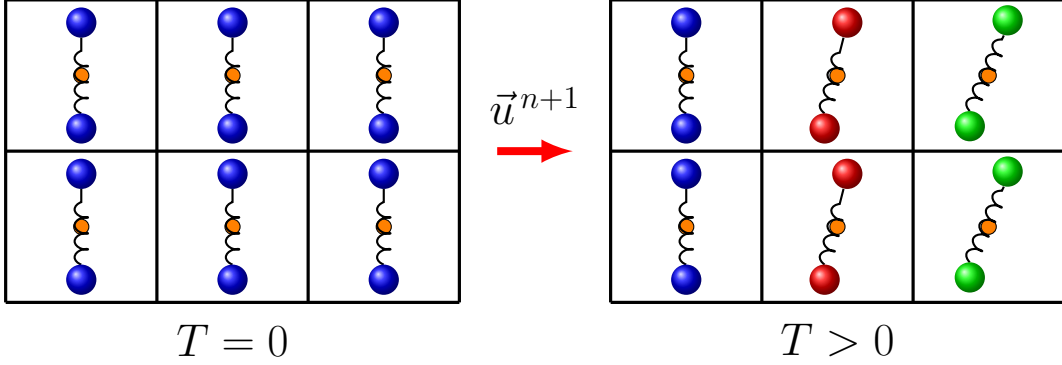
Figure 5.2: The BCF approach places N_f configuration fields at fixed spatial positions (indicated by an orange circle). For simplicity, we only consider one configuration field per cell (i.e. $N_f = 1$). Obviously, additional configuration fields for $N_f > 1$ would have different initial orientations related to the first orientation but would have identical orientations related to its neighbours in Ω. As each grid cell experiences the same Brownian force (i.e. stochastic noise does not depend on physical space Ω), the dumbbell orientations change primarily because of differences in the velocity field $\vec{u}$. Therefore, the spatial fluctuation in the stress tensor is vastly reduced.

Schematic overview:

- We use the current approximation of the velocity field $\vec{u}^n(x_i)$ to solve (5.3)

$$d\vec{Q}_{n+1}^{(s)}(x_i) = \left(-\vec{u}^n(x_i)\,\vec{\nabla}\vec{Q}_n^{(s)}(x_i) + \vec{\nabla}\vec{u}^n(x_i)\,\vec{Q}_n^{(s)}(x_i)\right.$$
$$\left. - \frac{1}{2\,Wi}\vec{F}(\vec{Q}_n^{(s)}(x_i))\right)\Delta t^n + \underbrace{\sqrt{\frac{1}{Wi}}\,\Delta\vec{W}_n^{(s)}}_{\text{independent of } i} \quad (5.6)$$

  in every grid cell $i = 1, \ldots, N_g$ and for every configuration field $s = 1, \ldots, N_f$. For simplicity of our notation, we have numbered the three-dimensional grid cell domain by using only one index "i" instead of (i, j, k).

- We calculate the new polymeric stress $\boldsymbol{\tau_p}^{n+1}(x_i)$ in each grid cell $i = 1, \ldots, N_g$ with the Kramers expression (cf (5.4)) by integrating over all N_f fixed configuration fields in that element.

- With the new stress tensor $\boldsymbol{\tau_p}^{n+1}$ we compute $\vec{u}^{n+1}$ and p^{n+1} in the Navier-Stokes equations.

Although the scheme is related to the CONNFFESSIT ansatz, it solves all its disadvantages we have mentioned before (cf. Figure 5.2):

- As the configuration fields have fixed spatial positions, the polymeric density in all grid cells is constant at all times.

- The Brownian force $\vec{W}_n^{(s)}$ in (5.6) depends on the configuration field (i.e. it depends on s) but does not depend on physical space (i.e. it does not depend on i). Therefore, the same initial orientations in different grid cells experience the same stochastic noise which reduces spatial fluctuations.

- In every time step, we have to compute N_f discrete approximations of the Wiener process $\vec{W}_n^{(s)}$, $s = 1, \ldots, N_f$ instead of $N_g N_f \approx M$ realisations as in the CONNFFESSIT method, because we reuse $\vec{W}_n^{(s)}$ for all N_g grid cells.
  $\rightarrow$ Reduced computational effort.

- It is unnecessary to track the BCF positions.

- For parallelisation, we have to communicate the BCFs in overlapping subdomains which is easier to implement due to a static communication pattern.

- It is comparatively easy to implement the equilibrium control variate method (cf. Section 4.2.3), because we only add the computation of N_f control variates to the system. Using the equilibrium control variates, we have to calculate $N_f N_g + N_f$ BCFs per time-step instead of $N_f N_g$ BCFs as in the normal case.

As a result, the BCFs method overcomes some of the limitations that we have investigated in the CONNFFESSIT approach. For this reason, some authors refer to the BCF method as a "second generation micro-macro technique" (cf. Lozinski et al. [59]).

5.3 Temporal Discretisation

Explicit Chorin Projection Method

The computation of the velocity field $\vec{u}$ and the pressure field p by solving the Navier Stokes equations (5.1) - (5.2) is a challenge on its own. Generally, a naive solution of the momentum equations (5.1) leads to a velocity field that violates the continuity equation (5.2). To circumvent this problem, we apply a projection method that decouples $\vec{u}$ and p. Furthermore, the method is explicit in $\vec{u}$ but implicit in p and first-order accurate in time. It was independently developed by Chorin [21] and Temam [85]. We have augmented the scheme with the computation of the non-Newtonian stress tensor yielding the following steps:

Step 1 Solve the Brownian configuration field equation in $i = 1, \ldots, N_g$ grid cells and for $s = 1, \ldots, N_f$ configuration fields by using an explicit Euler-Maruyama method

$$d\vec{Q}_{n+1}^{(s)}(x_i) = \left(-\vec{u}^{\,n}(x_i)\, \vec{\nabla}\vec{Q}_n^{(s)}(x_i) + \vec{\nabla}\vec{u}^{\,n}(x_i)\, \vec{Q}_n^{(s)}(x_i) - \frac{1}{2\,Wi}\vec{F}(\vec{Q}_n^{(s)}(x_i)) \right) \Delta t^n$$

$$+ \sqrt{\frac{\Delta t^n}{Wi}}\, \vec{N}(0,1)^{(s)}. \tag{5.7}$$

Step 2 Compute the new stress tensor at each node x_i by employing the Kramers expression

$$\boldsymbol{\tau_p}^{n+1}(x_i) = \frac{(1-\beta)}{Wi} \alpha_{b,d} \left(\frac{1}{N_f} \sum_{s=1}^{N_f} \vec{Q}_{n+1}^{(s)} \otimes \vec{F}\left(\vec{Q}_{n+1}^{(s)}\right) - \mathbf{Id} \right). \tag{5.8}$$

Step 3 Solve the momentum equation without considering the pressure gradient ∇p to obtain an intermediate velocity field $\vec{u}^*$, i.e.

$$\vec{u}^*(x_i) = \vec{u}^n(x_i) + \Delta t^n \left(- \vec{u}^n(x_i) \cdot \vec{\nabla}\vec{u}^n(x_i) + \frac{1}{Re} \beta \Delta \vec{u}^n(x_i) \right.$$
$$\left. + \frac{1}{Re} \vec{\nabla} \cdot \boldsymbol{\tau_p}^{n+1}(x_i) + \frac{1}{Fr^2} \vec{g}^n(x_i) \right). \tag{5.9}$$

Step 4 Solve the pressure Poisson equation

$$\Delta p^{n+1}(x_i) = \frac{1}{\Delta t^n} \vec{\nabla} \cdot \vec{u}^*(x_i) \tag{5.10}$$

with a preconditioned, iterative Krylov subspace solver like CG or BiCGStab.

Step 5 Project the intermediate velocity field $\vec{u}^*$ onto the space of divergence free velocities by enforcing $\vec{\nabla} \cdot \vec{u}^{n+1} = 0$ so that we obtain

$$\vec{u}^{n+1}(x_i) = \vec{u}^*(x_i) - \Delta t^n \nabla p^{n+1}(x_i). \tag{5.11}$$

Next, we consider boundary conditions for p that are necessary to calculate a numerical solution of the Poisson problem (5.10). If we use (5.11) to rewrite the normal derivative of the pressure at the boundary, i.e.

$$\left.\frac{\partial p^{n+1}}{\partial \vec{n}}\right|_\Gamma = \left.\nabla p^{n+1} \cdot \vec{n}\right|_\Gamma = \frac{\vec{u}_\Gamma^* - \vec{u}_\Gamma^{n+1}}{\Delta t^n} \cdot \vec{n},$$

we obtain homogeneous Neumann boundary conditions for the choice

$$\vec{u}^* = \vec{u}^{n+1} \quad \text{on } \partial\Omega.$$

Then, the pressure is determined except for an additive constant. We establish this constant by setting

$$\int_\Omega p^{n+1} \, dV = 0.$$

Due to an explicit discretisation of the velocities, we employ this ansatz for flow problems with comparatively moderate Reynolds numbers (i.e. $Re \leq 100$). Flow situations with lower Reynolds numbers require an implicit discretisation of the diffusive velocity terms to avoid restrictions in time-step size. We present the corresponding scheme subsequently. However, since we use the explicit projection method for flows with high polymeric viscosity (i.e. percentage of Newtonian viscosity only $\beta \approx 0.01$), we observe elastic behaviour even if the elasticity number El is comparatively low.

Time-step Restriction

The advantage of an explicit time-discretisation lies in its relatively low computational effort per time-step. On the contrary, explicit schemes are only stable for cases in which the time-step size does not exceed a critical limit. Therefore, we investigate the restriction in time-step size for the Navier-Stokes equations which requires a stability analysis of the linearised equations.

As the momentum equations in (5.1) contain an additional non-Newtonian stress tensor $\boldsymbol{\tau_p}$, this results in further restrictions in time-step size in comparison with purely Newtonian calculations. Trebotich et al. [87] specifies the restriction for the convective terms in x-direction as

$$\Delta t_x \leq \frac{\Delta x}{\max_{i,j,k} \left[|u_{i,j,k}| + \sqrt{2(\tau_{xx} + \frac{1-\beta}{Wi})/Re} \right]}.$$

In the exact same manner, we obtain restrictions Δt_y and Δt_z in the other coordinate directions (cf. Section 5.4 for an explanation of the used notation) so that the total restriction for the convective terms is

$$\Delta t_c = \min_\Omega (\Delta t_x, \Delta t_y, \Delta t_z). \tag{5.12}$$

This is the Courant-Friedrich-Levy (CFL) condition that we further investigate in Chapter 3.1 for finite differences on the sphere.

Additionally, we restrict the diffusion to take effect only on one further grid cell per time-step. This results in (cf. Peyret [70])

$$\Delta t_d \leq \left[\frac{\beta}{Re} \left(\frac{2}{(\Delta x)^2} + \frac{2}{(\Delta y)^2} + \frac{2}{(\Delta z)^2} \right) \right]^{-1} \tag{5.13}$$

as corresponding restriction.

A further restriction in time-step size comes from gravitational force $\vec{g}$. Croce [24] calculates the effect from the x-component as

$$\Delta t_{g_x} \leq \left[\frac{\max_{i,j,k}(|u_{i,j,k}|)}{\Delta x} + \sqrt{\left(\frac{\max_{i,j,k}(|u_{i,j,k}|)}{\Delta x} \right)^2 + \frac{4|g_x|}{\Delta x}} \right]^{-1} \tag{5.14}$$

and analogue for the other components as Δt_{g_y} and Δt_{g_z} which yields in combination a restriction of $\Delta t_g = \min_\Omega (\Delta t_{g_x}, \Delta t_{g_y}, \Delta t_{g_z})$.

As result, we restrict our adaptive time-step size according to

$$\Delta t \leq \theta \min_\Omega (\Delta t_c, \Delta t_d, \Delta t_g). \tag{5.15}$$

Semi-implicit Projection Method

Since we are also interested in fluid situations in which the elastic behaviour of the non-Newtonian fluid becomes important (i.e. $El = Wi/Re$ is high), we present an implicit discretisation scheme for the diffusive terms to avoid restrictions in time-step size. However, as the time-integration of the Brownian Configuration Field equation remains unchanged, we only

concentrate on the major characteristics of the ansatz and refer to the thesis of Klitz [48] for further information.

The semi-implicit scheme exhibits two differences according to the explicit Chorin method:

- We use a Crank-Nicolson ansatz for the discretisation of the diffusive velocity components, i.e.

$$\frac{\vec{u}^{n+1} - \vec{u}^n}{\Delta t^n} = -\nabla p^{n+\frac{1}{2}} - \vec{u}^n \cdot \vec{\nabla}\vec{u}^n + \underbrace{\frac{\beta}{2\,Re}\Delta(\vec{u}^{n+1} + \vec{u}^n)}_{\text{Crank-Nicolson}} + \frac{1}{Re}\vec{\nabla} \cdot \boldsymbol{\tau_p}^{n+1} + \frac{1}{Fr^2}\vec{g}^n.$$

- The calculation of the intermediate velocities $\vec{u}^*$ in Step 3 includes the pressure gradient term following a scheme proposed by Bell [6].

Then, we obtain a modified method that consists of the following steps:

Step 1 Solve the Brownian configuration field equation for every configuration field by using an explicit Euler-Maruyama method

$$d\vec{Q}^{(s)}_{n+1} = \left(-\vec{u}^n\,\vec{\nabla}\vec{Q}^{(s)}_n + \vec{\nabla}\vec{u}^n\,\vec{Q}^{(s)}_n - \frac{1}{2\,Wi}\vec{F}(\vec{Q}^{(s)}_n)\right)\Delta t^n + \sqrt{\frac{\Delta t^n}{Wi}}\,\vec{N}(0,1). \quad (5.16)$$

Step 2 Compute the new stress tensor with the Kramers expression, i.e.

$$\boldsymbol{\tau_p}^{n+1} = \frac{(1-\beta)}{Wi}\,\alpha_{b,d}\left(\left\langle\vec{Q}^{(s)}_n \otimes \vec{F}(\vec{Q}^{(s)}_n)\right\rangle - \mathbf{Id}\right). \quad (5.17)$$

Step 3 Solve a Helmholtz equation for an intermediate velocity field $\vec{u}^*$

$$\left(\mathbf{Id} - \frac{\Delta t^n \beta}{2\,Re}\Delta\right)\vec{u}^* = \vec{u}^n - \Delta t^n\left(\nabla p^{n-\frac{1}{2}} + \vec{u}^n \cdot \vec{\nabla}\vec{u}^n - \frac{\beta}{2\,Re}\Delta\vec{u}^n\right.$$
$$\left. - \frac{1}{Re}\vec{\nabla} \cdot \boldsymbol{\tau_p}^{n+1} - \frac{1}{Fr^2}\vec{g}^n\right). \quad (5.18)$$

by using an SSOR preconditioned CG method.

Step 4 Use $\vec{u}^*$ as the RHS of a Poisson problem which delivers a pressure correction ϕ^{n+1} and recovers $\vec{u}^{n+1}$, i.e.

$$\Delta\phi^{n+1} = \frac{1}{\Delta t^n}\nabla \cdot \vec{u}^*, \quad (5.19)$$

$$\vec{u}^{n+1} = \vec{u}^* - \Delta t^n\nabla\phi^{n+1}. \quad (5.20)$$

Step 5 We obtain the new pressure by computing

$$p^{n+\frac{1}{2}} = p^{n-\frac{1}{2}} + \phi^{n+1} - \frac{\Delta t^n \beta}{2\,Re}\Delta\phi^{n+1}. \quad (5.21)$$

Note that Step 1 and 2 are the same as for the explicit projection scheme. Additionally, the semi-implicit method requires additional boundary treatment for $\vec{u}^*|_\Omega$ in comparison to the explicit projection method (cf. Klitz [48]). Furthermore, we set homogeneous initial values for the pressure.

On the one hand, the semi-implicit ansatz necessitates the solution of an additional system of linear equations in every time-step which increases the computational effort. On the other hand, this ansatz abolishes the restriction in time-step size Δt_d from the diffusive terms (5.13). Accordingly, this ansatz is reasonable for low Reynolds numbers which we require for most viscoelastic simulations.

5.3.1 Algorithms

As a result, we present complete algorithms for the explicit Chorin method on the one hand and the semi-implicit projection on the other hand.

Algorithm 5: Explicit Chorin projection method for multiscale viscoelastic flows

Data: Initial conditions for $\vec{u}^0$ and p^0 and an equilibrium density ψ_{eq}
Result: Values for $\vec{u}$, p and $\boldsymbol{\tau_p}$ at time $t \leq t_{\text{max}}$
Set $t \leftarrow 0$, $n \leftarrow 0$;
Initialise velocity field with $\vec{u}^0$;
Generate $s = 1, \ldots, N_f$ realisations $\vec{Q}^{(s)} \sim \psi_{\text{eq}}$ // `von Neumann rejection sampling`
Initialise all BCFs with the equilibrium configuration, i.e. $\vec{Q}_{i,j,k}^{0,(s)} = \vec{Q}^{(s)}$ for all i, j, k;
Compute initial stress tensor values $\boldsymbol{\tau_p}^0$ by using (5.8) // `should be close to zero`
while $t \leq t_{max}$ **do**
    Compute new time-step size Δt^n according to (5.15);
    Set boundary values for $\vec{u}^{n+1}$ and p^{n+1};
    Set boundary values for the BCFs $\vec{Q}_{i,j,k}^{n+1,(s)}$;
    Use (5.7) to compute new configuration field values $\vec{Q}_{i,j,k}^{n+1,(s)}$;
    Obtain new stress tensor $\boldsymbol{\tau_p}^{n+1}$ with (5.8) // `Kramers expression`
    Set boundary values for intermediate velocities $\vec{u}^*$;
    Compute $\vec{u}^*$ according to (5.9);
    Solve the Poisson problem (5.10) which yields p^{n+1};
    Compute the new velocity field $\vec{u}^{n+1}$ using the pressure correction (5.11);
    $t \leftarrow t + \Delta t^n$, $n \leftarrow n + 1$
end

The explicit ansatz is useful for flows that involve higher Reynolds numbers ($Re \geq 100$) as the time-step restriction for the diffusive terms is negligible in these cases. However, note that in the case of multiscale viscoelastic computation the explicit scheme is only slightly cheaper than the semi-implicit method even for flows with high Reynolds numbers. This is caused by the high computational effort to compute the new configuration field values $\vec{Q}_{i,j,k}^{n+1,(s)}$ in (5.7). Therefore, if we can omit several time-steps because of a higher time-step size in the semi-implicit method this overcompensates all additional effort. In fact, although we simulate flow

problems, we spend most of the time to simulate stochastic processes.

Subsequently, we present an algorithm for the semi-implicit projection method.

Algorithm 6: Semi-implicit projection method for multiscale viscoelastic flows

---

Data: Initial conditions for $\vec{u}^0$ and p^0 and an equilibrium density ψ_{eq}

Result: Values for $\vec{u}$, p and $\boldsymbol{\tau_p}$ at time $t \leq t_{\max}$

Set $t \leftarrow 0$, $n \leftarrow 0$;

Apply boundary conditions for the Δ part of the Helmholtz matrix;

Initialise velocity and pressure field with $\vec{u}^0$ and $p^{\frac{1}{2}} = 0$;

Generate $s = 1, \ldots, N_f$ realisations $\vec{Q}^{(s)} \sim \psi_{\text{eq}}$ // `von Neumann rejection sampling`

Initialise all BCFs with the equilibrium configuration, i.e. $\vec{Q}_{i,j,k}^{0,(s)} = \vec{Q}^{(s)}$ for all i, j, k;

Compute initial stress tensor values $\boldsymbol{\tau_p}^0$ by using (5.17) // `should be close to zero`

while $t \leq t_{max}$ **do**

    Compute new time-step size Δt^n according to (5.15) without diffusive restriction;

    Set boundary values for $\vec{u}^{n+1}$ and $p^{n+\frac{1}{2}}$;

    Set boundary values for the BCFs $\vec{Q}_{i,j,k}^{n,(s)}$;

    Use (5.16) to compute new configuration field values $\vec{Q}_{i,j,k}^{n+1,(s)}$;

    Obtain new stress tensor $\boldsymbol{\tau_p}^{n+1}$ with (5.17) // `Kramers expression`

    Set boundary values for intermediate velocities $\vec{u}^*$;

    Solve the Helmholtz equation for $\vec{u}^*$ according to (5.18);

    Solve the Poisson problem (5.19) which yields the pressure difference ϕ^{n+1};

    Compute the new velocity field $\vec{u}^{n+1}$ using the pressure difference (5.20);

    Calculate the new pressure field $p^{n+\frac{1}{2}}$ with (5.21);

    $t \leftarrow t + \Delta t^n$, $n \leftarrow n + 1$

end

As a result, we underline the high computational effort of both algorithms. Therefore, if we want to use one of the schemes for multiscale simulations in three dimensions, we require an ansatz to parallelise our algorithms. Therefore, we concentrate on parallelisation in Chapter 5.6.

5.4 Spatial Discretisation

In Section 5.3, we have considered time-integration of the coupled Navier-Stokes-BCF system. Now, we concentrate on the spatial discretisation in Ω for a three-dimensional finite difference grid. Up to now, we have use a linearised index "i" for the position in physical space. This will be replaced by a three-component description (i, j, k) to denote the cell position within the grid.

Staggered Grid

For the discretisation of the Navier-Stokes equations (5.1) and (5.2) and the Brownian Con-figuration Field stochastic equation (5.3) in physical space Ω, we subdivide Ω into rectangular
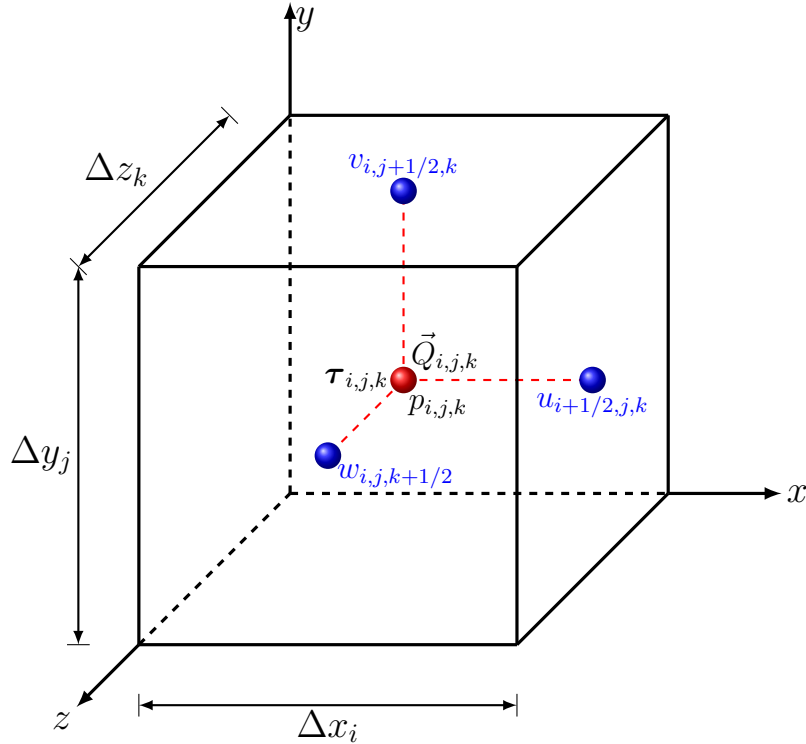
Figure 5.3: A staggered grid bases on the idea to store scalar values (e.g. p) in the cell centres and position the components of vector-valued variables (e.g. $\vec{u}$) at the cell faces. Our implementation for the second-order tensor $\boldsymbol{\tau_p}$ also uses a position at the cell centres to restrict the computation time.

subdomains and evaluate the unknown values $\vec{u}$, p, $\boldsymbol{\tau_p}$, and $\vec{Q}$ on a staggered grid. As we discretise in three dimensions, we work on a grid with N_x cells in the x-direction and in conformity N_y cells in the y-direction and N_z cells in the z-direction. The complete grid then consists of $N_g = N_x N_y N_z$ grid cells. Due to the staggered grid, we position the pressure $p_{i,j,k}$ (with $i = 1, \ldots, N_x$, $j = 1, \ldots, N_y$, $k = 1, \ldots, N_z$) as well as the six independent stress tensor components of $\boldsymbol{\tau_p}_{i,j,k}$ and the BCFs $\vec{Q}_{i,j,k}$ in the centre of cells and evaluate the velocity components $u_{i+1/2,j,k}$, $u_{i,j+1/2,k}$ and $u_{i,j,k+1/2}$ at the cell faces (cf. Figure 5.3). Here, $\vec{Q}_{i,j,k}$ represents a total number of N_f configuration fields that lie in the centre of the cell with index (i,j,k).

A staggered grid ensures a strong coupling between the pressure field on the one hand and the velocity field on the other hand. For the non-Newtonian extra stress, Gerritsma has investigated the additional coupling with $\boldsymbol{\tau_p}$ in Chapter 5 of his thesis [34]. He supposes to use a staggered grid for $\boldsymbol{\tau_p}$ as well but to position only the normal stress components (i.e. τ_{xx}, τ_{yy}, and τ_{zz}) in the centres of the cells. By contrast, he places the shear stress components (i.e. τ_{xy}, τ_{xz}, and τ_{yz}) at the edges of a grid cell.

Although his ansatz guarantees the coupling between $\boldsymbol{\tau_p}$ and p, it seems to be more suited to the case of constitutive equations for τ_p in which the computational effort is vastly reduced (cf. Section 5.6 for an analysis of the computational cost). Indeed, as the information for $\boldsymbol{\tau_p}$ is

completely incorporated in $\vec{Q}_{i,j,k}$, we would additionally have to place configuration fields at the grid edges, i.e. at $\vec{Q}_{i+1/2,j+1/2,k}$, $\vec{Q}_{i+1/2,j,k+1/2}$, and $\vec{Q}_{i,j+1/2,k+1/2}$. Consequently, the total number of configuration fields in Ω would add up to $4N_f N_g$ instead of $N_f N_g$. As a result, to restrict the computation time with NaSt3DGPF, we position the components in the cell centres in an analogous manner as in the thesis of Claus [22].

Discretised Equations

For the ongoing section, we denote the position in the cell centre with $[\cdot]_{i,j,k}$ and illustrate this choice in Figure 5.3. Consequently, we use $[\cdot]_{i\pm\frac{1}{2},j,k}$ to describe a position at the centre of the left/ right cell surface and a corresponding notation for the other cell faces. Furthermore, we employ Δx_i to term the length of cells with index i in the x-direction. At last, we use

$$\Delta x_{i+\frac{1}{2}} \;=\; (\Delta x_i + \Delta x_{i+1})$$

for the distance between the centre of the cell $[\cdot]_{i,j,k}$ on the one hand and $[\cdot]_{i+1,j,k}$ on the other hand.

We discretise all spatial derivatives, with the exception of the convective terms in the Brownian configuration field equation (5.7) and in the momentum equations (5.9), using central differences on a staggered grid. For the discretisation of the convective terms we apply high-order schemes like SMART, VONOS, ENO or WENO, indicate them with $\mathcal{C}(\cdot)$ in our equations and refer to Croce [24] for further implementation details. Since the spatial discretisation of the momentum and continuity equations has already been discussed in Claus [22] for the explicit case and in Klitz [48] for the semi-implicit approach, we only present a component-wise equation for Step 1 (cf. eqrefEquation:ChorinExplicitStep1) and Step 2 (cf. (5.8)) of the time-integration schemes.

Step 1: Brownian Configuration Field Equation

The x-component $Q_{i,j,k}^{x,n+1}$ of the configuration field $\vec{Q}_{i,j,k}^{n+1}$ in Step 1 for the FENE spring force with maximum extension b (cf. (2.66)) is approximated by

$$
\begin{aligned}
Q_{i,j,k}^{x,n+1} \;=\; Q_{i,j,k}^{x,n} + \Delta t^n \Bigg[&-\mathcal{C}\left(u\frac{\partial Q^x}{\partial x}\right)_{i,j,k}^n - \mathcal{C}\left(v\frac{\partial Q^x}{\partial y}\right)_{i,j,k}^n - \mathcal{C}\left(w\frac{\partial Q^x}{\partial z}\right)_{i,j,k}^n \\
&+ \left(\frac{\partial u}{\partial x}\right)_{i,j,k}^n Q_{i,j,k}^{x,n} + \left(\frac{\partial u}{\partial y}\right)_{i,j,k}^n Q_{i,j,k}^{y,n} + \left(\frac{\partial u}{\partial z}\right)_{i,j,k}^n Q_{i,j,k}^{z,n} \\
&- \frac{1}{2\,Wi} \cdot \frac{Q_{i,j,k}^{x,n}}{1 - [(Q_{i,j,k}^{x,n})^2 + (Q_{i,j,k}^{y,n})^2 + (Q_{i,j,k}^{z,n})^2]/b} \Bigg] \\
&+ \sqrt{\frac{\Delta t^n}{Wi}}\, r_x
\end{aligned}
\tag{5.22}
$$

with $r_x \sim N(0,1)$ and (u,v,w) as the components of $\vec{u}$. Note that we have to perform operation (5.22) in grid cell $[\cdot]_{i,j,k}$ not only once but for every of the $s = 1,\ldots,N_f$ realisations of the

stochastic process. Furthermore, the component-wise equation for the y-component of $\vec{Q}_{i,j,k}^{n+1}$ is

$$
\begin{aligned}
Q_{i,j,k}^{y,n+1} \;=\; Q_{i,j,k}^{y,n} \,+\, \Delta t^n \Bigg[& -\mathcal{C}\left(u\frac{\partial Q^y}{\partial x}\right)_{i,j,k}^{n} - \mathcal{C}\left(v\frac{\partial Q^y}{\partial y}\right)_{i,j,k}^{n} - \mathcal{C}\left(w\frac{\partial Q^y}{\partial z}\right)_{i,j,k}^{n} \\
& + \left(\frac{\partial v}{\partial x}\right)_{i,j,k}^{n} Q_{i,j,k}^{x,n} + \left(\frac{\partial v}{\partial y}\right)_{i,j,k}^{n} Q_{i,j,k}^{y,n} + \left(\frac{\partial v}{\partial z}\right)_{i,j,k}^{n} Q_{i,j,k}^{z,n} \\
& - \frac{1}{2\,Wi} \cdot \frac{Q_{i,j,k}^{y,n}}{1 - [(Q_{i,j,k}^{x,n})^2 + (Q_{i,j,k}^{y,n})^2 + (Q_{i,j,k}^{z,n})^2]/b} \Bigg] \\
& + \sqrt{\frac{\Delta t^n}{Wi}}\, r_y
\end{aligned}
\tag{5.23}
$$

with $r_y \sim N(0,1)$ and analogously

$$
\begin{aligned}
Q_{i,j,k}^{z,n+1} \;=\; Q_{i,j,k}^{z,n} \,+\, \Delta t^n \Bigg[& -\mathcal{C}\left(u\frac{\partial Q^z}{\partial x}\right)_{i,j,k}^{n} - \mathcal{C}\left(v\frac{\partial Q^z}{\partial y}\right)_{i,j,k}^{n} - \mathcal{C}\left(w\frac{\partial Q^z}{\partial z}\right)_{i,j,k}^{n} \\
& + \left(\frac{\partial w}{\partial x}\right)_{i,j,k}^{n} Q_{i,j,k}^{x,n} + \left(\frac{\partial w}{\partial y}\right)_{i,j,k}^{n} Q_{i,j,k}^{y,n} + \left(\frac{\partial w}{\partial z}\right)_{i,j,k}^{n} Q_{i,j,k}^{z,n} \\
& - \frac{1}{2\,Wi} \cdot \frac{Q_{i,j,k}^{z,n}}{1 - [(Q_{i,j,k}^{x,n})^2 + (Q_{i,j,k}^{y,n})^2 + (Q_{i,j,k}^{z,n})^2]/b} \Bigg] \\
& + \sqrt{\frac{\Delta t^n}{Wi}}\, r_z.
\end{aligned}
\tag{5.24}
$$

In (5.22) we have used

$$
\left(\frac{\partial u}{\partial x}\right)_{i,j,k}^{n} = \frac{u_{i+1/2,j,k}^{n} - u_{i-1/2,j,k}^{n}}{\Delta x_i}
\tag{5.25}
$$

$$
\left(\frac{\partial u}{\partial y}\right)_{i,j,k}^{n} = \frac{u_{i,j+1/2,k}^{n} - u_{i,j-1/2,k}^{n}}{\Delta y_j}
\tag{5.26}
$$

$$
\left(\frac{\partial u}{\partial z}\right)_{i,j,k}^{n} = \frac{u_{i,j,k+1/2}^{n} - u_{i,j,k-1/2}^{n}}{\Delta z_k}
\tag{5.27}
$$

for the velocity gradient and similar expressions for the other components of $\nabla \vec{u}^n$. Since the first velocity component u is defined on $[\cdot]_{i+1/2,j,k}$ and $[\cdot]_{i-1/2,j,k}$, we can use the values of u for (5.25) directly but first of all have to interpolate them for (5.26) and (5.27) onto the corresponding cell faces. Indeed, we perform similar interpolations for the other velocity components v and w.

Step 2: Kramers Expression

Before we present an expression for the xx- and xy-component of $\boldsymbol{\tau_p}_{i,j,k}^{n+1}$, we introduce a slight modification in the notation of the Brownian configuration fields. As the reference to the

current time-step $n+1$ in $\vec{Q}_{i,j,k}^{n+1}$ is less important in this case, we drop the corresponding index but rather reuse the indication "(s)" for the $s = 1, \ldots, N_f$ stochastic realisations. Again, we consider the case of the FENE spring force (2.66) with an extension parameter b.

Then, equation (5.8) for the explicit or (5.17) for the semi-implicit case in Step 2 becomes

$$\tau_{i,j,k}^{xx} = \frac{(1-\beta)}{Wi} \frac{b+5}{b} \left(-1 + \frac{1}{N_f} \sum_{s=1}^{N_f} \frac{\left(Q_{i,j,k}^{x,(s)}\right)^2}{1 - [(Q_{i,j,k}^{x,(s)})^2 + (Q_{i,j,k}^{y,(s)})^2 + (Q_{i,j,k}^{z,(s)})^2]/b} \right) \quad (5.28)$$

for the xx-component of the non-Newtonian stress tensor $\boldsymbol{\tau_p}$.

Additionally, we compute its xy-component in cell $[\cdot]_{i,j,k}$ using the expression

$$\tau_{i,j,k}^{xy} = \frac{(1-\beta)}{Wi} \frac{b+5}{b} \frac{1}{N_f} \sum_{s=1}^{N_f} \frac{Q_{i,j,k}^{x,(s)} Q_{i,j,k}^{y,(s)}}{1 - [(Q_{i,j,k}^{x,(s)})^2 + (Q_{i,j,k}^{y,(s)})^2 + (Q_{i,j,k}^{z,(s)})^2]/b}. \quad (5.29)$$

Obviously, the other four independent components of $\boldsymbol{\tau_p}_{i,j,k}^{n+1}$ base on a similar expression.

Initial Conditions

Since our coupled Navier-Stokes-BCF system is time-dependent, we require initial conditions for $\vec{u}$, p as well as for $\vec{Q}$ and $\boldsymbol{\tau_p}$. NaSt3DGPF [2] allows the setting of initial values for $\vec{u}$ with a parameter file that is parsed at the beginning of a simulation. Therefore, we set

$$\begin{aligned} \vec{u}_{i,j,k}^0 &= \vec{u}(x_{i,j,k}, 0), \\ p_{i,j,k}^0 &= p(x_{i,j,k}, 0), \end{aligned} \qquad \text{for } i = 1, \ldots, N_x, \ j = 1, \ldots, N_y, \ k = 1, \ldots, N_z.$$

For the micromolecular dumbbell model, we replace the initial value of $\boldsymbol{\tau_p}$ by the initial values of the Brownian configurations fields. In every grid cell, we position the same initial distributions of the stochastic process according to the chosen spring force, i.e. we generate $s = 1, \ldots, N_f$ configurations

$$\vec{Q}_{i,j,k}^{0,(s)} \sim \underbrace{\psi_{\text{eq}}}_{\substack{\text{independent} \\ \text{from i,j,k}}} \qquad \text{for } i = 1, \ldots, N_x, \ j = 1, \ldots, N_y, \ k = 1, \ldots, N_z.$$

Here, ψ_{eq} denotes the equilibrium distribution for the Hookean spring force (4.28), the FENE spring force (4.29) or the FENE-P spring force (4.30). For the sampling of the initial configuration in agreement with ψ_{eq}, we apply the von Neumann rejection sampling method that we describe in detail in Section 4.2.2.

At last, we consider initial values for the polymeric extra-stress. Since $\boldsymbol{\tau_p}$ is connected to the configuration fields by the Kramers expression, we already have prescribed initial values for the stress. As the equilibrium density ψ_{eq} correlates with a vanishing polymeric stress, we obtain

$$\boldsymbol{\tau_p}_{i,j,k}^0 \approx 0 \qquad \text{for } i = 1, \ldots, N_x, \ j = 1, \ldots, N_y, \ k = 1, \ldots, N_z.$$
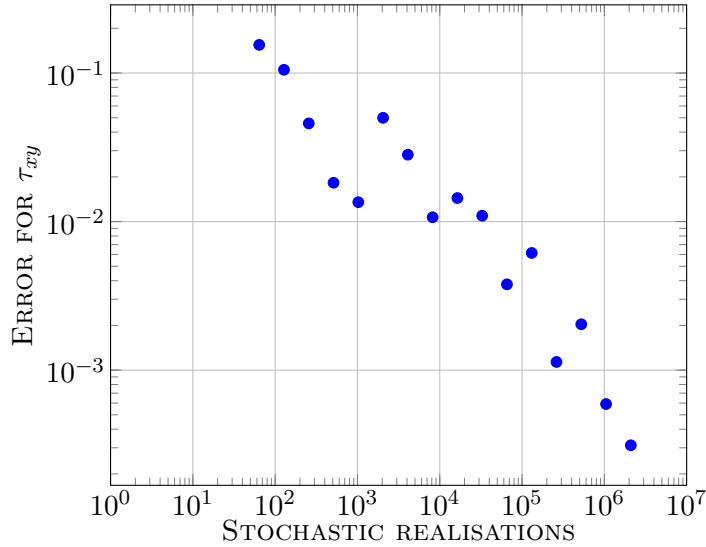
Figure 5.4: The figure presents absolute values for the stress tensor component τ_{xy} depending on the number of stochastic realisations (exact initial value is $\tau_{xy} = 0$). We have marked the error for 2^6 to 2^{21} realisations. Even if the error does not decay monotonically, the law of large numbers guarantees that we reach the exact value almost surely. For calculations using NaSt3DGPF we position 2000 to 8000 realisations in every grid cell as more stochastic realisations would lead to enormous computing times. Therefore, our initial error for τ_p lies in the order of $\mathcal{O}(10^{-2})$.

Note that $\tau_p{}^0$ is in general unequal to zero, because we only possess a stochastic approximation of zero. For illustration, in Figure 5.4 we present initial values for the stress tensor component τ_{xy} depending on the number of realisations N_f. Nevertheless, as the polymeric stress operates on the fluid field only via its divergence it has no effect in practical applications whether we actually start with a stress tensor of zero or not. Nevertheless, our results in τ_p have an uncertainty in the order of the initial error.

5.5 Discrete Boundary Values

This section describes the placement of boundary values in obstacle cells with an adjacent fluid cell. Let grid cell (i, j, k) be an obstacle cell and let cell $(i-1, j, k)$ be a fluid cell, then we distinguish four different types of boundary conditions:

- Inflow Dirichlet conditions,
- outflow Neumann conditions,
- no-slip boundary conditions, and
- slip boundary conditions.

Additionally, we can also decide to skip boundary treatment for $\partial\Omega$ at all by using periodic boundary conditions. Then, we continue the flow domain by using fluid information from the opposite side of $\partial\Omega$.
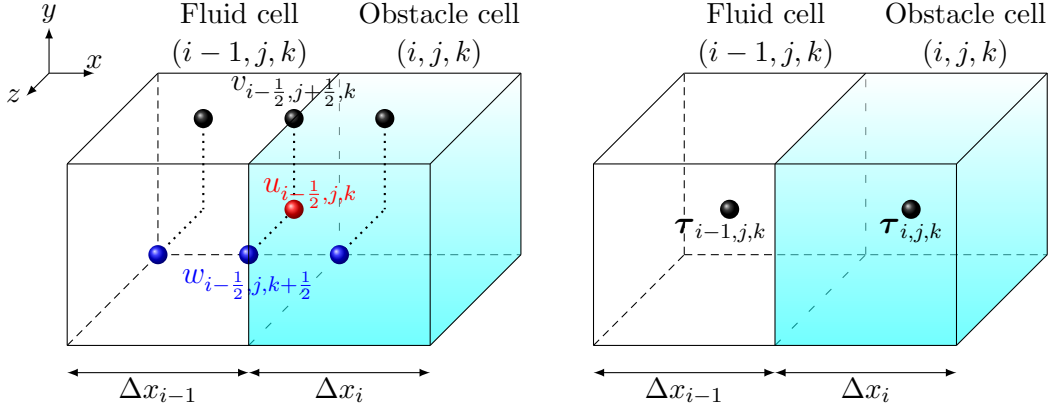
Figure 5.5: The left hand side of the figure illustrates the setting of boundary values for the velocities. Boundary values are either set on the cell face directly if the velocity component is already defined there ($u_{i-1/2,j,k}$ in this case) or are otherwise extrapolated into the obstacle cells ($v_{i-1/2,j+\frac{1}{2},k}$ and $w_{i-1/2,j,k+\frac{1}{2}}$). For the stochastic realisations and therefore for $\boldsymbol{\tau_p}$, we do not know the boundary values explicitly and additionally do not know how to extrapolate configuration fields into an obstacle cell. Therefore, our boundary method creates an error in the order of $\mathcal{O}(\Delta x_i/2)$ which decreases for finer grid resolutions.

A no-slip boundary condition for a fluid states that the fluid's velocity is zero relative to the boundary, i.e.

$$u_{\text{b}} = u_{i-1/2,j,k} = 0, \qquad v_{\text{b}} = v_{i-1/2,j,k} = 0, \text{ and} \qquad w_{\text{b}} = w_{i-1/2,j,k} = 0. \qquad (5.30)$$

Alternatively, a slip boundary condition demands the velocity component normal to the boundary to vanish as well as the normal derivative of the tangent velocity component. This yields

$$u_{\text{b}} = u_{i-1/2,j,k} = 0, \qquad \frac{\partial v_{\text{b}}}{\partial x} = \frac{\partial v_{i-1/2,j,k}}{\partial x} = 0, \text{ and} \qquad \frac{\partial w_{\text{b}}}{\partial x} = \frac{\partial w_{i-1/2,j,k}}{\partial x} = 0 \qquad (5.31)$$

in connection with the described fluid cells. In that case, the velocity component $u_{i-1/2,j,k}$ lies on the corresponding boundary face directly whereas $v_{i-1/2,j,k}$ and $w_{i-1/2,j,k}$ are defined on other faces. Therefore, we have to extrapolate the velocities $v_{i,j,k}$ and $w_{i,j,k}$ within the obstacle so that boundary conditions like (5.30) and (5.31) for v_{b} and w_{b} are fulfilled (cf. Figure 5.5).

In view of the non-Newtonian stress tensor $\boldsymbol{\tau_p}$, we also necessitate boundary conditions. For macroscopic constitutive equations like the Oldroyd-B model we constitute boundary values directly. In contrast, for a microscopic BCF model $\boldsymbol{\tau_p}$ is not the primary variable of interest, because we solve a stochastic equation for the stochastic processes. Therefore, we consider boundary conditions for $\vec{Q}$ instead of $\boldsymbol{\tau_p}$.

A common approach is to position equilibrium configuration fields on the boundary face at the beginning of the simulation and follow their evolution by taking the corresponding velocity $\vec{u}_{\text{b}}$ into account. Then, we actually know the configuration field and the stress tensor value at the boundary in every time-step and use them for our calculations. However, in Section 5.4 we motivate the reasons for placing the fields $\vec{Q}^{(s)}$ for $s = 1, \ldots, N_f$ in the cell centres. Therefore, we do not know explicitly which values the stress takes at the boundary. Even if we knew the

BCFs at the boundary, we would have to extrapolate these values into the obstacle cell which is not intuitively clear.

To keep it simple, we have implemented a pragmatic approach. In doing so, we set

- the boundary conditions for $\vec{u}$ according to the chosen boundary method (e.g. no-slip boundary conditions) and

- always use homogeneous Neumann boundary conditions for $\vec{Q}^{(s)}_{i-1,j,k}$, i.e. we set

$$\underbrace{\vec{Q}^{(s)}_{i,j,k}}_{\text{obstacle}} = \underbrace{\vec{Q}^{(s)}_{i-1,j,k}}_{\text{fluid}} \quad \text{for } s = 1, \ldots, N_f$$

which leads to $\frac{\partial \vec{Q}^{(s)}_{i-1,j,k}}{\partial x} = 0$.

Then, the configuration field $\vec{Q}^{(s)}_{i-1,j,k}$ evolves in agreement with the velocity field at the boundary. However, since the fields $\vec{Q}^{(s)}_{i-1,j,k}$ exhibit a distance of a half grid cell $\frac{1}{2}\Delta x_{i-1}$, we actually use velocity values with a distance of one half grid cell to the boundary. Otherwise, for arbitrarily fine discretisation (i.e. $\Delta x_{i-1} \to 0$) we expect our values for $\vec{Q}^{(s)}_{i-1,j,k}$ to tend to the boundary values so that the error converges to zero.

5.6 Parallelisation

Since we present a multiscale ansatz for viscoelastic flows in this thesis, in every grid cell and for every time-step we have to solve a system with ten unknowns that have a physical relevance and thousands of additional Brownian configuration fields. Therefore, two problems occur that accentuate the importance of parallelisation:

- The computational task requires large computing time to solve physical systems of interest.

- A large number of realisations for $\vec{Q}^{(s)}$, $s = 1, \ldots, N_f$ in every grid cell (i.e. N_f is large) leads to high memory requirements. In fact, the computational effort for a problem can be so large that it does not fit into the main memory of the computer.

In macroscopic fluid simulations using NaSt3DGPF [2] the former problem is of major interest, because in general situations the computing time increases faster than the primary storage amount. However, for the presented approach both problems have an equal priority. In this chapter, we start with an illustration of the memory requirements, then briefly describe domain decomposition approaches and at last present performance measurements using the parallel computers at the Institute for Numerical Simulation and the Sonderforschungsbereich 611.

Computational Effort

In Section 6.3.2, we examine the flow through an infinite channel which we resolve by using 80^3 grid cells and $N_f = 4000$ realisations for the stochastic differential equation. Without consideration of the ghost cell variables, the system necessitates about
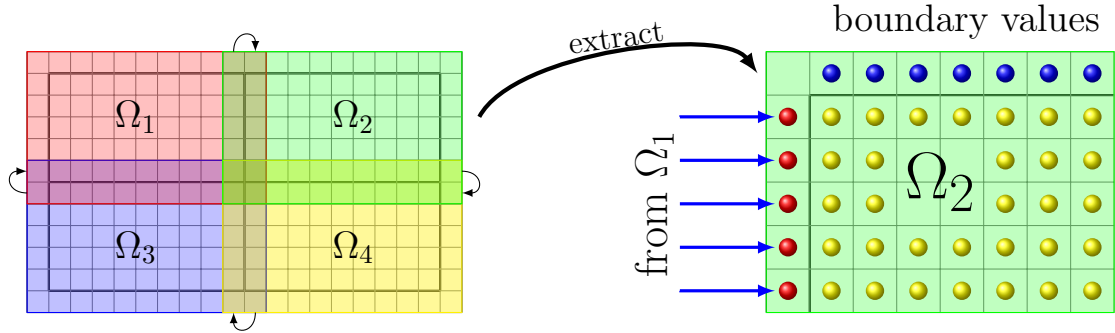
Figure 5.6: The parallelisation approach bases on domain decomposition of Ω into subdomain with an overlapping boundary region. In every time-step, boundary values are interchanged between the domains to guarantee a well defined problem for every processor. We illustrate boundary values for Ω_2 by red dots on the right-hand side of the figure.

- 4 MB for the pressure field p,

- 12 MB for the velocity field $\vec{u}$,

- 24 MB for the six independent components of $\boldsymbol{\tau_p}$, and

- 46 GB for 4000 stochastic variables in every grid cell.

Here we have used that each Brownian configuration field consists of three components whereas each component requires the size of an 8 byte double variable. Obviously, a sequential programme cannot fulfil the stated memory requirements. Furthermore, as long as we do not write the complete stochastic system into a file, we cannot continue an initial computation later on. Since we are only interested in the physical system, we only have to store the matrices that approximate p, $\vec{u}$, and $\boldsymbol{\tau_p}$ for postprocessing purposes.

Parallelisation Strategy

The most natural ansatz for the parallelisation of the Navier-Stokes equations is to decompose our domain Ω into several subdomains $\Omega_1, \ldots, \Omega_N$ so that each processor computes only the unknowns that belong to its domain (cf. Griebel [35]). As a processor does not necessitate access to the entire data structure, we can now solve problems that require high amounts of storage memory.

Since a parallelised algorithm has to achieve the same results as its sequential analogue, processors whose subdomains share a common boundary have to communicate with each other. Therefore, neighbouring processors have to exchange relevant data on their common processor boundary. For illustration, we present the processor boundary in Figure 5.6. Depending on the discretisation stencil, we need an overlapping domain of one to three cells. For instance, a WENO scheme (cf. Croce [24]) for the convective terms requires three overlapping grid cell rows but guarantees a 5th-order accuracy in space.

For our multiscale approach, we exchange not only boundary values for $\vec{u}$ and p but also boundary values for $\vec{Q}^{(s)}$, $s = 1, \ldots, N_f$ in every time-step. Therefore, the most expensive part of the communication between the processors belongs to the stochastic system. Furthermore, as

we interchange the Brownian configuration fields it is theoretically unnecessary to communicate stress tensor values at the boundary. However, it depends on the computer architecture and the problem size whether exchanging $\boldsymbol{\tau_p}$ or calculating the values with the Kramers expression is more efficient.

To obtain an optimal speed-up for our parallelised algorithm, we normally have to ensure that the load distribution for $\Omega_1, \ldots, \Omega_N$ is optimal. Therefore, the subdomains should possess the same size so that each processor has to treat the same number of unknowns. Unequal load balancing leads to waiting time for some processors which reduces the parallel efficiency.

Performance Measurement

For the communication between the processes we use the Message Passing Interface (MPI) which is designed for high performance computing on massively parallel machines and on workstation clusters (cf. MPI [3]). An MPI implementation (e.g. MPICH [1]) consists of a library with C, C++ or Fortran routines that enable message exchange between processors.

The numerical results that we present in this thesis using NaSt3DGPF were computed with the parallel computers Himalaya and Eifel II of the Institute for Numerical Simulation and the Sonderforschungsbereich 611. The HPC cluster Himalaya features

- 128 Dell PowerEdge 1850 nodes with a total of 256 Intel Xeon EM 64 T 3.2 GHz CPUs,

- a main memory of 4-6 GB per node, and

- a Linpack Performance of 1269 GFlop/s.

Furthermore, Eifel II exhibits

- 19 Dell PowerEdge 1950/2950 nodes with a total of 38 Intel Xeon X5355 2.66 GHz CPUs,

- a main memory of 12-16GB per node, and

- a Linpack Performance of 519.1 GFLop/s.

Both clusters are equipped with a Myrinet/ XP network interface that allows fast communication between the processors without having to rely on the TCP/IP protocol overhead.

As mentioned before, unequal load balancing reduces the parallel efficiency as some processors have to wait for the results of other processors. Therefore, we want to measure the efficiency of our parallel implementations in NaSt3DGPF so that the concepts of speed-up and scale-up become important. Unfortunately, the speed-up measurement is quite complicated for our multiscale approach as most complex problems (suited for a large number of processors) do not fit into the main storage of a small number of processors. On the other hand, problems that require less main storage are too small to be parallelised efficiently.

Accordingly, we measure the scale-up of our programme which we define subsequently.

p	$T_p(pN)_v\,[s]$	ScU_v	ScU_N
	multiscale viscoelastic		Newtonian
1	232.3	1.0	1.0
2	227.1	1.0	0.85
4	237.6	0.98	0.68
8	247.0	0.94	0.65
16	252.6	0.92	0.50
32	255.1	0.91	0.42
64	272.2	0.85	0.21
128	301.4	0.77	

Table 5.1: The table compares the scale-up behaviour of our multiscale viscoelastic method using NaSt3DGPF on the one hand with a purely Newtonian calculation on the other hand where each processor has a subdomain of $10 \times 20 \times 20$ cells. Note that the multiscale simulation takes about 80 times longer than its Newtonian counterpart. For small subdomain sizes, the multiscale approach scales much better in the number of processors which is an effect of the enormous increase in problem size. Therefore, our multiscale programmes are perfectly adapted to massively parallel computers.

Definition 5.2 [SCALE-UP]
*Let p be the number of processors, $T_1(N)$ the execution time of a problem with size N on one processor, and $T_p(pN)$ the time for the parallel execution of a problem with size pN on p processors. Then, we define the **scale-up** of a parallel algorithm by*

$$ScU \equiv \frac{T_1(N)}{T_p(pN)} = \frac{\text{execution time using serial algorithm for problem size } N}{\text{execution time using } p \text{ processors for problem size } pN}.$$

In Section 6.3.2, we present results for the infinite channel with $N_f = 4000$ using 60 computing nodes with two processors per node (i.e. altogether we use 120 processors) on a domain with 80^3 grid cells. For the benchmark measurement, we compute a scaled-up version of this problem by using 1 to 64 computing nodes with only one processors per node as this allows an accurate comparison in computing time between the sequential and the parallel programmes. We choose a fixed local problem size of $10 \times 20 \times 20$ cells per processor, i.e. on $p = 64$ processors we consider a problem $pN = 40 \times 80 \times 80$ cells in total. Then, we measure the computing time for performing twelve complete time-steps. In Table 5.1, we analyse the scale-up of our multiscale programme and compare the results with the scale-up of the NaSt3DGPF alone (i.e. without using the multiscale BCF method). To achieve proper results for solely using the macroscopic NaSt3DGPF solver, we measure the time for 5000 steps as the required time for one time-step is vastly reduced compared to the multiscale viscoelastic model. In fact, for $N_f = 4000$ realisations and the stated problem size the multiscale simulation takes about 80 times longer than its Newtonian counterpart but this factor varies strongly with the size of N_f.

Table 5.1 shows that the multiscale viscoelastic model scales very good which is not unexpected as the problem is vastly increased in terms of computational effort compared to the Newtonian case. The relatively small subdomain size seems to be sufficient for our multiscale computations so that we can apply a large number of processors even on small grid domains

which would lead to a poor parallel efficiency in the case of the Newtonian flow solver, cf. last column in Table 5.1. Note that, however, for subdomains that are larger in size, we also achieve a reasonable scale-up for the Newtonian calculations (cf. Croce [24]).

As a result, even if a multiscale approach seems to be very expensive at the moment, these disadvantages become less important the more processors are used for computing because of an excellent scale-up behaviour. Since we expect parallel computers to become faster every year, problems of the discussed size will be manageable in the near future.

6 Numerical Results

This chapter contains all numerical results using the described finite difference scheme (cf. Chapter 3.1) and spectral methods for the Fokker-Planck equation (cf. Chapter 4.1) and furthermore stochastic techniques for the equivalent stochastic equation (cf. Chapter 4.2). We classify our results into

- homogeneous flow field simulations in Chapter 6.1 (2D) and Chapter 6.2 (3D), i.e., the velocity field is analytically known and possesses a constant velocity gradient $\boldsymbol{\kappa} = \nabla \vec{u}$ throughout physical space Ω so that it is unnecessary to solve the Navier-Stokes equations and

- complex flow field simulations in Chapter 6.3, i.e. the general case in which the stress tensor $\boldsymbol{\tau_p}$ actually contributes information to $\vec{u}$ and p and vice versa. For the solution of the Navier-Stokes equations we employ the NaSt3DGPF [2] flow solver.

For illustration, we give a survey of the considered flow models. Subsequently, we investigate

- Newtonian flows,

- Oldroyd-B model flows,

- polymeric flows with a Hookean spring force,

- polymeric flows with a FENE spring force (**F**initely **E**xtensible **N**onlinear **E**lastic), and

- polymeric flows with a FENE-P spring force.

Obviously, a Newtonian flow does not exhibit any elastic behaviour in first approximation and is completely described by the Navier-Stokes equations (cf. Chapter 2.1). On the contrary, the Oldroyd-B model adds a constitutive equation for the polymeric stress to the flow system (cf. Chapter 2.2) and all polymeric models describe elastic behaviour as the effect of micromolecular dumbbells that interact with the Newtonian solvent (cf. Chapter 2.3). Actually, the micromolecular models are of different importance for practical applications. In fact, the Hooke and FENE-P model possess an equivalent closed-form constitutive equation and the Oldroyd-B model turns out to be the macroscopic analogue to the Hookean dumbbell system (cf. Section 2.3.6). Therefore, only the nonlinear FENE spring force leads to a fully multiscale system as it offers no equivalent macroscopic interpretation unless we consider closure approximations. Accordingly, the motivation for using Hookean and FENE-P spring forces in the following is to be able to compare different model predictions. In practice, we would employ the macroscopic formulation.

6.1 2D Homogeneous Flows

This chapter analyses homogeneous flow problems with a two-dimensional configuration space. Subsequently, we apply the spectral approach for the Fokker-Planck equation (cf. Chapter 4.1) and a stochastic technique (cf. Chapter 4.2) on

- a moderate extensional flow (i.e. $\dot{\epsilon} = 1.0$),

- a strong extensional flow (i.e. $\dot{\epsilon} = 5.0$),

- and a strong shear flow (i.e. $\dot{\gamma} = 10.0$).

We investigate the time-dependent behaviour of the non-Newtonian stress tensor using a non-linear FENE spring force for all flow problems in 2D. For a comparison between the FENE spring force on the one hand with the more simple linear spring forces on the other hand we refer to Chapter 6.2 which considers problems with 3D configuration spaces.

6.1.1 Moderate Extensional Flow

We now consider the case of a planar extensional flow in which the flow is stretched in one axis. In this case, the velocity field takes the form

$$\vec{u} = (\dot{\epsilon}x, -\dot{\epsilon}y) \tag{6.1}$$

and as the fluid undergoes a moderate extension we set $\dot{\epsilon} = 1$. For further explanation of an extensional flow, we refer to Section 2.1.3 and Figure 2.6 on page 25. The significance of extensional flows lies in the existence of an analytical solution for the steady state probability density function ψ (cf. Section 2.3.5) since the velocity gradient $\boldsymbol{\kappa}$ is symmetric for extensional flows.

Before we consider our numerical results, we concentrate on deriving the analytical solution. For extensional flows, we do not only know the initial condition ψ_{eq} (2.85) of the density function but also its steady state solution ψ_{sol} (2.91). Using the Kramers expression (4.13) we compute the analytical solution $\boldsymbol{\tau_p}^{\text{sol}}$ for process time $t \to \infty$ as

$$\boldsymbol{\tau_p}^{\text{sol}} = \frac{1-\beta}{Wi}\left(\frac{b+4}{b}\right)\left(-\mathbf{Id} + \underbrace{\int_{|\vec{q}|<\sqrt{b}} \vec{q} \otimes \frac{\vec{q}}{1 - \frac{\|\vec{q}\|^2}{b}}\, \psi_{ext}\, d\vec{q}}_{= \langle \vec{q} \otimes \vec{F}(\vec{q}) \rangle \text{ (i.e. expectation on a disc)}}\right). \tag{6.2}$$

Consequently, we insert the simulation parameters (cf. Table 6.1) into (6.2) and compute reference values for the three independent stress tensor components of $\boldsymbol{\tau_p}^{\text{sol}}$ as

> 1. $\tau_{xx}^{\text{sol}} \approx 9.3724227777324$
>
> 2. $\tau_{yy}^{\text{sol}} \approx -0.7297377607653$
>
> 3. $\tau_{xy}^{\text{sol}} = 0.0$

with zero shear stress components $\tau_{xy}^{\text{sol}} = \tau_{yx}^{\text{sol}}$. Obviously, the initial condition ψ_{eq} leads to zero stress tensor values.

Fokker-Planck Equation

Using the spectral method approach from Section 4.1.2 for the Fokker-Planck equation, we employ a set of parameters that we present in Table 6.1. As we decide for $\alpha_J = \beta_J = 0.0$ as Gauss-Jacobi parameters, this implies that we use Legendre polynomials as basis functions (cf. Chapter 3.2 on discretised FP equation for Gauss-Jacobi points). Furthermore, for time integration of the Fokker-Planck scheme (4.17) we use an explicit, low-storage 3rd-order Runge-Kutta method on the one hand or an implicit Crank-Nicolson method on the other hand (cf. Algorithm 2 on page 93). Both approaches are applicable, but the explicit method requires restrictions in time-step size. For more complex flow problems the time-step restriction for the explicit scheme becomes too severe so that we have to use the implicit method. Therefore, we use the 3rd-order Runge-Kutta method for the current extensional flow and the implicit ansatz for the problems in Section 6.1.2 and Section 6.1.3.

Moderate Extensional Flow (Fokker-Planck)		
Weissenberg number	Wi	1.0
Newtonian viscosity	β	0.0
Extensional rate	$\dot{\epsilon}$	1.0
Maximum spring extension	b	10.0
Transformation factor	s	2.0
Gauss-Jacobi $\big\{$	α_J	0.0
	β_J	0.0
Spring force	$\vec{F}(\vec{q})$	FENE
Time Discretisation		RK3rd
Time-step size (const.)	Δt	10^{-5}

Table 6.1: Parameters for two-dimensional extensional flow with moderate extensional rate.

As we only know initial and steady state values for ψ and τ_p, we cannot compare intermediate values with an analytical solution. However, we expect a smooth evolution for τ_p since a moderate extensional flow slowly leads to a preferred orientation of the dumbbells and elongates the dumbbells in this direction. We present our results for the stress tensor development in Figure 6.1. The figure contains the three independent stress tensor components as well as the integral of ψ over the configuration space which yields 1.0 if ψ is a probability density function. As ψ specifies the probability of a certain dumbbell orientation and therefore necessarily has to be a density function, we use the computed result as an error indicator. For our simulations we always obtain an integral of ψ that is equal to 1.0 with an accuracy of six significant digits which emphasizes that spectral methods are appropriate for this problem.

The advantage of a spectral approach lies in its high accuracy which occurs after all essential structures of the unknown have been resolved. For illustration, we present the computed steady state results (i.e. at $t = 50s$) for different polynomial orders N_F and N_R, i.e. for different degrees of freedom. Here, N_R denotes the number of Gauss-Legendre quadrature points
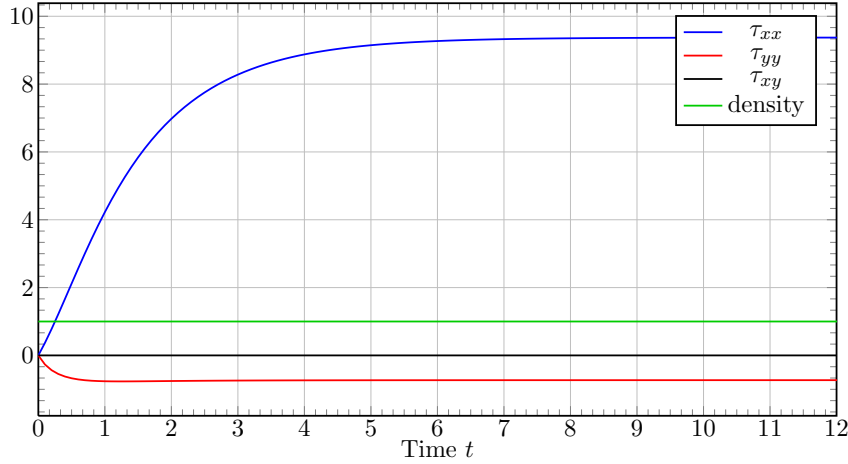
Figure 6.1: Numerical results for a planar extensional flow with extensional rate $\dot{\epsilon} = 1.0$. The plot does not only contain the three independent stress tensor components but also the integral of ψ over the configuration space. We use the integral as an error indicator to prove that ψ is still a probability density function (i.e. integral over ψ yields 1.0).

N_F	N_R	Computed result	Relative error	$\int \psi \, d\vec{q}$
3	7	9.4302870616314	6.2_{-3}	1.000000
5	11	9.3727693397900	3.7_{-5}	1.000000
7	15	9.3724237716453	1.1_{-7}	1.000000
11	23	9.3724227773931	3.6_{-11}	1.000000
15	31	9.3724227777387	6.7_{-13}	1.000000

Table 6.2: The table presents the relative error and the computed results for the first stress tensor component τ_{xx} in relation to the degrees of freedom (extensional flow with $\dot{\epsilon} = 1.0$). The plot of ψ over the configuration space yields 1.0 for all computations so that there does not exist any additional error resulting from a violation of the normalisation property.

$(\eta_0, \eta_1, \ldots, \eta_{N_R})$ so that the corresponding Lagrange interpolation polynomials are of degree N_R (cf. Section 4.1.2). Furthermore, N_F states the highest frequency for our real-valued Fourier basis functions. As the solution is symmetric in the angular component ϕ, we only need half of the trigonometric functions (i.e. the even ordered ones). Therefore, we choose N_F to be half of the size of N_R and present our computed results for the first stress tensor component τ_{xx} in Table 6.2. As mentioned before, the spectral approach is perfectly adapted to the problem as it is described on a regular domain and its initial state and steady state are smooth (i.e. $\psi_{eq}, \psi_{sol} \in C^\infty(B_{\sqrt{10}}(0))$).

Subsequently, we analyse the evolution of the probability density function itself towards its steady state (cf. Figure 6.2). We plot the density function by evaluating the basis system on a Cartesian grid with 40×40 evaluation points. At the beginning, the dumbbells possess no preferred orientation which results in an initial condition that does not depend on the angular coordinate ϕ. Note that the initial condition ψ_{eq} (2.85) for the FENE spring force is not Gaussian in contrast to the Hookean and FENE-P spring forces. Then the dumbbell system evolves into a preferred orientation due to the stretching of the flow in one direction. As we

can exchange both beads of the dumbbell or rotate the system by an angle of π and obtain the same physical system, the solution also features this symmetry. After about $t = 10$, we further note that the plot of ψ as well as the results for $\boldsymbol{\tau_p}$ are close to their steady state and exhibit only minor changes henceforth.

### 6.1.2 Strong Extensional Flow

Fokker-Planck Equation

We now consider an extensional flow with increased extensional rate $\dot{\epsilon} = 5.0$. An increase in $\dot{\epsilon}$ leads to a more challenging problem as the solution contains local regions with very high gradients. If we used a finite difference or finite element scheme, this would necessitate an adaptive discretisation ansatz that produces fine meshes at these regions or would otherwise lead to very long computing times. On the contrary, our basis functions are defined globally so that we can only increase the polynomial orders N_F and N_R. Accordingly, we have to apply more polynomials to achieve an accurate solution in this case. Furthermore, we notice that our problem features characteristics of a stiff equation as our 3rd-order Runge-Kutta scheme becomes numerically unstable unless we choose small time-step sizes (in the order of 10^{-8}). Therefore, we decide for an implicit Crank-Nicolson scheme that only features a second-order accuracy in time but allows the usage of higher time-step sizes. We present the parameters for the strong extensional flow in Table 6.3.

Strong Extensional Flow (Fokker-Planck)		
Weissenberg number	Wi	1.0
Newtonian viscosity	β	0.0
Extensional rate	$\dot{\epsilon}$	5.0
Maximum spring extension	b	10.0
Transformation factor	s	2.0
Gauss-Jacobi $\Big\{$	α_J	0.0
	β_J	0.0
Spring force	$\vec{F}(\vec{q})$	FENE
Time Discretisation		CN2nd
Time-step size (const.)	Δt	10^{-4}

Table 6.3: Parameters for a two-dimensional extensional flow with strong extensional rate.

In an analogous manner as before, we calculate the analytical solutions for the stress tensor components τ_{xx}, τ_{yy}, and $\tau_{xy} = \tau_{yx}$. Therefore, we insert the parameters of Table 6.3 into the steady state solution ψ_{sol} for FENE spring forces (2.91) and evaluate the result using the Kramers stress tensor relation (6.2). Then we obtain

(a) $t = 0.0$ (equilibrium state)

(b) $t = 0.5$

(c) $t = 1.0$

(d) $t = 2.0$

(e) $t = 4.0$

(f) $t = 50.0$ (steady state)
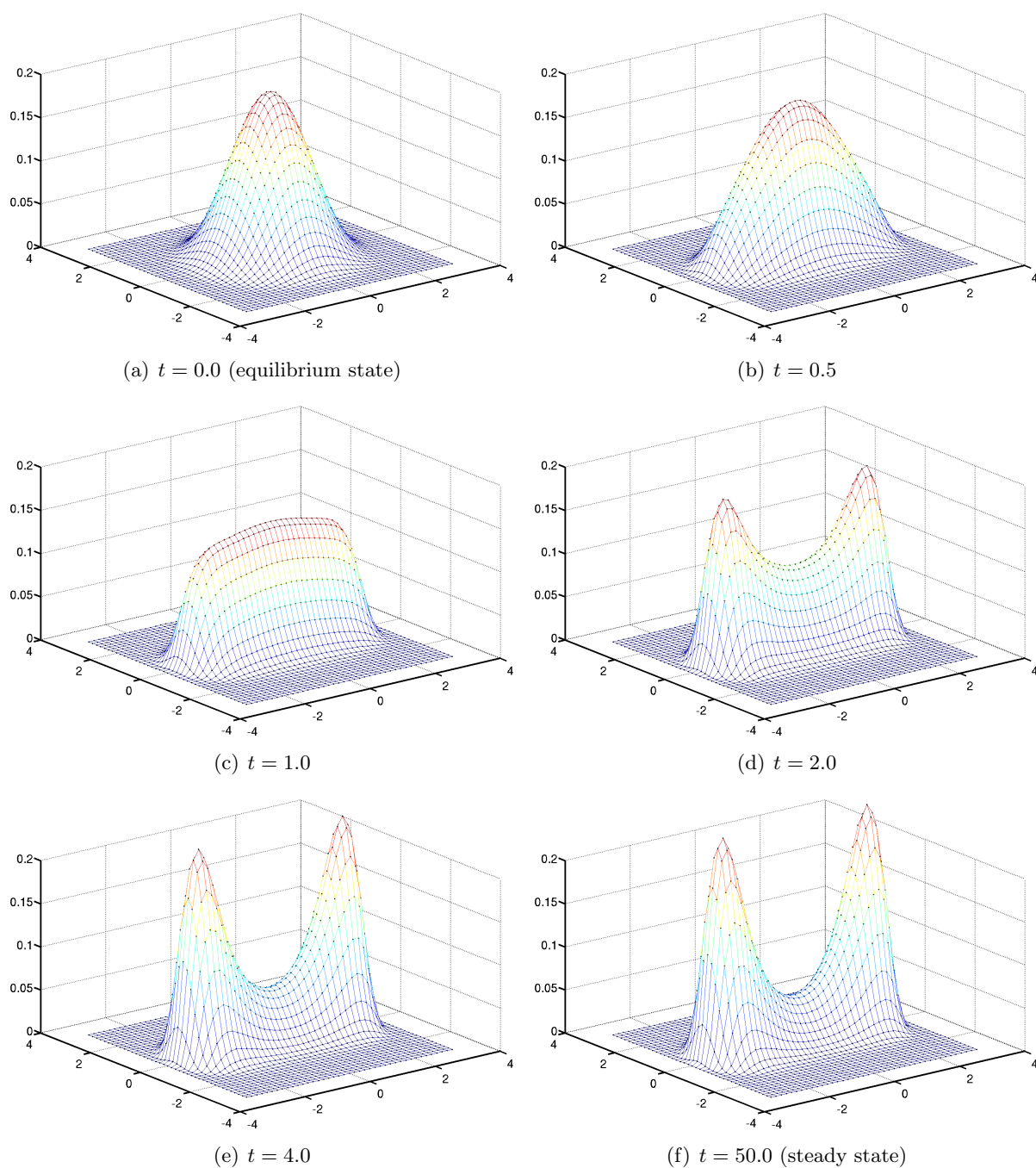
Figure 6.2: The figure illustrates the evolution of the probability density function ψ for a moderate planar extensional flow with $\dot{\epsilon} = 1.0$. In this case, ψ is defined on a disc with radius $\sqrt{10}$ around the origin. We evaluate the basis system on a Cartesian grid with the area $[-\sqrt{10}, \sqrt{10}] \times [-\sqrt{10}, \sqrt{10}]$ by using 40×40 evaluation points. The system evolves towards a steady state that is known analytically.

N_F	N_R	Computed result	Relative error	$\int \psi \, d\vec{q}$
7	15	156.0844321	2.8_{-1}	1.000000
11	23	123.3704929	8.8_{-3}	1.000000
13	27	122.4502169	1.3_{-3}	1.000000
15	31	122.3131260	1.4_{-4}	1.000000
23	47	122.2958174	2.5_{-9}	1.000000

Table 6.4: The table shows the relative error and the computed results for the first stress tensor component τ_{xx} compared to the degrees of freedom (extensional flow with $\dot{\epsilon} = 5.0$). Interestingly, even though coarse approximations yield results that are far away from the exact results, they actually fulfil the normalisation property. After all essential structures of the unknown are resolved, a spectral approach converges rapidly.

1. $\tau_{xx}^{\text{sol}} \approx 122.29581709311495$

2. $\tau_{yy}^{\text{sol}} \approx -0.7040923275873284$

3. $\tau_{xy}^{\text{sol}} = 0.0$

as analytical solution for $\boldsymbol{\tau_p}$. Consequently, in Table 6.4 we compare the computed results that we achieve using a spectral approach with the analytical solution. We note that we need more degrees of freedom to obtain the same relative error as for an extensional flow with $\dot{\epsilon} = 1.0$. We explain this effect due to a faster change of the dumbbells' orientation as the fluid velocity is strongly increased. Therefore, the stress tensor reaches its steady state value in a shorter period of time as can be seen in Figure 6.4.

Moreover, a spectral approach offers the opportunity that the asymptotic error converges with an order higher than any finite polynomial (spectral accuracy). We illustrate this by plotting the relative error against the degrees of freedom in Figure 6.3. As we consider real-valued sine and cosine functions, we obtain $2(N_F + 1)(N_R + 1)$ real degrees of freedom for certain choices of N_F and N_R. We notice that our approach outperforms classical low-order finite difference, finite element and finite volume schemes by far and achieves a superpolynomial convergence rate.

At last, we illustrate the evolution of ψ in Figure 6.5 by plotting the density function at different process times. Consequently, we decide for other time steps to plot ψ as the most important changes take place directly after the simulation has started. As mentioned above, the density function exhibits two localised regions with very high gradients. The physical interpretation of this behaviour is that the dumbbells can take only one specific orientation if we consider flow fields with high velocities. As the considered problem demands a high computational effort to be solved deterministically, we subsequently investigate the same problem with a stochastic approach to be able to compare the characteristics of both approaches.
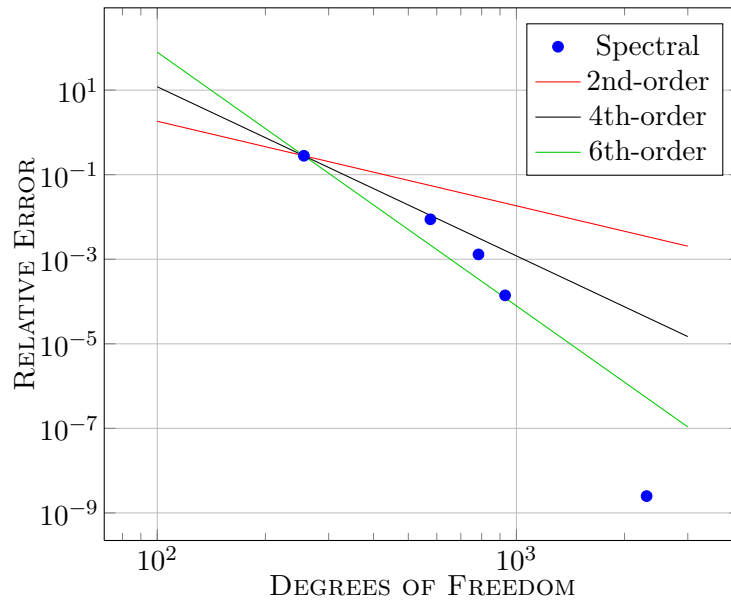
Figure 6.3: The figure illustrates the relative error for a given number of degrees of freedom (i.e. $2(N_F + 1)(N_R + 1)$) and compares the result with some typical orders of convergence that are fitted through the first spectral error measurement and represent no actual computation. As stated previously, spectral approaches achieve a high accuracy for comparatively few degrees of freedom and outperform any methods with polynomial convergence rates in the asymptotic.
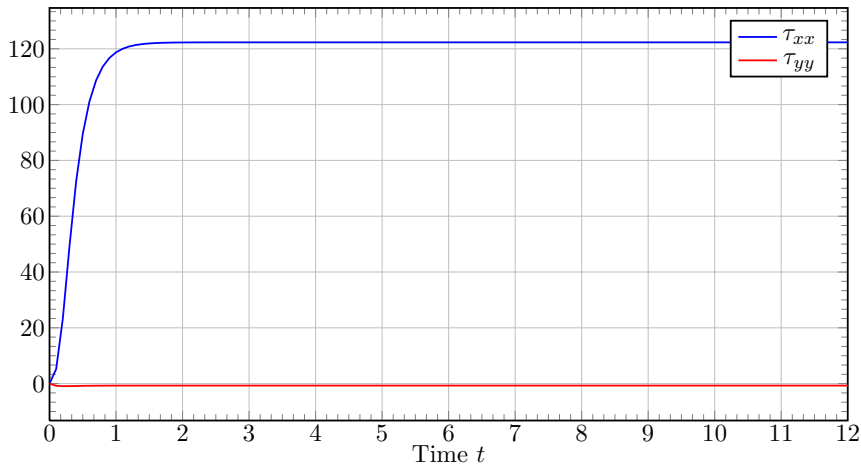
Figure 6.4: Numerical results for a planar extensional flow with extensional rate $\dot{\epsilon} = 5.0$. In this case, in comparison to the moderate extensional flow, we only plot the stress tensor components τ_{xx} and τ_{yy} since τ_{xy} and the integral of ψ over the configuration space cannot be distinguished from τ_{yy} in the chosen measure of the plot. The strong extensional flow results in fast stress tensor changes within a short period of time.

(a) $t = 0.0$ (equilibrium state)

(b) $t = 0.1$

(c) $t = 0.2$

(d) $t = 0.3$

(e) $t = 0.5$
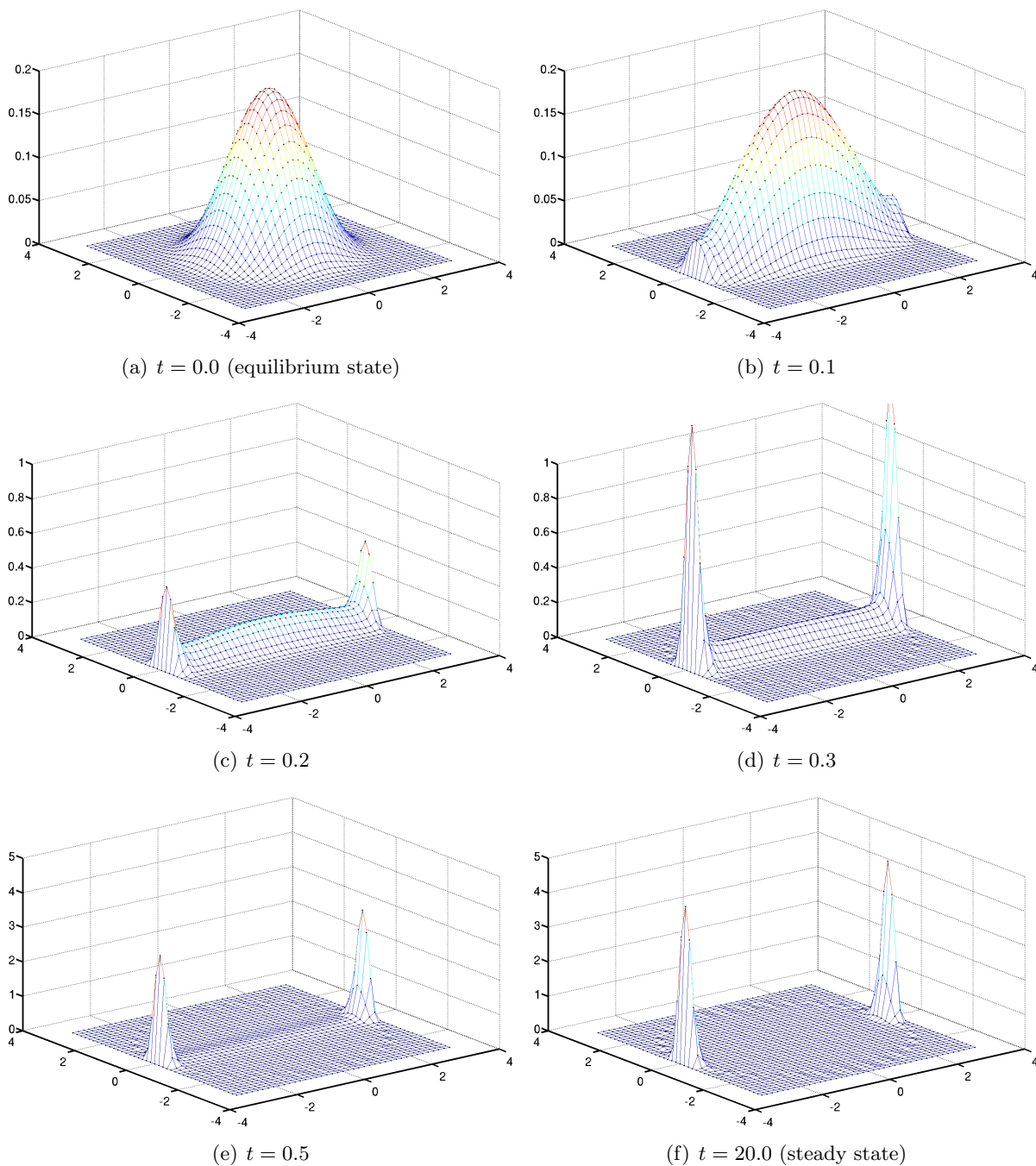
(f) $t = 20.0$ (steady state)

Figure 6.5: The strong extensional flow with $\dot{\epsilon} = 5.0$ reveals much stronger spatial gradients of ψ compared to $\dot{\epsilon} = 1.0$. Note that the density function takes a form close to its steady state in a much shorter period of time (after $t \approx 1.0$) and that we adapt the z-axis according to the new shape of ψ. A physical interpretation of this occurrence is that the variance of the dumbbells' alignment is substantially reduced for stronger flow fields.

Stochastic Partial Differential Equation

We subsequently present the results for an analogous computation using the stochastic method described in Chapter 4.2. Now, in contrast to the deterministic approach, we do not model a density function but describe the evolution of a discrete set of $s = 1, \ldots, N_f$ realisations for the stochastic process. In Table 6.5 we present the parameters for a stochastic simulation which we choose analogously to the parameters in Table 6.3. Note that we decide for a small time-step size to be able to solely investigate the stochastic noise for a given number of realisations N_f and do not catch an additional error in time. As our steady state approximations feature a stochastic noise, we do not only present one specific stress tensor value of τ_{xx} but an arithmetic mean over a time interval, i.e. we compute the expectation of τ_{xx} as

$$\langle \tau_{xx} \rangle \;=\; \frac{1}{\#M} \sum_{i \in M} \tau_{xx}(t_i) \qquad \text{for } M \equiv \{t_j | t_j \geq 2.0\}\,. \tag{6.3}$$

Strong Extensional Flow (Stochastic)		
Weissenberg number	Wi	1.0
Newtonian viscosity	β	0.0
Extensional rate	$\dot{\epsilon}$	5.0
Maximum spring extension	b	10.0
Spring force	$\vec{F}(\vec{Q})$	FENE
Time Discretisation		Eu-Maruyama
Time-step size (const.)	Δt	10^{-5}

Table 6.5: Parameters for a two-dimensional extensional flow with strong extensional rate using a stochastic approach.

We have decided to use an approximation after $t = 2.0$ as the stress tensor component τ_{xx} only exhibits minor changes henceforth (cf. Figure 6.4). Furthermore, we calculate its variance using the formula

$$\text{Var}(\tau_{xx}) \;=\; \frac{1}{\#M} \sum_{i \in M} (\tau_{xx}(t_i) - \langle \tau_{xx} \rangle)^2 \qquad \text{for } M \equiv \{t_j | t_j \geq 2.0\}\,. \tag{6.4}$$

In Table 6.6, we show the results for $\langle \tau_{xx} \rangle$, $\text{Var}(\tau_{xx})$ and the relative error in comparison to the analytical solution that we have stated before depending on the number of stochastic realisations N_f. We note that the variance of τ_{xx} depends linearly on N_f. On the contrary, the error in τ_{xx} does not converge monotonically to zero but only in probability.

Next, we plot the evolution of τ_{xx} against the process time t for different numbers of stochastic realisations N_f in Figure 6.6. Note that we plot our approximation for τ_{xx} at discrete intervals $\Delta t = 0.1$ and not in agreement with the time-step size in Table 6.5. In accordance with Table 6.6, we observe that the more stochastic realisations we use the less oscillation occurs in the stress tensor. On the contrary, the computation time also scales linearly with the number of unknowns so that 10^6 approximations increase the computation time by a factor of 10^4 in comparison with only 10^2 stochastic values.

Realisations N_f	$\langle \tau_{xx} \rangle$	Rel. error $\langle \tau_{xx} \rangle$	$\mathrm{Var}(\tau_{xx})$
10^2	122.464877	1.4_{-3}	44.83021
10^3	121.939040	2.9_{-3}	4.588844
10^4	122.195037	8.2_{-4}	0.467596
10^5	122.189977	8.6_{-4}	0.046170
10^6	122.257581	3.1_{-4}	0.003982

Table 6.6: The table illustrates the variance and relative error for τ_{xx} depending on the number of stochastic realisations (extensional flow with $\dot{\epsilon} = 5.0$). As stated before, the error does not converge monotonically to zero as it only converges in probability. However, the variance of the result depends on the number of realisations.
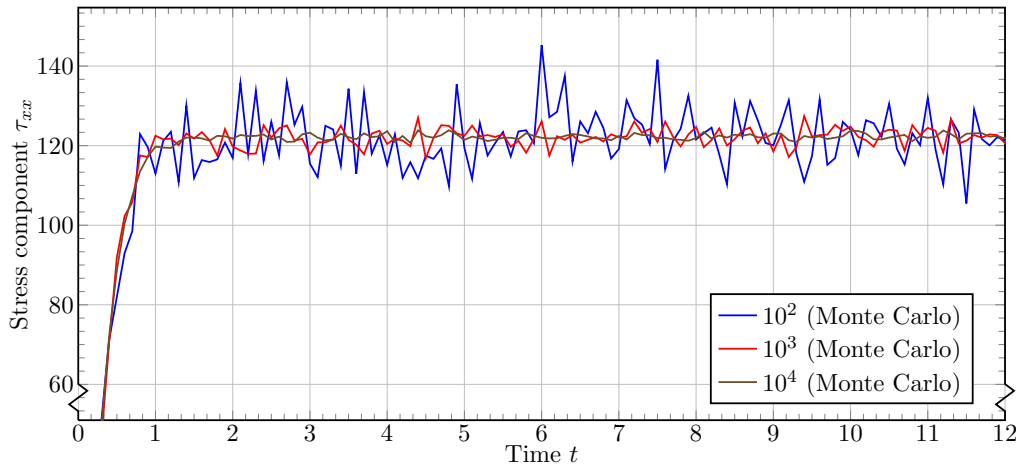
Figure 6.6: The plot displays the evolution of τ_{xx} for an extensional flow ($\dot{\epsilon} = 5.0$) in time using three different coarse stochastic approaches. Obviously, the more stochastic realisations we use the less stochastic noise appears in the plot. We do not present the graph using 10^5 or 10^6 realisations as it cannot be distinguished from the deterministic results in Figure 6.4.

Comparison of Both Approaches

We compare the advantages and disadvantages of both approaches in two space dimensions with each other. A discretisation of the 2D Fokker-Planck equation using spectral methods

- allows computation of the analytical solution within machine accuracy,

- features a high order of convergence and

- is relatively cheap for its high accuracy.

A stochastic approach features the advantages that

- it is very cheap if only a coarse approximation is required and

- it is very robust with regard to the complexity of the problem.

Indeed, although we might have to adapt the time-step size for a stochastic method depending on whether we compute a moderate flow with $\dot{\epsilon} = 1.0$ or a strong flow with $\dot{\epsilon} = 5.0$ we do not

require any additional stochastic realisations to achieve numerically stable results regardless of the complexity of the flow. On the contrary, for the spectral approach, the more complex the flow problem, the more basis polynomials will be required. If we do not employ sufficient basis functions, the deterministic scheme becomes numerically unstable.

Furthermore, the stochastic approach features a further advantage that becomes important for high-dimensional configuration spaces. A three-dimensional configuration space implies a three-dimensional Fokker-Planck equation for homogeneous (cf. (2.62)) and a six-dimensional equation for transient flow fields (cf. (2.61)). Due to the complexity of the equation, a spectral approach then becomes much more expensive in higher dimensions than for two dimensions. In contrast, a stochastic method is also suited for problems with high-dimensional configuration spaces. Therefore, from a specific dimension of the configuration space we have to rely on stochastic approaches. As far as we know, it is a matter of current investigation whether a deterministic Fokker-Planck approach is suited for dealing with general three-dimensional flow fields or not.

6.1.3 Strong Shear Flow

In this section, we investigate homogeneous shear flows in the plane in which the velocity field takes the form

$$\vec{u} = (\dot{\gamma}y, 0) \tag{6.5}$$

with $\dot{\gamma}$ as shear rate. For further illustration of the flow field we refer to Section 2.1.3. In contrast to homogeneous extensional flows, there exists no analytical solution for the density function in this case but only a first order approximation in $\dot{\gamma}$ (cf. (2.87)). However, since we examine a shear flow using the same parameters as Chauvière et al. [20] and Knezevic [49], we can compare the results for the time-dependent evolution of the stress tensor.

Fokker-Planck Equation

In Table 6.7 we list the parameters for the shear flow using the deterministic spectral approach for the Fokker-Planck equation. As the shear rate $\dot{\gamma}$ is comparatively high, we use more polynomial basis functions and a small time-step size to achieve a numerically stable approximation. In literature, the product "Wi $\dot{\gamma}$" is, ignoring a normalisation constant, often denoted as the *reduced shear rate* (cf. Section 4.3.2 of Öttinger [66]).

In Figure 6.7 we illustrate the evolution of τ_{xx}, τ_{xy} and τ_{yy} using a discretisation with polynomial order $N_F = 19$ and $N_R = 39$. Comparing our results with Chauvière et al. [20] and Knezevic [49], we observe quite a good qualitative agreement in the evolution of $\boldsymbol{\tau_p}$. Furthermore, for the density function our approximation yields 1.0 within machine accuracy which proves that our approximations fulfil the requirements of a probability density function for all times.

Overshoots and undershoots of the fluid velocities and the stress tensor components are typical for most viscoelastic flow problems. In Figure 6.7 we also observe that maximum values for τ_{xx}, τ_{xy}, and τ_{yy} directly occur after the beginning of the calculation and decrease subsequently. Actually, the maxima for the stress tensor components occur at different times. First, τ_{yy} takes its maximum value at $t \approx 0.7$ and afterwards τ_{xy} and τ_{xx} reach their maxima at $t \approx 0.9$ and $t \approx 1.5$ respectively. Furthermore, there are more over- and undershoots of

| Strong Shear Flow (Fokker-Planck)		
Weissenberg number	Wi	1.0
Newtonian viscosity	β	0.0
Shear rate	$\dot{\gamma}$	10.0
Maximum spring extension	b	150.0
Transformation factor	s	2.0
Gauss-Jacobi $\Big\{$	α_J	0.0
	β_J	0.0
Spring force	$\vec{F}(\vec{q})$	FENE
Time Discretisation		CN2nd
Time-step size (const.)	Δt	10^{-4}

Table 6.7: Parameters for a two-dimensional strong shear flow.

the stress tensor afterwards which are not visible in Figure 6.7 as the amplitude decays with ongoing time. Interestingly, the second normal stress component τ_{yy} returns to its initial value of zero with high accuracy. Since Chauvière et al. [20] and Knezevic [49] do not investigate the evolution of τ_{yy}, we present our detailed analysis of $|\tau_{yy}|$ in Figure 6.8 without further proof.

Subsequently, we exhibit the time-dependent evolution of the probability density function in Figure 6.9. For the shear flow we do not observe two separated peaks for the density function but instead we note two maxima that are still connected with each other. Accordingly, a shear flow orientates the dumbbells primarily and does not change their extension in the same way as an extensional flow. In theory, the density function for a shear flow does not reach a steady state value since it still exhibits oscillations which decay with ongoing time.

As the two-dimensional stochastic approach delivers the same results for the stress tensor evolution as the Fokker-Planck method in Figure 6.7, we only apply stochastic techniques on three-dimensional shear flows in Section 6.2.4.

As a conclusion, we have shown that a Fokker-Planck approach using spectral methods delivers approximations with high accuracy for two-dimensional flow problems. In the next chapter, we concentrate on analogous problems that are defined on three-dimensional configuration spaces.
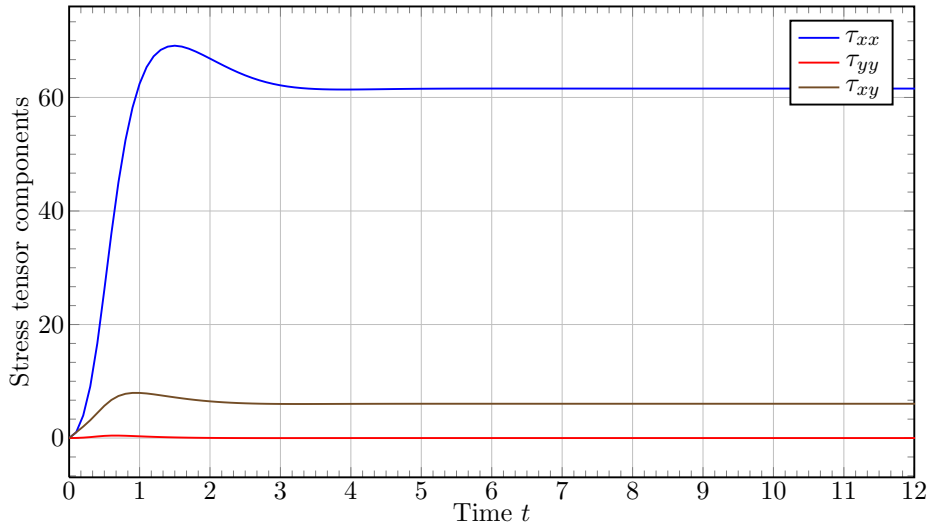
Figure 6.7: The plot shows the evolution of τ_{xx}, τ_{xy}, and τ_{yy} for a strong shear flow with shear rate $\dot{\gamma} = 10$. For shear flows, we observe over- and undershoots in the stress tensor values, but only the first overshoot is visible in the plot as the oscillations decay in time.
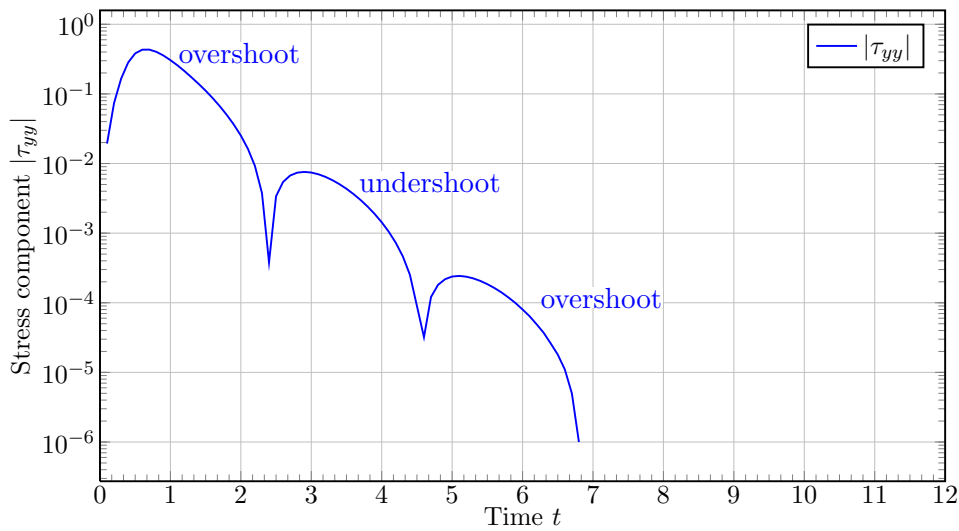
Figure 6.8: The plot illustrates the absolute value of the stress tensor component τ_{yy} in a semilogarithmic scale in detail so that we can observe the decaying oscillation around the initial value of zero (cf. Figure 6.7). Since we consider $|\tau_{yy}|$ instead of simply τ_{yy}, we observe points of discontinuity for the first derivative of the graph every time τ_{yy} changes its sign. After $t = 6.8$ the values are undistinguishable to zero for the given accuracy.

(a) $t = 0.0$ (equilibrium state)

(b) $t = 0.2$

(c) $t = 0.5$

(d) $t = 0.8$

(e) $t = 1.5$ (maximum overshoot of τ_{xx})

(f) $t = 12.0$
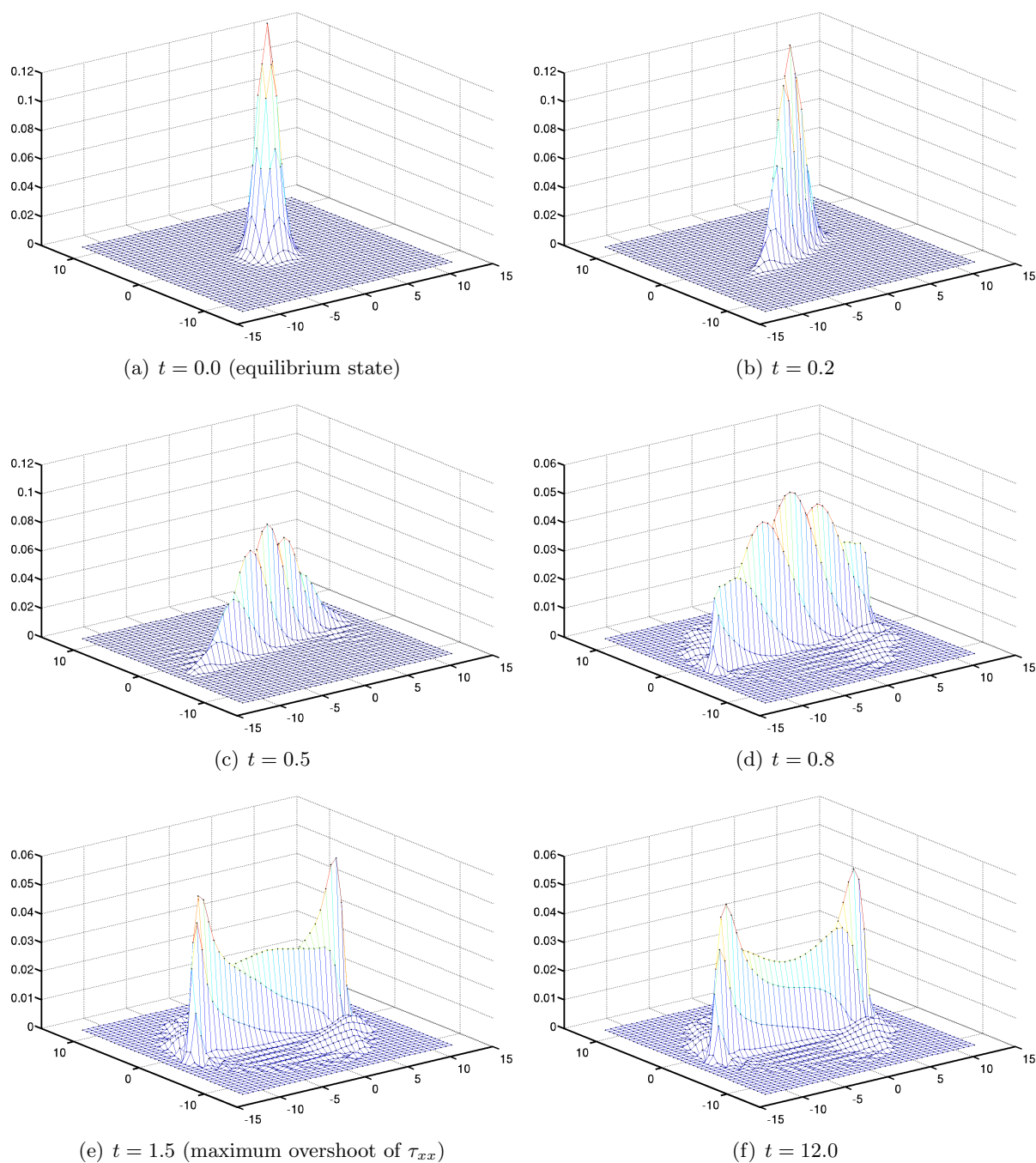
Figure 6.9: The plot visualises the evolution of ψ for a strong shear flow ($\dot{\gamma} = 10.0$). Since the maximum extension is $b = 150$ we plot ψ on a grid with area $[-\sqrt{150}, \sqrt{150}]^2$. In contrast to an extensional flow, we do not observe isolated peaks of the density function but instead identify a wider support of ψ that connects the maximum values. We explain the result by assuming that dumbbells primarily change their orientation in a shear flow instead of being extended as in an extensional flow.

6.2 3D Homogeneous Flows

In this chapter, we present our numerical approximation for three-dimensional, homogeneous flow fields like extensional and shear flows using a stochastic approach (cf. Chapter 4.2). Unless noted otherwise, we employ the nonlinear, multiscale FENE spring force for all our computations.

6.2.1 Extensional Flow with Different Spring Forces

We subsequently analyse uniaxial, three-dimensional extensional flows in the x-direction that are described by a velocity field of the form

$$\vec{u} = (\dot{\epsilon}x, -\frac{\dot{\epsilon}}{2}y, -\frac{\dot{\epsilon}}{2}z) \tag{6.6}$$

with $\dot{\epsilon}$ as extensional rate. The aim of this section is

- to investigate the accuracy of our three-dimensional stochastic schemes and

- to illustrate that the Hookean dumbbell/ Oldroyd-B and UCM model predict unrealistic stress tensor values in this case.

For an illustration of an uniaxial extensional flow field we refer to Figure 2.6 in Section 2.1.3 where we further describe the characteristics of extensional flows.

Apart from that, we set $\dot{\epsilon} = 1.0$ and Weissenberg number $Wi = 0.5$ for all spring forces that we investigate in this section. This choice will become clear when we examine the Hookean dumbbell model. Furthermore, the analytical results for the FENE and the Hookean spring forces are known so that we are able to analyse the error for these models.

FENE Spring Force

Analogously to the two-dimensional case, we insert the steady state solution ψ_{eq} (2.85) into the Kramers expression (4.13) which takes the form

$$\boldsymbol{\tau_p}^{\text{sol}} = \frac{1-\beta}{Wi} \left(\frac{b+5}{b} \right) \left(-\mathbf{Id} + \int_{|\vec{q}|<\sqrt{b}} \vec{q} \otimes \frac{\vec{q}}{1 - \frac{\|\vec{q}\|^2}{b}} \, \psi_{ext} \, d\vec{q} \right) \tag{6.7}$$

in three dimensions. Note that we have to evaluate the integral in (6.7) over a sphere with radius $\sqrt{b}$ in contrast to the integration over a disc in (6.2); note further that the 3D Kramers expression features slightly different coefficients as its 2D analogon. Inserting the parameters of Table 6.8 into (6.7) yields

1. $\tau_{xx}^{\text{sol}} \approx 4.024546$,

2. $\tau_{yy}^{\text{sol}} \approx -0.741848$,

3. $\tau_{zz}^{\text{sol}} \approx -0.741848$,

4. zero for all shear stresses

as analytical solutions for the stress tensor components.

| Extensional Flow (Stochastic)		
Weissenberg number	Wi	0.5
Newtonian viscosity	β	0.0
Extensional rate	$\dot{\epsilon}$	1.0
Maximum spring extension	b	10.0
Time Discretisation		Eu-Maruyama
Time-step size (const.)	Δt	10^{-3}

Table 6.8: Parameters for a three-dimensional extensional flow using a stochastic approach.

Table 6.9 presents our numerical approximations for the expectation $\langle \tau_{xx} \rangle$ and the variance $\text{Var}(\tau_{xx})$ of τ_{xx} using formulae (6.3) and (6.4) for all $t_i \in M \equiv \{t_j | t_j \geq 3.0\}$. We have chosen to employ all computed stress tensor values at $t \geq 3.0$ for the computation of $\langle \tau_{xx} \rangle$ and $\text{Var}(\tau_{xx})$ since the stress tensor has reached a value close to its steady state result henceforward (cf. Figure 6.10). Furthermore, from Table 6.9 we conclude that an increase in stochastic realisations $s = 1, \ldots, N_f$ primarily reduces the variance of the expectation $\langle \tau_{xx} \rangle$ but increases the accuracy of the approximation very slowly in the order of $\mathcal{O}(N_f^{-0.5})$.

Interestingly, the other spring force models predict differing results for the same flow parameters as in Table 6.8 which we will analyse subsequently.

Realisations N_f	$\langle \tau_{xx} \rangle$	Rel. error $\langle \tau_{xx} \rangle$	$\text{Var}(\tau_{xx})$
10^2	3.974353	1.2_{-2}	1.233224
10^3	4.066180	1.0_{-2}	0.108274
10^4	4.039051	3.6_{-3}	0.010986
10^5	4.028225	9.1_{-4}	0.001220
10^6	4.026106	3.9_{-4}	0.000118

Table 6.9: The table displays the relative error and the variance for the first stress tensor component in a 3D extensional flow with a FENE spring force. On the one hand, we conclude that the variance decreases in the order of $\mathcal{O}(N_f^{-1})$ but on the other hand the relative error only decreases with an order of $\mathcal{O}(N_f^{-0.5})$.
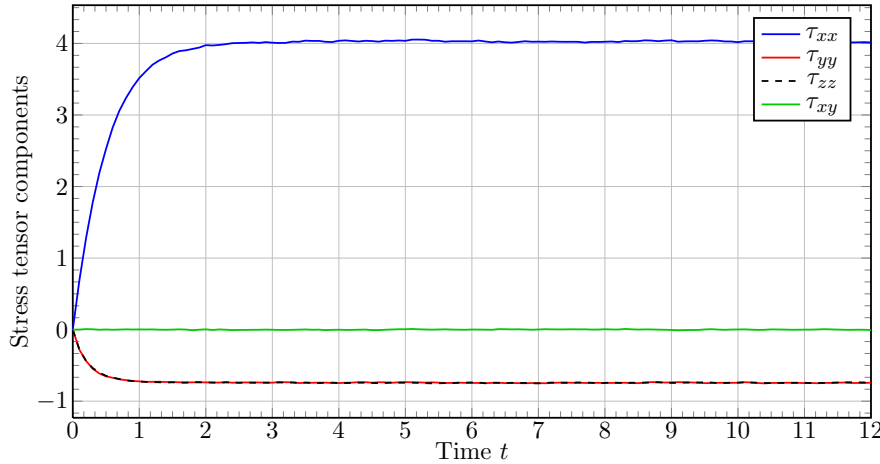
Figure 6.10: The plot illustrates the development of the stress tensor components for a 3D extensional flow with a FENE spring force. Interestingly, the stress tensor for the FENE spring force reaches finite steady state values in contrast to the Hookean dumbbell model which predicts an infinite first stress tensor component τ_{xx} for the same flow parameters (cf. Figure 6.11).

Hookean Spring Force

We now consider the analogous extensional flow problem for a linear Hookean spring model. First, we are interested in deriving steady state values for the stress tensor so that we can compare our approximations with an analytical solution. For a Hookean dumbbell fluid we do not have to consider the probability density function in the extensional flow case, because there exist analytical solutions for the equivalent macroscopic UCM (i.e. $\beta = 0$) and Oldroyd-B models (i.e. $\beta \in (0,1)$). Since we have already discussed the results in formulae (2.35) and (2.36) of Section 2.2.2 for the Oldroyd-B case, we only present the major results for $\beta = 0$ which are

$$\tau_{xx} = \frac{2\dot{\epsilon}}{1 - 2\,Wi\,\dot{\epsilon}}, \quad \tau_{yy} = \tau_{zz} = -\frac{\dot{\epsilon}}{1 + Wi\,\dot{\epsilon}} \tag{6.8}$$

and zero for all other tensor components. If we insert the parameters of Table 6.8 into equation (6.8), we obtain $\tau_{yy} = \tau_{zz} = \frac{2}{3}$ but an infinite first stress tensor component τ_{xx} as its denominator becomes zero. We confirm this result in Figure 6.11 in which we match our approximation of τ_{xx} for the Hookean dumbbell with the previous results for the FENE dumbbell. Although we achieve the analytical results for τ_{yy} and τ_{zz} from (6.8), we skip them in Figure 6.11, because we intend to explain the unrealistic results of the Hookean model for τ_{xx}.

In addition to the results in Figure 6.11, we have computed Hookean first stress tensor approximations for process times $t > 12$ and further observe a continuous increase of τ_{xx}. In Chapter 2.3 we have already given a micromolecular interpretation as the Hookean dumbbell model is not restricted in its length. Due to the constant stretching in an extensional flow the Hookean spring becomes more and more extended so that the stress grows continuously. Therefore, only the restriction in length prevents the peaks of the 2D density function in Figure 6.5 to move more and more from the origin.

Furthermore, in Figure 6.11 we observe another difference between the FENE and the
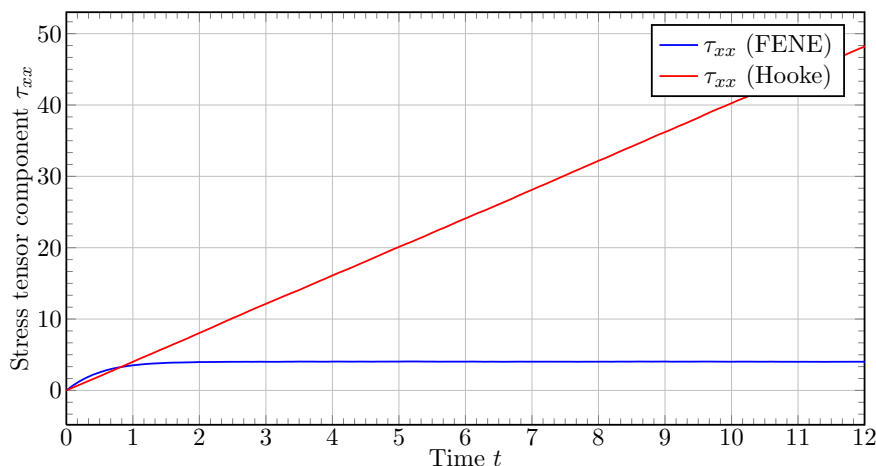
Figure 6.11: The plot compares the first stress tensor component τ_{xx} (FENE) from Figure 6.10 with the results for a Hookean spring in the case of a 3D extensional flow. We observe that τ_{xx} is unbounded for Hookean dumbbells and because of that the model is unsuited for the description of extensional flows. Furthermore, we note that the FENE model exhibits a quicker response on a sudden force as its stress tensor exhibits a steeper increase for $0 \le t \le 0.8$.

Hookean spring. Although the FENE spring force predicts much lower (i.e. finite) first stress tensor values, it shows a much quicker response to a sudden force which can be seen at initial time $0 \le t \le 0.8$ in Figure 6.11 where the predicted FENE stress exceeds the Hookean stress values.

FENE-P Spring Force

At last, we investigate the difference between the original FENE spring force on the one hand and one of its closure approximations, the FENE-P closure, on the other hand. The aim of the FENE-Peterlin spring force (2.79) is to convey the advantages of the exact micromolecular FENE model into a macroscopic constitutive equation (cf. Section 2.3.6). Accordingly, any differences between both models are the result of a poor approximation of the FENE model by the closure approximation.

In Figure 6.12, we compare the predictions of the FENE and FENE-P model for the first and second stress tensor components τ_{xx} and τ_{yy} with each other. We note that the FENE-P closure tends to overestimate the FENE amplitudes. For this reason, the FENE-P approach predicts higher stress tensor values than the FENE model. Again, we explain this effect by a micromolecular interpretation. As the FENE-P model only restricts the average of all configurations $\langle \vec{q}^2 \rangle^{1/2}$ by $\sqrt{b}$ this does not prevent the existence of configurations whose length exceeds $\sqrt{b}$. However, the FENE-P model actually restricts the stress tensor to finite steady state results so that the FENE-P model delivers at least better results than the Oldroyd-B model for extensional flows.
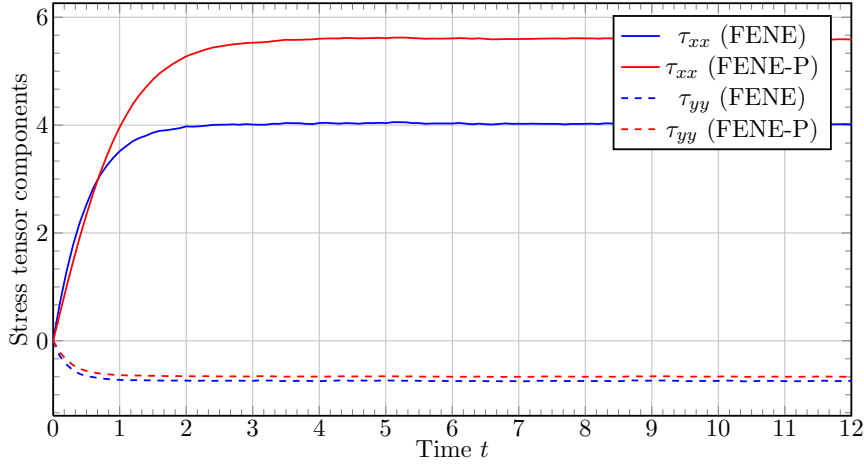
Figure 6.12: The figure compares the first and second normal stress tensor values predicted by the FENE and the FENE-P dumbbell model. As the predictions for τ_{zz} are indistinguishable from the values for τ_{yy} in both models and as all other stress components are zero, we do not present them in the figure. We note that the FENE-P closure overestimates the stresses as it restricts only the average dumbbell configuration vector by $\sqrt{b}$ which still allows several configurations to remain outside of the sphere.

6.2.2 Reconstruction of 3D Density Function

One important difference between the Fokker-Planck approach and the stochastic techniques is that the Monte Carlo method does not consider a density function ψ at all but instead evolves a random variable that is distributed according to ψ. Consequently, as we use a stochastic method, we have to develop density recovering techniques so that we can present plots of the density function as shown in Figure 6.2, Figure 6.5, and Figure 6.9. Note that we reconstruct the probability density function only to illustrate that the stochastic realisations are actually distributed according to ψ. For viscoelastic computation we only need results for the stress tensor $\boldsymbol{\tau_p}$ while ψ is no variable of interest.

In this section we present

- a reconstruction of the density function ψ by analysing the distribution of $\vec{Q}_t$ and

- a finite difference ansatz for the Fokker-Planck equation (cf. Chapter 3.1) that yields quantitative information for ψ.

In both cases, we consider a moderate uniaxial 3D extensional flow that is similar to the 2D case in Table 6.1 (i.e. $\dot{\epsilon} = 1.0$, $Wi = 1.0$, $b = 10.0$). Hence, we are able to compare the results in this section with Figure 6.2 for the 2D probability density function.

Density Recovering

Our ansatz for recovering the probability density function from the stochastic process $\vec{Q}_t$ is based on subdividing the computational domain into cells, counting the number of stochastic realisations in each grid cell and then calculating the percentage of realisations in each sub-domain cell. As the obtained density function $\psi : D \subset \mathbb{R}^3 \to \mathbb{R}^+$ is difficult to visualise, we

(a) Equilibrium state (stochastic)

(b) Steady state (stochastic)

(c) Equilibrium state (exact)

(d) Steady state (exact)
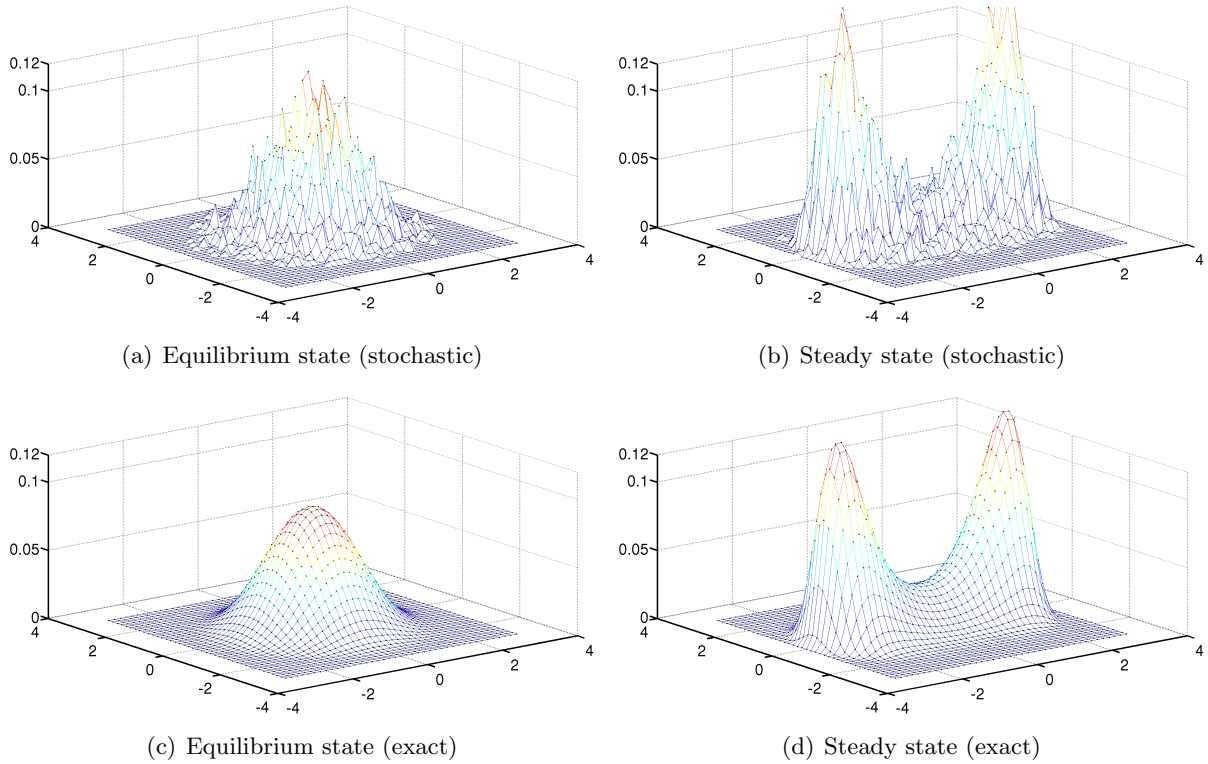
Figure 6.13: The figure presents a two-dimensional cut through the 3D density function on the sphere. Altogether we employ 10^5 stochastic realisations, but only a few thousand are used for the density functions in (a) and (b) so that the approximation only reconstructs the coarse shape of the exact solutions (c) and (d). Nevertheless, we can prove that the stochastic realisations are actually distributed according to ψ.

restrict our results to the density values on the x-y-plane $z = 0$. In Figure 6.13 we compare the reconstructed density functions for 10^5 realisations on the whole sphere with the analytical solutions for the equilibrium and the steady state density function (2.85) and (2.91).

The applied density approximation reproduces a very coarse shape of ψ, because only a few thousand realisations on the sphere actually contribute information for the density function at $z = 0$. Furthermore, as we employ a histogram scheme for the reconstruction of ψ, we introduce an additional error depending on the size of a histogram cell. Nevertheless, we can prove that the stochastic realisations are actually distributed according to ψ.

Deterministic Finite Difference Approach

In Chapter 3.1 we have considered an ansatz using finite differences for the discretisation of the 3D Fokker-Planck equation defined on $B_{\sqrt{b}}(0) \subset [-\sqrt{b}, \sqrt{b}]^3$. Although this approach is not suited to compute exact steady state stress tensor values, it delivers a noise-free approximation of the density function ψ in contrast to the stochastic method that we use in Figure 6.13. We employ the same parameters as before and present the evolution of ψ with 200^3 gird points at discrete process times $t = 0$, $t = 1$, $t = 2$, and $t = 5$ in Figure 6.14 and Figure 6.15. Here, we

N_f	Euler-Maruyama			Euler-Maruyama with reduction		
	$\langle \tau_{xx} \rangle$	Relative error	$\mathrm{Var}(\tau_{xx})$	$\langle \tau_{xx}^v \rangle$	Relative error	$\mathrm{Var}(\tau_{xx}^v)$
10^2	3.974353	1.2_{-2}	1.233224	3.991044	8.3_{-3}	0.494604
10^3	4.066180	1.0_{-2}	0.108274	4.050090	6.3_{-3}	0.046528
10^4	4.039051	3.6_{-3}	0.010986	4.030791	1.6_{-3}	0.004472
10^5	4.028225	9.1_{-4}	0.001220	4.025878	3.3_{-4}	0.000511
10^6	4.026106	3.9_{-4}	0.000118	4.026851	5.7_{-4}	0.000040

Table 6.10: For an extensional flow, we observe that an equilibrium control variate reduces the variance by about 60 percent. Furthermore, the accuracy of the stress tensor approximation $\langle \tau_{xx}^v \rangle$ also seems to be improved, but this cannot be stated precisely as the error does not decay monotonically. In the case of a homogeneous flow field with one stochastic process in total an equilibrium control variate roughly doubles the computational cost. Nevertheless, for non-homogeneous flow fields with thousands of stochastic processes the additional cost for a control variate is negligible.

consider three different slices through the origin that are defined by $x = 0$, $y = 0$, and $z = 0$.

As a result, we discover that not only the equilibrium condition (2.85) and the steady state solution (2.91) possess a symmetry around the x-axis, but also all intermediate values for the density function ψ in 3D feature this symmetry. Consequently, our plots for the x-y plane (i.e. $z = 0$) and the x-z plane (i.e. $y = 0$) are indistinguishable from each other. Furthermore, the y-z plane (i.e. $x = 0$) in Figure 6.15 illustrates that the density function is stretched towards the positive and negative x-axis so that the probability of having small dumbbell extensions reduces with ongoing time.

6.2.3 Variance Reduced Extensional Flow

In Section 4.2.3 we have introduced the basic concepts of variance reduction for stochastic simulations. A common approach in polymeric simulations is the usage of an equilibrium control variate which evolves a second stochastic process in time by applying the same diffusive noise and the same spring force on the system but omitting the influence of the velocity field $\vec{u}$ (cf. Section 4.2.3).

In the following section, we investigate the success of an equilibrium control variate for an extensional flow with the same parameters as in Table 6.8. We present the variance reduced results in Table 6.10 where we compare the approximations for the Euler-Maruyama scheme from Table 6.9 with the approximations using a variance reduced Euler-Maruyama method. Indeed, the equilibrium variate reduces the variance of our approximation by about 60 percent and also seems to increase the accuracy which we achieve for the expectation $\langle \tau_{xx} \rangle$.

For a homogeneous flow field an equilibrium control variate doubles the cost as we now have to evolve two stochastic processes in time. As the variance for $\vec{Q}_t$ scales linearly with N_f, we could also halve the variance by just using $2N_f$ realisations for $\vec{Q}_t$ without using a control variate. Nevertheless, for a non-homogeneous flow field (i.e. we additionally have to solve the Navier-Stokes equations) the computational cost for an equilibrium control variate is negligible, because we can reuse one equilibrium control variate for all grid cells in which we have to compute a stochastic process. If we could reduce the stochastic noise only by several

(a) $t = 0.0$ (plane z=0)

(b) $t = 1.0$ (plane z=0)

(c) $t = 2.0$ (plane z=0)

(d) $t = 5.0$ (plane z=0)

(e) $t = 0.0$ (plane y=0)

(f) $t = 1.0$ (plane y=0)
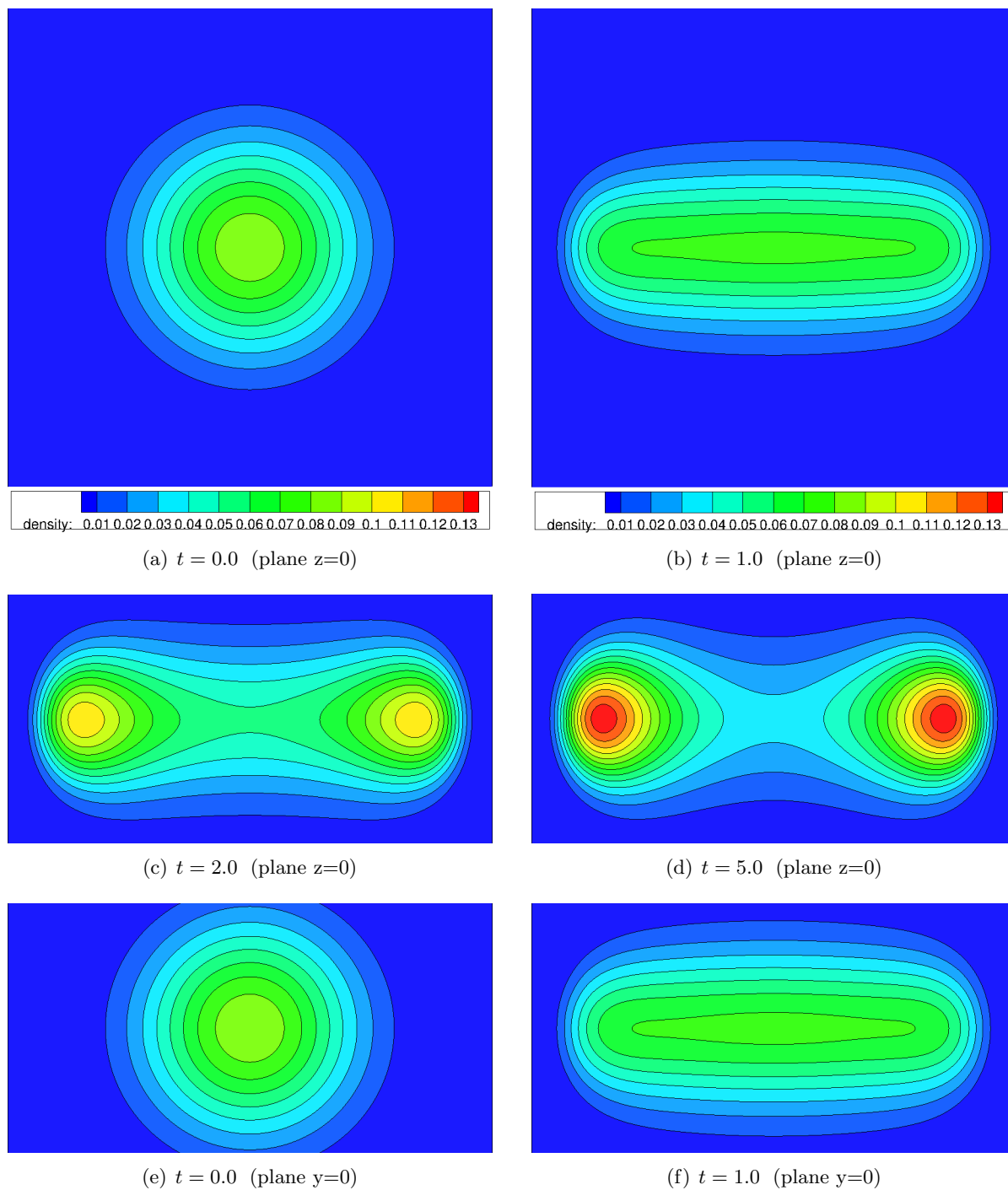
Figure 6.14: Figures (a) to (d) present density values for the x-y plane through the origin which are identical to results for the x-z plane in (e) and (f) and the results (a) and (b) in Figure 6.15.

(a) $t = 2.0$ (plane y=0)

(b) $t = 5.0$ (plane y=0)

(c) $t = 0.0$ (plane x=0)

(d) $t = 1.0$ (plane x=0)

(e) $t = 2.0$ (plane x=0)

(f) $t = 5.0$ (plane x=0)
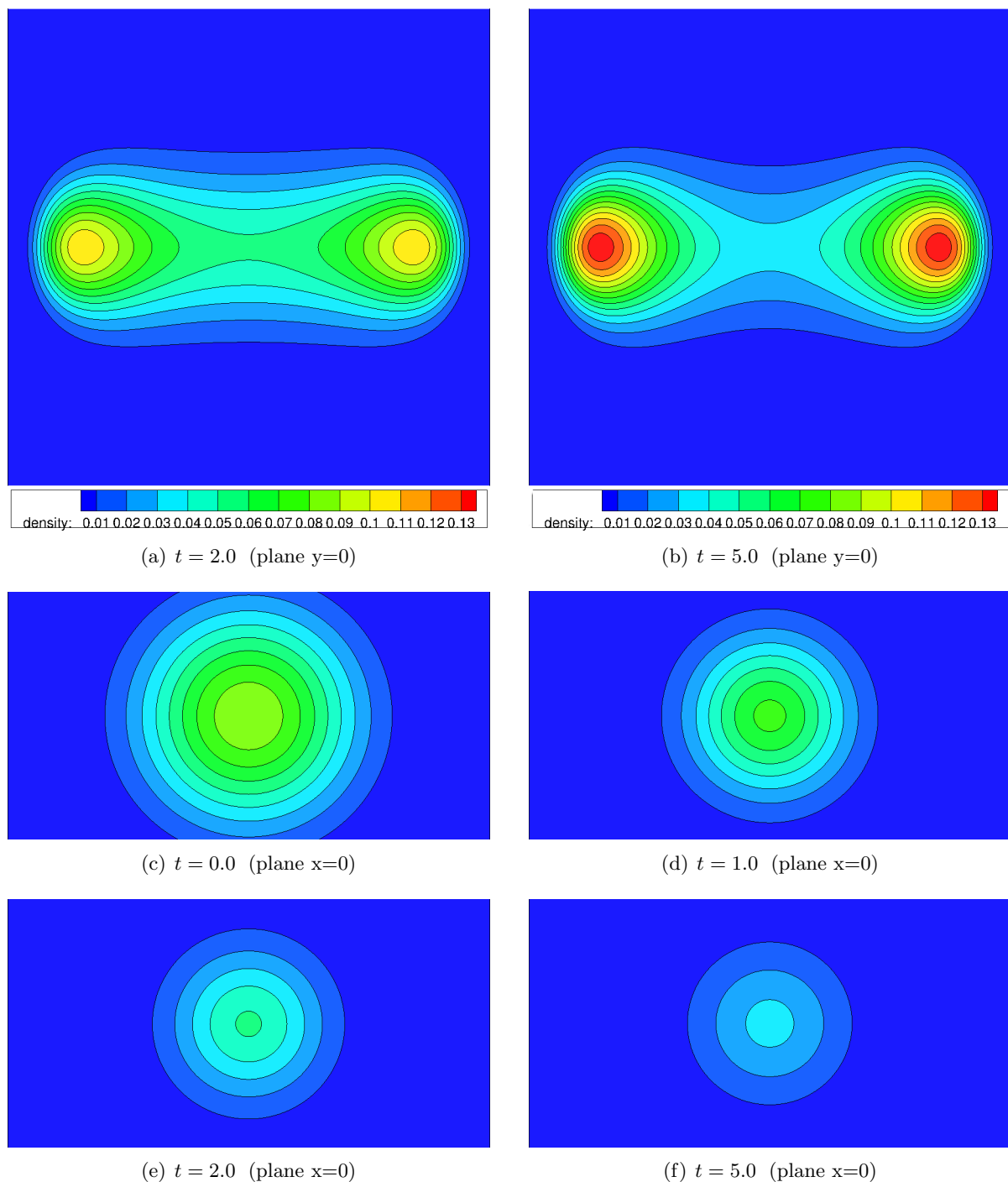
Figure 6.15: Figures (a) and (b) continue the 3D density function results (e) and (f) from Figure 6.14. Furthermore, in (c) to (f) we illustrate density values for the y-z plane through the origin.
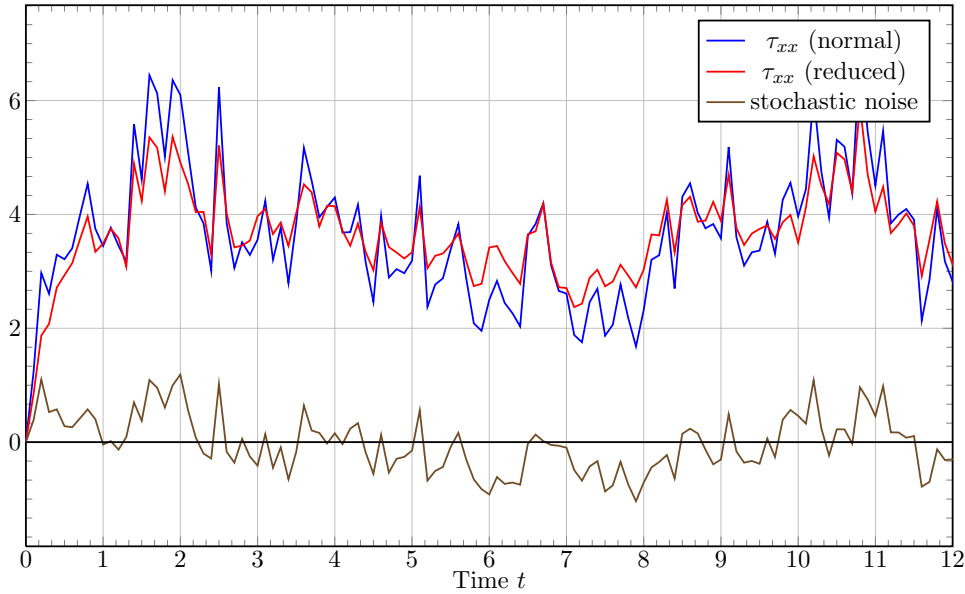
Figure 6.16: The figure compares the stochastic noise between two coarse approximations of the stochastic process in the extensional flow case where one approximation uses an equilibrium control variate and the other one does not. Furthermore, we add the plot for the equilibrium control variate (stochastic noise) which performs oscillations around the zero stress tensor value. Since the exact solution for τ_{xx} is approximately 4.02 (cf. Section 6.2.1), we note that the approximations of "τ_{xx} (reduced)" are actually better than without any reduction.

percent in the non-homogeneous flow case, this would nevertheless be useful, as any decrease in the number of realisations N_f actually saves computing time. Unfortunately, an equilibrium control variate does not generally reduce the variance of our stochastic approach so that one has to consider whether to use it for transient flow solvers (cf. Section 4.2.3).

For illustration, we visualise the effect of an equilibrium control variate in Figure 6.16 for a simulation with only $N_f = 100$ realisations so that the effect of variance reduction becomes obvious. As the exact result for the stochastic noise term which we simulate by the control variate is zero, we expect these disturbances to also appear for the stochastic process $\vec{Q}_t$. Consequently, we subtract these deviations from the original approximation for τ_{xx} and obtain a variance reduced result.

6.2.4 Shear Flow with Different Spring Forces

The last homogeneous flow example considers a three-dimensional shear flow with the same parameters as in the two-dimensional case since the 3D shear flow takes place in the x-y plane (cf. Table 6.11), i.e. we analyse a flow field of the form

$$\vec{u} = (\dot{\gamma} y, 0, 0) . \tag{6.9}$$

Additionally, we employ a stochastic approach and compare the 3D shear flow results that are predicted by the FENE, the Hookean, and the FENE-P spring force. Again, we present the

parameters for simulation in Table 6.11.

Shear Flow (Stochastic)		
Weissenberg number	Wi	1.0
Newtonian viscosity	β	0.0
Shear rate	$\dot{\gamma}$	10.0
Maximum spring extension	b	150.0
Time Discretisation		Eu-Maruyama
Time-step size (const.)	Δt	10^{-4}
Realisations	N_f	$5 \cdot 10^4$

Table 6.11: Parameters for a three-dimensional strong shear flow using a stochastic approach.

In Figure 6.17 we illustrate the evolution of the stress tensor components τ_{xx} and τ_{xy} for all considered spring forces models (i.e. FENE, Hooke, FENE-P) by using $N_f = 5 \cdot 10^4$ stochastic realisations. Similar to the 2D shear flow, the Hookean dumbbell model predicts more pronounced stresses which can be explained by considering that the dumbbells are not restricted in length. On the contrary, we have chosen a comparatively high maximum spring extension $b = 150$ in Table 6.11 so that the FENE and FENE-P models are not as strongly restricted in length as in the extensional flow case, but they still predict lower values than the Hookean model. Furthermore, we observe that the FENE-P closure only recovers the major characteristics of the FENE spring but not its actual stress tensor values.

If we compare the steady state results (not the complete plot) for the FENE spring in Figure 6.17 with the analogous 2D FENE results in Figure 6.7, we note that the final values are quite similar. Indeed, they are nearly indistinguishable in certain parameter ranges. Fan [29] states that the 2D shear flow is a very good approximation to the 3D case for reduced shear rate $Wi\,\dot{\gamma} \approx 4$ or less. Although we consider a shear flow with a reduced shear rate $Wi\,\dot{\gamma} = 10$, at least the steady state values still seem to be comparable with the 2D case. Chauvière et al. [20] have compared the 2D and 3D steady state values for τ_{xy} (exactly the shear viscosity $\eta(\dot{\gamma})$ (2.12) that depends on τ_{xy}) depending on the product $Wi\,\dot{\gamma}$. They have found only small steady state differences as long as $Wi\,\dot{\gamma} \leq 10$. As a result, we note that the 2D shear flow yields similar results to the 3D flow and is suited as a more or less coarse 3D approximation to reduce computing time.

6.2.5 The High Weissenberg Number Problem

So far we have considered moderate Weissenberg numbers ($Wi \approx 1$) for the FENE spring force model. Since the beginning of viscoelastic fluid simulation in the 1970's, it was observed by all researchers that simulations of viscolelastic flows fail beyond a critical Weissenberg number Wi_{crit}. The problem is normally denoted as high Weissenberg number problem (HWNP) in literature. The occurrence of instabilities at Wi_{crit} is caused either by the mathematical model itself or by numerical approximation errors. For a detailed description of the problem we refer to Chapter 7 of Owens and Phillips [68] and an article from Keunings [47].

Due to the nonlinearity of the governing equations, there exists no general theory on existence and uniqueness results in mathematical modelling of viscoelastic flows. One the contrary,
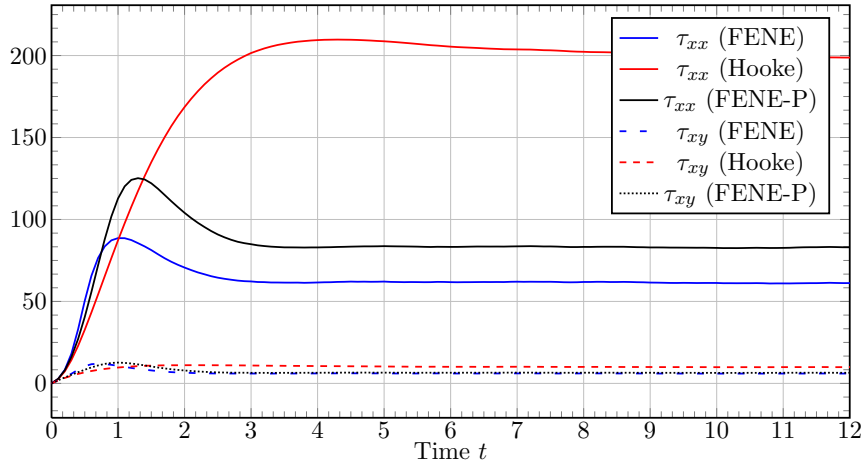
Figure 6.17: The plot visualises the stress components τ_{xx} and τ_{xy} for three different spring forces in a homogeneous 3D shear flow. Again, we note that the values for the first stress tensor components differ strongly between each spring force and we presume that the FENE spring actually delivers the best approximations of a real polymeric fluid.

the limiting factor in most situations is the numerical method. Van Heel [89] observed that a multiscale BCF method (cf. Chapter 6.3) allows the solution of complex flow problems with $Wi > 1.0$ which can not be simulated adequately by macroscopic constitutive equations. Consequently, since multiscale models incorporate more relevant aspects of physics, they seem to be more robust regarding to the HWNP.

In Figure 6.18 we once again discuss a 3D shear flow with a FENE spring force. We employ the same parameters as in Table 6.11 except for the chosen Weissenberg number which we vary between $Wi = 1$ and $Wi = 10$. Obviously, an increase in the Weissenberg number leads to a more pronounced first stress tensor amplitude and a stronger decline afterwards. Despite the higher complexity of the problem, the stochastic approach does not require an additional computational effort. This is a further advantage of the stochastic description over a deterministic calculation.

Since we observe an adequate description of homogeneous shear flows even for high Weissenberg numbers, this might also lead to a better description of transient flow fields that we will investigate subsequently. In Chapter 6.3 we employ our stochastic BCF method for transient flows with Weissenberg numbers up to 1.0. Due to our experiences with homogeneous flow calculations, we also expect correct stress tensor predictions for our multiscale flow solver even for high Weissenberg numbers. However, since the occurrence of over- and undershoots in the stress tensor results leads to similar effects for the fluid velocities (cf. Section 6.3.2), it has to be further investigated in future whether a flow solver like NaSt3DGPF [2] can cope with such increased oscillations in the velocity field.
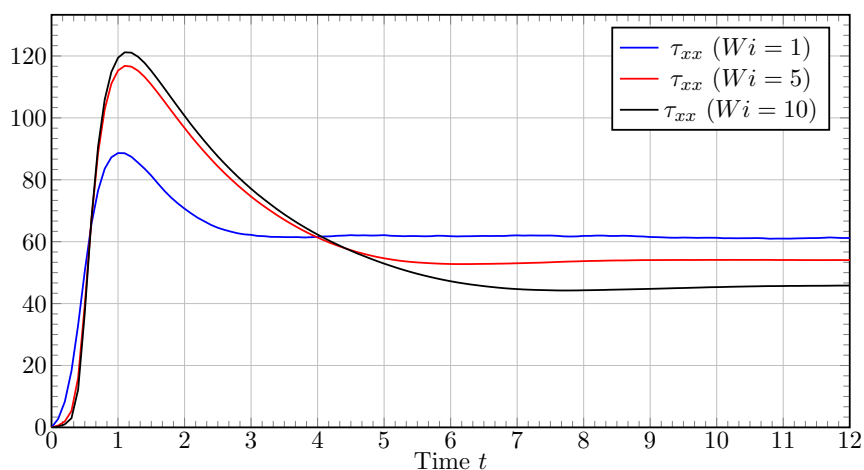
Figure 6.18: The figure shows the τ_{xx} stress component for a shear flow with the parameters from Table 6.11 except for the Weissenberg number which we vary from 1.0 to 10.0. Depending on the Weissenberg number, the stress tensor overshoots are strongly increased in size. Furthermore, despite the increased complexity of the problem, our stochastic scheme does not increase the computational effort or the number of stochastic realisations in contrast to a deterministic approach for the Fokker-Planck equation.

6.3 3D Multiscale Flows

This chapter contains the multiscale flow results using the three-dimensional flow solver NaSt-3DGPF [2] for approximating the Navier-Stokes equations on the one hand and a stochastic Brownian Configuration Field (BCF) method for solving the nonlinear FENE spring force equation one the other hand. Further information can be found in Chapter 5 where we describe the coupling between the corresponding equations.

Altogether, we discuss four coupled flow problems which are

- an uniaxial extensional flow,

- a flow through an infinite channel,

- a 4-1 contraction flow, and

- a flow around a sphere.

We validate our implementation by comparing the stress tensor predictions for the extensional flow with analytical predictions for the corresponding flow field. Furthermore, we compare our results for the 4-1 contraction flow and the flow around a sphere with similar experiments in literature (cf. Knezevic [50]) since both flow fields are considered as model problems for viscoelastic flows. Additionally, we show the equivalence between the macroscopic Oldroyd-B model and the micromolecular Hookean dumbbell model.

6.3.1 Uniaxial Extensional Flow

First, we start with an analysis of the differences between the extensional flow for a coupled multiscale model as considered in this chapter and an analogue homogeneous 3D flow problem in Chapter 6.2. Theoretically, both approaches deliver the same results. However, in the homogeneous case of Chapter 6.2 we employ the prescribed velocity field

$$\vec{u}(\vec{x}) \,=\, (\dot{\epsilon}x, -\frac{\dot{\epsilon}}{2}y, -\frac{\dot{\epsilon}}{2}z), \qquad \vec{x} \in \Omega, \, \dot{\epsilon} \in \mathbb{R} \tag{6.10}$$

in all time-steps and we are aware that we only have to solve a reduced, $\vec{x}$-independent equation (cf. (2.68))

$$d\vec{Q}_t \,=\, \left(\boldsymbol{\kappa}\,\vec{Q}_t \,-\, \frac{1}{2\,Wi}\vec{F}(\vec{Q}_t) \right) dt \,+\, \sqrt{\frac{1}{Wi}}\, d\vec{W}_t. \tag{6.11}$$

Now, we disregard these simplifications and concentrate on the complete six-dimensional equation (cf. (2.67))

$$d\vec{Q}_t(\vec{x}) \,=\, \left(-\vec{u}(\vec{x},t)\,\nabla\vec{Q}_t(\vec{x}) \,+\, \left(\nabla\vec{u}(\vec{x},t)\right)\vec{Q}_t(\vec{x}) \,-\, \frac{1}{2\,Wi}\vec{F}(\vec{Q}_t(\vec{x})) \right) dt \,+\, \sqrt{\frac{1}{Wi}}\, d\vec{W}_t \tag{6.12}$$

that we discretise by using a Brownian Configuration Field approach (cf. Chapter 5). Here, we set a prescribed number of N_f configuration fields in every grid cell of physical space Ω and solve the $\vec{x}$-dependent stochastic equation (6.12). The stress tensor values obtained from (6.12)

and the Kramers expression (5.4) are then incorporated into the Navier-Stokes equations (5.1) and (5.2) which hopefully return the extensional flow field (6.10).

Obviously, the approach in this section is much more challenging as

- we have to solve a stochastic equation for every grid cell of our computational domain Ω which is far more expensive than in the homogeneous flow field case and

- we do not prescribe the velocity field analytically but employ velocity field values that are actually computed numerically.

Nevertheless, we simulate an uniaxial extensional flow for the coupled Navier-Stokes-BCF system (5.1) - (5.4) since this validates the correctness of our implementation. Furthermore, this is an example of a flow field in which simple approaches (e.g. Oldroyd-B, Hookean dumbbell model) deliver wrong results.

Problem Description

We perform all simulations in this section on a cubical domain illustrated in Figure 6.19. Here, we have transformed the domain from $[0, 2]^3$ onto $[-1, 1]^3$ so that the extensional flow field can be used in the form of (6.10). Note that the domain possesses four inflow boundaries where two of them lie normal to the y-direction and the other two lie normal to the z-axis. Consequently, the outflow domain is orthogonal to the x-axis. The velocity field is illustrated in Figure 6.19 with twenty steamtraces that represent the path of a particle under the current flow field.

We employ Dirichlet boundary conditions at the inflow domain given by (6.10) but set homogeneous Neumann boundary conditions at the outflow domain. Indeed, we could also use Dirichlet boundary conditions at the outflow domain, but if the non-Newtonian stress led to oscillations in the velocity field this would cause numerical instabilities. For the discrete velocity field and the Brownian configuration fields we apply the initial conditions

- $\vec{u}_0(x_i, y_j, z_k) = (x_i, -0.5\, y_j, -0.5\, z_k)$ for $i, j, k = 1, \ldots, 50$ grid cells,

- $\vec{Q}_{i,j,k}^{0,(s)} \sim \underbrace{\psi_{\text{eq}}}_{\substack{\text{indep} \\ \text{from i,j,k}}}$ for $s = 1, \ldots, 8000$ realisations.

Moreover, in Table 6.12 we present the common parameters for all three viscoelastic models (i.e. FENE, Hooke, FENE-P). A Newtonian simulation uses the same parameters except for β which is equal to one for Newtonian simulations and Wi and N_f which are omitted as no non-Newtonian stress tensor is computed.

Newtonian simulation

An extensional flow which uses the prescribed velocity field (6.10) as initial condition is rather uninteresting for purely Newtonian calculations (i.e. $\beta = 1$), because the initial condition is already the solution of the problem. Consequently, the iterative solver for the pressure Poisson problem that appears in the Chorin scheme in Chapter 5.3 only requires one step to solve the linear system of equations. Therefore, we obtain the same result as illustrated in Figure 6.19 for all times.
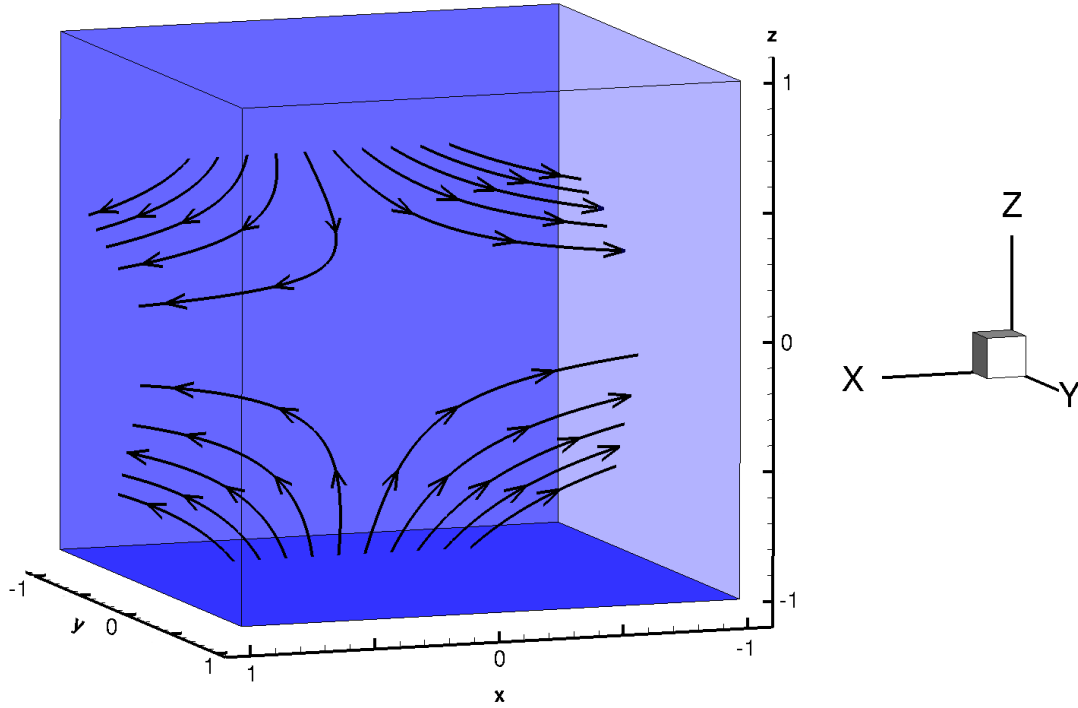
Figure 6.19: We investigate the extensional flow field on a cube $[-1, 1]^3$ with a discretisation using 50 grid cells in each coordinate direction and $N_f = 8000$ realisations per cell which leads to $50^3 \cdot N_f = 10^9$ configuration fields in total. According to (6.10) we set Dirichlet conditions in direction of the y- and the z-axis whereas we apply homogeneous Neumann boundary conditions at the faces normal to the x-direction. For illustration, we have displayed twenty steamtraces to visualise the velocity field within the cube.

FENE Spring Force

Once again, we first investigate the nonlinear FENE model with maximum extension $b = 10$, as it represents the only purely multiscale model without a macroscopic equivalence. In an analogous manner as in Section 6.2.1, we compute steady state stress tensor values for an ideal extensional flow by inserting the parameters from Table 6.12 and the steady state density function ψ_{eq} (2.85) into the Kramers expression (6.7) and obtain

$$
\begin{aligned}
&1.\ \tau_{xx}^{\text{sol}} \approx 3.984, \\
&2.\ \tau_{yy}^{\text{sol}} \approx -0.734, \\
&3.\ \tau_{zz}^{\text{sol}} \approx -0.734, \\
&4.\ \text{zero for all shear stresses.}
\end{aligned}
$$

We note that the results are slightly different to the values in Section 6.2.1 as we now incorporate the viscosity of a Newtonian fluid represented by $\beta = 0.01 > 0$. Nevertheless, the

3D Extensional Flow (Navier-Stokes-BCF)		
Grid resolution		50^3 cells
Physical domain		$[-1, 1]^3$
Simulation time	t_{max}	7.0
Reynolds number	Re	200
Newtonian viscosity	β	0.01
Weissenberg number	Wi	0.5
Extensional rate	$\dot{\epsilon}$	1.0
Realisations per cell	N_f	8000
Maximum spring extension	b (FENE)	10.0
Time Discretisation		Explicit (Chorin)
Convective Terms		Quick

Table 6.12: The table contains the parameters for a 3D multiscale extensional flow using one of three different spring force models (FENE, Hooke, FENE-P). For a purely Newtonian simulation we omit the parameters Wi and N_f and set $\beta = 1$.

Newtonian viscosity only contributes one percent to the total viscosity of the fluid so that the fluid behaviour is essentially non-Newtonian.

One aspect that is not intuitively clear is the development of the velocity field $\vec{u}$ in the viscoelastic case. For the Newtonian case, we have stated that the initial velocity field is already the solution of the flow problem. This is also the case for the non-Newtonian flow field even though the system indicates stress because of stretching in one direction. Despite an increase in the stress tensor field, the velocity field remains unchanged in theory as the polymeric stress acts on the momentum equations (5.1) only via its divergence. Since the stress should evolve uniformly in each of the 50^3 grid cells the polymeric stress tensor field is divergenceless for an extensional flow. On the contrary, if our coupled system exhibited spatial differences for the stress tensor field this would result in oscillations for the velocity field so that the extensional flow is disturbed. By indicating that the stress tensor components evolve according to analytical results we show that this problem does not occur.

Apart from the problem to assure that the velocity field fulfils the analytical values for an extensional flow field (6.10) for all time there occurs an additional problem caused by an increase in computation time. As we simulate the extensional flow on a grid using 50 cells in each direction, we have to solve a stochastic differential equation with 50^3 positions $\vec{x}$ in physical space Ω to obtain 50^3 stress tensor values $\boldsymbol{\tau_p}(\vec{x})$ and therefore have to restrict the number of configuration fields or stochastic realisations N_f per cell. Actually, even by using a massively parallel computer we restrict the number of realisations per cell N_f to 8000 in Table 6.12, leading to $50^3 \cdot N_f = 10^9$ stochastic realisations on the whole domain, as more configuration fields become too expensive. Nevertheless, in literature we note that two-dimensional computations do not apply more than 2000 configuration fields per cell which, for instance, can be seen in a current article from Vargas, Manero and Phillips [90]. Although this results in a rather coarse approximation of the stress tensor in every grid cell, the coupled system is numerically stable which we will illustrate subsequently.
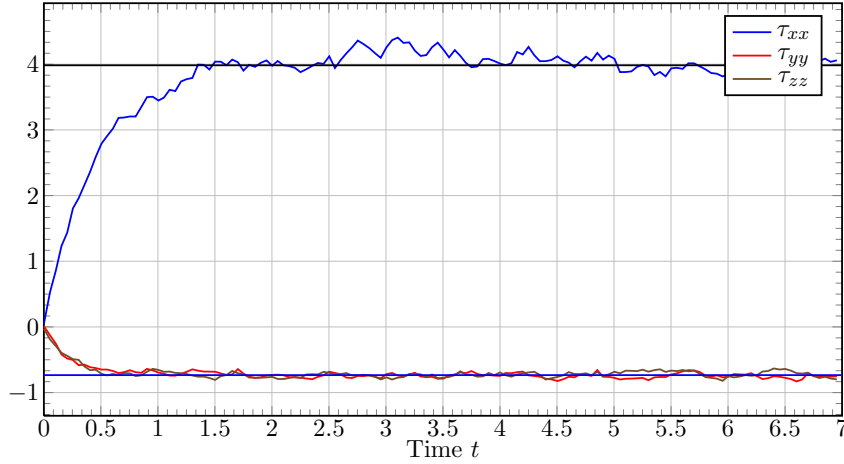
Figure 6.20: The plot presents the stress tensor development at the centre of the cube (i.e. $x = y = z = 0$). We observe small deviations for the stress tensor component τ_{xx} from the steady state results. A reason for this can be found by analysing the velocity values at the centre which hold the prescribed values not exactly and exhibit small deviations. Furthermore, as we employ $N_f = 8000$ configuration fields in each of the 50^3, the accuracy is restricted in every cell.

As mentioned previously, for this problem we compute $i = 1, \ldots, 50^3$ stress tensor values $\boldsymbol{\tau_p}(x_i)$ with six independent components altogether but all 50^3 results shall be absolutely equal. Therefore, we first present the stress tensor development for one grid cell, compare the result with the analytical steady state values and then analyse the spatial differences between each cell. In Figure 6.20 we measure the stress tensor components τ_{xx}, τ_{yy}, and τ_{zz} at the origin of the cube, i.e. at the coordinates $x = y = z = 0$ in physical space Ω. Additionally, we have marked the steady state stress tensor values that we expect for an ideal extensional flow. We observe that the stress tensor components τ_{yy} and τ_{zz} approximate the exact values restricted by the stochastic accuracy for $N_f = 8000$ stochastic realisations in each grid cell. On the contrary, we discover small overpredictions for the stress tensor component τ_{xx} for $2.5 \leq t \leq 4.5$ that we can explain by analysing the velocity field values.

Since we apply extensional flow field values (6.10) as initial condition, the velocity field at $(x, y, z) = (0.5, 0, 0)$ is initialised with $\vec{u} = (u, v, w) = (0.5, 0, 0)$. Consequently, any deviation from these values results in an error for the velocity field at $(0.5, 0, 0)$. In Figure 6.21 we present the relative error of the first velocity component u in a semilogarithmic scale with $u^* = 0.5$ as exact solution. We note that u does not keep the initial value of 0.5 exactly but performs small oscillations in the order of $\mathcal{O}(10^{-4})$ around this value. Accordingly, we presume that there is a mutual dependency between small differences in the stress tensor component τ_{xx} and the velocity component u because the stress tensor only reaches its analytical steady state results for exact velocity values and vice versa. We have further added the steady state error (i.e. for $t \geq 2.0$) for τ_{xx} at this point to allow a comparison between fluid velocity and stress tensor computation. As expected, the relative error in the velocity field is reduced by a factor of 100 compared to the error in τ_{xx}.
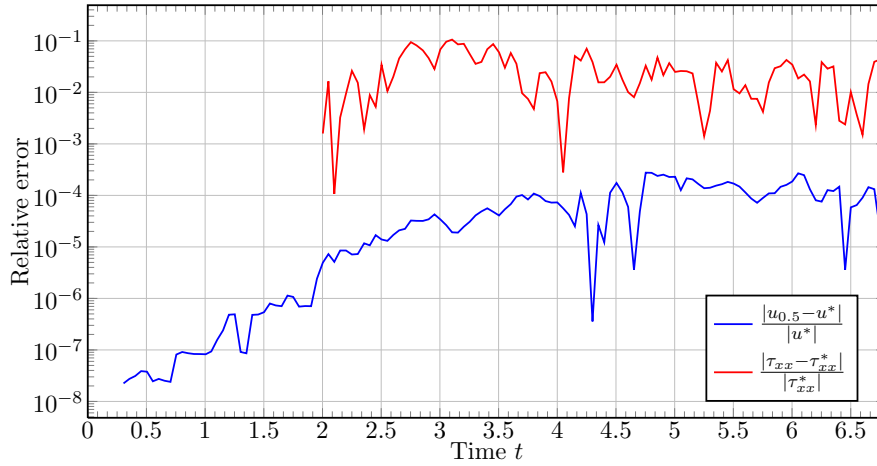
Figure 6.21: The figure compares the relative error in u with the error τ_{xx} at the grid point $(0.5, 0, 0)$. We observe that stochastic noise in the stress tensor also leads to oscillations in u which are much reduced in size. Therefore, the accuracy in u is comparatively high considering that we include a stochastic term in the momentum equations. This underlines the advantage of a BCF approach (cf. Chapter 5.2) which applies a stochastic noise that is uniform in physical space Ω (cf. Figure 6.22). Note that we plot the relative error for τ_{xx} at $t \geq 2.0$ when the stress has reached its steady state value.

Next, we investigate the spatial differences between stress tensor values in adjacent cells. The global velocity field is undisturbed only if the stress tensor values in each cell evolve uniformly so that $\nabla \cdot \boldsymbol{\tau_p}$ is equal to zero in the momentum equations. As the stress for the considered problem evolves primarily in the τ_{xx}-component, we illustrate its development on a plane $x = 0$ in Figure 6.22 (a) and (b) for $t = 2.0$ and $t = 6.0$. We further include two figures for a Hookean dumbbell computation in Figure 6.22 (c) and (d) which we will discuss in the next section.

We determine that the stress tensor for the FENE spring in Figure 6.22 (a) and (b) exhibits slightly different values when we compare the cell centre with the boundary regions. A comparison with other cuts through the cube reveals that τ_{xx} features small deviations between the inflow boundary and the central region as well as the outflow boundary. We presume that the velocity field close to the inflow boundary follows the exact extensional flow values more closely as we apply Dirichlet boundary conditions there. Indeed, we observe that the stress tensor close to the inflow boundary matches the exact steady state value within the stochastic accuracy.

Nevertheless, the stress tensor varies smoothly between adjacent cells which underlines the advantages of a BCF approach over a CONNFFESSIT ansatz (cf. Chapter 5.2). If we used the original CONNFFESSIT method, we would have observed wild spatial fluctuations of the stress tensor. These oscillations are more critical for the stability of the algorithm than minor differences in τ_{xx}. Consequently, $\nabla \cdot \boldsymbol{\tau_p}$ is also smooth between different grid cells which explains the lower error in the velocity component $\vec{u}$ in comparison to the stress tensor. As our major variables of interest are the fluid parameters $\vec{u}$ and p, we conclude that our Navier-Stokes-BCF system is appropriate for the simulation of a multiscale viscoelastic fluid.

(a) FENE spring at $t = 2.0$ (plane x=0)

(b) FENE spring at $t = 6.0$ (plane x=0)

(c) Hookean spring at $t = 6.0$ (plane x=0)

(d) Hookean spring at $t = 18.0$ (plane x=0)
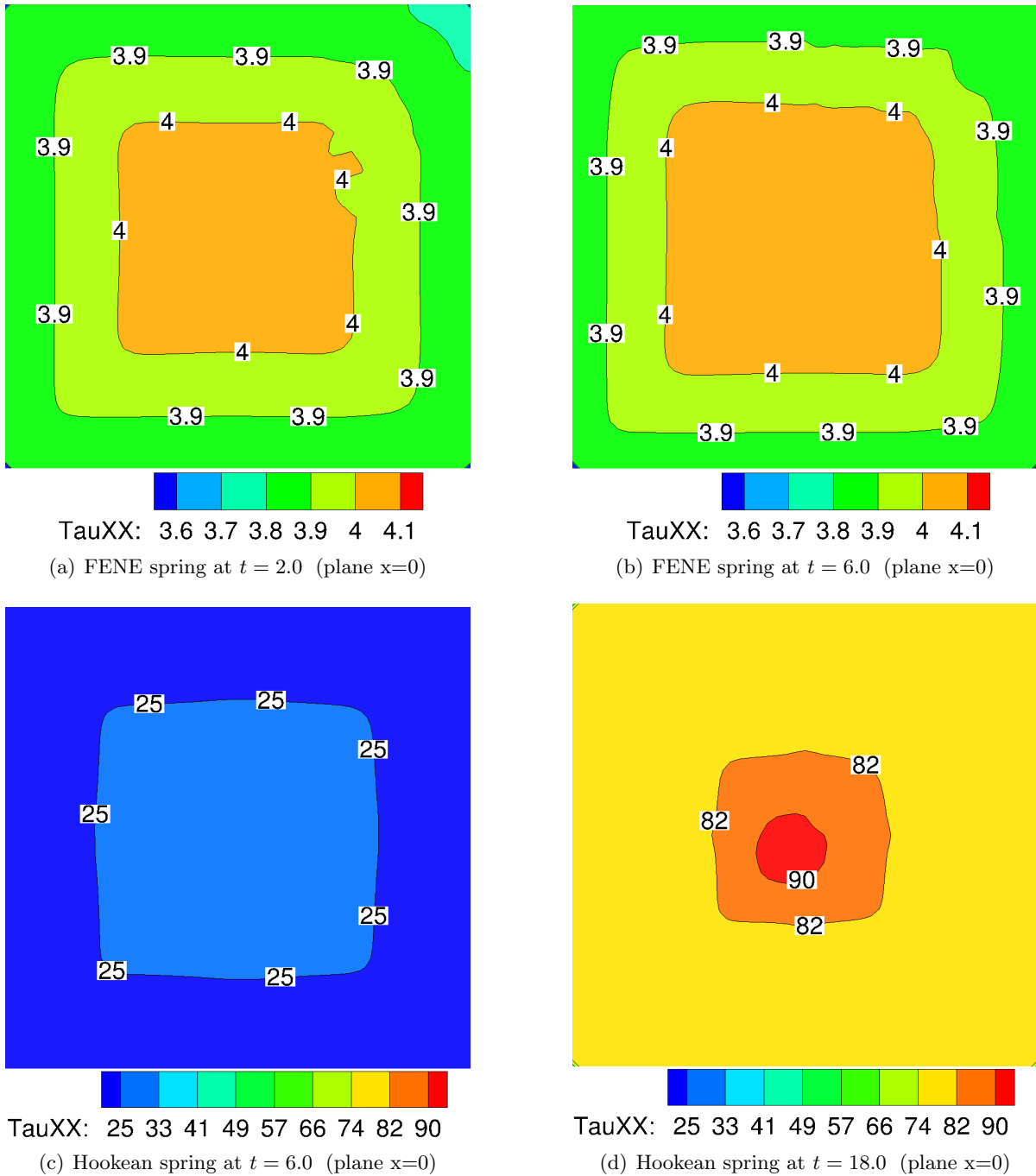
Figure 6.22: The figure presents stress tensor values for the FENE model in (a) and (b) as well as for the Hookean dumbbell system in (c) and (d). Smooth spatial variation in the stress tensor $\boldsymbol{\tau_p}$ is essential for the accuracy of $\vec{u}$ and the pressure p since we include $\nabla \cdot \boldsymbol{\tau_p}$ in the momentum equations. As we observe only small variations for the stress in space (not in time) this underlines the importance of the chosen BCF approach. Furthermore, the figure illustrates that a Hookean dumbbell model is not suited for the description of extensional flows. While the FENE stress reaches a steady state so that the results at $t = 2.0$ in (a) and at $t = 6.0$ in (b) are very similar, the stress is not restricted in size for the Hookean spring and for the equivalent Oldroyd-B model (cf. Figure (c) and (d) for $t = 6.0$ and $t = 18.0$).

Computation Time

As previously mentioned, the number of stochastic realisations N_f has a crucial influence on computation time. Therefore, we have to balance the computation time on the one hand with the accuracy of our stochastic approach on the other hand. For this simulation, we have employed $N_f = 8000$ configuration fields per cell. The complete solution of the system required 40 hours on Himalaya (cf. Chapter 5.6) using 48 processors. In contrast, an analogue Newtonian simulation necessitates about twenty minutes on 16 processors. One has to consider that a Newtonian computation reaches a steady state for $\vec{u}$ and p after a few time-steps which the viscoelastic computational does not since there are always small oscillations in the macroscopic variables. Therefore, the percental increase in computation time is much reduced in those flow cases that do not reach a steady state.

As a result, we always obtain stress tensor values with a reduced accuracy as long as parallel computers are not strongly increased in computing speed. However, we do not have a modelling or closure error as is the case for constitutive models. The errors of macroscopic models, even though they do not exhibit any stochastic noise, can be much more profound than the stochastic noise that we experience.

Hookean and FENE-P Model Predictions

In Section 6.2.1 we have already analysed the stress tensor predictions of the Hookean dumbbell and the FENE-P model. In both cases the model predictions differed strongly from the FENE spring force results. Consequently, we experience the same differences using the coupled Navier-Stokes-BCF model. For both simulations we use analogue parameters from Table 6.12 as for the FENE spring force simulation.

In Figure 6.22 (c) and (d) we present the Hookean dumbbell results for τ_{xx} at $t = 6.0$ and $t = 16$ by cutting the cube with a y-z plane through the origin. We note that the stress tensor values increase with ongoing time in contrast to the FENE model in Figure 6.22 (a) and (b). In theory, the values should be identical in every grid cell, but one has to consider that enormous values easily lead to inaccuracies and instabilities. Furthermore, we cannot present results for the equivalent Oldroyd-B model as an appropriate implementation leads to numerical instabilities. Nevertheless, we will compare our macromolecular Hookean dumbbell results with the corresponding deterministic Oldroyd-B model afterwards.

In Figure 6.23 we compare the stress tensor predictions between the FENE and the FENE-P model (cf. Section 6.2.1 for a comparison using a prescribed flow field $\vec{u}$). Here, we compare the approximations at $x = y = z = 0$ (origin) but indicate that the results are comparable for all other grid cells. Consequently, unless we pay attention to choose a constitutive equation that is suited for the considered problem we have to rely on the FENE spring force model if we want to avoid modelling errors.

Comparison Hookean Dumbbell - Oldroyd-B model

In Section 2.3.6 we have derived the constitutive equation for the Oldroyd-B model from a micromolecular Hookean dumbbell model. Since NaSt3DGPF [2] already features an implementation of the Oldroyd-B model (cf. Claus [22]) we are able to demonstrate this equivalence in practical applications. However, as the deterministic Oldroyd-B model does not exhibit any
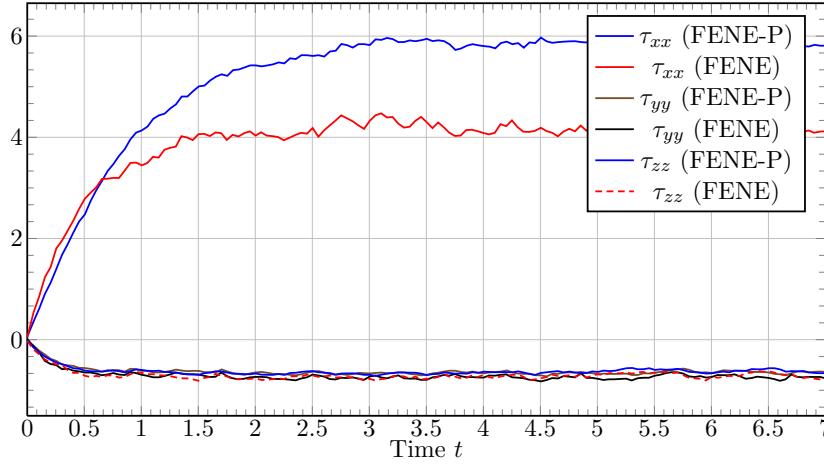
Figure 6.23: The figure presents the stress tensor evolution for the FENE-P and FENE model at the origin $(0, 0, 0)$ of a cube $[-1, 1]^3$. The simulation is comparable to the homogeneous flow field experiment in Figure 6.12, but we additionally simulate the properties of a Newtonian solvent as $\beta = 0.01 > 0$ and only use $N_f = 8000$ realisations per grid cell. Again, we observe that the closure model cannot predict correct values for stress tensor component in direction of the elongation.

stochastic noise and requires less computing time, there is no practical reason to implement a Hookean dumbbell model except for allowing comparisons.

Again, we investigate an extensional flow but restrict the extensional rate $\dot{\epsilon}$ to 0.5 to obtain finite stress tensor values. In this case, the velocity field is too weak to extend the dumbbell molecules to an infinite length. We state the parameters for this simulation in Table 6.13. After nondimensionalising the analytic steady state equations for an Oldroyd-B fluid (2.35), we obtain

$$\tau_{xx} = \frac{2\,(1-\beta)\dot{\epsilon}}{1 - 2\,Wi\,\dot{\epsilon}}, \quad \tau_{yy} = \tau_{zz} = -\frac{(1-\beta)\dot{\epsilon}}{1 + Wi\,\dot{\epsilon}}. \tag{6.13}$$

Consequently, we derive

$$
\begin{array}{l}
1. \ \tau_{xx}^{\text{sol}} \approx 1.98, \\[2mm]
2. \ \tau_{yy}^{\text{sol}} \approx -0.396, \\[2mm]
3. \ \tau_{zz}^{\text{sol}} \approx -0.396,
\end{array}
$$

as non-zero stress tensor values after inserting the parameters from Table 6.13 into (6.13).

In an analogous manner as before, in Figure 6.24 we compare the development of the stress tensor values between the Hookean dumbbell model and its macroscopic counterpart at the cube centre (i.e. $x = y = z = 0$). Apart from the stochastic noise in the dumbbell model, we obtain a good qualitative agreement between both stress predictions. Further investigations reveal that the Oldroyd-B model computes the predicted values within an accuracy of five digits.

Weak Extensional Flow (Navier-Stokes-BCF)		
Grid resolution		50^3 cells
Physical domain		$[-1, 1]^3$
Simulation time	t_{max}	15.0
Reynolds number	Re	200
Newtonian viscosity	β	0.01
Weissenberg number	Wi	0.5
Extensional rate	$\dot{\epsilon}$	0.5
Realisations per cell	N_f	8000
Time Discretisation		Explicit (Chorin)
Convective Terms		Quick

Table 6.13: For the comparison between the Hookean dumbbell and the Oldroyd-B model we simulate a weak extensional flow with $\dot{\epsilon} = 0.5$. Note that the parameter N_f for the number of stochastic realisations belongs solely to the Hookean dumbbell system as the Oldroyd-B model computes the stress tensor deterministically.

Next, in Figure 6.25 we compare the stress tensor development on a complete plane defined by $x = 0$. Here, we analyse the stress tensor component τ_{xx} at three different process times $t = 0.5$, $t = 1$, and $t = 1.5$. As we investigate a y-z plane for an extensional flow in the x-direction, all edges represent an inflow boundary. Despite the good qualitative agreement for the Oldroyd-B model in the central region of the Ω, we observe deviations near the inflow boundary. This is caused by the boundary treatment of the Oldroyd-B model. The constitutive equation necessitates Dirichlet boundary conditions at the inflow boundary that are not generally known. For simplicity, one usually decides to set $\boldsymbol{\tau}_{\boldsymbol{p}_{\mathrm{inflow}}} = 0$. Although this choice is reasonable for general flow situations, it yields wrong results at the inflow boundary for an extensional flow. As our Hookean dumbbell model exhibits a different boundary treatment the problem does not occur there.

As a conclusion, despite the differences at the inflow boundary between the Oldroyd-B model on the one hand (Dirichlet boundary conditions) and the Hookean dumbbell model on the other hand (homogeneous Neumann boundary conditions) we indicate that both models approximate the exact values at the centre within the accuracy of the chosen ansatz. Furthermore, the errors for the Oldroyd-B model are negligible for general flow situations in which the major stresses occur far away from the inflow boundary.
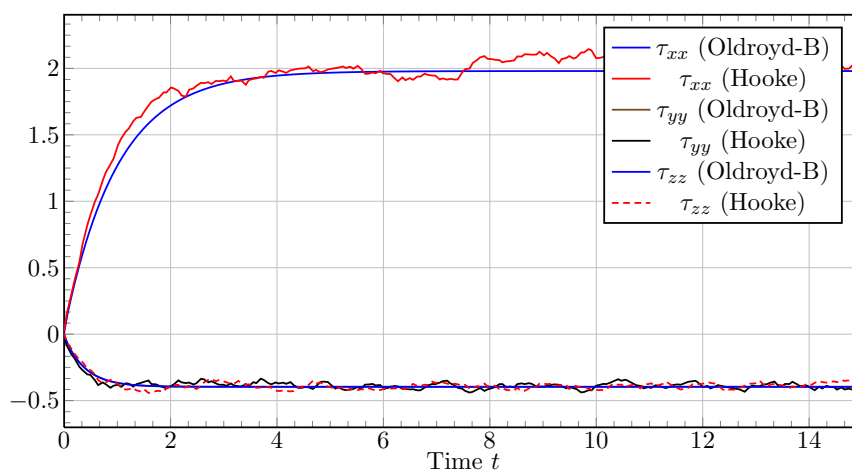
Figure 6.24: The figure displays the stress tensor evolution for a macroscopic Oldroyd-B and a micromolecular Hookean dumbbell model at the centre of the computational domain. We observe that both approaches predict similar stress tensor values within the accuracy of the chosen method. This verifies the equivalence between both models as stated in Section 2.3.6.

(a) Hookean dumbbell $(t = 0.5)$

(b) Oldroyd-B $(t = 0.5)$

(c) Hookean dumbbell $(t = 1.0)$

(d) Oldroyd-B $(t = 1.0)$

(e) Hookean dumbbell $(t = 1.5)$

(f) Oldroyd-B $(t = 1.5)$
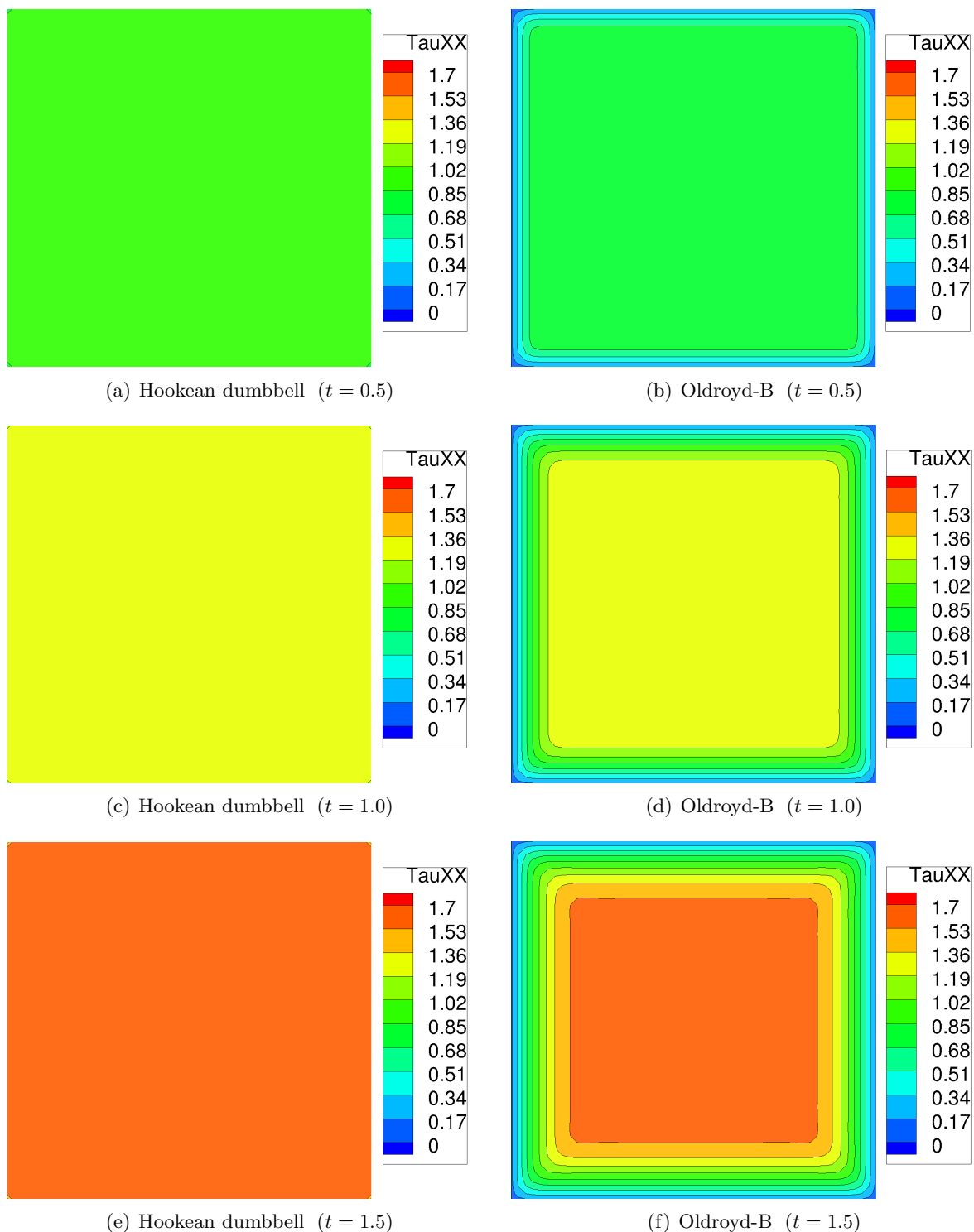
Figure 6.25: The figure compares the τ_{xx} stress tensor predictions from the Hookean dumbbell model on the left hand side with the corresponding results predicted by the Oldroyd-B model on the right hand side. The results are considered for the process times $t = 0.5$, $t = 1.0$ and $t = 1.5$. As the Oldroyd-B model utilises homogeneous Dirichlet boundary conditions at the inflow domain, we observe deviations from the predicted values there. This problem does not occur for the Hookean dumbbell model.

6.3.2 Flow Through an Infinite Channel

In this section we investigate a transient flow through an infinite channel with rectangular cross section. We describe an infinite channel by employing periodic boundary conditions in direction of the x-axis. In the other directions we set no-slip boundary conditions. The fluid is at rest first but is driven by a gravitational force $\vec{g} = (g_x, 0, 0)$ that leads to an increasing velocity in the channel. The maximum velocity is restricted by effects of viscosity and elasticity (for non-Newtonian fluids) that occur due to the movement of the fluid. We are interested in analysing the increase in the velocity component u for a purely Newtonian as well as for two different non-Newtonian FENE fluids. For illustration, in Figure 6.26 we present the setting for one viscoelastic simulation.

In view of non-Newtonian channel flows, we expect the occurrence of the so called *velocity overshoot phenomenon*. This effect describes the effect that the fluid velocity does not increase monotonically as for a Newtonian fluid but exhibits oscillations that decay with ongoing time. A detailed description of the effect for flows around a sphere is given in Chapter 9.2.4 of Owens and Phillips [68]. Considering the velocity overshoots one important aspect is that the maximum velocity at the first overshoot and the period of oscillation are proportional to the square root of the relaxation time λ and the Weissenberg number Wi (cf. $Wi \equiv \lambda U_0 / L_0$ in Definition 2.15), respectively. Furthermore, if the Weissenberg number is too large, the channel velocity is overdamped so that we only observe a single overshoot without any further
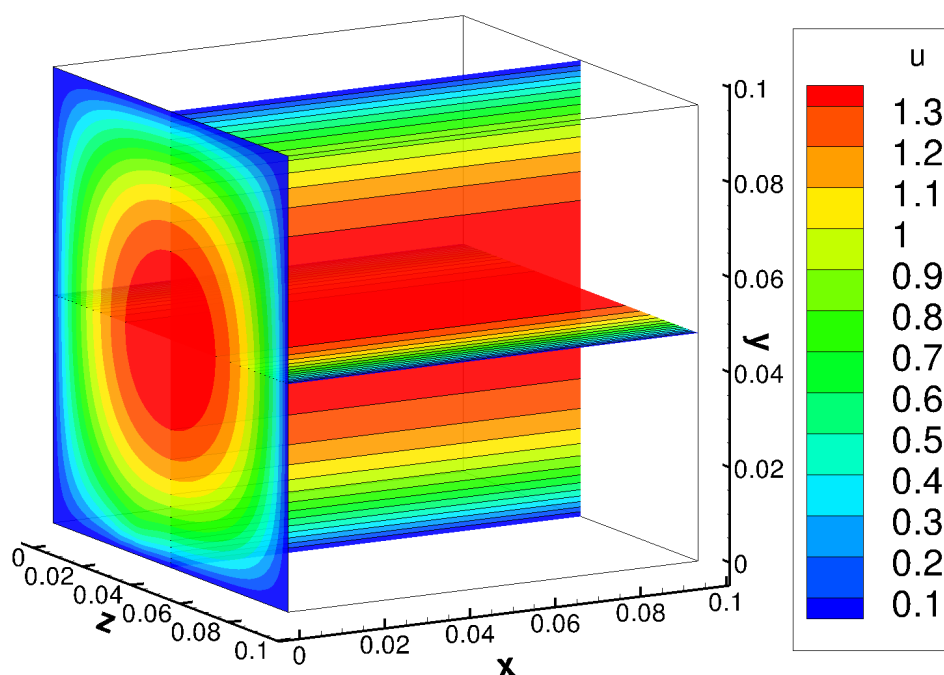
Figure 6.26: The experiment describes a fluid in an infinite channel which we realise by using periodic boundary conditions in the flow direction x. As the fluid is driven by gravitational force, we normally expect that the flow reaches its highest values at the end of the simulation. For a non-Newtonian simulation this primarily depends on the Weissenberg number. The figure illustrates a velocity field that we will denote by FENE SimB later on.

Infinite Channel Flow (Navier-Stokes-BCF)			
	Newtonian	**FENE SimA**	**FENE SimB**
Grid resolution	80^3 cells		48^3 cells
Physical domain	$[0, 0.08]^3$		$[0, 0.096]^3$
Simulation time	$t_{max} = 1.7$		
Reynolds number Re	20		200
Newtonian viscosity β	1.0	0.1	
Weissenberg number Wi	-	0.5	
Realisations per cell N_f	-	4000	
Maximum spring extension b	-	10.0	
Gravitational force g_x	5.0		4.0
Time discretisation	Semi-implicit		
Convective terms	SMART		

Table 6.14: The table includes all parameters for the Newtonian simulation as well as for the viscoelastic cases that we denote as FENE Simulation A and Simulation B. Since the grid resolution for the FENE SimA computation is high concerning that we simulate a 3D Navier-Stokes-BCF model, we have to restrict the number of configuration fields to 4000 to achieve a moderate computation time.

oscillation.

In Table 6.14 we summarise the parameters for a Newtonian and a FENE simulation using a grid resolution of 80^3 cells on the one hand and a lower resolved FENE calculation with 48^3 grid cells on the other hand. For a better distinction between both FENE simulations we term the first one *Simulation A* and the second one that employs a lower resolution *Simulation B*. Note that the usage of 80^3 grid cells in FENE SimA requires an enormous computational effort as it is in fact our computation with the highest number of grid cells as well as the number of Brownian configuration fields throughout this thesis. Therefore, we restrict our computation to $N_f = 4000$ BFCs per cell which increases the stochastic noise in each cell in comparison to 8000 realisations for the other examples.

In Figure 6.27 we compare the increase in channel velocity between the Newtonian computation and the viscoelastic counterpart FENE SimA at the physical positions $(x, y, z) = (0.04, 0.04, 0.04)$ (i.e. the centre of Ω) and $(x, y, z) = (0.04, 0.06, 0.04)$. We note an overdamped velocity overshoot for the FENE model which does not occur for the Newtonian case. The velocity overshoot for the FENE SimA approximation leads to an amplitude that is double the size of the steady state velocity. We explain the occurrence of this overdamping due to the relative small Reynolds number Re = 20 in comparison to the Weissenberg number and the low percentage of Newtonian viscosity since $\beta = 0.1$.

In Figure 6.28 we also observe a velocity overshoot for SimB at $(x,y,z)=(0.048,0.048,0.048)$ (i.e. centre of $\Omega_{\text{Sim B}}$), but this time we note an additional undershoot and a further increase in u afterwards. Beside other differences between FENE SimA and SimB, both computations differ in the chosen Reynolds number Re which we increased by a factor of 10 for the second simulation. Consequently, the elasticity number El = Wi/Re is reduced by the same proportion. Moreover, we further discuss the development of τ_{xx} in Figure 6.28 which exhibits stochastic noise since $N_f = 4000$. By comparing u and τ_{xx} in Figure 6.28, we are able to comprehend

the explanation of Harlen [37] with regard to the velocity overshoots. If the velocity field has changed, a molecule adjusts its orientation delayed so that elastic effects occur later on. As a result, the system reaches a velocity that is actually higher than its Newtonian counterpart at the same time. We realise this behaviour in Figure 6.28 where we observe a further increase in τ_{xx} after u has reached a relative maximum at $t \approx 0.26$.

At last, we present results for the x-y plane $z = 0$ using values from Simulation B. In Figure 6.29 (a) - (c) we visualise the velocity field in flow direction at three different times which are $t = 0.26$ (maximum velocity overshoot), $t = 0.35$ (maximum velocity undershoot), and $t = 1.7$ (end of computation). We observe that the total velocity field for all cells in Figure 6.29 (a) is larger in size in comparison to (b). Nevertheless, we obtain the highest values for $\vec{u} = (u, 0, 0)$ at the end as the fluid velocity increases again after $t = 0.35$.

Note that the temporal evolution of u is smooth even though the stress tensor τ_{xx} shows stochastic oscillations with respect to time due to the low number of realisations per cell (cf. Figure 6.28). I.e., the stochastic noise is not present in the velocity field, rendering the Navier-Stokes-BCF model an adequate approach at least for the considered simulation case FENE SimB. Note further that the spatial profile of both u and τ_{xx} is smooth (cf. Figure 6.29).

We also observe the occurrence of overshoots in velocity for the simulations in Section 6.3.3 (4-1 Contraction Flow) and Section 6.3.4 (Flow Around a Sphere). This emphasises the importance of this effect for non-Newtonian calculations.
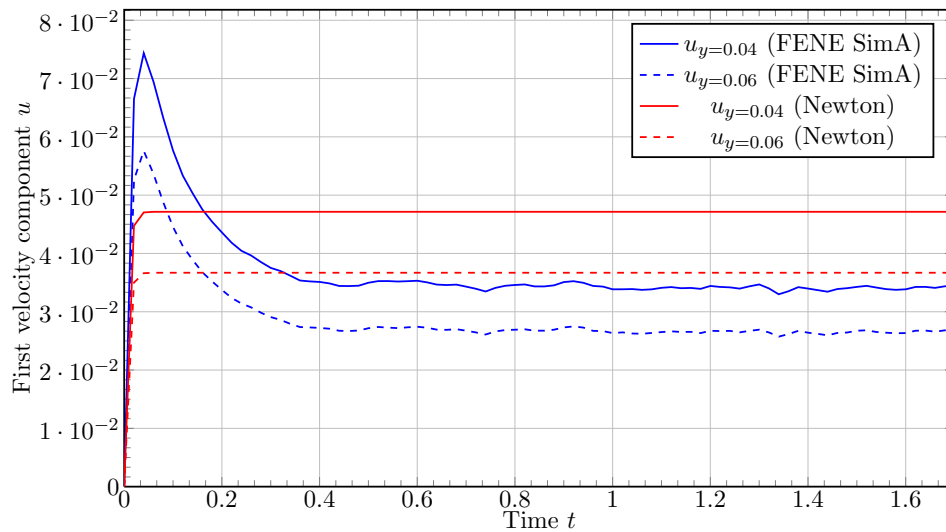
Figure 6.27: The figure compares the channel velocity for a Newtonian simulation with the results using a FENE spring force at two different positions. We measure u at the centre of the channel (i.e. $x = y = z = 0.04$) and at position $x = z = 0.04$ and $y = 0.06$. As expected, the channel velocity reaches its maximum at the centreline. Although the Reynolds number and the gravitational force are identical for the Newtonian and non-Newtonian case, we observe different steady state values. Furthermore, the FENE model features a velocity overshoot with an amplitude that is double the size of the result at t_{max}.
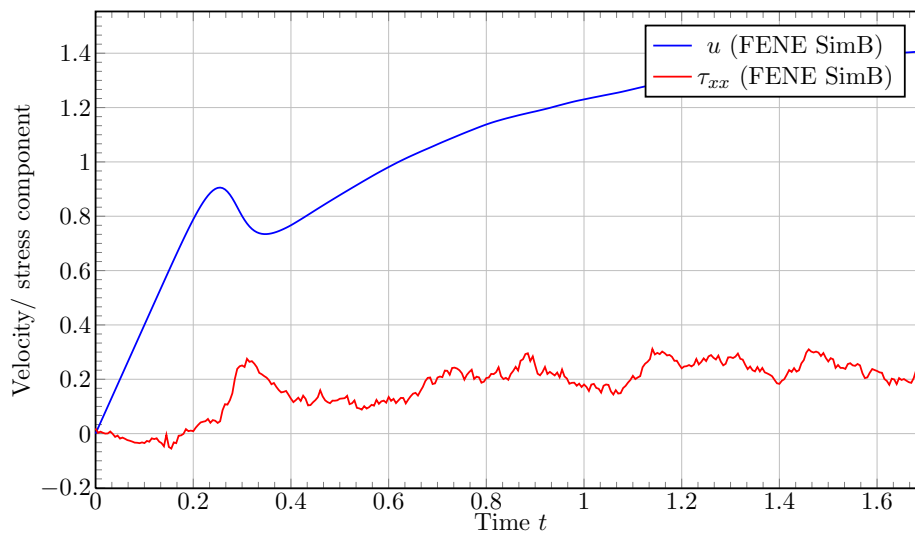
Figure 6.28: For the second simulation using a FENE spring force we compare the velocity in flow direction at the centre of $\Omega_{\mathsf{Sim\ B}}$ with the results for τ_{xx} at the same place. Following an argumentation from Harlen [37] we observe that the increase in τ_{xx} directly occurs after the velocity overshoot. This can be explained by the delayed extension of a dumbbell considering a changed flow field.

(a) u velocity component $(t = 0.26, \text{overshoot})$

(b) u velocity component $(t = 0.35 \text{ undershoot})$

(c) u velocity component $(t = 1.7\,t_{\max})$

(d) τ_{xx} stress component $(t = 0.35)$
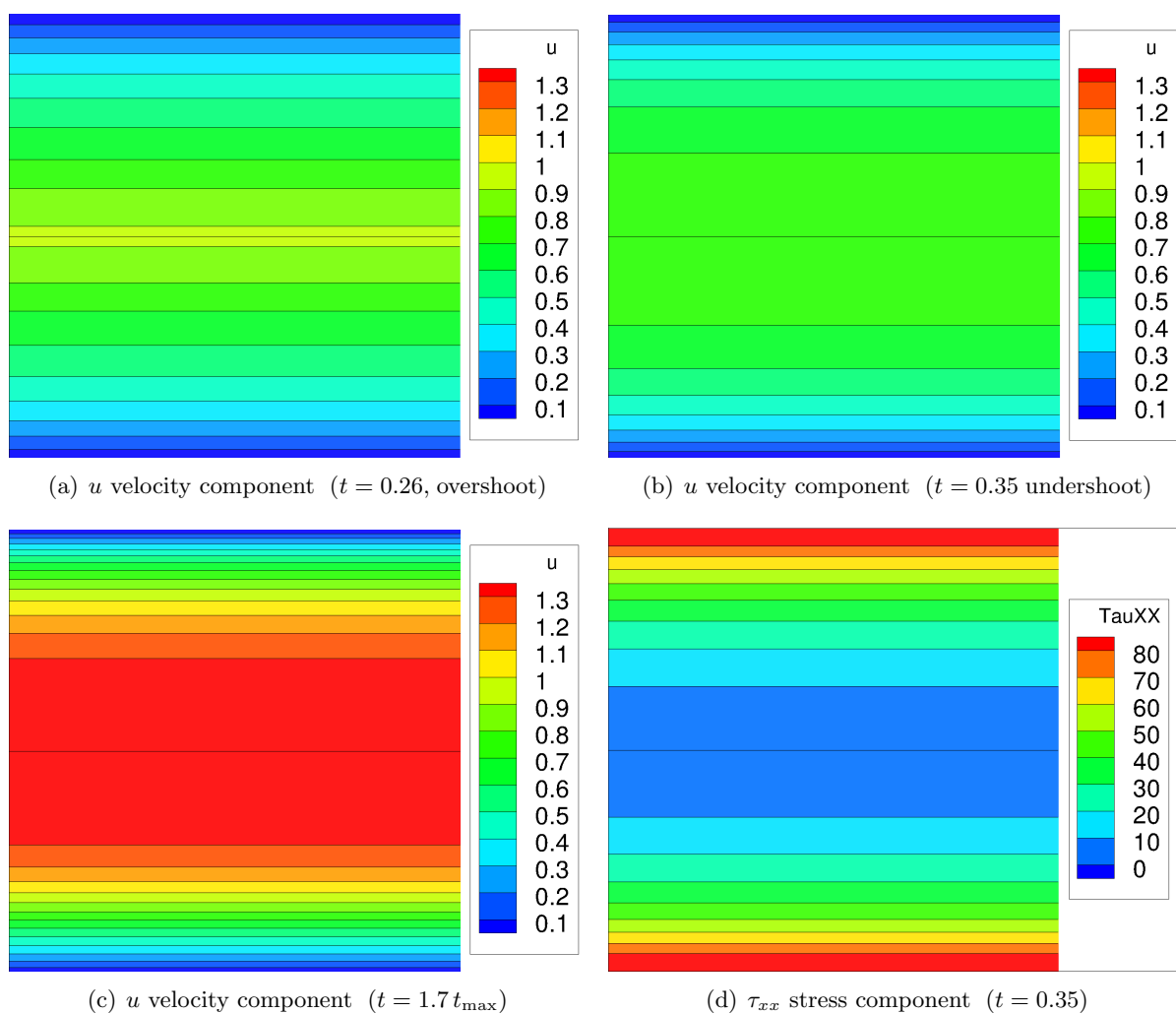
Figure 6.29: We visualise the velocity profile for the second FENE simulation with the velocity values on a x-y plane through the centre of Ω at three different process times. Indeed, the velocity field at the overshoot (a) exceeds the latter velocity field in (b). Figure (c) presents the velocity field at the end of the simulation. In Figure (d) we present the stress tensor component τ_{xx} at $t = 0.35$ (undershoot). As expected, the friction of the fluid at the channel walls leads to high stress tensor values.

6.3.3 Contraction Flow with ratio 4:1

**Description of Experiment**

A fluid in a contraction flow undergoes a contraction while passing from a wide channel into another one with a smaller diameter. The contraction experiment generates a complex flow as it features

- strong shearing near the walls and

- uniaxial extension along the centreline.

We illustrate a 4:1 planar contraction with a ratio of four to one between the upstream and the downstream channel in Figure 6.30.

Contraction flows are a classical benchmark problem in computational rheology as they are numerically challenging on the one hand and are relevant in industrial applications on the other hand. Since effects of shearing and extension occur during the experiment there are situations in which non-Newtonian fluids behave differently than their Newtonian counterparts. In particular, two effects that are often observed for contraction flows are vortex growth near the re-entrant corners and velocity overshoots along the centreline.

Nevertheless, up to now the mechanism for the vortex development is not understood completely since it depends not only on the flow parameters (Reynolds number, Weissenberg number, elasticity number, inflow velocity) but also on the geometry of the considered channel. For instance, Walters and Webster [92] have investigated the vortex development for polyacrylamide (PAA) in a water/ maltose syrup mixture and observed no vortex activity for a 4:1 planar contraction in a channel as in Figure 6.30 but very strong vortex activity for a 4.1:1 circular contraction in a tube. However, the elasticity of the fluid seems to be the major parameter for vortex growth. For further information on different kinds of contraction flows we refer to Chapter 8 of Owens and Phillips [68].
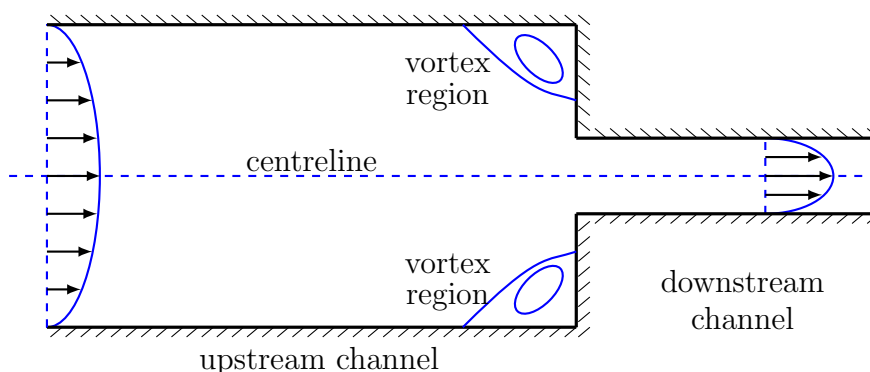
Figure 6.30: The figure illustrates the geometry for a 2D contraction flow with a ratio four to one between the upstream and the downstream channel. In the viscoelastic flow case two important characteristics of the contraction flow are vortex dynamics near the re-entrant corners and velocity overshoots along the axis of symmetry (centreline). As the problem is symmetric along the centreline, most numerical simulations cut the domain into halves to reduce the computational effort.

Three-dimensional Numerical Simulation

As contraction flows are common benchmark experiments, there are various results for macroscopic viscoelastic models (e.g. Xue et al. [95] for the Oldroyd-B and PTT model) and several simulations for multiscale models like Bonvin [12] for a coupled 2D BCF model and Knezevic [50] for a 2D Navier-Stokes-Fokker-Planck system. On the contrary, since most simulations differ in the chosen parameters and geometric dimensions they are not comparable among each other.

In this thesis, we perform an analogous simulation to Knezevic [50] but we now describe the setting in three dimensions and do not halve the problem in size at the centreline. Our simulation considers a problem with an extension of 10 units in the x-direction, 8 units in the direction of the y-axis and an extension of 1 unit in the direction of z (cf. Figure 6.31). We employ a parabolic inflow profile at $x = 0$ that corresponds to a steady Poiseuille flow with $u_{\max} = 1$ at the centreline. Furthermore, we use homogeneous Neumann boundary conditions at $x = 10$, set no-slip boundary conditions at $y = 0$ and $y = 8$ as well as for the obstacle surface, and apply periodic boundary conditions in the direction of z. We summarise the parameters for the subsequent simulation in Table 6.15.

4:1 Contraction Flow (Navier-Stokes-BCF)		
Grid resolution		$100 \times 80 \times 10$ cells
Physical domain		$[0, 10] \times [0, 8] \times [0, 1]$
Simulation time	t_{max}	6.0
Reynolds number	Re	1
Newtonian viscosity	β	0.59
Weissenberg number	Wi	0.8
Realisations per cell	N_f	8000
Maximum spring extension	b (FENE)	12.0
Time Discretisation		Semi-implicit
Convective Terms		SMART

Table 6.15: The 4:1 contraction flow uses a comparatively low Reynolds number to emphasise elastic behaviour. To prevent restrictions in time-step size, we employ an implicit discretisation of the diffusive velocity terms in the Navier-Stokes equations. However, since the percentage of Newtonian viscosity β is high, viscous effects dominate the fluid behaviour.

Next, we illustrate the Poiseuille profile at the inflow boundary in Figure 6.31. Bonvin [12] points out that this is only a reasonable assumption for low and moderate Weissenberg numbers as we use for this simulation. For higher Weissenberg numbers a FENE fluid exhibits shear thinning effects (cf. Section 2.1.3) that act on the inflow profile. However, in our case the error in the inflow velocity profile is negligible. Note that this effect does not occur for Newtonian fluids as well as for those viscoelastic models that do not include shear thinning effects (e.g. the Oldroyd-B model).

In Figure 6.32 and Figure 6.33 we present approximations for the velocity field as well as for the stress tensor field. Since the flow system reaches a steady state after process time $t \approx 1.5$ our result at $t = 6$ visualises an identical flow field with the exception of small stochastic noise in $\boldsymbol{\tau_p}$. Furthermore, we show the velocity field at $t = 0.05$ just after the initialisation.
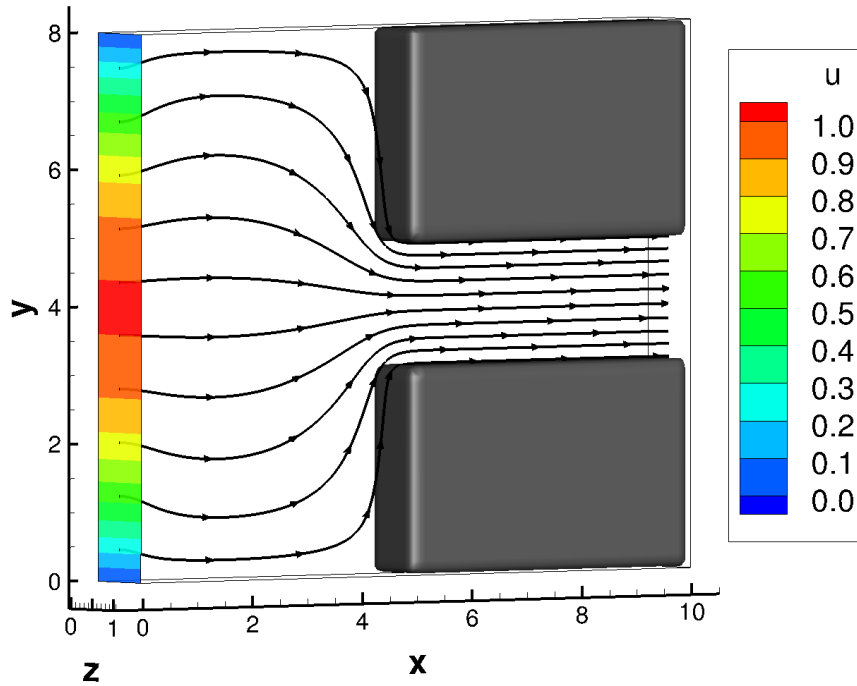
Figure 6.31: We consider a 3D contraction flow with periodic boundary conditions in the direction of z so that the results are comparable with a two-dimensional computation in a x-y plane. Furthermore, we illustrate the flow field by setting ten stream traces at the inflow boundary. The plane at $x = 0$ illustrates the Poiseuille inflow profile.

The analysis of the stress tensor field in Figure 6.33 reveals that the first stress tensor component τ_{xx} occurs primarily at the channel walls whereas the shear stress component τ_{xy} and the second normal stress component τ_{yy} emerge near the corner singularities. This result is in agreement with the investigations from Bonvin [12] and Knezevic [50]. We further note that the third stress component τ_{zz} in Figure 6.33 (d) is not zero, although we only consider a two-dimensional problem. This is in agreement with the results in literature (cf. Chapter 4 of Lozinski [56]), because a dumbbell molecule in a 2D flow still has three degrees of freedom as the physical space Ω (2D) and the configuration space D (3D) are nearly independent from each other.

Figure 6.34 (a) presents a detailed view of the shear stress contour τ_{xy} near the upper obstacle. We observe a characteristic form for the contour lines that is also noted in extensional flow simulations from Bonvin [12]. He interprets the result by shear thinning effects that occur near the corner singularity. Since shear thinning behaviour cannot be described adequately with the Oldroyd-B model (cf. Section 2.2.2), more advanced models (e.g. FENE) have to be applied to analyse the complex characteristics of most viscoelastic fluids.

For a more detailed analysis of the flow field in the steady state at $t = 6$, we plot the evolution of several relevant variables at two characteristic lines through the channel. Furthermore, we measure the temporal evolution of the velocity component u at the end of the downstream channel. For clarification, we draw the rough position of the evaluation points in Figure 6.34 (b) and additionally state the precise coordinates of measurement. In Figure 6.35 we present

(a) u velocity component $(t = 0.05)$

(b) u velocity component $(t = 6.0)$

(c) v velocity component $(t = 0.05)$

(d) v velocity component $(t = 6.0)$

(e) absolute velocity $|\vec{u}|$ $(t = 0.05)$

(f) absolute velocity $|\vec{u}|$ $(t = 6.0)$
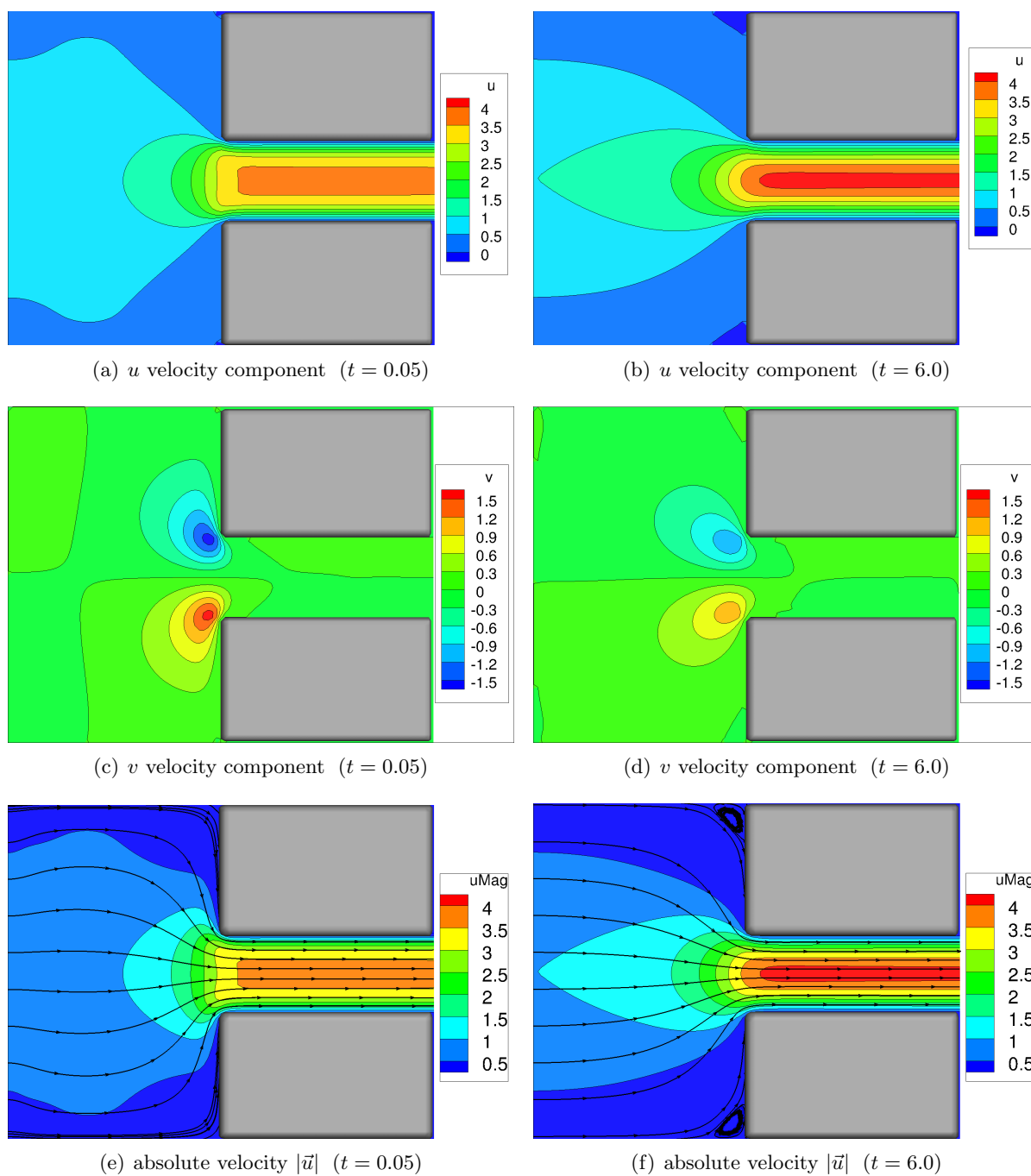
Figure 6.32: The figure displays the velocity components u and v as well as the velocity magnitude $|\vec{u}|$ shortly after the beginning of the simulation and when the system has reached a steady state. Due to the reduced cross section of the downstream channel the velocity magnitude is strongly increased. We further observe a small vorticity development near the re-entrant corners.

(a) normal stress component τ_{xx} $(t = 6.0)$

(b) shear stress component τ_{xy} $(t = 6.0)$

(c) normal stress component τ_{yy} $(t = 6.0)$

(d) normal stress component τ_{zz} $(t = 6.0)$

(e) first normal stress difference S_1 $(t = 6.0)$

(f) second normal stress difference S_2 $(t = 6.0)$
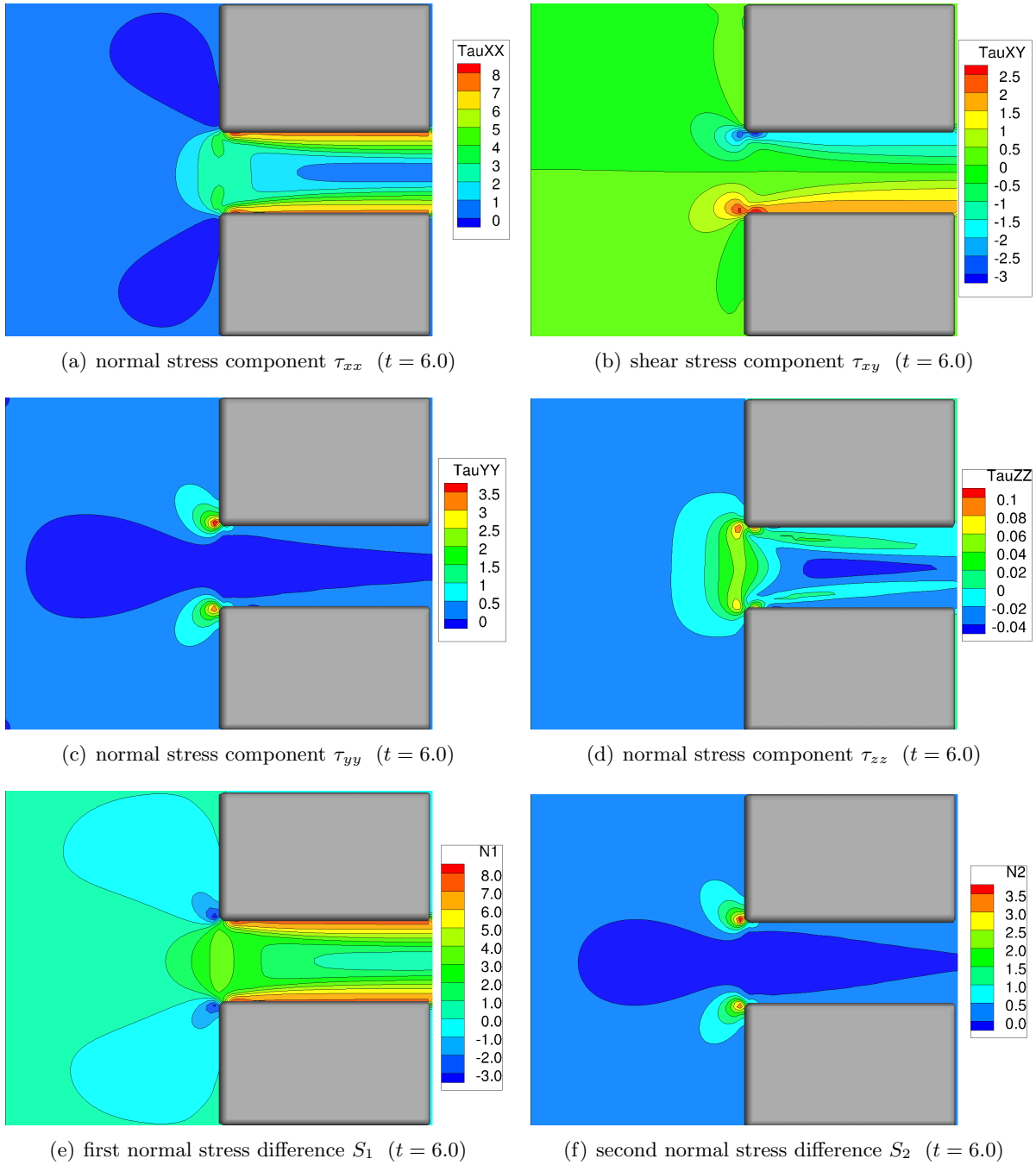
Figure 6.33: The stress tensor components reach its maxima near the corner singularity with the exception of τ_{xx}. This can be explained by considering the high fluid velocity in the contracted channel. Although we consider a two-dimensional problem due to periodic boundary conditions in z we observe comparatively small stress in the τ_{zz} component. This is in agreement with the results in literature since even problems in a two-dimensional physical space Ω exhibit a 3D configuration space D (cf. Chapter 4 of Lozinski [56]).

(a) Detail of τ_{xy} near upper obstacle ($t = 6.0$)

(b) Illustration of evaluation lines and point in Figures 6.35, 6.36, and 6.37
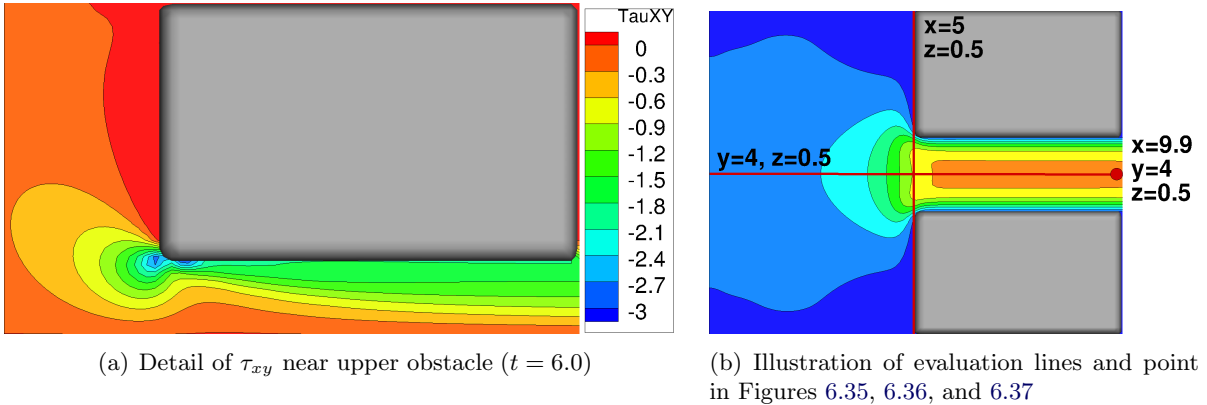
Figure 6.34: The left figure presents a zoom of the corner region showing the stress tensor component τ_{xy} which reveals a characteristic shape for the contour lines. In the right figure we have marked the evaluation points from which we extract flow field data represented in Figures 6.35, 6.36, and 6.37.

the results for a measurement at the centreline defined by $(x_c, 4, 0.5)$, $x_c \in [0, 10]$. As τ_{xy} and the velocity component v change their sign at the centreline, we do not plot their values at this position. The channel contraction starts at $x = 5$ so that we observe relative maxima for the normal stress tensor components at the beginning of the downstream channel. Obviously, the velocity in flow direction increases strongly due to a smaller cross section at the contraction.

The data measurement in Figure 6.36 visualises the growth of the u velocity component and the stress tensor components τ_{xx} and τ_{xy} in front of the downstream channel. Since the contraction has an extension from $y = 3$ to $y = 5$, we perceive a maximum amplitude for the stress tensor near the corners of the obstacle.

At last, we perform a velocity measurement of the first velocity component u at the end of the downstream channel. As mentioned before (cf. Section 6.3.2), a viscoelastic fluid exhibits velocity overshoots at the centreline which are not observed for Newtonian fluids. For comparison, we have used the parameters in Table 6.15 for an analogue Newtonian computation. In contrast to the viscoelastic case, we set $\beta = 1$ and ignore the Weissenberg number Wi as well as the coefficients b and N_f. We present the results for the velocity comparison in Figure 6.37. Obviously, we recognise an overshoot at $t = 0.3$ and an undershoot at $t = 1.1$ for the FENE model which are not present for the Newtonian case. Additionally, the Newtonian case reaches its steady state earlier after about $t = 1.2$ in contrast to $t = 1.5$ for the FENE fluid. However, as the percentage of Newtonian viscosity in the simulated FENE fluid is comparatively high (i.e. $\beta = 0.59$ in Table 6.15) the differences in u are not very pronounced but become the more obvious the more β is reduced. A further difference between both simulations lies in the computational effort which we will analyse subsequently.

Computation Time

We have obtained our results for the FENE fluid by computing 70 hours on 64 processors of the HPC cluster Himalaya (cf. Chapter 5.6). The analogue computation for the Newtonian flow case took 1 hour on 8 processors. This yields an increase of the computational effort by a
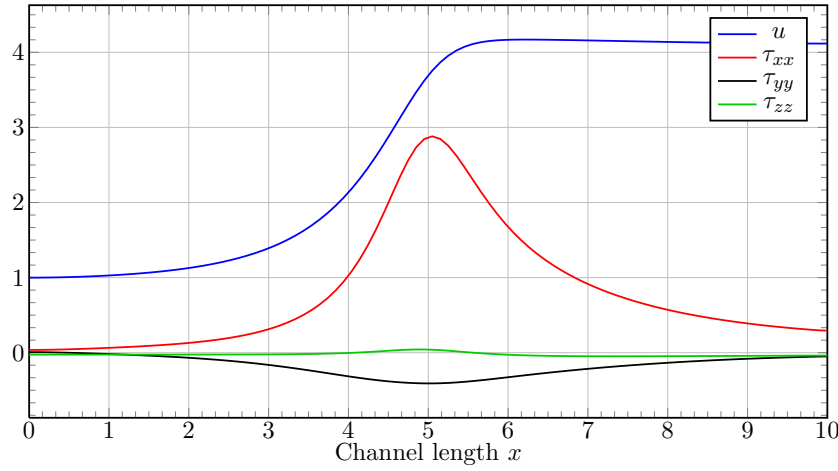
Figure 6.35: The figure exhibits the flow data at the horizontal centreline marked in Figure 6.34 (b). We observe maxima for the normal stress components near the contracted channel entry at $x = 5$.

factor of 560 under the assumption of perfect parallel efficiency. However, one has to consider that the Newtonian computation only requires a few iterations to solve the pressure Poisson problem after the steady state has been reached. Due to a small stochastic noise in $\vec{u}$ and p the multiscale calculation normally does not reach a steady state. Indeed, since there is an interaction between $\boldsymbol{\tau_p}$ on the one hand and $\vec{u}$ and p on the other hand this also increases the number of iterations that the BiCGStab solver requires to obtain p. For each calculation we have to carefully consider which grid resolution and number of configuration fields N_f can actually be computed in an acceptable amount of time.
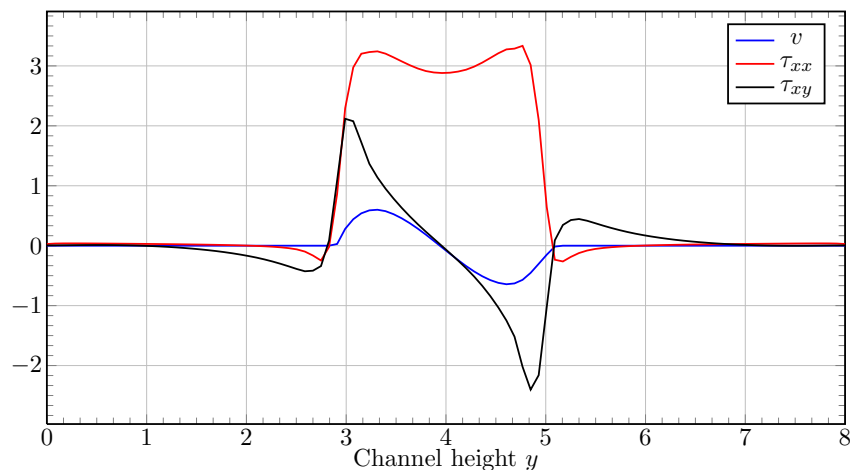
Figure 6.36: In this figure we measure velocity and stress field values on a vertical line in y-direction at $x = 5$ and $z = 0.5$. Here we observe peaks for the stress tensor components near the corners.
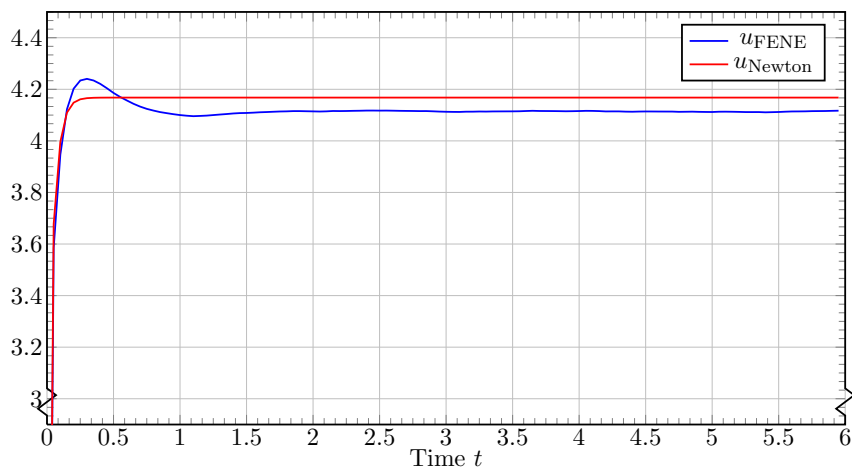

Figure 6.37: The figure presents a comparison for the velocity component u between the Newtonian fluid and its FENE counterpart. We observe an over- and an undershoot for the non-Newtonian fluid which is not featured by the Newtonian computation. The phenomenon is well known for contraction flow measurements at the centreline.

6.3.4 Flow Around a Sphere

The motion of a sphere through a viscous fluid with a low Reynolds number is a further classical benchmark problem for Newtonian as well as for non-Newtonian fluids. The non-Newtonian case exhibits several differences to the Newtonian experiment since we observe

- regions of strong shearing especially between the sphere and the surrounding channel walls and

- the occurrence of extensional effects especially near the centreline in the wake of the sphere.

Due to shear effects, we observe velocity overshoots for the sphere in the viscoelastic case that correlate to the chosen Weissenberg number. In general, the higher the Weissenberg number, the higher the amplitude of the first velocity overshoot. For low Weissenberg numbers the frequency of the oscillation is increased in exchange for the reduced amplitude. Interestingly, viscoelastic flows with low Weissenberg numbers can have such velocity undershoots that the flow direction is inversed for a short period of time (*sphere bouncing*). An explanation of this effect was given by Harlen [37]. As the dumbbell system requires to change its orientation and extension for a new velocity field, the elastic contribution to the drag on the sphere reaches its final value at a later point in time. Accordingly, the sphere may reach a higher speed as it would normally be the case without elastic effects. This was first confirmed in simulations by Zheng and Phan-Thien [99] in 1992.
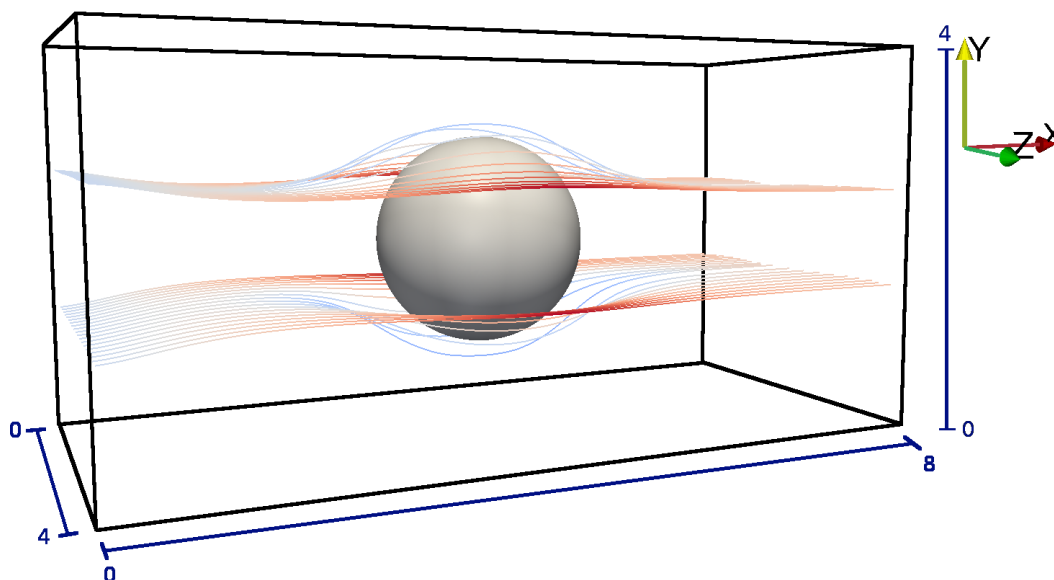
Figure 6.38: We consider the flow around the sphere on a physical domain with 8 units in x-direction as well as 4 units in the direction of y and z. The sphere has a radius of one unit with its centre at $(x, y, z) = (4, 2, 2)$. Note that we employ no-slip boundary conditions in the y-direction but use periodic boundary conditions in the direction of the z-axis. We illustrate the velocity field by placing several steamtraces around the sphere.

We simulate the flow around a sphere with radius $r = 1$ on a domain with a 4×4 cross section and a length of 8 units in flow direction x. This setting corresponds to the geometry in Knezevic [50]. A complete analysis of the problem for a stochastic 2D micro-macro approach can be found in an article from Vargas, Manero, and Phillips [90]. We illustrate the physical domain Ω and the flow field around the sphere in Figure 6.38. In contrast to the flow field in Knezevic [50], we employ no-slip boundary conditions in y-direction and periodic boundary conditions in the direction of z. Thereby, we can show that the velocity overshoot effect only occurs in the flow domain between the sphere and the no-slip wall and not in z-direction. For the inflow domain at $x = 0$ we chose $u_{\text{inflow}} = 1$ and apply homogeneous Neumann boundary conditions for u_{outflow} at $x = 8$. We summarise the parameters of this calculation in Table 6.16. Since we have decided for $Re = 0.5$ and $Wi = 1$ we calculate the problem with a comparatively high elasticity number $El = 2$.

Flow Around a Sphere (Navier-Stokes-BCF)		
Grid resolution		$80 \times 40 \times 40$ cells
Physical domain		$[0, 8] \times [0, 4] \times [0, 4]$
Simulation time	t_{max}	4.0
Reynolds number	Re	0.5
Newtonian viscosity	β	0.59
Weissenberg number	Wi	1.0
Realisations per cell	N_f	8000
Maximum spring extension	b (FENE)	12.0
Time Discretisation		Semi-implicit
Convective Terms		SMART

Table 6.16: The table summarises the simulation parameters which are identical to the simulation in Knezevic [50].

In Figure 6.39, we analyse the velocity component u at two different positions P_1 and P_2 in Ω. Using the illustration from Figure 6.38 we recognise that the first measuring point $P_1 = (4, 3.5, 2)$ lies directly above the sphere in y-direction and the second measuring point $P_2 = (4, 2, 3.5)$ has been placed beside the sphere in z-direction. Interestingly, velocity overshoots only occur at position P_1 since we employ no-slip boundary conditions solely in y-direction. We further note that this is caused by shearing effects as the shear stress component $\tau_{xy}(P_1)$ is unequal to zero in contrast to $\tau_{xy}(P_2) = 0$. As a result, we realise a coherence between velocity overshoot effects and the emergence of shear stress.

We analyse the velocity field as well as the first normal and shear stress tensor field around the sphere at $t_{\max} = 4$ in Figure 6.40. As expected, we observe high shear stresses τ_{xy} above and below the sphere (cf. Figure 6.40 (d)) but not at its sides (cf. Figure 6.41 (b)). In contrast, the normal stress component τ_{xx} becomes dominant at the left and right side of the sphere (due to periodic boundary conditions in z-direction) and at its back in flow direction (cf. Figure 6.40 (c) and Figure 6.41 (a)). The latter result coincides with strong extensional effects which are reported in literature for the domain behind the sphere.

Next, in Figure 6.41 we indicate the stress that occurs directly on the surface of the sphere. Again, we note strong shear stress τ_{xy} at the top of the sphere and first normal stress τ_{xx} at its
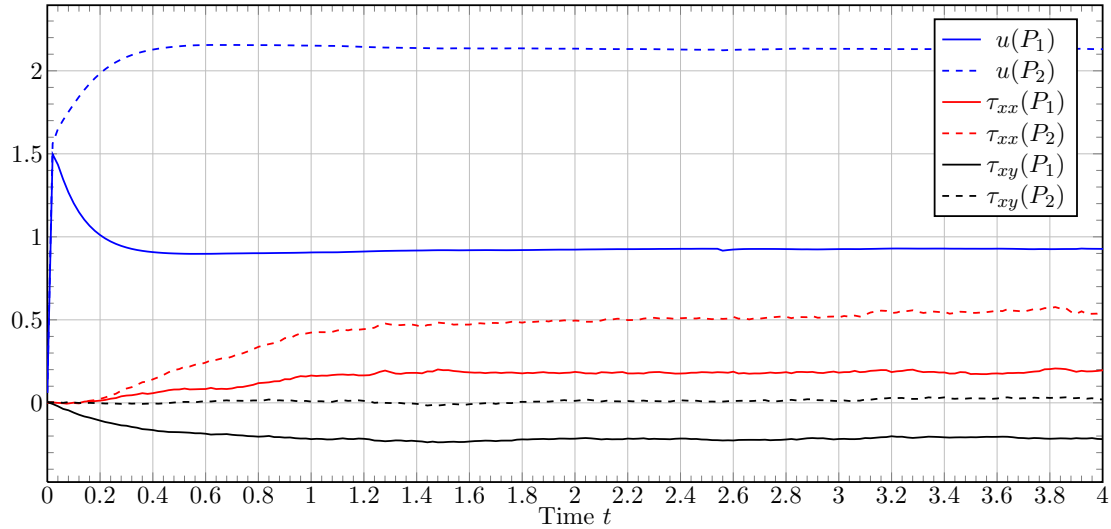
Figure 6.39: We only observe a velocity overshoot at position P_1 where u reaches a maximum of 1.5 directly after initialisation and a steady state value of 0.9. This only correlates with the occurrence of shear stress τ_{xy} at position P_1. Therefore, we observe a stronger normal stress component τ_{xx} due to a higher fluid velocity u at position P_2 beside the sphere.

side. In comparison to τ_{xx}, the other normal stress components τ_{yy} and τ_{zz} reach comparatively low amplitudes.

Computation Time

At last, we state the computational effort that is required to simulate a multiscale non-Newtonian flow with the listed parameters. The simulation took about 97 hours using 64 processors in total (cf. Chapter 5.6 on parallelisation and the computer architecture). In comparison, a Newtonian calculation with analogue parameters required about 2 hours with 8 processors. Accordingly, the computation time is increased by a factor of 400 for the setting in Table 6.16.

As a result, one has to consider that 3D multiscale flow simulations require an enormous effort so that this kind of computation has become possible only recently due to more powerful supercomputers.
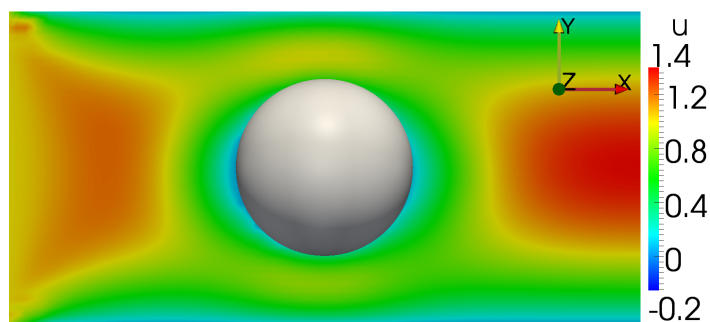
(a) u velocity component at $z = 2$ $(t = 4.0)$
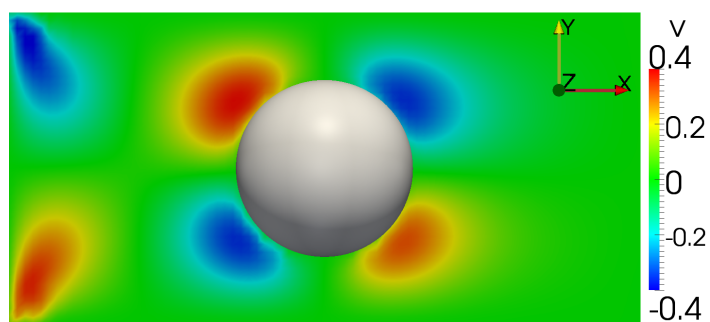
(b) v velocity component at $z = 2$ $(t = 4.0)$
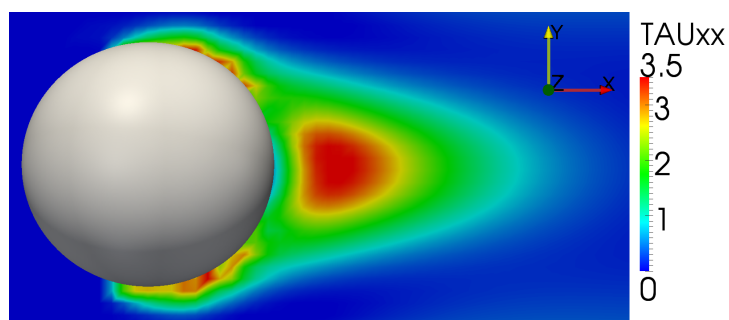
(c) τ_{xx} stress component extract at $z = 2$ $(t = 4.0)$
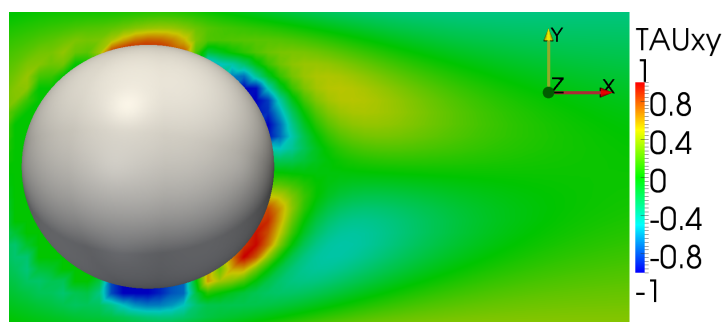
(d) τ_{xy} stress component extract at $z = 2$ $(t = 4.0)$

Figure 6.40: All figures display the stress on the plane $z = 2$ but (c) and (d) concentrate on a magnified extract around the sphere. We observe high normal stress τ_{xx} at the averted side of the sphere as well as shear stress τ_{xy} at its top and bottom. We conclude that the sphere possesses regions with dominant shear tension at the top and bottom side which coincides with the velocity overshoot in u that we observe in Figure 6.39 for position P_1.

(a) τ_{xx} stress component at $x = 4$ $(t = 4.0)$

(b) τ_{xy} stress component at $x = 4$ $(t = 4.0)$

(c) τ_{xx} on the sphere $(t = 4.0)$

(d) τ_{xy} on the sphere $(t = 4.0)$

(e) τ_{yy} on the sphere $(t = 4.0)$

(f) τ_{zz} on the sphere $(t = 4.0)$
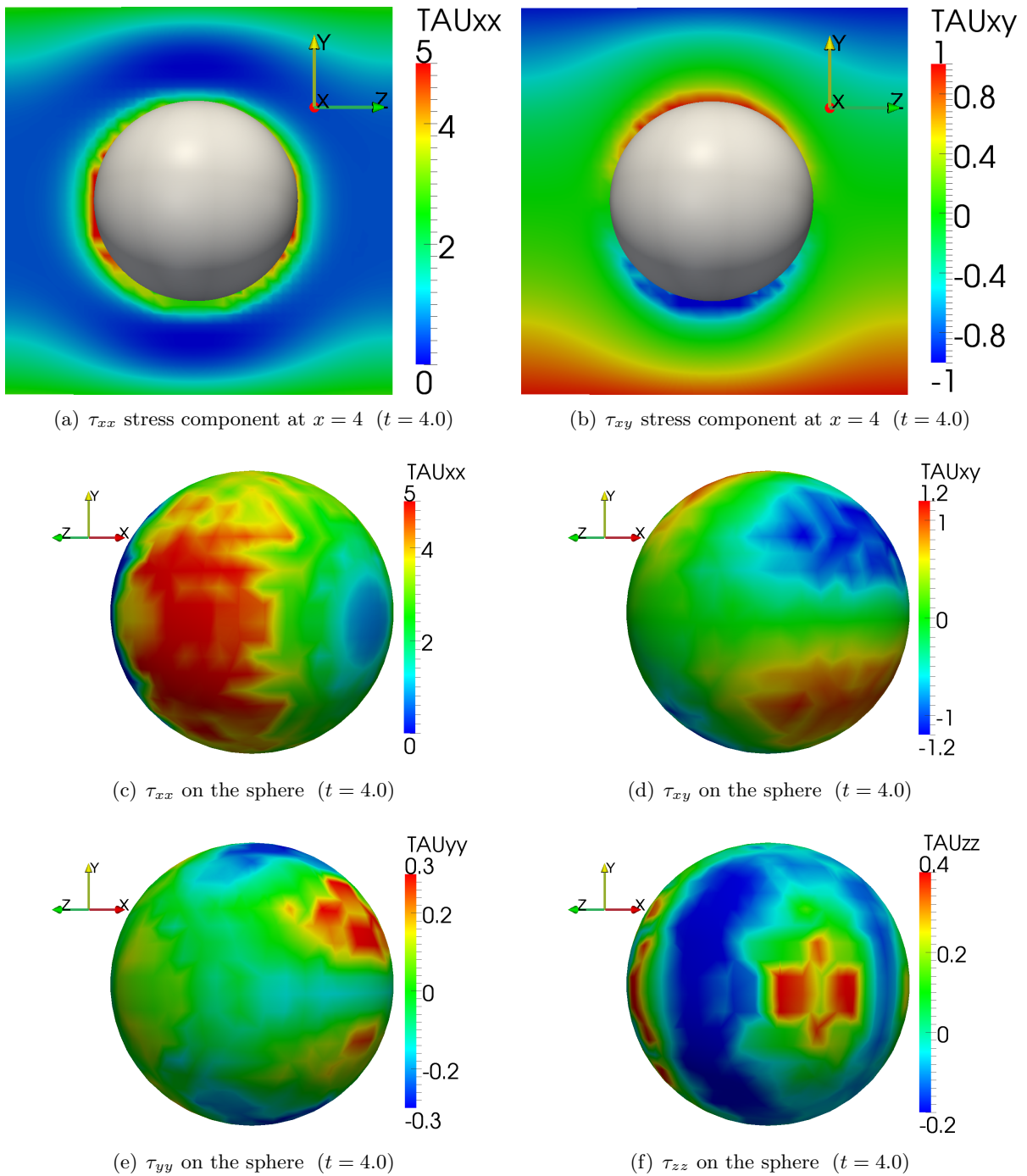
Figure 6.41: In (a) and (b) we present the stress on a y-z plane through the centre of the sphere. We only observe shear stress occurrence τ_{xy} for those sides of the sphere which lie in direction of a no-slip wall. The figures (c)-(f) illustrate the stress components τ_{xx}, τ_{xy}, τ_{yy}, and τ_{zz} on the surface of the sphere. Due to the chosen boundary conditions, we observe high normal stress τ_{xx} on the sides of the sphere in z-direction and regions of strong shearing at top and bottom in y-direction. The other normal stress contributions are comparatively small.

7 Conclusion

Summary

In this thesis, we investigated and implemented a multiscale FENE model for dilute polymeric fluids. We have chosen this approach due to fundamental modelling errors of macroscopic constitutive equations even in simple flow fields (e.g. homogeneous extensional flows). The main advantages of a nonlinear FENE spring force are

- an adequate description of molecule orientation for a changed flow field and

- a correct description of molecule extension.

Although macroscopic models obtained by closure approximations often simulate one of these aspects correctly, their predictions for the other are mediocre at best.

Since our multiscale model can be described in the form of a Fokker-Planck equation on the one hand or an equivalent stochastic formulation on the other hand, we discussed both formulations. We solved the deterministic Fokker-Planck equation with a spectral method approach achieving spectral accuracy in asymptotics for two-dimensional homogeneous flow fields. Furthermore, we

- implemented an Euler-Maruyama scheme for the time-integration of the two- and three-dimensional stochastic equations in homogeneous flow fields,

- analysed an equilibrium control variate for variance reduction, and

- introduced a method for generating initial configurations that are distributed according to the FENE probability density function.

We demonstrated that the stochastic approach impressively succeeds in simulating strong shear and extensional flow problems with high Weissenberg numbers up to 10.

For the description of three-dimensional, transient, polymeric fluids we coupled a stochastic BCF method using a FENE spring force with the NaSt3DGPF flow solver. Note that the underlying polymeric equation is six-dimensional in this case. We observed that the BCF method led to results that were noisy in time, as with every stochastic method, but more importantly smooth in physical space. Since the polymeric stress acts on the momentum equations only via its divergence in physical space, it caused weak variations in the velocities as well as in the pressure term so that their oscillations were reduced by a factor of 100 in comparison to the stress tensor noise.

Concerning the immense complexity of a six-dimensional problem, we did not only have to parallelise our Navier-Stokes-BCF solver to reduce the computing time but also to restrict the amount of memory per processor so that it fitted into the main memory of a computer. We confirmed the velocity and stress tensor predictions for an extensional flow using our multiscale

scheme and extended this further to incorporate the Hookean and the FENE-P spring forces. Both models feature an equivalent macroscopic formulation which turns out to be the Oldroyd-B model in the case of a Hookean spring force. As the results for the Hookean dumbbell and the FENE-P spring significantly differed from the FENE predictions, we actually proved the necessity for a multiscale approach. Furthermore, we demonstrated the formal equivalence between the Oldroyd-B and the Hookean dumbbell model by analysing the predictions of an existing Oldroyd-B implementation in NaSt3DGPF with the Hookean spring that we implemented within the Navier-Stokes-BCF system.

Beside the extensional flow case, we applied our programme on three further fundamental flow problems which are

- a flow through an infinite channel,

- a 4:1 contraction flow, and

- a flow around a sphere.

Although there do not exist any detailed three-dimensional, multiscale FENE fluid results as far as we know, we were able to compare our simulations with practical experiments since the latter two problems are classical benchmark experiments. In accordance with physical observations, we identified the regions with strong shearing, regions with extensional effects and the domains with the occurrence of velocity overshoots in our simulations. Moreover, we observed that the major parameter for the stability of this model is not the accuracy of the stress tensor approximation but the smoothness of the stress field on the computational domain. As a conclusion, we presented a first-time implementation of a multiscale BCF approach that employs a FENE spring force into a three-dimensional, complex flow solver.

Future Perspectives

We conclude this thesis by considering possible future directions of research related to the problem of multiscale viscoelastic flow simulation.

Problems with high Weissenberg numbers. We showed that the stochastic FENE model copes with homogeneous, high Weissenberg number flow problems leading to oscillating stress tensor results in time (i.e. over- and undershoots of the stress tensor). It remains to be verified that a three-dimensional, transient flow solver can also handle the resulting over- and undershoot effects for the fluid velocities if we employ $Wi \geq 2$. However, this is a problem regarding the flow solver itself and not the stochastic approximation of the non-Newtonian stress tensor.

Advanced parallelisation techniques. Multiscale, three-dimensional flow problems in general require a parallelisation of the algorithm to gain reasonable computing time. We have shown that a three dimensional multiscale flow solver can be implemented efficiently and achieves excellent scale-up results (cf. Chapter 5.6). Recently, Nvidia introduced the parallel computing architecture CUDA that allows software developers to perform their calculations on the graphics processing unit (GPU). If the programme is adapted to CUDA, this leads to enormous increases in computing power. Our stochastic scheme

is perfectly suited to be used with CUDA as the problem requires a high computational effort but features a low communication overhead.

Free surfaces. Practical experiments with non-Newtonian fluids show results like the Weissenberg, the Barus and the tubeless siphon effect which are unknown for Newtonian liquids. For an adequate simulation of these effects, we have to implement our multiscale approach into a two-phase flow solver which NaSt3DGPF already provides.

More advanced multiscale models. Although we consider a complex FENE spring force, our polymeric molecule is actually represented by a dumbbell model. As real polymers have a very complex microstructure, it may be necessary to investigate more advanced bead-spring chain models and consider the interaction between surrounding molecules. This would lead to problems with more than six dimensions in space.

Sparse grid techniques. If we solved the Fokker-Planck equation directly instead of its stochastic interpretation, the result would contain no stochastic noise. Since the problem is six-dimensional for the multiscale dumbbell model, Knezevic [50] applied an operator splitting approach proposed by Lozinski and Chauvière [57, 20]. An interesting extension would be the direct solution of the six-dimensional problem using sparse grid methods in a similar manner as Delaunay et al. for steady flow problems [26]. Given sufficient smoothness, sparse grids allow a considerably reduced cost-benefit ratio compared to classical methods (cf. Bungartz and Griebel [17]). On the contrary, concerning the involved coefficients of the complexity estimates and the logarithmic terms, we cannot assume that the effective dimension of the problem can be reduced such that we have to cope with the full size of the problem (cf. Feuersänger [30]).

In summary, due to the complexity of high-dimensional polymers much exciting work remains to be done.

Bibliography

[1] MPICH - a freely available, portable implementation of MPI. http://www.mcs.anl.gov/research/projects/mpich2/.

[2] NaSt3DGPF - A Parallel 3D Free Surface Flow Solver. http://wissrech.ins.uni-bonn.de/research/projects/NaSt3DGPF/index.htm.

[3] The Message Passing Interface (MPI) standard. http://www-unix.mcs.anl.gov/mpi/.

[4] L. Arnold. *Stochastic differential equations: theory and applications.* Wiley-Interscience, 1974.

[5] J.W. Barrett and E. Suli. Existence of global weak solutions to some regularized kinetic models for dilute polymers. *Multiscale Modeling and Simulation*, 6(2):506–546, 2008.

[6] J.B. Bell, P. Colella, and H.M. Glaz. A second-order projection method for the incompressible Navier-Stokes equations. *Journal of Computational Physics*, 85(2):257–283, 1989.

[7] H. Bend. Non-Newtonian Fluid on a Speaker Cone. http://www.youtube.com/watch?v=3zoTKXXNQIU, November 2008.

[8] B. Bernstein, E.A. Kearsley, and L.J. Zapas. A study of stress relaxation with finite strain. *Journal of Rheology*, 7:391–410, 1963.

[9] R.B. Bird, R.C. Armstrongs, and O. Hassager. *Dynamics of Polymeric Liquids - Volume 1 Fluid Mechanics.* John Wiley and Sons Inc, Hoboken, 2. edition, 1987.

[10] R.B. Bird, R.C. Armstrongs, and O. Hassager. *Dynamics of Polymeric Liquids - Volume 2 Kinetic Theory.* John Wiley and Sons Inc, Hoboken, 2. edition, 1987.

[11] G. Böhme. *Strömungsmechanik nichtnewtonscher Fluide.* Vieweg+ Teubner Verlag, 2000.

[12] J.C. Bonvin. *Numerical simulation of viscoelastic fluids with mesoscopic models.* PhD thesis, Département de mathématiques, Ecole Polytechnique Fédérale de Lausanne, 2000.

[13] J.C. Bonvin and M. Picasso. Variance reduction methods for CONNFFESSIT-like simulations. *Journal of Non-Newtonian Fluid Mechanics*, 84(2-3):191–215, 1999.

[14] Z. Botev. Kernel Density Estimator. From MATLAB Central - An open exchange for the MathWorks MATLAB and Simulink user community. http://www.mathworks.com/matlabcentral/fileexchange/17204-kernel-density-estimation.

[15] J.P. Boyd. *Chebyshev and Fourier spectral methods.* Dover Pubns, 2001.

[16] C. Le Bris and T. Lelièvre. Multiscale modelling of complex fluids: A mathematical initiation. In *Multiscale Modeling and Simulation in Science*, volume 66 of *Lecture Notes in Computational Science and Engineering*. Springer, Berlin, 2009.

[17] H.J. Bungartz and M. Griebel. Sparse grids. *Acta Numerica*, 13:147–269, 2004.

[18] C. Canuto. *Spectral methods: Fundamentals in single domains*. Springer Verlag, 2006.

[19] C. Chauvière and A. Lozinski. Simulation of complex viscoelastic flows using the Fokker-Planck equation: 3D FENE model. *Journal of Non-Newtonian Fluid Mechanics*, 122(1-3):201–214, 2004.

[20] C. Chauvière and A. Lozinski. Simulation of dilute polymer solutions using a Fokker-Planck equation. *Computers & fluids*, 33(5-6):687–696, 2004.

[21] A.J. Chorin. Numerical solution of the Navier-Stokes equations. *Mathematics of Computation*, 22(104):745–762, 1968.

[22] S. Claus. Numerical Simulation of Unsteady Three-Dimensional Viscoelastic Oldroyd-B and Phan-Thien Tanner Flows. Diplomarbeit, Institut für Numerische Simulation, Universität Bonn, July 2008.

[23] R. Courant, K. Friedrichs, and H. Lewy. Über die partiellen Differenzengleichungen der mathematischen Physik. *Mathematische Annalen*, 100(1):32–74, 1928.

[24] R. Croce. Ein paralleler, dreidimensionaler Navier-Stokes-Löser für inkompressible Zweiphasenströmungen mit Oberflächenspannung, Hindernissen und dynamischen Kontaktflächen. Diplomarbeit, Institut für Angewandte Mathematik, Universität Bonn, Bonn, Germany, 2002.

[25] R. Croce, M. Griebel, and M. A. Schweitzer. A Parallel Level-Set Approach for Two-Phase Flow Problems with Surface Tension in Three Space Dimensions. Preprint 157, Sonderforschungsbereich 611, Universität Bonn, 2004.

[26] P. Delaunay, A. Lozinski, and R.G. Owens. Sparse tensor-product Fokker-Planckbased methods for nonlinear bead-spring chain models of dilute polymer solutions. In *CRM Proceedings and Lecture Notes*, volume 41, 2007.

[27] Q. Du, C. Liu, and P. Yu. FENE dumbbell model and its several linear and nonlinear closure approximations. *Multiscale Modeling and Simulation*, 4(3):709–731, 2005.

[28] Q. Du, C. Liu, and P. Yu. FENE dumbbell model and its several linear and nonlinear closure approximations. *Multiscale Modeling and Simulation*, 4(3):709–731, 2006.

[29] X. Fan. Viscosity, first normal-stress coefficient, and molecular stretching in dilute polymer solutions. *Journal of Non-Newtonian Fluid Mechanics*, 17(2):125–144, 1985.

[30] Chr. Feuersänger. *Sparse Grid Methods for Higher Dimensional Approximation*. Dissertation, Institut für Numerische Simulation, Universität Bonn, September 2010.

[31] B. Fornberg. *A practical guide to pseudospectral methods.* Cambridge Univ Pr, 1998.

[32] B. Fornberg and D. Merrill. Comparison of finite difference and pseudospectral methods for convective flow over a sphere. *Geophysical Research Letters*, 24:3245–3248, 1997.

[33] T.C. Gard. *Introduction to stochastic differential equations.* Marcel Dekker Inc - New York, 1988.

[34] M.I. Gerritsma. *Time dependent numerical simulations of a viscoelastic fluid on a staggered grid.* PhD thesis, 1996.

[35] M. Griebel, T. Dornseifer, and T. Neunhoeffer. *Numerical Simulation in Fluid Dynamics, a Practical Introduction.* SIAM, Philadelphia, 1998.

[36] P. Halin, G. Lielens, R. Keunings, and V. Legat. The Lagrangian particle method for macroscopic and micro-macro viscoelastic flow computations1. *Journal of Non-Newtonian Fluid Mechanics*, 79(2-3):387–403, 1998.

[37] O.G. Harlen. High-Deborah-number flow of a dilute polymer solution past a sphere falling along the axis of a cylindrical tube. *Journal of Non-Newtonian Fluid Mechanics*, 37(2-3):157–173, 1990.

[38] M. Herrchen and H.C. Öttinger. A detailed comparison of various FENE dumbbell models. *Journal of Non-Newtonian Fluid Mechanics*, 68(1):17–42, 1997.

[39] D.J. Higham. An algorithmic introduction to numerical simulation of stochastic differential equations. *SIAM review*, 43(3):525–546, 2001.

[40] R.R. Huilgol and N. Phan-Thien. *Fluid mechanics of viscoelasticity.* Elsevier Amsterdam, 1997.

[41] M.A. Hulsen, A.P.G. Van Heel, and B. Van den Brule. Simulation of viscoelastic flows using Brownian configuration fields. *Journal of Non-Newtonian Fluid Mechanics*, 70(1-2):79–101, 1997.

[42] Y.K. Hyon, Q. Du, and C. Liu. An enhanced macroscopic closure approximation to the micromacro FENE model for polymeric materials. *Multiscale Model. Simul*, 7:978–1002, 2008.

[43] D.D. Joseph. *Fluid dynamics of viscoelastic liquids.* Springer New York, 1990.

[44] G. Kallianpur. *Stochastic filtering theory.* Springer Berlin, 1980.

[45] G. Karniadakis and S.J. Sherwin. *Spectral/hp element methods for CFD.* Oxford University Press, USA, 1999.

[46] A. Kaye. Non-Newtonian flow in incompressible fluids. *College of Aeronautics*, 1962.

[47] R. Keunings. On the high Weissenberg number problem. *Journal of Non-Newtonian Fluid Mechanics*, 20:209–226, 1986.

[48] M. Klitz. Homogenised Fluid Flow Equations in Porous Media with Application to Permeability Computations in Textiles. Diplomarbeit, Institut für Numerische Simulation, Universität Bonn, July 2006.

[49] D. Knezevic. Finite Element Methods for Deterministic Simulation of Polymeric Fluids. 2007.

[50] D. Knezevic. *Analysis and Implementation of Numerical Methods for Simulating Dilute Polymeric Fluids.* PhD thesis, Balliol College, University of Oxford, 2008.

[51] D.A. Kopriva. *Implementing Spectral Methods for Partial Differential Equations: Algorithms for Scientists and Engineers.* Springer Verlag, 2009.

[52] H.A. Kramers. The behavior of macromolecules in inhomogeneous flow. *The Journal of Chemical Physics*, 14:415, 1946.

[53] M. Laso and H.C. Öttinger. Calculation of viscoelastic flow using molecular models: the CONNFFESSIT approach. *Journal of Non-Newtonian Fluid Mechanics*, 47:1–20, 1993.

[54] T. Li and P. Zhang. Mathematical analysis of multi-scale models of complex fluids. *Commun. Math. Sci*, 5(1):1–51, 2007.

[55] G. Lielens, P. Halin, I. Jaumain, R. Keunings, and V. Legat. New closure approximations for the kinetic theory of finitely extensible dumbbells1. *Journal of non-newtonian fluid mechanics*, 76(1-3):249–279, 1998.

[56] A. Lozinski. *Spectral Methods for Kinetic Theory Models of Viscoelastic Fluids.* PhD thesis, Institut des sciences de l'énergie, EPFL Lausanne, 2003.

[57] A. Lozinski and C. Chauvière. A fast solver for Fokker-Planck equation applied to viscoelastic flows calculations: 2D FENE model. *Journal of Computational Physics*, 189(2):607–625, 2003.

[58] A. Lozinski, R.G. Owens, and J. Fang. A Fokker-Planck-based numerical method for modelling non-homogeneous flows of dilute polymeric solutions. *Journal of Non-Newtonian Fluid Mechanics*, 122(1-3):273–286, 2004.

[59] A. Lozinski, R.G. Owens, and T.N. Phillips. *Handbook of Numerical Analysis*, chapter The Langevin and Fokker-Planck Equations in Polymer Rheology. Elsevier Science B.V., Amsterdam, to appear (2010).

[60] C.W. Macosko and R.G. Larson. *Rheology: principles, measurements, and applications.* Wiley-Vch New York, 1994.

[61] A. Meister. *Numerik linearer Gleichungssysteme: Eine Einführung in moderne Verfahren. Mit Matlab-implementierung von C. Vömel.* Springer, 2007.

[62] M. Melchior and H.C. Öttinger. Variance reduced simulations of stochastic differential equations. *The Journal of Chemical Physics*, 103:9506, 1995.

[63] M. Melchior and H.C. Öttinger. Variance reduced simulations of polymer dynamics. *The Journal of Chemical Physics*, 105:3316, 1996.

[64] B. Mercier. An introduction to the numerical analysis of spectral methods. Springer Verlag, 1989.

[65] B. Øksendal. *Stochastic differential equations*. Springer Berlin, 1998.

[66] H.C. Öttinger. *Stochastic Processes in Polymeric Fluids*. Springer, Berlin, 1996.

[67] H.C. Öttinger, B. Van Den Brule, and M.A. Hulsen. Brownian configuration fields and variance reduced CONNFFESSIT. *Journal of Non-Newtonian Fluid Mechanics*, 70(3):255–261, 1997.

[68] R.G. Owens and T.N. Phillips. *Computational Rheology*. Lectures in Environmental Sciences. Imperial College Press, London, 2. edition, 2005.

[69] A. Peterlin. Hydrodynamics of macromolecules in a velocity field with longitudinal gradient. *Journal of Polymer Science Part B: Polymer Letters*, 4(4):287–291, 1966.

[70] R. Peyret and T.D. Taylor. *Computational methods for fluid flow*. Springer, Berlin, 1985.

[71] J.R. Prakash. Micro and macro in the dynamics of dilute polymer solutions: Convergence of theory with experiment. *Korea-Australia Rheology Journal*, 21(4):245–268, 2009.

[72] J.R. Prakash and H.C. Ottinger. Viscometric functions for a dilute solution of polymers in a good solvent. *Macromolecules*, 32(6):2028–2043, 1999.

[73] W.H. Press, B.P. Flannery, S.A. Teukolsky, W.T. Vetterling, et al. *Numerical recipes*. Cambridge university press, 2007.

[74] Psidot. Fano Flow. http://www.youtube.com/watch?v=aY7xiGQ-7iw, July 2007.

[75] Psidot. The Barus Effect. http://www.youtube.com/watch?v=KcNWLIpv8gc, July 2007.

[76] Psidot. The Weissenberg Effect. http://www.youtube.com/watch?v=npZzlgKjs0I, July 2007.

[77] Psidot. Three Viscoelastic Effects. http://www.youtube.com/watch?v=nX6GxoiCneY, July 2007.

[78] A.M. Quarteroni and A. Valli. *Numerical approximation of partial differential equations*. Springer, 2008.

[79] D.A. Randall. Numerical Modeling of the Atmosphere. 2009.

[80] M. Renardy. Mathematical analysis of viscoelastic flows. *Annual Review of Fluid Mechanics*, 21(1):21–34, 1989.

[81] M.N.O. Sadiku and R.J.A. Kiem. Newton-Cotes rules for triple integrals. *IEEE Southeastcon'90. Proceedings.*, pages 471–475, 1990.

[82] J.D. Schieber and H.C. Öttinger. The effects of bead inertia on the Rouse model. *The Journal of Chemical Physics*, 89(11):6972, 1988.

[83] G.D. Smith. *Numerical solution of partial differential equations: finite difference methods.* Oxford University Press, USA, 1985.

[84] R.I. Tanner. *Engineering rheology.* Oxford University Press, USA, 2000.

[85] R. Temam. Sur l'approximation de la solution des équations de Navier-Stokes par la méthode des pas fractionnaires (I). *Archive for Rational Mechanics and Analysis*, 32(2):135–153, 1969.

[86] G. Teschl. Ordinary differential equations and Dynamical Systems. *Lecture Notes from http://www. mat. univie. ac. at/gerald/ftp/book-ode/index. html*, 2004.

[87] D. Trebotich, P. Colella, and G.H. Miller. A stable and convergent scheme for viscoelastic flow in contraction channels. *Journal of Computational Physics*, 205(1):315–342, 2005.

[88] L.N. Trefethen. *Spectral methods in MATLAB.* Society for Industrial Mathematics, 2000.

[89] A.P.G. Van Heel. *Simulation of viscoelastic fluids - From microscopic models to complex macroscopic flows.* PhD thesis, Technische Universiteit Delft, 2000.

[90] R.O. Vargas, O. Manero, and T.N. Phillips. Viscoelastic flow past confined objects using a micro-macro approach. *Rheologica Acta*, 48(4):373–395, 2009.

[91] J. von Neumann. Various techniques used in connection with random digits, notes by GE Forsythe. *National Bureau of Standards, Applied Math Series*, 12:36–38, 1951.

[92] K. Walters and M.F. Webster. On dominating elastico-viscous response in some complex flows. *Philosophical Transactions of the Royal Society of London. Series A, Mathematical and Physical Sciences*, 308(1502):199–218, 1982.

[93] H.R. Warner Jr. Kinetic theory and rheology of dilute suspensions of finitely extendible dumbbells. *Industrial & Engineering Chemistry Fundamentals*, 11(3):379–387, 1972.

[94] E.W. Weisstein. Spherical Harmonic. From MathWorld–A Wolfram Web Resource. http://mathworld.wolfram.com/SphericalHarmonic.html.

[95] S.C. Xue, N. Phan-Thien, and R.I. Tanner. Three dimensional numerical simulations of viscoelastic flows through planar contractions. *Journal of Non-Newtonian Fluid Mechanics*, 74(1-3):195–245, 1998.

[96] P. Yu, Q. Du, and C. Liu. From micro to macro dynamics via a new closure approximation to the FENE model of polymeric fluids. *Multiscale Modeling and Simulation*, 3(4):895–917, 2005.

[97] P. Yu, Q. Du, and C. Liu. From micro to macro dynamics via a new closure approximation to the FENE model of polymeric fluids. *Multiscale Modeling and Simulation*, 3(4):895–917, 2005.

[98] A. Zettl. *Sturm-Liouville Theory.* American Mathematical Society, 2005.

[99] R. Zheng and N. Phan-Thien. A boundary element simulation of the unsteady motion of a sphere in a cylindrical tube containing a viscoelastic fluid. *Rheologica Acta*, 31(4):323–332, 1992.